

Karl Jakob Sand

On the Design and Simulation of Electromagnetic Traps and Guides for Ultra-Cold Matter

Thesis for the degree of Philosophiae Doctor

Trondheim, October 2010

Norwegian University of Science and Technology
Faculty of Information Technology, Mathematics
and Electrical Engineering
Department of Electronics and Telecommunications



NTNU – Trondheim
Norwegian University of
Science and Technology

NTNU

Norwegian University of Science and Technology

Thesis for the degree of Philosophiae Doctor

Faculty of Information Technology, Mathematics and Electrical Engineering
Department of Electronics and Telecommunications

© Karl Jakob Sand

ISBN 978-82-471-2317-1 (printed ver.)
ISBN 978-82-471-2318-8 (electronic ver.)
ISSN 1503-8181

Doctoral theses at NTNU, 2010:172

Printed by NTNU-trykk

Summary

The objective of this thesis is the design and simulation of new electromagnetic traps and guides for ultra-cold matter. The traps and guides are intended for future experiments with small amounts of alkali atoms to study the quantum-mechanical effects of condensation and coupling between trapped drops of cold matter.

The main results are with the development and simulation of new wire traps and guides based on the dressing effect realised in strong DC magnetic and RF fields of certain frequencies. Some designs are proposed using only trapping by the DC magnetic field.

The principal methodology used in the thesis is to first develop the necessary theory and design formulas to make an initial design, followed by analytical and numerical simulation of the effective trapping potential. This may be followed by optimization of the geometry and the DC driving currents to enhance the trapping performance of the structure.

A wire carrying both DC and RF currents is surrounded by a cylindrical minimum potential manifold and can be used as a guide for cold atoms. Bias rings are necessary around the wire to avoid a potential minimum of zero and to move the resulting circular potential minimum up and down along the wire. The minimum potential surfaces around two crossed or two parallel wires touch each other for certain critical values of the DC currents in the two wires. The DC currents must be in opposite directions in two parallel wires. Equations are derived in Chapter 2 for the distance to the circular minimum potential manifold for a single wire, for two crossed wires and for two parallel wires. It is then explained how prospective cold atom transfer between two crossed wires can be achieved by changing the magnitudes of the RF currents in the bias rings around the wires. Electrically controlled atom transfer between two parallel wires does not seem to be practical.

A four-wire cell trap made from two crossing pairs of parallel wires has been designed and optimized using a simple Matlab script. It can be used to trap both strong- and weak-field-seeking atoms and may possibly be used to study collision and entanglement between the two types of atoms. With only DC excitation the trap becomes a trap for weak-field-seeking atoms. It then unfortunately has a potential minimum of zero at its centre. A similar 3 x 3 wire dual-well trap has also been designed and optimized in Matlab. It is prospective for the study of entanglement of BEC matter placed in the two wells. A quite low potential barrier in the direction normal to the wire-planes when the two wells are merged could however entail that the trap is inadequate for this purpose or that additional bias fields are necessary.

Several multi-wire cell-grids that may find use as part of a quantum register are also described. The cell-grids can be stacked in three-dimensions and can trap both strong- and weak-field-seeking atoms. The optimization, also here performed in Matlab, showed weaknesses due to a lack of complexity. A different and better optimization technique is most likely necessary to improve the optimization further.

Scaling to micrometre and nanometre size is demonstrated in Chapter 3. When scaling to micrometre size thermally induced spin-flip transitions should be considered. Scaling to nanometre size demands that both thermally induced spin-flips and the effect of the Casimir-Polder force must be taken into account. The effect of the Casimir-Polder force is minimized by the use of carbon nanotubes as conductors. The minimum feasible trapping distance is expected to be no less than 100 nm from the surface of a carbon nanotube.

A four micro-wire cell and a 3 x 3 micro-wire structure, both adapted for future realization on a micro-machined substrate, are given as examples of micrometre size structures. Several nanometre size structures are also demonstrated. It is shown that prospective atom transfer between two crossed nanotubes can be done essentially in the same way as for two crossed wires.

A four-nanotube cell and several nanotube cell-grids are also exemplified. The depth of the trapping potential is found to be proportional to the RF frequency. If the RF frequency is increased then the DC current level must also increase to maintain the same DC current to angular frequency ratio. The depth of the trap is accordingly also proportional to the DC current level in the conductors. The depth of the trap is thus ultimately limited by the maximum conductor current.

A quadrupolar trap similar to the well known Ioffe-Pritchard trap is studied in Chapter 4 with combined DC and RF current excitation of the

bias rings. A non-uniform potential minimum is found around the local maximum at the centre of the trap, but this does not prevent the trap from being used to trap weak-field-seeking atoms. The potential maximum at the centre of the quadrupolar trap is more than sufficient for trapping strong-field-seeking atoms. The quadrupolar trap can therefore be used to trap both strong- and weak-field-seeking atoms if the DC bar currents are large enough. Simulations also indicate that the bias rings can be placed relatively closely together to compress clouds of cold atoms into successively smaller traps. As the gap distances become very small the B-field becomes very strong between the bias rings and there is a risk of dielectric breakdown.

A metallic cylinder atom guide consisting of a cylinder with a small hole and an external wire is described analytically in Chapter 5 and simulation results from Amperes are compared favourably with the results of calculations in Matlab. It is found that there can only be a B-field zero at the centre of the hole in the cylinder when there is a second field zero further inside the cylinder. The barrier between the two field zeros typically increases in width with increasing cylinder radius and in height with decreasing cylinder radius for a given cylinder current (DC). The smallest cylinder had the highest barrier between the field zeros, but also required the highest DC current in the external wire. Bias rings around the guide must be centred on the hole in the cylinder and the DC ring currents and the spacing between the bias rings must be scaled by the same factor as the ring radius to maintain the same shape and height of the trapping potential along the centre of the hole. The cylinder guide looks promising as a hermetic guide for cold matter. Bias rings are required both to pump atoms along the guide and to remove the zero in the B-field inside the hole.

Acknowledgements

This thesis is submitted in partial fulfilment of the requirements for the degree *Philosophiae Doctor* (Ph.D.) at the Norwegian University of Science and Technology (NTNU). The research has been carried out at the Department of Electronics and Telecommunications. It has been financed partly by the Norwegian Research Council (NFR) under the program WIWIC¹, by the Department of Electronics and Telecommunications for one year and later with my own personal money.

I would first like to thank my supervisor Professor Guennadi Kouzaev for his guidance and encouragement throughout this work. He motivated me from the beginning and introduced me to the topic of atom traps, which is rather far from wireless communications where my background is from.

The plan was originally that my thesis was going to be on the topic of power transistors. For several reasons, including that I had a temporary supervisor after my first supervisor retired, and that NTNU no longer has vibrant ongoing research activity in the field of RF/microwave devices, it eventually became clear that this research was not getting anywhere. I think that it would have been necessary to fetch inspiration at another university, or to already have it from industry, to have successfully pursued a direction of research close to the original plan. This was not considered seriously at the time. I did however get some experience with measurement and deembedding of microwave MMIC components out of this earlier work. I would in connection with this like to thank Terje Mathiesen for his assistance with the measurement arrangements in the lab.

1. WIWIC - Radio design principles for low-cost terminals and base stations of wideband wireless communications.

I would also like to thank the department for allowing me to keep the office workplace at my disposal and colleagues for their interest in the progress with this thesis.

The work with this thesis has been interesting but also time consuming and costly, mostly because of the change in research topic. I would like to express my gratitude to my parents Ruth and Kåre Sand, who sadly and for different reasons have not been among us for some time. It is some of their savings that have helped to finance part of the work of this thesis in addition to money inherited after several of my father's brothers, who have died in recent times of age related reasons. I would finally like to thank my friends and relatives who I have stayed in contact with for their encouragement and support during these years.

Trondheim, October 2010

Karl Jakob Sand

Table of Contents

Summary	i
Acknowledgements	v
Table of Contents	vii
1 An Introduction to Atom Traps and Quantum Effects	1
1.1 Introduction and Chapter outline	1
1.2 Thesis contributions	3
1.3 A brief history of magnetic and optical atom traps	4
1.4 Miniaturized magnetic atom traps	9
1.5 An introduction to quantum effects and BEC condensates	16
1.6 A short introduction to quantum computing	24
1.7 B-field equations for a conductor and an infinitesimally thin ring	30
1.7.1 B-field equations for an infinitesimally thin conductor	31
1.7.2 The introduction of a finite conductor radius	32
1.7.3 B-field equations for an infinitesimally thin current ring	34
2 Wire Structures for Cold Atom Handling	39
2.1 Introduction	39
2.2 The effective potential around a single wire	39
2.3 The effective potential around a single wire with bias rings	42
2.4 The effective potential around two crossed wires	51
2.4.1 The effect of the RF current on U_{eff} for two crossed wires	57
2.5 Prospective atom transfer between two crossed wires with bias rings	61
2.6 The effective potential around two parallel wires	73
2.6.1 The effect of the RF current on U_{eff} for two parallel wires	78
2.7 Prospective atom transfer between two parallel wires with bias rings	82
2.8 The four-wire cell	87
2.8.1 The four-wire cell and a quadrupolar trap	96

2.9 Single-layered cell-grids	103
2.10 Multi-layered cell-grids	119
2.11 Conclusion	130
3 Micrometre and Nanometre Scale Structures	133
3.1 Introduction	133
3.2 Scaling to micrometre size	134
3.3 A four micro-wire cell	136
3.4 A 3 x 3 micro-wire geometry	141
3.5 Scaling to nanometre size	151
3.6 Atom transfer between two crossed CN's with bias rings	154
3.7 A four carbon nanotube cell	163
3.8 A single-layered CN cell-grid	167
3.9 Multi-layered CN cell-grids	170
3.10 Conclusion	181
4 Millimetre Sized Quadrupolar Traps	183
4.1 Introduction	183
4.2 The effect of different excitations of a quadrupolar trap	184
4.3 The effect of changing the bias ring spacing in a quadrupolar trap	198
4.4 Conclusion	205
5 A Cylinder Guide for Cold Atoms	207
5.1 Introduction	207
5.2 Cylinder equations and expressions for zeros in the B-field	208
5.3 Numerical and calculated results for unbiased cylinder guides	212
5.4 Trapping and pumping of cold atoms in cylinder guides	220
5.5 Conclusion	228
6 Conclusion	231
6.1 Suggestions for future work	234
Appendix A: The AMPERES software tool	237
References	241

Chapter 1

An Introduction to Atom Traps and Quantum Effects

1.1 Introduction and Chapter outline

This thesis is on the design and simulation of magnetic atom traps and guides for ultra-cold matter. The main objective has been to develop atom guides and traps based on one single or a few straight conductors in the RF dressing regime. Atom traps with combined DC and RF current excitation are known as dynamical traps. Such traps can be used to trap strong-field-seeking atoms including ground state atoms, which are atoms in the lowest energy atomic state, as well as weak-field-seeking atoms. The multi-conductor traps presented can also be used to trap only weak-field-seeking atoms if only DC currents are applied.

A quadrupolar trap which is similar to the Ioffe-Pritchard trap except for ring currents in opposite directions has been investigated with both DC and RF currents in the rings with the aim of studying the effective potential shapes for trapping strong- and weak-field-seeking atoms. A new cylinder guide for weak-field-seeking atoms has additionally been developed. It can be made hermetically sealed, which is an advantage compared to other magnetic atom guides.

This first Chapter continues with a brief history of magnetic and optical atom traps in Section 1.3 and a review of miniaturized magnetic atom traps in Section 1.4. These sections are intended to put the work of this thesis in perspective and to present the current state of research. Two important fields of research within which atom traps find application are cold matter physics and quantum computing. These research areas are introduced in some depth in Section 1.5 and 1.6. Section 1.5 begins by explaining several important quantum mechanical concepts such as the particle-wave duality of matter, the Schrödinger equation, particle tunnelling through potential barriers, quantum numbers and Bose and Fermi particles. The Section

continues by describing the conditions for Bose-Einstein condensation and certain quantum mechanical phenomena that can be observed in Bose condensates. Section 1.6 addresses the questions of why we are interested in quantum computing and what quantum computing is. The present state of research is also indicated. Section 1.7 lists the equations for the magnetic field of a conductor and an infinitesimally thin ring. Much of this section can be considered to be part of the research work of this thesis.

Wire structures for cold atom handling are presented in Chapter 2. One way of transporting cold atoms is along the minimum potential manifold around a wire or conductor carrying both DC and RF currents. This is quite different from atom transport through sealed capillaries. It is explained how weak-field-seeking atoms may be transferred between two crossed wires or conductors. This makes addressed transportation of cold matter to a collision area possible. Multiple wires or conductors can also be placed in a two- or three-dimensional grid to form cells that can be used to trap both strong- and weak-field-seeking atoms. Such structures can be used to study Bose-Einstein condensates or used as part of a register for a quantum computer. Cold atoms may be loaded into the cells using hollow optical fibres placed between the wires or conductors.

Chapter 3 concerns the downscaling of the wire structures in Chapter 2 to micrometre and nanometre size. Although the scaling is straightforward in principle, different conductors must be used and the influence of decoherence mechanisms such as thermally-induced spin-flips and the Casimir-Polder force must be taken into account. Examples are given of both micrometre and nanometre sized structures designed for micro-wires and nanotubes respectively.

In Chapter 4 simulation results from Amperes are presented and compared for millimetre-sized quadrupolar traps. The quadrupolar trap consists of two current loops around a 4 wire magnetic guide. It is similar to the Ioffe-Pritchard trap except for currents in opposite directions in the two loops. The trap is here studied with combined DC and RF excitation of the bias loops. The effect of changing the spacing between the bias loops is also explored. This is done to find out whether successively smaller traps can be made that can be used to compress clouds of BECs for experimental study. The Amperes software program is presented in Appendix A.

Chapter 5 contains calculated and simulated results for a new cylinder atom guide. The atom guide consists of a metallic cylinder with a small hole and a parallel external wire. Analytical equations are presented for the guide together with calculated results and data from Amperes simulations. The cylinder atom guide is hermetically sealed not considering the ends.

1.2 Thesis contributions

Most of the material in Chapter 2 to Chapter 5 is original in the sense that similar research work is not known to have been published previously. The equations for the magnetic field of an infinitesimally thin wire or ring and equation (2.1) for the effective potential have however been taken from the literature. Much research related to magnetic fields has also been done to this day. Some aspects may thus be already known to researchers from unrelated work.

The main contributions of this thesis are the equations for the distance to the circular potential minimum for a single conductor, for two crossed conductors and for two parallel conductors, the demonstration of prospective atom transfer between two crossed conductors and the design and optimization of the four-wire cell and different multi-cell grids. The four-wire cell and the 3 x 3 wire (dual-well potential) structure are the most important cell-grid structures from the viewpoint of realizing experiments with ultracold matter. The cell-grid structures in this thesis represent a departure from the single layer planar wire-patterns that have been the focus of recent atom chip implementations.

Emphasis has been placed on providing a complete description of atom transfer between two crossed wires. This has included a study of the effect of the amplitude of the RF currents in the wires as well as a study of different RF current phase combinations in the bias ring. The possible use of the four-wire cell to replace the bias rings of a quadrupolar trap has also been explored in another section. These parts may be seen as minor contributions that give a deeper understanding of the conditions for cold atom transfer and the potential of the four-wire cell. The downscaling of many of the structures and related considerations is another important contribution, although the scaling itself is quite straightforward.

A quadrupolar trap similar to the well known Ioffe-Pritchard trap is here studied with combined DC and RF excitations in the bias rings. The quadrupolar trap is also studied for different gap sizes between the bias rings. The simulation results may be seen as supplementary information intended to give further insight.

The cylinder atom guide is one of the main contributions of this thesis. The rigid construction of the guide clearly limits its applicability to more or less permanent setups.

1.3 A brief history of magnetic and optical atom traps

The trapping of atoms within a small volume is a fundamental physical problem that concerns both the physical investigation of quantum effects involving small amounts of atoms and the development of new technologies based on the localization of the spatial motion of atoms.

The physical applications of the methods of trapping atoms in 3D spatial regions include studies into matter-wave interference and the spectral properties of trapped atoms, improvement of the accuracy and sensitivity of spectral measurements and studies of quantum statistical effects in atomic ensembles at low temperatures such as Bose-Einstein condensates (BEC) [1]. Several interesting quantum phenomena can be observed in BECs including Rabi oscillations, the influence of the coupling to an external environment or decoherence effects and the atomic Josephson effect when a BEC is divided by a movable barrier.

The technological applications include the use of trapped atoms in atomic frequency and time standards, high precision matter-wave interference based sensors for applications such as inertial and gravitational field sensing [2], and system components for controlling and engineering quantum states for use in the implementation of scalable quantum information processing.

The practically developed methods for trapping atoms in one, two or three dimensions in space are in essence based on the use of the forces of electric dipole interaction of atoms with off-resonance laser fields and/or magnetic dipole interaction of atoms with static magnetic fields. The basic methods are optical trapping using the forces of electric dipole interaction between atoms and laser fields, magnetic trapping based on the forces of magnetic dipole interaction, mixed magneto-optical trapping drawing on the simultaneous interaction between atoms and magnetic and laser fields and mixed gravito-optical and gravito-magnetic trapping. The last two methods make use of the gravitational force in part to control the trapped atoms.

The historic account of the evolution of magnetic and optical traps given below follows the main points in the introduction in “Electromagnetic trapping of cold atoms” by Balykin et al. [1], and is accordingly not a result of independent background research.

Magnetic trapping of atoms was the method to be developed first. The first suggestions on the possibility of electromagnetic trapping of atoms were made already in 1921 when experiments were conducted on the deflection of atomic beams by a nonuniform magnetic field [3]. The idea of magnetic deflection of atoms and molecules eventually led to the development of hexapole magnetic lenses and magnetic traps for particles with a permanent magnetic moment [4], [5]. These traps were later successfully used to trap ultracold neutrons [6] – [8].

In the mean time many types of traps for particles with a permanent magnetic moment, starting with the most simple quadrupole trap and ending with the Ioffe trap, had been proposed in works on plasma physics [9] – [11]. Concrete magnetic traps for atoms started to be discussed from the 1960s onwards [12] – [17].

The use of magnetic traps to trap cold atoms could not be experimentally confirmed for a long time mainly because of an absence of methods to obtain cold atoms. The potential well depth $U_{eff} = \mu_B |\Delta B_{DC}|$ of an inhomogeneous magnetic field varying in the interval ΔB_{DC} is usually very small compared with the thermal energy of atoms at room temperature. Magnetic traps can accordingly only be used to trap very cold atoms whose temperature T does not exceed the potential well depth $T < \mu_B |\Delta B_{DC}| / k_B$, where k_B is Boltzmann's constant and μ_B is the Bohr magneton.

The method of optical trapping originated in the late 1960s, when it was suggested that atoms might be trapped in the nodes or loops of an off-resonance standing laser wave [18]. The idea was based on the use of the electric dipole interaction between atoms and a standing laser wave to form a periodic lattice of potential wells whose minima coincided with the nodes or antinodes of the standing laser wave. Optical trapping using an off-resonance standing laser wave was subsequently developed in several works [19], [20].

At the time interesting proposals were also published on the laser trapping and levitation of dielectric micro-particles [21], [22], which later led to the development of 'optical tweezers'. These have become an important tool in biological investigations [23]. From the mid 1960s three important Doppler-free laser spectroscopy techniques had been developed. These were standing-wave saturated absorption spectroscopy [24] – [29], standing-wave two-photon spectroscopy suggested by Chebotayev and co-workers [30], and particle trapping spectroscopy [31]. Particle trapping

spectroscopy is completely free from the transit broadening effect resulting from the finite particle-field interaction time.

Optical atom traps based on off-resonance laser fields could at first not be realized experimentally because the methods for obtaining sufficiently cold atoms were still not available. The depth of the potential well produced by the dipole interaction of an atom with an off-resonance standing laser wave is $U_{eff} = \alpha E_0^2$, where α is the off-resonance detuning dependent atomic polarizability, and E_0 is the amplitude of the laser wave. Off-resonance optical trapping can accordingly only be used to trap very cold atoms whose temperature T is below $T < \alpha E_0^2 / k_B$, where k_B is Boltzmann's constant [18]. For a typical intensity of the counter-propagating travelling laser waves of $I = (c / 8\pi) E_0^2 \cong 500 \text{ kW cm}^{-2}$ and a typical atomic polarizability of $\alpha \approx 3 \cdot 10^{-23} \text{ cm}^3$, the maximum temperature $T < 0.91 \text{ mK}$. This value for the temperature T is significantly lower than for most magnetic traps. A good reference on optical traps is found in [32].

In the mid 1970s it was first proposed that atoms might be deep cooled by a resonance optical radiation red-detuned with respect to the atomic transition [33]. Concrete schemes were then put forward for cooling atoms by standing laser waves [34], [35]. From the quantum mechanical point of view the idea of optical cooling lies in the reduction of atomic velocities by the photon recoil associated with the absorption by the moving atoms of counter-propagating laser photons. Owing to the Doppler effect an atom is known to predominantly absorb the laser photons when the laser field is red-detuned with respect to the atomic transition. From the semiclassical point of view the mechanism of optical cooling consists in the retardation of atoms by the radiation pressure force which is directed opposite to the atomic velocity for a red-detuned laser light.

In the following years two different experimental schemes were developed for the laser cooling of atoms. One is the simultaneous deceleration and longitudinal cooling of an atomic beam by a counter-propagating red-detuned laser beam [36] – [42]. The other is the cooling of atoms in counter-propagating red-detuned laser beams [34], [35]. This scheme effects the cooling of atoms with a zero average velocity. If an atomic gas is irradiated by three pairs of counter-propagating laser waves 3D cooling of atoms is possible [43], [44].

Theoretical analysis of a most simple model of interaction of a two-level atom with counter-propagating laser beams has shown that the cooling

mechanism is based on single-photon absorption (emission) processes and that the minimum temperature of atoms is reached at a red-detuning equal to the natural half-width of the atomic transition line $\delta = -\gamma$. The minimum temperature is determined by the atomic transition natural half width [35], and is defined as $T_D = \hbar\gamma/k_B$. The temperature T_D is known as the Doppler cooling limit. It is defined by the natural line width and not by the Doppler width. For a typical value of the natural line width of $\Gamma = 2\gamma 2\pi \cdot 10 \text{ MHz}$ the temperature T_D is of the order of $100 \mu\text{K}$.

Multi-level atoms are in practise frequently cooled by counter-propagating laser beams down to temperatures of the order of $10 \mu\text{K}$ [45] – [48]. The deeper cooling of multi-level atoms compared to the idealized two-level atoms is possible because of the contribution from the two-photon friction mechanism specific to multilevel atoms [49] – [57]. In multilevel dipole interaction schemes, the laser field excites the atoms from many magnetic sublevels of the ground electronic state. Accordingly, in multilevel cooling schemes the two-photon and higher order multi-photon processes produce an additional friction that lowers the atomic temperature below T_D .

The fundamental lower temperature limit for laser cooling processes based on the photon recoil has been shown to be determined by the quantum fluctuations of the atomic momentum and accordingly can not be lower than the value defined by the recoil energy. The recoil temperature is given as $T_r = \hbar^2 k^2 / (M k_B)$, where $k = \omega_0/c$ is the wave-vector corresponding to the frequency ω_0 of the atomic transition excited by the laser light. For atoms of moderate mass whose resonance transitions are in the visible spectrum the recoil temperature is typically a few micro-Kelvin.

In addition to the laser cooling methods based on the photon recoil, laser methods have been developed for the optical pumping of the velocity selective translational atomic states described by the effective temperatures below the recoil temperature T_r [58] – [61]. One of these methods is based on the velocity-selective coherent trapping of atomic population in the superpositional state composed of the ground state substates [58], [60]. Another method is based on the use of the narrow two-photon Raman transitions between two hyperfine levels in the ground state to select a narrow velocity group of atoms and push it towards zero velocity [59].

After the development of the laser cooling techniques the first successful experiment on the trapping of cold atoms was done using a quadrupole magnetic trap [62]. Numerous experiments on magnetic trapping of neutral

atoms have since been conducted [63] – [66]. The magnetic traps in these first experiments were quite large with typical features on a centimetre scale. In the mid 1990s focus shifted to the development of miniaturized magnetic traps, especially traps suitable for photolithographic patterning on integrated circuits. Some of the recently proposed miniaturized atom traps are introduced in Section 1.4.

The development of purely optical atom traps ran into some difficulty at this time. All proposals for purely optical traps were affected by the problem that the trapped atoms had a limited lifetime due to the momentum diffusion in laser fields [67] – [69]. A solution was suggested of using two laser fields separated in time, one for cooling the atoms and the other for trapping them [70], [71]. Similar approaches based on time-varying fields were also considered [72] – [74].

It had at first been presumed that a central-symmetric light field composed of several divergent red-detuned laser beams could be used to make a potential well for cold atoms due to the coordinate-dependent radiation force [75]. The idea was that the red-detuned laser beams could simultaneously cool and trap the atoms. It was however shown that such laser fields could not produce stable potential wells for atoms [76]. The limitations formulated by Ashkin and Gordon on the structures of the trapping laser fields came to be known as the optical Earnshaw theorems.

On this background Dalibard proposed a magneto-optical trap (MOT) [77], which was soon realized experimentally [78], and later gained wide recognition. In the MOT a nonuniform magnetic field produces the Zeeman shifts of atomic magnetic sublevels, so that the counter-propagating laser beams not only cool the atoms but also trap them in the central region of the trap.

In 1982 the atom mirror was proposed by Cook and Hill [79]. The idea is to use an evanescent laser wave propagating along a dielectric-vacuum interface as a reflecting mirror for cold atoms. The evanescent light wave penetrates into the vacuum to a distance of the order of the optical wavelength and the high gradient of the evanescent wave field produces a substantial dipole gradient force on the atom. At a large blue detuning of the evanescent wave with respect to the atomic transition the radiation force is very weak and the dipole gradient force dominates completely. The gradient force produces a repulsive barrier which reflects atoms in the vacuum region. The barrier is not very high but sufficient for its purpose.

The atom mirror was continually improved and this has led to the development of hollow-core atom waveguides similar to optical waveguides [80] – [82]. Optical atom waveguides have since been successively verified [83] – [85] and improved [86].

The atom mirror also led to the development of gravito-optical atom traps. An atom trap based on a horizontally arranged concave atom mirror was theoretically demonstrated [87] and experimentally verified [88]. Half-open gravito-optical traps have also been proposed and realized [89], [90]. 3D atomic cavities based on evanescent waves have been suggested and analyzed [91].

1.4 Miniaturized magnetic atom traps

The observation of Bose-Einstein condensation in a magnetic trap in 1995 caused increased interest in miniaturized magnetic traps from the mid 1990s. It is well known that the magnetic field from current carrying wires typically scales as I/S , where I is the wire current and S is the characteristic size of the system. The magnetic field gradients and curvatures similarly scale as I/S^2 and I/S^3 respectively [92]. The practical limits to attainable wire currents in larger traps and the possibility of producing much larger field gradients and curvatures, as well as improvements in micro-fabrication techniques, has been the driving force behind efforts toward miniaturization. Another incentive is of course to keep the physical equipment as small as possible when observing or manipulating very small clouds of cold atoms, particles or molecules.

Some of the first micrometre sized atom traps to be proposed were planar versions of macroscopic traps. Several magnetostatic traps including a planar two-coil trap, a planar one-coil trap with an external bias field, a planar hexapole trap and four different planar and pseudoplanar Ioffe-Pritchard trap configurations were discussed and briefly analyzed in [92]. The article also described a dynamic two-coaxial ring trap capable of trapping atoms in either weak- or strong-field-seeking states.

The depths of the trapping potentials of the planar Ioffe-Pritchard trap geometries were found to be relatively shallow enabling the trapping of only very cold atoms. The depth of the dynamic two-coil trap with RF ring currents and a static axial bias field was also found to be quite shallow but sufficiently deep to be used. The proposed use of very small superconducting loops with a minimum radius of 10 μm required to realize

the geometries can however be seen as an impediment to easy and cost-effective implementation.

Magnetic waveguides on a chip were first proposed by Mara Prentiss and co-workers in 1999 [93], [94]. By making the waveguide circular a storage ring for cold atoms can be constructed. A magnetic storage ring of this type for neutral atoms was later described and experimentally analyzed in [95]. The storage ring consisted of a two-wire magnetic guide forming a ring 2 cm in diameter. The distance between the copper wires, each 280 μm in diameter, was 0.84 mm. The wire currents were 8A in the same direction in both wires. This produces a 2D quadrupole field minimum between the wires. Cold atoms were loaded into the magnetic ring from a magneto-optical trap (MOT) through a tapered two-wire magnetic guide section. Seven revolutions of ^{87}Rb atoms were observed in the ring corresponding to a $1/e$ lifetime of 180 ms for the atoms.

The applications of the magnetic storage ring include large area single-mode guided atom interferometers and continuous wave monochromatic beam generation. The ring can be multiply or continuously loaded to increase the number of atoms in the ring and both the longitudinal and transverse velocity distributions of the atoms can be manipulated and cooled in the ring. Highly directional output beams can be created using a coherent variable output coupler.

Miniaturized atom traps micro-patterned on integrated circuits were first implemented by the research group of Jakob Reichel in 1999 [96]. This group was also the first to observe BEC on a chip [97]. Around the same time a BEC was also produced in a micro-trap by Claus Zimmermann and co-workers [98]. Integrated circuits containing traps or guides for cold atoms have become known as atom chips. Several other miniaturized atom traps were proposed and experimentally demonstrated within a few years [99] – [103].

The use of adiabatic potentials dressed by a RF field in an inhomogeneous magnetic field was first proposed by Zobay and Garraway in 2001 [104]. The same potentials are also implied in RF-induced cooling [105], where they are used to limit the depth of the trap. The theory of dressed potentials was originally developed by Claude N. Cohen-Tannoudji in the 1970's. A first attempt at demonstrating a trap based on the RF dressing effect was regrettably hampered by technical noise during the loading process, which caused heating and prevented 2D BECs from being observed [106].

The first coherent or phase-preserving matter-wave beam splitter constructed on an atom chip was demonstrated experimentally in 2005 [107]. An RF induced adiabatic two-well potential was used to split a BEC into two clouds separated by distances in the range of 3 – 80 μm , which enabled both the tunnelling and isolated regimes to be studied.

The beam splitter consisted of a straight 50 μm wide DC wire placed 80 μm from a 10 μm wide RF wire on the surface of an atom chip mounted upside-down, as shown in Fig. 1.1. The DC wire current was ~ 1 A and the RF current ~ 60 mA at 500 kHz. The BEC was trapped in a position 80 μm beneath the RF wire which allowed for symmetric splitting of the BEC.

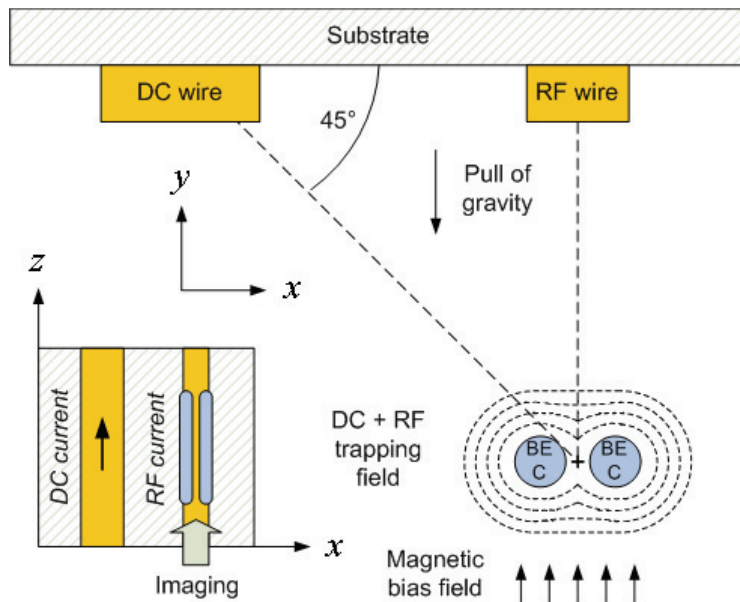


Fig. 1.1. The basic geometry of the matter-wave beam splitter in Schumm et al. Adapted by permission from Macmillan Publishers Ltd: [nature physics](#) [107], copyright 2005.

During the experiments the atoms were detected by resonant absorption imaging along the weak trapping direction, which amounts to integrating over the long axis of the one-dimensional clouds. The images were taken *in situ* or after time of flight expansion. The splitting distances were measured using *in situ* images. The coherence of the splitting was studied by recombination of the split clouds in time of flight expansion after a non-adiabatically fast (< 50 μs) extinction of the double well potential. The experiments showed an interference pattern with a fixed phase so long as the two wells were not completely separated, i.e. so long as the chemical

potential exceeded the potential barrier. Once the wells were completely separated, so that tunnelling was fully inhibited ($d > 3.4 \mu\text{m}$), the phase distribution remained non-random and its centre started to evolve deterministically.

The matter-wave beam splitter in [107] was constructed as part of an interferometer for applications such as inertial and gravitational field sensing. The beam splitter also allows numerous experiments exploring the phase dynamics in complex interacting quantum systems, for example Josephson oscillations [108], or the influence of the coupling to an external environment (decoherence). Atom-Chip beam splitters may also constitute building blocks for quantum information processing.

Two similar but more elaborate wire geometries on atom chips that offer even greater flexibility have since been proposed [109]. The first of these uses four straight wires carrying counter-propagating DC currents to set up a quadrupole field. A broad RF wire passes through in the middle between the two DC wire pairs. Sufficiently close to this wire the RF field can be considered to be homogeneous. By varying the strength of the RF field a single-well or a double-well potential can be created underneath the RF wire. The use of an RF field enables a smooth transition between the single-well and double-well potentials. Additional wires are used to generate the Ioffe-field in the longitudinal direction. A longitudinal variation of the RF amplitude is obtained by modifying the cross-sectional size of the RF wire according to the authors. This makes the single- or double-well potentials three-dimensionally confining and may also allow a Mach-Zehnder interferometer to be realized.

The second geometry in [109] consists of a three straight wires on the surface of an atom chip mounted upside-down. The centre wire carries a DC current and the two wires on the sides carry DC currents in the opposite direction in addition to RF currents. The RF currents are used to generate two phase shifted and orthogonally polarized oscillating homogeneous fields near the centre of the quadrupole field set up by the DC currents. Depending on the phase shift δ between the RF currents either a single well, a double-well or a ring-shaped potential is formed, something which makes the proposed geometry very versatile. The ring-shaped potential is promising for making a ring interferometer (Sagnac-interferometer) for matter waves. 3D confining potentials can also here be created by making the RF amplitude spatially dependent in the longitudinal direction. A ring trap with RF currents was also proposed in [110] at about the same time.

The use of multiple RF frequencies has been proposed for implementing radio frequency combs, which give rise to periodic potentials that act as gratings for cold atoms [111]. The combination of static magnetic fields with multimode RF radiation can be used to make almost arbitrary 3D potential geometries. A one dimensional RF comb is described with the approximation that the frequency components are not too closely spaced. The RF comb forms a periodic grating that propagates in space and its main application is for accelerating cold atoms in Bragg-scattering experiments. Bragg scattering is briefly explained in Section 1.5.

Radio frequency lattices have certain advantages over optical lattices and micro structured gratings. It is possible to make local variations or disorder with the aim of studying for example Bose and Anderson glasses [112], [113]. Potential applications of time- or position-dependent RF combs include Bragg velocity filters, Bragg interferometers, quasi-random potentials with disorder on a very small length scale and other atom optical elements.

Theoretical considerations on the creation and modification of magnetostatic traps and electrostatic traps with rotation and divergence free fields have been presented in [114]. It is shown that Ioffe-Pritchard traps (IP-traps) and other stationary points of B (non-zero minima and saddle points) are confined to a two-dimensional curved surface or manifold M , defined by $\det(\partial B_i / \partial x_j) = 0$. An expression is given that describes how stationary points can be moved over the manifold under the influence of an external uniform field. It is shown how IP-traps can be created or moved on the manifold. The relationship between the manifold and points of zero field is investigated. Field zeros of two different types occur in pairs in separate regions of space divided by the manifold. Pairs of zeros of opposite type can be created or annihilated on the manifold. When two zeros of opposite type annihilate on the manifold an IP-trap is created.

The conceptual tool of the manifold M , which allows IP-traps and stationary points to be moved, finds application in situations where the magnetic field configuration is fixed, e.g. by permanent magnets, and control over the field is limited to the application of uniform external fields. This is frequently the case in atom chip experiments. Precise control over the magnetic field is important in loading procedures, during transport or dynamical splitting of atom clouds and during movement of qubits on atom chips in quantum information processing experiments.

A novel class of trapping potentials which has recently been proposed is time-averaged adiabatic potentials (TAAP) [115]. The behaviour of atoms relative to the frequency of the modulation falls into three different regimes: the quasi-static, the time-averaging and the RF-dressing regimes. In the quasi-static regime the modulation is so slow that the atoms follow adiabatically. In the time-averaging regime the atoms are confined to a trap that is the time average of the modulated potential [64]. The modulation frequency ω_m is in this case much larger than the trap frequency ω so that the atoms do not follow the modulation, but much slower than the Larmor frequency. In the RF-dressing regime the modulation creates an RF field which resonantly couples the atomic Zeeman levels of the static magnetic trap. The coupled states are here described by dressed atomic potentials. For the coupling to take place the frequency ω_{RF} of the RF field has to be close to the Larmor frequency $\Omega_L = |g_F \mu_B \cdot \mathbf{B}(\mathbf{r})|/\hbar$ that is associated with the difference in energy between the Zeeman levels. g_F is here the Landé factor of the considered hyperfine manifold and μ_B is the Bohr magneton.

TAAPs combine the RF-dressing and the time-averaging regimes to produce trapping potentials of high complexity and flexibility. TAAPs can be made by starting with any static magnetic field $\mathbf{B}(\mathbf{r})$, for example an Ioffe-Pritchard or quadrupole field. A TAAP is made by modulating an existing RF-dressed effective potential by a frequency ω_m . The modulation frequency must be fast compared to the trap frequency of the static trap but much smaller than the Larmor frequency so that the atoms experience the time-average of the modulated dressed potential. The conditions on the frequencies are that $\omega \ll \omega_m \ll \Omega_L$. When the dressed adiabatic potential $V(\mathbf{r})$ is modulated it becomes a time dependent potential $V(\mathbf{r},t)$ from which the TAAP can be calculated by time-averaging over one period $\tau = 2\pi\omega_m^{-1}$ of the modulation.

Both a ring-shaped and a double-well TAAP are exemplified in [115] starting with a magnetic quadrupole field. The ring trap requires that both the modulation field $\mathbf{B}_m(t)$ and ω_{RF} be modulated to ensure that the dressed potential has its minimum on the ring $z_{\text{min}} = 0, \rho_{\text{min}} = \rho_0$ at all times. The diameter of the ring can be tuned over a wide range by changing the RF frequency. The double-well trap has two wells, each created by a modulation sideband, that can be merged into a single minimum for a modulation index of $\beta = 1$. The trap is pancake shaped for modulation indices of $\beta < 1$ and cigar shaped for $\beta > 1$. Multiple TAAP traps can be made simply by using multiple RF frequencies instead of just one. The different traps can be fully separated or have tunable tunnelling barriers

between them. Multiple traps can be adiabatically merged into a single one, or a single trap be split.

A clear advantage of TAAP traps and waveguides is that they can be much smaller than the field generating coils. This virtually eliminates corrugations in the guiding potential caused by imperfections in the field generating structures. As a result decoherence is greatly reduced leading to increased lifetimes for the trapped atoms. TAAP traps have recently been demonstrated in practise [116].

In the last few years the possibility of trapping cold atoms close to magnetic nanowires [117] and carbon nanotubes [118] has been examined theoretically. In [117] it is proposed to trap cold atoms above movable domain walls in planar magnetic nanowires. The position of domain walls in 2D magnetic nanowire circuits can be controlled by moderate in-plane magnetic fields. Cold atoms in a low-field-seeking state are repelled from a domain wall and trapped on a surface above it if a uniform out-of-plane magnetic field B_{DC} is applied. A point does however exist on this surface where $|\mathbf{B}|_{\min} = 0$. Majorana spin flip transitions can be avoided by additionally applying a rotating magnetic field of amplitude B_{AC} , as in a conventional time-orbiting potential trap. A single bias field plus a rotating field can create the necessary trap conditions throughout a 2D nanowire network. Additional in-plane fields are required to propagate the domain walls through the nanowires for the implementation of quantum information processing.

Cold atoms trapped near the outside of a carbon nanotube are subject to two principal mechanisms leading to trapping losses: thermally induced spin-flip transitions [119] and tunnelling brought on by the Casimir-Polder force. Both these mechanisms were studied mathematically in [118] and graphs were produced for the spin flip lifetime and the sum of the Casimir-Polder potential and the magnetic trapping potential as a function of the trapping distance from a nanotube. A (9, 0) carbon nanotube of radius $R_{CN} = 3.52 \text{ \AA}$ carrying a current of $20 \mu\text{A}$ was considered for $f_0 = 70 \text{ kHz}$ and $T = 380 \text{ K}$. The Casimir-Polder force was found to dominate and a conclusion was reached that the minimal feasible trapping distance appeared to be at least 100 nm. The proposed use of nanotubes to implement many of the trapping structures in this thesis is treated in Chapter 3.

The idea of using metallic carbon nanotubes as current-carrying wires in miniaturized magnetic traps seems attractive for several reasons. Nanotubes contain very little dielectric material which minimizes the Casimir-Polder

force. They also possess very homogeneous surfaces which limits electromagnetic field fluctuations which can drive spin transitions and lead to trapping losses. The current carrying ability of nanotubes is also very good relative to their small cross-sectional size.

1.5 An introduction to quantum effects and BEC condensates

Physical experiments have shown that light possesses both wavelike and particlelike properties [120]. Photons, which give rise to light, can be considered to be particles of zero mass. At the same time a ray of photons produces an interference pattern where the probability distribution which governs the paths taken by the individual photons is in agreement with wave theory. It was first proposed by de Broglie that the wave-particle duality may be characteristic not only of light but may also apply to matter. Experiments with electron and neutron diffraction have since gone a long way toward proving this by yielding results analogous to those obtained using x-rays.

X-ray diffraction can be examined by considering a monochromatic x-ray beam of wavelength λ impinging at an angle θ with respect to a set of atomic planes of spacing d in a crystal. Constructive interference happens when the waves reflected from the various planes in the crystal are in phase. This requires that the difference in path length between the waves reflected from the different planes be an integral number n of wavelengths. The angle of reflection is in this case equal to the angle of incidence. This leads to the Bragg condition $n\lambda = 2d \sin \theta$ for constructive interference between the reflected waves.

The wavelength of an x-ray beam is related to the photon energy E_p by $E_p = h\nu = hc/\lambda$, where h is Planck's constant, ν is the frequency and c is the propagation velocity. The wavelength of a beam of particles is also energy dependent and is found from the de Broglie relation to be $\lambda_{dB} = h/p$, where h is Planck's constant and $p = mv$ is the momentum of the individual particles, m is the particle mass and v is the particle velocity. Particle energy E is related to the rest mass energy E_0 and the momentum p through $E^2 = E_0^2 + p^2c^2$, so that zero rest mass particles such as photons and neutrinos have particle energy $E = pc$. For free particles with energy E and momentum p the energy can also be found as $E = \hbar\omega = p^2/2m = \hbar^2k^2/2m$, where $\hbar = h/2\pi$, $\omega = 2\pi\nu/\lambda$ and $k = 2\pi/\lambda$.

Atoms are Bragg-reflected at a lattice if their de Broglie wavelength is roughly the same as the lattice constant. Their velocity is then given by $v = h/(md)$, where h is Planck's constant, m is the atomic mass and d is the lattice constant [111]. Bragg-reflection may be observed if resting atoms are accelerated using RF gratings propagating at the Bragg velocity. RF gratings have however not been used for diffraction experiments to date. Optical standing waves have instead been used to observe Compton scattering, which corresponds to the diffraction of matter waves from a light grating [121].

The wave-particle duality forms the basis for the development of a wave equation for matter, best known as the Schrödinger equation. The three-dimensional time-dependent form of the Schrödinger equation is as follows

$$-\frac{\hbar}{2m}\nabla^2\psi + V(\mathbf{r})\psi = i\hbar\frac{\partial\psi}{\partial t}, \quad (1.1)$$

where ∇^2 is the Laplacian operator and $V(\mathbf{r})$ is the potential energy of the particles. Plane waves of the form $\psi(\mathbf{r}, t) = A \exp[(i/\hbar)(\mathbf{p} \cdot \mathbf{r} - Et)]$ are solutions to the Schrödinger equation so long as the potential energy V is not a function of position or time ($V = \text{const}$). The vector $\mathbf{p} = \hbar\mathbf{k} = p_x\hat{x} + p_y\hat{y} + p_z\hat{z}$ is here a momentum vector parallel to the wave vector \mathbf{k} of magnitude $(2\pi/\lambda)$ which points in the direction of propagation of the plane wave. $\mathbf{r} = x\hat{x} + y\hat{y} + z\hat{z}$ is the position vector.

Because the time-dependent Schrödinger equation is linear any linear combination of plane waves will also be a solution. This makes it possible to superimpose or combine a group of plane waves of different wavelengths to form a wave packet. A wave packet is the physical analogue of the mathematical superposition of wave components in a Fourier series or Fourier integral to represent more complex waveforms. Wave packets for matter waves have been found to disperse with time in contrast to packets of electromagnetic waves propagating in free space. The spreading of the packet with time reflects that there is uncertainty in initial momentum of the particle corresponding to the spread in k values. This results with time in greater uncertainty in the position of the particle.

The probability of finding a particle described by the wave function ψ in a small (differential) region surrounding the position x is proportional to $|\psi|^2 = \psi^* \psi$, the square of the magnitude of the wave function evaluated in the position x . This is known as Born's postulate [120]. A surprising effect concerning the use of the probability density $|\psi|^2$ is that an increase in the spread in the wave number Δk , corresponding to uncertainty in our

statistical knowledge of the wavelength and accordingly also the momentum of the particle, results in a reduction in the uncertainty $\Delta\mathbf{x}$ in the position of the particle. This leads to the position-momentum form of the Heisenberg uncertainty relation, which states that an increase in our knowledge of the position of the particle requires a corresponding decrease in our knowledge of the momentum of the particle, and vice versa.

For particles in free space the energy eigenvalue $E = \hbar\omega$ and the momentum eigenvalue $\mathbf{p} = \hbar\mathbf{k}$ corresponding to a given plane wave $A_k \exp[(i/\hbar)(\mathbf{p} \cdot \mathbf{r} - Et)]$ are related by $E = p^2 / 2m$, and there is no restriction on the values of E or p . This leads to an energy spectrum which is a continuum. For negative energy eigenvalues, representing particles trapped in a potential $V(\mathbf{r})$, the boundary conditions effectively restrict the eigenvalues to discrete values leading to a discrete energy spectrum.

Particles generally interact with external energy potentials U . Particles encountering a potential step U_0 are either transmitted or reflected when the kinetic energy of each particle E is greater than U_0 . If $E \gg U_0$ the transmission coefficient approaches one. When the particle energy is not much greater than the step height the reflection coefficient is close to one and the wavelength of the transmitted particles becomes long corresponding to particles with small momentum and kinetic energy.

When the particle energy E is less than U_0 all particles are reflected. The particle density is however nonzero inside the potential step. Instead it decays exponentially away from the step with a fall-off length that is inversely proportional to $U_0 - E$. This makes it possible for particles to tunnel through a potential barrier of limited width even though the particle energy E is less than the barrier height. Electron tunnelling in semiconductors is the principle behind several quantum electronic devices such as Esaki and Zener diodes.

Particles trapped in potential wells delineated by the surrounding energy barriers move inside the well with a continuous interchange of kinetic and potential energies. The total energy of the particles is conserved. It is also confined to a discrete set of levels. The details of the energy level spectrum depend upon the shape of the potential well.

The Coulomb attraction between two point charges of opposite sign gives rise to a potential energy $U(r) = q_1 q_2 / 4\pi\epsilon_0 r$, where $r \equiv |\mathbf{r}|$ is the separation distance between the charges and ϵ_0 is the permittivity of free space. If one assumes that q_1 is a proton ($q_1 = Ze$) and q_2 an electron ($q_2 = -e$) this corresponds to the hydrogen atom ($Z = 1$ and $e = 1.602 \times 10^{-19}$ C). Solution of

the Schrödinger equation for this case yields three different quantum numbers, the principal quantum number n , the angular momentum or orbital quantum number l and the magnetic quantum number m_l . The electron spin $m_s = \pm 1/2$ can be regarded as a fourth quantum number. The quantized energy levels depend in this case only on the principal quantum number n . The energy eigenvalues are $E_n = -0.5 \cdot Z^2 e^2 / 4\pi\epsilon_0 a_0 n^2$ for ($n = 1, 2, 3, \dots$), where $a_0 = 4\pi\epsilon_0 \hbar^2 / me^2$ is the Bohr radius. A finite amount of energy is required to promote an electron from a given quantum state to a higher energy quantum state. Similarly, when an electron decays from a quantum state to a lower energy quantum state energy is given off, for example in the form of a photon. The lowest energy state ($n = 1, l = 0, m = 0$) is called the ground state. The Pauli Exclusion Principle states that no two electrons can have the same set of quantum numbers.

In the case of atoms with multiple electrons the angular momentum, magnetic and electron spin quantum numbers are the same as for the hydrogen atom. The principal quantum number is replaced by a generalized total quantum number n . One important difference is that both the total quantum number n and the orbital angular momentum quantum number l generally correspond to different energy eigenvalues, where states of lower l value lie at a lower energy for a given value of n .

An atomic shell is specified by a given value of n . The shells are labelled K, L, M, N, O, P, Q in standard spectroscopic notation. A given set of values for both n and l specifies an atomic subshell, each of which contains $2(2l+1)$ unique electronic states. In spectroscopic notation the n value of a shell is often given as a number and the l value is assigned a lowercase letter from the set s, p, d, f, g.

The ground state of a many-electron atom is the one in which a sufficient number of electrons populate the lowest energy states in accordance with the Pauli Exclusion Principle to give a neutral entity. At temperatures above 0°K atoms are often not in the ground state. The degree to which the uppermost shell is occupied by electrons determines the chemical properties of the atoms by defining how easily they form chemical bonds in molecules and solids. Atoms where the uppermost shell is full tend to be chemically inert.

If one considers a system of N identical and distinguishable particles which do not interact with one another one possible wave function for the total system is the product of the single-particle eigenfunctions $\Phi_{i_1 i_2 \dots i_N} = \phi_{i_1}(1)\phi_{i_2}(2)\dots\phi_{i_N}(N)$, where the subscript i_1 is the index for the first particle

corresponding to one of the possible single-particle wave functions and the ϕ_i are stationary states of energy E_i ($i = 0, 1, 2, \dots$) which are available for occupation by the particle. Because the particles are identical they are in practise only distinguishable if they are spatially separated, which requires that the wave functions must be completely nonoverlapping.

In the case of a system of N identical indistinguishable particles which do not interact with one another the wave functions for the individual particles overlap. The property of indistinguishability is characteristic of the quantum nature of particles. Because one cannot tell the particles apart the wave function must be invariant to any permutation of the particles. One possible wave function for the system of N particles is a gigantic function made up of the sum of all possible permutations of the N particle wave function consisting of the product of the individual single particle eigenfunctions. For a given set of N different eigenstates there are at most $N!$ terms in this sum.

The requirement that the wave function must be invariant to all possible interchanges of identical particles in the system is accommodated by introducing an exchange operator or permutation operator P_{jk} which interchanges any pair of particles j and k in any function involving their coordinates. The only possible eigenvalues of the permutation operator P_{jk} can be shown to be either $+1$ or -1 . The eigenvalue of $+1$ requires that the wave function must be symmetric under the exchange of any two particles in the system of N particles. The eigenvalue of -1 requires that the wave function must be antisymmetric under the exchange of any two particles. The anti-symmetric wave function is zero, in which case there can be no particles, unless every particle in the system of N noninteracting particles is in a different single-particle eigenstate. This is a remarkable situation considering that all N particles in the system are noninteracting.

The Pauli Exclusion Principle for particles with an antisymmetric many-particle wave function postulates that no two half-odd-integer spin particles in a system can have the same set of quantum numbers. The wave function for a system of half-odd-integer particles must accordingly always be totally antisymmetric. Particles with an antisymmetric many-particle wave function are known as Fermi particles or fermions. The statistical distribution function for the occupation of the energy levels in a system of such particles is known as the Fermi-Dirac distribution function. Examples of fermions are electrons, protons, neutrons and μ mesons, which all have spin $\frac{1}{2}$. Fermi particles exhibit a quantum-mechanical repulsion for one another and accordingly do not tend to be found spatially near each other.

Particles with a symmetric many-particle wave function have no restriction on the occupation of the various quantum states, and any number of the N particles can be in a given single-particle eigenstate. Particles of this type are known as Bose particles or bosons. The statistical distribution function for the occupation of the energy levels in a system of such particles is known as the Bose-Einstein distribution function. Photons (spin 1), neutral helium atoms in the ground state (spin 0) and alpha particles (spin 0) are examples of Bose particles. Bosons exhibit a quantum-mechanical attraction for one another and tend to be found spatially near each other. They also tend to occupy the same low-energy quantum states, something which is allowed since they do not obey the Pauli Exclusion Principle.

When a dilute gas of Bose particles is cooled to below a critical temperature, of the order of a fraction of a micro Kelvin, the conditions for Bose-Einstein condensation are met. Below the critical temperature the population of the lowest energy state becomes macroscopic and this corresponds to the onset of Bose-Einstein condensation. The fraction of particles in the lowest state $N_0(T)/N$ is called the condensate fraction. The gases used are very dilute. The average distance between atoms is typically more than ten times the range of interatomic forces. For an atomic gas BEC occurs when the density of atoms n and the de Broglie wavelength $\lambda_{dB} = h/p$ are related by the relation $n\lambda_{dB}^3 \geq 2.62$ [1].

For a gas the equilibrium configuration of the system is normally the solid phase at temperatures close to absolute zero. In order to observe BEC the system must be preserved in a metastable gas phase for a sufficiently long time. This is possible because three-body collisions are rare events in dilute and cold gases and their lifetime is hence long enough to carry out experiments [122].

Bose gases are usually both inhomogeneous and finite sized systems owing to the use of harmonic trapping potentials. Because the systems are inhomogeneous two-body interactions between atoms play an important role, in spite of the diluteness of the gases. The effects of two-body interactions are taken into account by the Gross-Pitaevskii theory for weakly interacting bosons. This is a mean-field approach for the order parameter or wave function associated with the condensate. It provides closed and relatively simple equations that describe most relevant phenomena associated with BECs.

Bose-Einstein condensation manifests itself as a sharp peak both in the velocity distribution and in coordinate space. Two-body interactions mean

that the central density at very low temperature can be one or two orders of magnitude smaller than the density predicted for an ideal non-interacting gas in the same trap. In a BEC the wave functions of the condensed particles overlap as they occupy the same single-particle state. The BEC exhibits quantum behaviour as a macroscopic trapped drop and resembles a micron-sized quantum particle.

The development of RF evaporative cooling allowed the first observations of BECs trapped in magnetic traps to be made in 1995 [63], [65], [66]. Most experiments with BECs that have been conducted since have used cold alkali metal atoms, but also hydrogen atoms and meta-stable helium atoms have been used. Alkali metals are any element other than hydrogen found in the first column of the periodic table. Alkali atoms are well suited to laser-based cooling methods because their optical transitions can be excited by available lasers and because they have a favourable internal energy level structure for cooling to very low temperatures. The study of BECs in atomic samples is these days one of the fastest developing areas in atomic physics [123], [124].

The Josephson Effect was discovered by Brian Josephson in 1962 and concerns the tunnelling of electrons through a thin insulator placed between two superconducting plates [125], [108]. In a superconductor the current can flow without resistance and the quantum state of the electrons is highly correlated so that the tunnelling becomes coherent. Josephson's breakthrough was to realize that this meant that interference could be observed since the tunnelling wave function from one electrode combines with that from the other in a way that depends on their relative phases. This interference gives rise to two main effects. First, a steady current can flow through the junction when no voltage is applied. This is known as the DC Josephson effect. Second, when a steady voltage is applied the current oscillates. This is known as the AC Josephson effect.

In [126] BECs of Rb atoms are used instead of superconducting plates to trigger the Josephson effects in a system of quantum gases. Condensates are a kind of super-fluid in which the atoms share a quantum wave function just as electrons do in a superconductor. A narrow laser beam was sent through the centre of the BEC thus forming a barrier for the atoms analogous to the insulating layer in the original Josephson junction.

By moving the beam from the centre of the condensate towards one side the AC Josephson effect was observed as the atoms became compressed on one side. The compression caused an increase in the energy of the atoms since atoms in a condensate normally repel each other. This increase in

interaction energy, also known as the chemical potential, served as the equivalent of voltage applied to an electrical circuit. The compressed atoms consequently wanted to tunnel through the laser barrier. It was however observed that the number of atoms on the compressed side did not simply decrease, instead it oscillated in time. This is because the tunnelling rate depends on the interference of the two quantum waves representing the two separated condensates, and the sign of this interference oscillates in time when the condensates have different energies.

When the laser barrier was moved towards one side much more slowly ($v < \sim 40 \mu\text{m/s}$) atoms continued to flow through the barrier, but the densities of the atoms, and therefore the chemical potentials of the two condensates, remained precisely equal. This is the analogue of a supercurrent, a flow without a voltage to drive it, and represents a manifestation of the DC Josephson effect. These observations of the Josephson effects demonstrate the underlying unity of solid and gaseous systems.

Aside from spectroscopic measurements and the study of quantum effects in BECs, magnetic traps have a variety of other applications in different areas of physics. These include the making of atom lasers and sources of incoherent but intense atomic beams, the production of atomic antihydrogen and its spectroscopic investigation, ultrasensitive isotope trace analysis and the study of collision and entanglement between different samples of cold atoms [1]. Magnetic traps are also used in techniques for formation of cold molecules [1], although optical traps are usually preferred.

Quantum entanglement is a strange property of quantum mechanics for which there is not yet a complete theory. In recent years some progress has been made in trying to understand the properties of entanglement [127]. The state of a composite system is said to be entangled when it can not be written as a product of states of its component systems. Entangled states play a key role in many of the most interesting applications of quantum computation and quantum information [127]. This brings us to the topic of the next section.

1.6 A short introduction to quantum computing

From around the year 1990 the field of quantum computation has seen fast development. There are several reasons behind this recent interest from the research community. One reason is that electronic devices in conventional computers have already been scaled down to the point where quantum effects are beginning to interfere with how they function. The reason for this is that the energy bands of solid state physics assume crystalline materials made up of a large number of atoms. When very few atoms are involved the energy bands go over to become discrete energy levels governed by the theory of quantum mechanics.

At this point one may turn the problem around and ask how many atoms are needed to do the computation rather than to ask how many atoms are needed to make the electronic devices of the traditional computer circuit work. It may in fact be easier to make a quantum computer based on single atoms or particles than to make conventional electronic devices work outside of the validity range of their theoretical foundation. Quantum computing can thus be seen as a natural way forward for computer science.

Additional incentives to pursue quantum computing were provided by Peter Shors demonstration in 1994 that the problem of finding the prime factors of an integer and the ‘discrete logarithm’ problem could be solved efficiently on a quantum computer [128]. In 1995 Lov Grover showed that also the problem of conducting a search through an unstructured search space could be sped up on a quantum computer [129]. Research teams have also found that quantum computers can simulate quantum mechanical systems efficiently, something which is often difficult on a classical computer. The efficient simulation of large quantum mechanical systems is a problem of profound scientific and technological implications in the future. It is suspected that the mentioned problems can not be solved efficiently on a classical computer, although this has not been proved.

Shors quantum algorithms are useful in cryptanalysis for inverting the encryption stage of RSA and other public key cryptosystems. Quantum computing is also interesting to the field of cryptography for other reasons. By exploiting the quantum mechanical principle that observation in general disturbs the system being observed it appears possible to always detect an eavesdropper on a quantum channel. If somebody tries to intercept a key sequence being transmitted this will be visible as a disturbance in the communication channel. The compromised key bits can then be thrown out and a new attempt at transferring a key sequence be made. This procedure

is known as quantum cryptography or quantum key distribution. The first practical systems of this type are already commercially available.

In the same way that classical computing is based on information theory a parallel field of quantum information has arisen to provide support for quantum computing. In contrast to classical computing where bits are used to represent information quantum computing uses quantum bits, or qubits for short, for this purpose [127].

A classical bit has two states 0 and 1. A quantum bit can also be in the two states $|0\rangle$ and $|1\rangle$, which correspond to the states 0 and 1 for a classical bit. Notation like ' $| \ \rangle$ ' is called Dirac notation and it is the standard notation for states in quantum mechanics. Unlike a classical bit a qubit can also be in a linear combination or superposition of the two states $|0\rangle$ and $|1\rangle$ so that $|\psi\rangle = \alpha |0\rangle + \beta |1\rangle$, where α and β are complex numbers. Because the probabilities must sum to one $|\alpha|^2 + |\beta|^2 = 1$. A qubit's state is a unit vector in a two-dimensional complex vector space. The special states $|0\rangle$ and $|1\rangle$ are known as computational basis states and form an orthonormal basis for the vector space.

When a qubit is measured one will either get the result 0 with probability $|\alpha|^2$ or the result 1 with probability $|\beta|^2$. The measurement collapses the state of the qubit from the superposition state to the specific state consistent with the measured result. It is not known why this collapse happens. It is therefore in general not possible to determine the values of α and β . The laws of quantum mechanics dictate that one can only acquire much more restricted information about the quantum state. Measurements on multiple identically prepared qubits combined with the use of different sets of computational basis states can nevertheless be used to acquire more information about a given quantum state, but this is far from easy to do in practise. This lack of observability of quantum states does not affect the possibility to realize quantum computing however.

A system of two qubits has four computational basis states denoted $|00\rangle$, $|01\rangle$, $|10\rangle$ and $|11\rangle$. A pair of qubits can also be in superpositions of these four states. The quantum state of two qubits has a complex coefficient – sometimes called an amplitude – associated with it so that the state vector describing the two qubits is $|\psi\rangle = \alpha_{00} |00\rangle + \alpha_{01} |01\rangle + \alpha_{10} |10\rangle + \alpha_{11} |11\rangle$.

An important two qubit state is the Bell state $(|00\rangle + |11\rangle)/\sqrt{2}$. It is also known as an EPR pair after Einstein, Podolsky and Rosen, who wrote a paper that first pointed out the strange properties of this state. The measurement of the first qubit of a Bell state gives the result 0 or 1 with probability $1/2$. The post measurement state will be $|\psi\rangle = |00\rangle$ or $|\psi\rangle = |11\rangle$

respectively. A measurement of the second qubit will consequently always give the same result as the measurement of the first qubit. This correlation of the measurement outcomes forms the prototype for many other interesting quantum states and constitutes the key ingredient in quantum teleportation and super dense coding.

Quantum teleportation is a technique for sending a qubit from A to B by sending only two classical data bits. It requires one qubit of an EPR pair to be at A and the other one at B. A system of n qubits has computational basis states of the form $|x_1 x_2 \dots x_n\rangle$ and a quantum state of such a system is specified by 2^n amplitudes. For $n = 500$ this number is larger than the estimated number of atoms in the universe. This gives quantum computers enormous potential computational power if it can be exploited.

Classical computers are built using logic gates such as the NOT, AND, OR, NAND, NOR and XOR gates in addition to shift-registers and buffers. Several quantum logic gates that operate on qubits have similarly been developed. The most important single qubit gates are the NOT, Z and Hadamard gates and the most important multiple qubit gate is the controlled-NOT (CNOT) gate. The CNOT gate flips the target qubit if the control qubit is set to 1 and leaves the target qubit unchanged if the control qubit is set to 0. The operation of these gates is summarized in Fig. 1.2 and will not be explained in more detail here.

$$\begin{array}{l}
 \alpha|0\rangle + \beta|1\rangle \longrightarrow \boxed{X} \longrightarrow \beta|0\rangle + \alpha|1\rangle \quad X \equiv \begin{bmatrix} 0 & 1 \\ 1 & 0 \end{bmatrix} \\
 \alpha|0\rangle + \beta|1\rangle \longrightarrow \boxed{Z} \longrightarrow \alpha|0\rangle - \beta|1\rangle \quad Z \equiv \begin{bmatrix} 1 & 0 \\ 0 & -1 \end{bmatrix} \\
 \alpha|0\rangle + \beta|1\rangle \longrightarrow \boxed{H} \longrightarrow \alpha \frac{|0\rangle + |1\rangle}{\sqrt{2}} + \beta \frac{|0\rangle - |1\rangle}{\sqrt{2}} \quad H \equiv \frac{1}{\sqrt{2}} \begin{bmatrix} 1 & 1 \\ 1 & -1 \end{bmatrix} \\
 \begin{array}{l} |A\rangle \longrightarrow \bullet \longrightarrow |A\rangle \\ |B\rangle \longrightarrow \boxed{X} \longrightarrow |B \oplus A\rangle \end{array} \quad U_{CN} = \begin{bmatrix} 1 & 0 & 0 & 0 \\ 0 & 1 & 0 & 0 \\ 0 & 0 & 0 & 1 \\ 0 & 0 & 1 & 0 \end{bmatrix}
 \end{array}$$

Fig. 1.2. A summary of operation of the most important quantum gates.

A remarkable universality result is that any multiple qubit logic gate may be composed from CNOT and single qubit gates. These gates are therefore the prototypes for all other logic gates. This result is the quantum parallel of the universality of the classical NAND gate.

The normalization condition with requires that $|\alpha|^2 + |\beta|^2 = 1$ for a quantum state places the constraint on a matrix U representing a quantum gate that it must be unitary so that $U^\dagger U = I$. U^\dagger is the adjoint of U obtained by transposing and then complex conjugating U and I is the two by two identity matrix. This unitarity condition is the only constraint on quantum gates and any unitary matrix hence represents a valid quantum gate.

Unitary quantum logic gates are inherently reversible whereas many classical logic gates such as the NAND gate are inherently irreversible. This means that quantum circuits can not be used to simulate classical circuits directly. By using a reversible quantum logic gate known as a Toffoli gate to simulate irreversible classical logic gates, quantum computers become able to perform any computation that a classical computer may do. The Toffoli gate looks similar schematically to the CNOT gate, but has two control inputs instead of one. It flips the target qubit only when both the control qubits are set. The Toffoli gate has itself as its inverse.

The task of building a quantum computer in real life has turned out to be extremely challenging. Four basic requirements have been outlined for the design of a successful quantum computer. These are the robust representation of quantum information, the ability to perform a universal family of unitary transformations, the ability to prepare a specific initial qubit state and successful measurement of the output result.

The qubit states should be chosen from a finite set of accessible states. It is also generally desirable for the state space to have some aspect of symmetry. The position x of a particle along a one-dimensional line is for example a poor choice even though the particle may be in a quantum state or superposition state. This is because x has a continuous range of possibilities where the information capacity is limited by quantum noise, also known as decoherence. Spin- $\frac{1}{2}$ particles are nearly ideal qubits. A poor qubit representation generally leads to problems with decoherence.

Quantum computing requires the implementation of single spin operations and CNOT gates, which can be used to realize any unitary transform. The ability to address individual qubits and to apply the quantum gates to select qubits or pairs of qubits is implicitly also required. This is not simple to accomplish in many physical systems. Unrecorded

imperfections in unitary transforms lead to decoherence. The cumulative effect of systematic errors is also decoherence. The length of the longest possible quantum computation is roughly given by the ratio of τ_Q , the time for which a system remains quantum-mechanically coherent, to τ_{op} , the time it takes to perform elementary unitary transformations which involve at least two qubits. These two times are in fact related in many systems since they are both determined by the strength of the system's coupling to the external world. The preservation of coherence is both a critical and a challenging aspect in the design of any quantum mechanical circuit.

It is necessary to be able to repeatedly produce one specific quantum state with high fidelity to prepare the desired input states. A unitary transform can then be used to turn this specific quantum state into any other desired input state. Ions may for example be cooled into their ground state, but this is a challenging procedure.

Projective measurements or strong measurements collapse the wave function leading to the detection of one of the basis states. The output from a good quantum algorithm is a superposition state which gives a useful answer with high probability when it is measured. One step in Shors quantum factoring algorithm is for example to find an integer r close to qc/r from the measurement result, where q is the dimension of a Hilbert space. The output state is in a nearly uniform superposition of all possible values of c , but a measurement collapses this into a single random integer, thus allowing r to be determined with high probability using a continued fraction expansion technique. Things like inefficient photon counters and thermal amplifier noise can reduce the information obtained about measured qubit states in such schemes.

Projective measurements are often difficult to implement and require a large and switchable coupling between the quantum and classical systems. Measurements can be a decoherence process and should not occur when not desired. Weak measurements, which are performed continuously, are possible if the computation is completed in a short time compared with the measurement coupling and if large ensembles of quantum computers are used. Weak measurements are for instance relevant in physical implementations based on nuclear magnetic resonance, as described briefly in the following.

A number of physical quantum computer implementations have been proposed. Three of the more promising systems which have been extensively investigated are based on optical cavity quantum electrodynamics (QED) [130], ion traps [131] and nuclear magnetic

resonance (NMR). In cavity QED qubits are represented by the locations of single photons between two modes $|01\rangle$ and $|10\rangle$, or polarizations. Well isolated single atoms are used as a medium to allow the photons to interact with each other. The single atoms are placed within optical cavities of very high Q , something which results in very high atom-field dipole coupling due to the high electric field strength of the one or two electromagnetic modes in the cavity. Because the coupling of two photons is mediated by an atom it is desirable to increase the atom-field coupling. This unfortunately limits cascability since coupling of a photon into and out of the cavity then becomes difficult.

In the ion trap scheme qubits are represented by the hyperfine state of an atom and the lowest level vibrational modes (phonons) of trapped atoms. Fine and hyperfine transitions of a trapped atom correspond to electron and nuclear spin flips respectively. Because the energy difference between different spin states is very small compared with for example the kinetic energy of atoms at room temperature the spin states of an atom are usually difficult to observe and control. By isolating and trapping small numbers of charged atoms in electromagnetic traps and cooling them down until their kinetic energy is much lower than the spin energy contribution it becomes possible to tune incident monochromatic (laser) light to selectively cause transitions between different spin states. The magnetic trapping structures in Chapter 3 of this thesis may be of use for trapping ions with this approach. The problems with ion traps are that phonon lifetimes are short and that ions are difficult to prepare in their motional ground state.

In quantum computers based on NMR qubits are represented by the spins of atomic nuclei. To circumvent the weakness of the phonon mediated spin-spin coupling technique of ion traps and its susceptibility to decoherence molecules are used instead of atoms thus allowing the chemical bonds between neighbouring atoms to provide the coupling between spins. Because of the smallness of the nuclear magnetic moment a large number (more than 10^8) of molecules are needed to produce a measurable induction signal. The use of ensembles of quantum computers and difficulties in producing pure input states creates a new set of problems, nearly all of which can be solved by applying the techniques of refocusing and temporal and logical labelling. Since only weak measurements of an ensemble average is possible, quantum algorithm which assume a strong projective measurement must be modified to run on an NMR computer. Quantum algorithm based on the hidden subgroup problem can be executed by appending a classical post-processing step to the quantum computation. This involves checking the answer of each

individual quantum computer (molecule) by plugging the result into the original problem. Only the computers which succeed in the verification give an output to the final ensemble average which is then measured.

Laboratory implementations of quantum computation schemes like the ones mentioned have allowed small quantum computers capable of doing dozens of operations on a few qubits to be realized. This represents the state of the art in quantum computing. Unfortunately none of the above mentioned techniques allow a large-scale quantum computer to be realized in the near future. Other physical implementations of quantum computers have recently been proposed based on representing qubits by magnetic-flux [132] and on the use of neutral atoms trapped in optical lattices [133]. The latter implementation relies on the ability to dynamically change the lattice geometry, something which is possible only with optical lattices. It is not clear whether a similar implementation which combines the use of a magnetic grid and laser excited dipole-dipole interactions to manipulate drops of condensed neutral atoms could be feasible.

There is tremendous motivation to envision some kind of a solid state quantum computer to take advantage of the enormous investments in silicon technology worldwide to date. It may eventually become possible to place, control and measure single nuclear spins on semiconductor chips [134], [135]. Such possibilities depend however on future advances particularly in nanotechnology and in fabrication techniques.

1.7 B-field equations for a conductor and an infinitesimally thin ring

The equations for the magnetic field from a straight wire or conductor and from an infinitesimally thin current loop have been made use of in the investigation of the geometries studied throughout the thesis. The relevant equations are presented here as supplementary information to the four following chapters. The equations for the magnetic field from an infinitesimally thin conductor in the z -direction and an infinitesimally thin ring around the origin in the xy -plane are known from the literature. These equations have been transformed to describe conductors and rings in the orthogonal directions and include the displacement from the origin of the plane. The case of a finite conductor radius is also considered. A realistic wire radius is then calculated as an example. This wire radius will be used frequently in the subsequent chapters.

1.7.1 B-field equations for an infinitesimally thin conductor

The static magnetic field $\mathbf{B}_{\text{DC}}(\mathbf{r})$ or the RF magnetic field $\mathbf{B}_{\text{RF}}(\mathbf{r})$ of an infinitesimally thin bar or conductor in the z -direction is computed as the sum of two field components [136] – [138]

$$B_x^{(\text{bar},i)}(x,y) = -\frac{\mu_0 I^{(\text{bar},i)} \cdot (y - \Delta_i^{(y)})}{2\pi r_i^2}, \quad (1.2)$$

$$B_y^{(\text{bar},i)}(x,y) = \frac{\mu_0 I^{(\text{bar},i)} \cdot (x - \Delta_i^{(x)})}{2\pi r_i^2}, \quad (1.3)$$

where $\mu_0 = 4\pi \cdot 10^{-7}$ H/m, $I^{(\text{bar},i)}$ is either the DC or RF current of bar i and $r_i = \sqrt{(x - \Delta_i^{(x)})^2 + (y - \Delta_i^{(y)})^2}$. $\Delta_i^{(x)}$ and $\Delta_i^{(y)}$ are the shifts of the bars from the coordinate system centre ($x = y = 0$). The same equations can be used for both the DC and RF magnetic fields by invoking the quasi-static approximation for the RF field. The quasi-static approximation is valid so long as the characteristic size of the geometry is small compared to the wavelength of the RF current.

The corresponding equations for the field components of an infinitesimally thin bar or conductor in the x -direction or y -direction can be found from direct inspection. For a bar or conductor in the x -direction

$$B_y^{(\text{bar},i)}(y,z) = -\frac{\mu_0 I^{(\text{bar},i)} \cdot (z - \Delta_i^{(z)})}{2\pi r_i^2}, \quad (1.4)$$

$$B_z^{(\text{bar},i)}(y,z) = \frac{\mu_0 I^{(\text{bar},i)} \cdot (y - \Delta_i^{(y)})}{2\pi r_i^2}, \quad (1.5)$$

where $\mu_0 = 4\pi \cdot 10^{-7}$ H/m, $I^{(\text{bar},i)}$ is either the DC or RF current of bar i and $r_i = \sqrt{(y - \Delta_i^{(y)})^2 + (z - \Delta_i^{(z)})^2}$. $\Delta_i^{(y)}$ and $\Delta_i^{(z)}$ are the shifts of the bars from the coordinate system centre ($y = z = 0$). For a bar or conductor in the y -direction

$$B_x^{(\text{bar},i)}(x,z) = \frac{\mu_0 I^{(\text{bar},i)} \cdot (z - \Delta_i^{(z)})}{2\pi r_i^2}, \quad (1.6)$$

$$B_z^{(\text{bar},i)}(x,z) = -\frac{\mu_0 I^{(\text{bar},i)} \cdot (x - \Delta_i^{(x)})}{2\pi r_i^2}, \quad (1.7)$$

where $\mu_0 = 4\pi \cdot 10^{-7}$ H/m, $I^{(\text{bar},i)}$ is either the DC or RF current of bar i and $r_i = \sqrt{(x - \Delta_i^{(x)})^2 + (z - \Delta_i^{(z)})^2}$. $\Delta_i^{(x)}$ and $\Delta_i^{(z)}$ are the shifts of the bars from the coordinate system centre ($x = z = 0$).

The overall static magnetic field \mathbf{B}_{DC} or RF magnetic field \mathbf{B}_{RF} from multiple bars or conductors is given as

$$\mathbf{B}_{\text{DC or RF}}^{(\text{bar})} = \sum_i B_x^{(\text{bar},i)} \cdot \hat{x} + \sum_i B_y^{(\text{bar},i)} \cdot \hat{y} + \sum_i B_z^{(\text{bar},i)} \cdot \hat{z}, \quad (1.8)$$

where \hat{x} , \hat{y} and \hat{z} are unit vectors.

1.7.2 The introduction of a finite conductor radius

An equation for the magnetic field $\mathbf{B}_{\text{DC}}(\rho)$ from an infinitesimally thin line or conductor expressed in cylindrical coordinates is found in (7.25) in [139] as

$$\mathbf{B}_{\text{DC}}(\rho) = \frac{\mu_o I}{2\pi\rho} \hat{\mathbf{a}}_\phi. \quad (1.9)$$

A wire or conductor with a finite radius r can also be seen as a solid cylinder. In equation (7.33) in [139] expressions are given for the magnetic field $\mathbf{B}_{\text{DC}}(\rho)$ of a solid cylinder of current in cylindrical coordinates. This equation is as follows:

$$\mathbf{B}_{\text{DC}}(\rho) = \begin{cases} \frac{\mu_o \rho I_o}{2\pi a^2} \hat{\mathbf{a}}_\phi, & \rho < a \\ \frac{\mu_o I_o}{2\pi\rho} \hat{\mathbf{a}}_\phi, & \rho > a \end{cases} \quad (1.10)$$

where a is the radius of the cylinder and ρ is the distance from the centre of the cylinder. It is seen that the expression for $\rho > a$ is identical to equation (1.9) for an infinitesimally thin line of current. The introduction of a finite conductor radius does not in other words change the expression for the magnetic field outside of the wire, a point that was also made in [139].

It is here useful to convert also the expression for the B-field for $\rho < a$ to Cartesian coordinates. This is done with the help of unit vector

transformations that are found in the literature, for example in Table B-3 in [139]. The relevant transformations are

$$\hat{\mathbf{a}}_x = -\hat{\mathbf{a}}_\varphi \sin \varphi = -\hat{\mathbf{a}}_\varphi y/\rho, \quad (1.11)$$

$$\hat{\mathbf{a}}_y = \hat{\mathbf{a}}_\varphi \cos \varphi = \hat{\mathbf{a}}_\varphi x/\rho. \quad (1.12)$$

This yields the following equations for the magnetic field inside a conductor in the z -direction:

$$B_x = \frac{-\mu_o I_o \left(y - \Delta^{(y)} \right)}{2\pi a^2}, \quad (1.13)$$

$$B_y = \frac{\mu_o I_o \left(x - \Delta^{(x)} \right)}{2\pi a^2}, \quad (1.14)$$

where a is the radius of the conductor and $\Delta^{(x)}$ and $\Delta^{(y)}$ define the displacement of the centre of the conductor in the x - and y -directions respectively.

The equations for the field components in (1.13) and (1.14) are seen to be identical to the equations for the corresponding field components outside of the conductors in (1.2) and (1.3), except that r_i^2 has been replaced by a^2 in the denominators.

This facilitates a very simple implementation of conductors with a finite radius in Matlab. It is first checked whether a field point lies inside of or outside of the conductor radius for the conductor in question. If the point lies inside of the conductor radius then r_i^2 is simply replaced with a^2 . To be specific a new variable is defined which is set equal to a^2 whenever the field point lies inside of or on the conductor radius. Otherwise the variable is set equal to r_i^2 . This enables a single set of equations to be used for conductors with a finite radius by substituting the new variable for r_i^2 in the equations for infinitesimally thin conductors.

An appropriate conductor radius should now be decided on. In the case of free-standing wires the maximum current density is limited by practical fabrication and heat dissipation issues to less than 10^5 A/cm². Wires on a chip can however sustain currents of up to 10^8 A/cm² because of the ability of the substrate to dissipate power [93], [140]. For the millimetre sized structures in Chapter 2 it turns out that it is not necessary to use particularly large wire currents to achieve sufficiently deep trapping potentials. A current density of 1000 A/cm² will therefore be used here. This value

corresponds to the maximum current density used in today's computers [141]. The current density can be used to calculate a minimum wire radius. For a DC current of 92.5 mA and an RF current of 10 mA, the minimum wire radius becomes

$$a_{\min} = \sqrt{\frac{I_{w,DC} + I_{w,RF}}{\pi \cdot I_{\max}}} = \sqrt{\frac{(0.0925 + 0.01)[A]}{\pi[\text{rad/s}] \cdot (10^3 \cdot 10^4)[A/m^2]}} = 5.72 \cdot 10^{-5} \text{ m}. \quad (1.15)$$

The DC and RF currents and the wire radius in this example have been used for many of the millimetre-sized geometries in this thesis. When the geometries are scaled, by changing the ratio of the DC current I to the cyclic RF frequency ω_{RF} , the radius of the conductors should be adjusted to keep the current density within a reasonable range.

In the case of the micrometre-sized geometries in Chapter 3 a much higher wire current density of around 22 kA/cm² will be used. The proposed geometries are here intended to be patterned on a chip. Much of the substrate should however be removed and this will strongly limit the ability of the chip to dissipate additional power.

1.7.3 B-field equations for an infinitesimally thin current ring

The equations for the field components of an infinitesimally thin current ring in a plane normal to the z -direction are [17], [137], [138]:

$$B_z^{(\text{ring},j)}(x,y,z) = \frac{\mu_0 I^{(\text{ring},j)}}{2\pi} \cdot \frac{1}{\left[(R+\rho)^2 + (z-z_{r_j})^2 \right]^{0.5}} \cdot \left[K(k^2) + \frac{R^2 - \rho^2 - (z-z_{r_j})^2}{(R-\rho)^2 + (z-z_{r_j})^2} E(k^2) \right], \quad (1.16)$$

$$B_x^{(\text{ring},j)}(x,y,z) = \frac{\mu_0 I^{(\text{ring},j)}(x - \Delta_j^{(x)})}{2\pi\rho^2} \cdot \frac{z - z_{r_j}}{\left[(R+\rho)^2 + (z-z_{r_j})^2 \right]^{0.5}} \cdot \left[-K(k^2) + \frac{R^2 + \rho^2 + (z-z_{r_j})^2}{(R-\rho)^2 + (z-z_{r_j})^2} E(k^2) \right], \quad (1.17)$$

$$B_y^{(\text{ring},j)}(x,y,z) = \frac{\mu_0 I^{(\text{ring},j)}(y - \Delta_j^{(y)})}{2\pi\rho^2} \cdot \frac{z - z_{r_j}}{\left[(R + \rho)^2 + (z - z_{r_j})^2 \right]^{0.5}} \cdot \left[-K(k^2) + \frac{R^2 + \rho^2 + (z - z_{r_j})^2}{(R - \rho)^2 + (z - z_{r_j})^2} E(k^2) \right], \quad (1.18)$$

where K and E are the elliptic integrals with the argument

$$k^2 = \frac{4R\rho}{(R + \rho)^2 + (z - z_{r_j})^2}. \quad (1.19)$$

In (1.16) - (1.18), $I^{(\text{ring},j)}$ is the DC or RF current in the j th ring, R is the radius of this infinitely thin ring ($d_r = 0$), z_{r_j} is the position of the centre of the j th ring on the z -axis, and $\rho = \sqrt{(x - \Delta_j^{(x)})^2 + (y - \Delta_j^{(y)})^2}$. $\Delta_j^{(x)}$ and $\Delta_j^{(y)}$ are the shifts of the rings from the coordinate system centre ($x = y = 0$).

Just as was the case for the straight conductors the same equations can be used for both the static and RF magnetic fields by invoking the quasi-static approximation for the RF field. The quasi-static approximation is valid so long as the characteristic size of the geometry is smaller than about one tenth of the RF wavelength. Since the RF frequencies used in the atom traps of this thesis are relatively low and the wavelengths several hundred metres long, the atom traps are small enough by a good margin. The validity of the quasi-static approximation, under which the RF field is equivalent to the static magnetic field, has been confirmed through simulations of millimetre-size traps with the software tool AMPERES, which is described in Appendix A.

The equations for the field components of a similar current ring in a plane normal to the x -direction are obtained by tilting the coordinate system on the side through the use of Euler angle transformations. The rotation of the field vectors is described in [142]. The Euler angles that have been used are $\alpha = 0^\circ$, $\beta = 90^\circ$ and $\gamma = 0^\circ$. The new field components \hat{B}_x , \hat{B}_y and \hat{B}_z are found from the original field components B_x , B_y and B_z for rings in a plane normal to the z -direction as $\hat{B}_x \cdot \hat{x} = B_z \cdot z$, $\hat{B}_y \cdot \hat{y} = B_y \cdot y$ and

$\hat{B}_z \cdot \hat{z} = -B_x \cdot -x$. \hat{x} , \hat{y} and \hat{z} are here the unit vectors of the new axes and x , y and z the unit vectors of the original axes. The minus sign for the field component \hat{B}_z disappears because the original x -axis points in the negative z -axis direction after the rotation. This is accounted for by the unit vectors. It is intuitively correct that all three field components become positive for rings in a plane normal to the x -direction, just as they were for rings in a plane normal to the z -direction.

The resulting B-field components are as follows:

$$B_x^{(\text{ring},j)}(x,y,z) = \frac{\mu_0 I^{(\text{ring},j)}}{2\pi} \cdot \frac{1}{\left[(R+\rho)^2 + (x-x_{r_j})^2 \right]^{0.5}} \cdot \left[K(k^2) + \frac{R^2 - \rho^2 - (x-x_{r_j})^2}{(R-\rho)^2 + (x-x_{r_j})^2} E(k^2) \right], \quad (1.20)$$

$$B_y^{(\text{ring},j)}(x,y,z) = \frac{\mu_0 I^{(\text{ring},j)}(y-\Delta_j^{(y)})}{2\pi\rho^2} \cdot \frac{x-x_{r_j}}{\left[(R+\rho)^2 + (x-x_{r_j})^2 \right]^{0.5}} \cdot \left[-K(k^2) + \frac{R^2 + \rho^2 + (x-x_{r_j})^2}{(R-\rho)^2 + (x-x_{r_j})^2} E(k^2) \right], \quad (1.21)$$

$$B_z^{(\text{ring},j)}(x,y,z) = \frac{\mu_0 I^{(\text{ring},j)}(z-\Delta_j^{(z)})}{2\pi\rho^2} \cdot \frac{x-x_{r_j}}{\left[(R+\rho)^2 + (x-x_{r_j})^2 \right]^{0.5}} \cdot \left[-K(k^2) + \frac{R^2 + \rho^2 + (x-x_{r_j})^2}{(R-\rho)^2 + (x-x_{r_j})^2} E(k^2) \right], \quad (1.22)$$

where K and E are the elliptic integrals with the argument

$$k^2 = \frac{4R\rho}{(R+\rho)^2 + (x-x_{r_j})^2}. \quad (1.23)$$

In (1.20) - (1.22), $I^{(\text{ring},j)}$ is the current in the j th ring, R is the radius of this infinitely thin ring ($d_r = 0$), x_{r_j} is the position of the centre of the j th ring

on the x -axis, and $\rho = \sqrt{(y - \Delta_j^{(y)})^2 + (z - \Delta_j^{(z)})^2}$. $\Delta_j^{(y)}$ and $\Delta_j^{(z)}$ are the shifts of the rings from the coordinate system centre ($y = z = 0$).

The equations for the field components of an infinitesimally thin current ring in a plane normal to the y -direction are found in a similar way. The Euler angles in this case are $\alpha = 90^\circ$, $\beta = 90^\circ$ and $\gamma = -90^\circ$. The new field components are found from the original field components for rings in a plane normal to the z -direction as $\hat{B}_x \cdot \hat{x} = B_x \cdot x$, $\hat{B}_y \cdot \hat{y} = B_z \cdot z$ and $\hat{B}_z \cdot \hat{z} = -B_y \cdot y$. \hat{x} , \hat{y} and \hat{z} are the unit vectors of the new axes and x , y and z the unit vectors of the original axes. The minus sign for the field component \hat{B}_z disappears because the original y -axis points in the negative z -axis direction after the rotation. It again makes sense that all field components are positive for rings in a plane normal to the y -direction in the same way as for rings in a plane normal to the x -direction or the z -direction.

The resulting B-field components are as follows:

$$B_y^{(\text{ring},j)}(x, y, z) = \frac{\mu_0 I^{(\text{ring},j)}}{2\pi} \cdot \frac{1}{\left[(R + \rho)^2 + (y - y_{r_j})^2 \right]^{0.5}} \cdot \left[K(k^2) + \frac{R^2 - \rho^2 - (y - y_{r_j})^2}{(R - \rho)^2 + (y - y_{r_j})^2} E(k^2) \right], \quad (1.24)$$

$$B_x^{(\text{ring},j)}(x, y, z) = \frac{\mu_0 I^{(\text{ring},j)} (x - \Delta_j^{(x)})}{2\pi \rho^2} \cdot \frac{y - y_{r_j}}{\left[(R + \rho)^2 + (y - y_{r_j})^2 \right]^{0.5}} \cdot \left[-K(k^2) + \frac{R^2 + \rho^2 + (y - y_{r_j})^2}{(R - \rho)^2 + (y - y_{r_j})^2} E(k^2) \right], \quad (1.25)$$

$$B_z^{(\text{ring},j)}(x, y, z) = \frac{\mu_0 I^{(\text{ring},j)} (z - \Delta_j^{(z)})}{2\pi \rho^2} \cdot \frac{y - y_{r_j}}{\left[(R + \rho)^2 + (y - y_{r_j})^2 \right]^{0.5}}$$

$$\left[-K(k^2) + \frac{R^2 + \rho^2 + (y - y_{r_j})^2}{(R - \rho)^2 + (y - y_{r_j})^2} E(k^2) \right], \quad (1.26)$$

where K and E are the elliptic integrals with the argument

$$k^2 = \frac{4R\rho}{(R + \rho)^2 + (y - y_{r_j})^2}. \quad (1.27)$$

In (1.24) - (1.26), $I^{(\text{ring},j)}$ is the current in the j th ring, R is the radius of this infinitely thin ring ($d_r = 0$), y_{r_j} is the position of the centre of the j th ring on the y -axis, and $\rho = \sqrt{(x - \Delta_j^{(x)})^2 + (z - \Delta_j^{(z)})^2}$. $\Delta_j^{(x)}$ and $\Delta_j^{(z)}$ are the shifts of the rings from the coordinate system centre ($x = z = 0$).

The overall static magnetic \mathbf{B}_{DC} and RF magnetic \mathbf{B}_{RF} fields are computed by vectorial summation of the corresponding fields from the bars or straight conductors and infinitesimally thin rings as

$$\begin{aligned} \mathbf{B}_{\text{DC or RF}}^{(\text{total})} = & \left(\sum_i B_x^{(\text{bar},i)} + \sum_j B_x^{(\text{ring},j)} \right) \hat{x} + \left(\sum_i B_y^{(\text{bar},i)} + \sum_j B_y^{(\text{ring},j)} \right) \hat{y} \\ & + \left(\sum_i B_z^{(\text{bar},i)} + \sum_j B_z^{(\text{ring},j)} \right) \hat{z}, \end{aligned} \quad (1.28)$$

where \hat{x} , \hat{y} and \hat{z} are unit vectors. The magnitude of the field is given as the square root of the sum of the three field components squared.

In later chapters of this thesis very large currents of up to three and a half amperes have occasionally been used in bias rings, in part for the purpose of illustration. If very high currents are to be realized experimentally the radius of the infinitesimally thin rings must be made large enough to take into account that the real rings must have a cross-section large enough to support the currents. It should be possible to greatly reduce the need for the highest currents by placing the rings closer together and by accepting a smaller field gradient between the bias rings.

Chapter 2

Wire Structures for Cold Atom Handling

2.1 Introduction

Cold atoms interact with the effective potential because of their magnetic polarization. By shaping the effective potential clouds of cold atoms can be transported along and between wires as well as held in magnetic traps. This Chapter begins with a look at the effective potential around a single wire, first without and then with external bias. Then a system of two crossed wires is considered and it is shown how cold atoms may be transferred between the wires. A system of two parallel wires is subsequently described in an analogous fashion. The Chapter continues with a look at the effective potential in a cell consisting of two pairs of crossing parallel wires. The cell can be used to trap both weak- and strong-field-seeking atoms. A double-well potential formed in a three-by-three wire structure is then considered. The two wells can be merged electrically by reducing the DC currents in the two centre wires. Finally cell-grids consisting of parallel wires in two orthogonal layers are examined. The cell-grids can also be stacked to form an elaborate 3D effective potential pattern.

2.2 The effective potential around a single wire

The effective potential $U_{\text{eff}}(\boldsymbol{\rho})$, which is induced by a combination of the DC and the RF fields, is computed according to a formula in [104], [143], [107], [138] and [144]

$$U_{\text{eff}}(\boldsymbol{\rho}) = m_F \sqrt{\left[\mu_B g_F |\mathbf{B}_{\text{DC}}(\boldsymbol{\rho})| - \hbar \omega_{\text{RF}} \right]^2 + \left[\mu_B g_F B_{\text{RF}}^{(\perp)}(\boldsymbol{\rho}) / 2 \right]^2}, \quad (2.1)$$

where $m_F = 2$ is the magnetic quantum number of the atomic state, μ_B is the Bohr magneton, g_F is the Landè factor, $\mathbf{B}_{\text{DC}}(\boldsymbol{\rho})$ is the static magnetic trap field, \hbar is the reduced Planck constant, ω_{RF} is the cyclic frequency of the RF field, and $B_{\text{RF}}^{(\perp)}$ is the RF magnetic field normal to the local DC magnetic vector. The validity of this equation, which is specific for linear polarization of the RF field, has been experimentally verified [106], [107].

The effective potential around a single wire has a minimum of zero at a constant radius d . The second term in the square root of (2.1) is always zero for a single wire. The reason for this will be explained later in this section. For also the first term to be zero

$$\mu_B g_F |\mathbf{B}_{\text{DC}}(\boldsymbol{\rho})| = \hbar \omega_{\text{RF}}. \quad (2.2)$$

A simple expression for the magnetic field $\mathbf{B}_{\text{DC}}(\rho)$ is found in (7.25) in [139],

$$\mathbf{B}_{\text{DC}}(\rho) = \frac{\mu_0 I}{2\pi\rho} \hat{\mathbf{a}}_\phi. \quad (2.3)$$

This expression is for the B-field of an infinitesimally thin line. By substituting equation (2.3) into equation (2.2) it is clear that the radius d is a function of the ratio of the DC current I to the cyclic RF frequency ω_{RF} . The expression for the radius d where the effective potential around a single wire becomes zero is found to be

$$d = \frac{\mu_B g_F \mu_0}{2\pi\hbar} \left(\frac{I}{\omega_{\text{RF}}} \right). \quad (2.4)$$

This expression is plotted in Fig. 2.22 as a function of the ratio I/ω_{RF} . The range of DC current to cyclic frequency ratios in the figure applies to millimetre sized structures, which are relatively large. The purpose of the figure is however just to illustrate the linear relation between the distance d and the DC current to cyclic frequency ratio I/ω_{RF} . This sort of figure should not be used as a design graph since high accuracy in the variables d , I and ω_{RF} is critical to obtain a good result.

As a numeric example, the following data can be entered into (2.4):

$$\mu_B = 9.2741 \cdot 10^{-24} \text{ J/T } (= \text{Am}^2), m_F = 2, g_F = 0.66,$$

$$\mu_0 = 4\pi \cdot 10^{-7} \text{ Vs/Am } (= \text{H/m}), \hbar = 1.05459 \cdot 10^{-34} \text{ Js},$$

$$I = 0.0925 \text{ A}, \omega_{\text{RF}} = 2\pi \cdot 800000 \text{ rad/s}.$$

The radius is in this case found to be $d = 0.2136 \text{ mm}$ for a single wire.

It was explained above that the second term in the square root of (2.1) is zero for a single wire. This can be seen by examining the expression for $B_{\text{RF}}^{(\perp)}(\boldsymbol{\rho})$, given by equation (2) in [138]

$$B_{\text{RF}}^{(\perp)}(\boldsymbol{\rho}) = \sqrt{(\mathbf{B}_{\text{RF}}(\boldsymbol{\rho}))^2 - \left(\frac{\mathbf{B}_{\text{RF}}(\boldsymbol{\rho})\mathbf{B}_{\text{DC}}(\boldsymbol{\rho})}{|\mathbf{B}_{\text{DC}}(\boldsymbol{\rho})|} \right)^2}. \quad (2.5)$$

$\mathbf{B}_{\text{RF}}(\boldsymbol{\rho})$ is of the same form as $\mathbf{B}_{\text{DC}}(\boldsymbol{\rho})$ given in (2.3). The second term under the root sign in (2.5) is the squared product of $\mathbf{B}_{\text{RF}}(\boldsymbol{\rho})$ multiplied by $\mathbf{B}_{\text{DC}}(\boldsymbol{\rho})/|\mathbf{B}_{\text{DC}}(\boldsymbol{\rho})|$. The factor $\mathbf{B}_{\text{DC}}(\boldsymbol{\rho})/|\mathbf{B}_{\text{DC}}(\boldsymbol{\rho})|$ is in this case either 1 or -1 depending on the sign of the DC current. The sign is however of no consequence since the product is squared.

The expression for d in (2.4) is only useful in the case of a single wire when there are no crossing wires or other wires that come close to it. The cases of two crossed wires and two parallel wires will be treated later in this Chapter.

The effective potential around a wire of radius 57.2 μm , which carries a DC current of -92.5 mA and an RF current of -10 mA at 800 kHz, is shown in Fig. 2.1. In the figure the potential peak around the centre of the wire has been cut to better show the circular potential minimum further out from the wire. The full height of the peak is actually about $2.88\text{e-}27$ J.

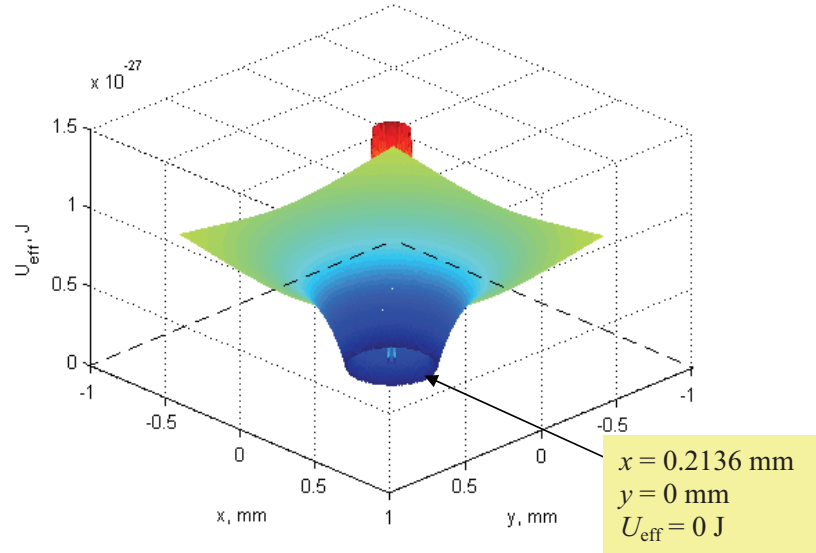


Fig. 2.1. U_{eff} for a single wire without external bias for $z = 0$ mm.

A circular minimum of $U_{\text{eff}} = 0$ J is found at a radius of 0.2136 mm from the centre of the wire. There is also another circular minimum of $U_{\text{eff}} \approx 2.326 \times 10^{-29}$ J inside the wire, at a radius of about 0.015 mm from the centre of the wire. Inside this minimum the effective potential begins to increase again toward the centre of the wire due to the RF current in the wire. If the frequency is reduced toward zero the radius of the circular minimum inside the wire becomes smaller and the circular minimum eventually becomes a point at the centre of the wire at zero frequency.

The depth of the trapping potential is most conveniently measured in Kelvin. The potential in Kelvin is calculated simply by dividing the effective potential U_{eff} [J] by Boltzmann's constant $k = 1.3807 \cdot 10^{-23}$ [J/K]. As can be seen in Fig. 2.1 the effective potential increases to approach a certain level some distance away from the conductor. For the wire in Fig. 2.1 this level is at about 76 μK , which is taken to be the depth of the trapping potential. The potential barrier for stable trapping should typically be no less than 15 μK from private communication between G. A. Kouzaev and W. A. van Wijngaarden, depending on the temperature of the trapped atoms.

The skin effect has been neglected in the computations of the effective potential in this thesis. A uniform RF current distribution is consequently assumed inside the wires corresponding to infinite conductivity. For copper wires the skin depth $\delta_s = 73.8$ μm at 0.8 MHz. A wire radius of 57.2 μm thus amounts to 77.5 % of the skin depth. The skin-effect is accordingly of limited severity even at the centre of the wires in this case. For the microwires and nanotubes used in the next Chapter the skin-effect is much smaller still and can be safely ignored.

2.3 The effective potential around a single wire with bias rings

A minimum of zero of the effective potential is strongly unwanted because it will lead to Majorana spin-flip transitions. The minimum of zero can be removed by applying an additional magnetic field for biasing. Such a field can be created by placing a pair of current carrying loops or rings around the wire as shown in Fig. 2.2(a). When two rings are used a deeper minimum in the shape of a circular band is created between the rings. This minimum can be moved up and down along the wire by applying different bias currents in the two rings. This control over the position of the minimum can in turn be used to move clouds of cold atoms around in structures consisting of multiple wires.

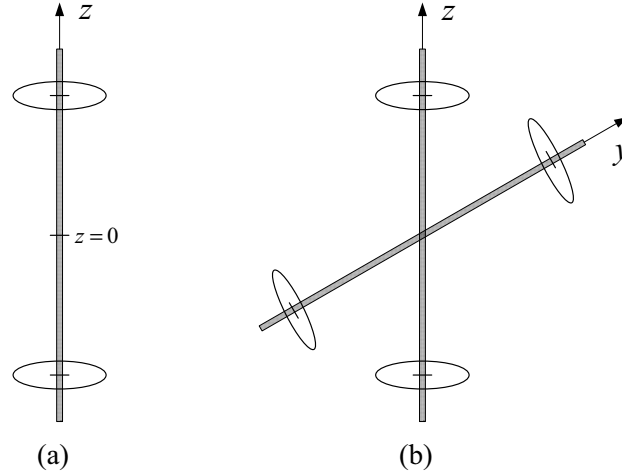


Fig. 2.2. The geometry of a single wire with bias rings (a) and two crossed wires with bias rings (b), which will be considered in Section 2.5.

The bias currents used for moving clouds of cold atoms are RF currents of the same frequency as the RF currents in the wires. The use of RF ring currents enables the movement of cold atoms up and down along wires as well as the transfer of cold atoms between two crossed wires, a topic that will be considered later in Section 2.5. The possibility of using DC bias currents instead has also been examined. The conclusion is that DC bias currents have a very different effect on the minimum potential manifold associated with a wire. To be specific, DC bias currents, when large enough, lead to a bending of the minimum potential manifold out from around the wire so that it wraps around the outside of the bias rings. At the same time the depth of the minimum potential manifold stays relatively flat at the bottom. This makes the gradient of the minimum small in relation to the applied bias. Attempts to move the absolute minimum away from the centre between the bias rings by using different bias currents have additionally lead to new minima being formed in places where they should not be. Consequently DC bias currents are considered unsuitable for moving clouds of cold atoms along wires with DC + RF currents. There remains a possibility however of applying a small DC bias in addition to the RF bias if this is considered useful in terms of increasing the margin against Majorana spin-flip transitions. The use of RF currents for trapping of BECs in the time-averaging regime has been described in [64], [145].

The use of DC bias currents is illustrated in Fig. 2.3. The wire currents are the same as in Fig. 2.1. The bias rings have a radius of 1 mm and are

spaced 6 mm apart on the z -axis. Fig. 2.3(a), where the DC bias currents are ± 0.05 A, is directly comparable with Fig. 2.5, and Fig. 2.3(b), where the DC bias currents are ± 1.5 A, can be compared with Fig. 2.8. From this point onwards all bias currents mentioned in Chapter 2 and Chapter 3 will be RF currents.

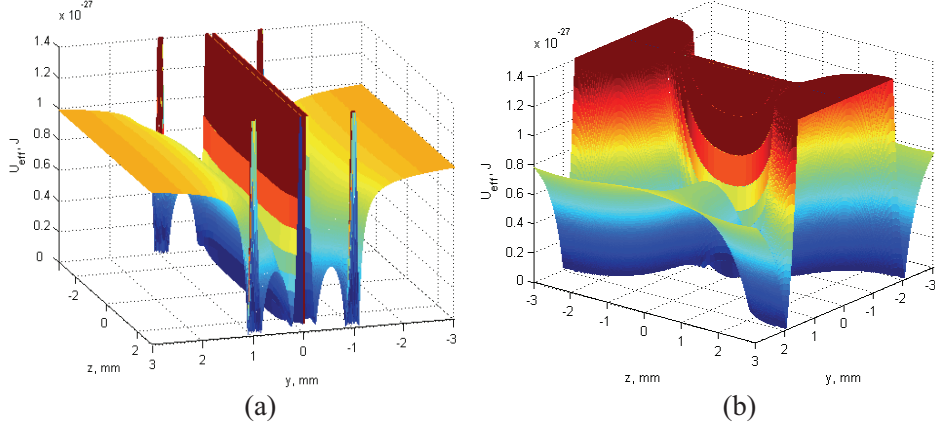


Fig. 2.3. U_{eff} for a single wire with bias rings with DC bias currents. ($x = 0$ mm). The DC bias currents are ± 0.05 A in (a) and ± 1.5 A in (b).

Simulations have shown that the circular minimum around the wire is lifted slightly more up from the zero potential when the bias currents go in the same direction in the two rings, compared to the case when the bias currents go in opposite directions in the two rings. When the currents go in opposite directions in the two rings, the bias field from the rings will be zero at the centre of the wire in the middle between the bias rings when the bias currents in the rings are of equal magnitude. Because the effective potential is a little higher than zero along the centre of the wire, due to the RF current in the wire, there will be no effective potential minimum of zero. In Section 2.5, it will be explained that the bias currents should preferably go in opposite directions, i.e. be of opposite sign, in the bias rings around both wires when atom transfer between two crossed wires is considered.

The effective potential around a wire with bias rings with currents in opposite directions is shown in the xy -plane in Fig. 2.4 and in the yz -plane in Fig. 2.5. The infinitely thin bias rings have a radius of 1 mm and are spaced 6 mm apart. The RF bias currents are -50 mA and 50 mA at 800 kHz in the lower and upper ring respectively. The DC current in the wire is -92.5 mA, and the RF current -10 mA at 800 kHz. The plot for the xz -plane is identical to that of the yz -plane and is not shown. Notice that the circular

minimum around the wire is now no longer at zero potential. The depth of the trapping potential remains practically unchanged since the bias currents are relatively small. In Fig. 2.5 four potential spikes are seen next to the wire where the bias rings intersect the yz -plane.

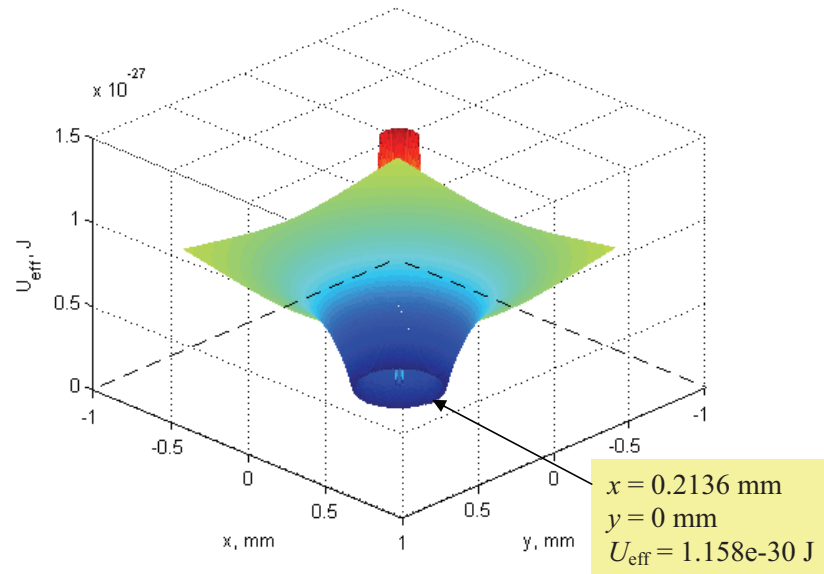


Fig. 2.4. U_{eff} for a single wire with two bias rings with $r = 1$ mm. ($z = 0$ mm).

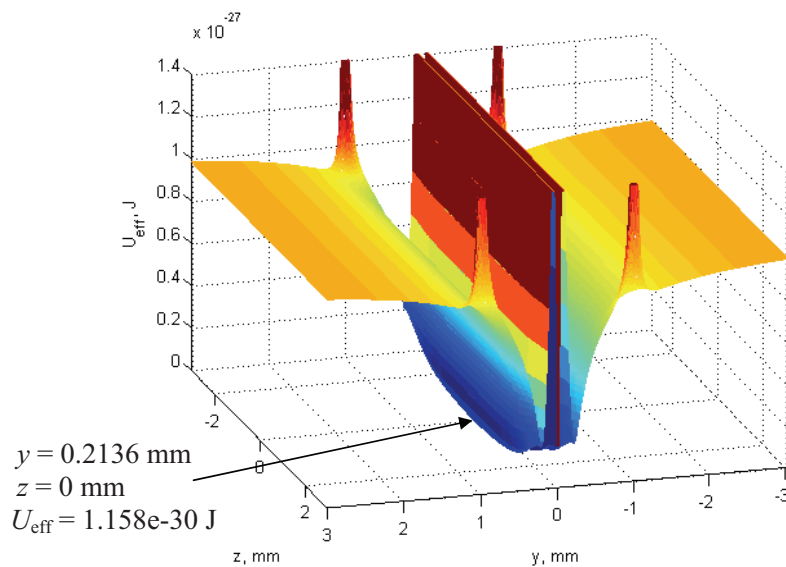


Fig. 2.5. U_{eff} for a single wire with two bias rings with $r = 1$ mm. ($x = 0$ mm).

The computations of the effective potential were first made with equations for infinitesimally thin wires. This meant that the narrow circular minima inside the wires were not seen. It seems however that the minima inside the wires are isolated and will not interfere with the operations of moving atoms along a wire or between wires. There seems to be a large potential barrier between the “internal” and “external” minima associated with a wire. The size of this barrier is linked to the current density in the wire, which should normally be extremely high. Strong external bias would be needed for atoms to overcome this barrier. The “internal” minimum in a wire can in a way be thought of as a parasitic storage area for cold atoms.

Because parallel wires have to be placed relatively close to each other it is of interest find out what happens when the radius of the bias rings is made smaller. If the ring radius is reduced from 1 mm to 0.14 mm, and the RF ring currents are kept at -50 mA and 50 mA, the minimum effective potential falls to $U_{\text{eff}} = 2.929\text{e-}32$ J, but the shape of the potential otherwise looks just like in Fig. 2.4. If the RF ring currents are increased by a factor of $1.1581\text{e-}030 / 2.9287\text{e-}032 = 39.54$ from 50 mA to 1.977 A, the effective potential in the xy -plane still looks identical to that in Fig. 2.4 and the minimum effective potential is back at $U_{\text{eff}} = 1.158\text{e-}30$ J. The effective potential in the yz -plane is now as shown in Fig. 2.6. The effective potential in the xz -plane is the same as that in the yz -plane. Notice that the four potential spikes next to the wire have been transformed into continuous surfaces because of the smaller ring radius and the much increased bias currents.

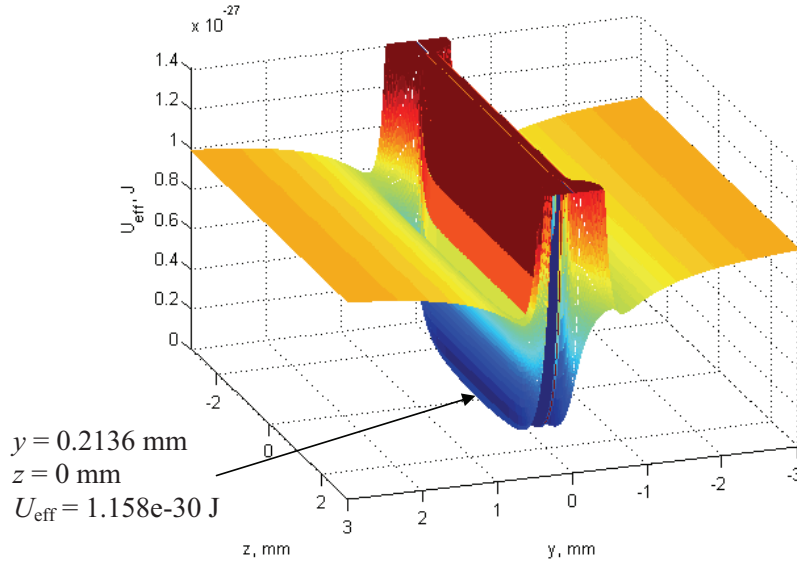


Fig. 2.6. U_{eff} for a single wire with two bias rings with $r = 0.14$ mm. ($x = 0$ mm).

This shows that the ring currents must be greatly increased to maintain the same minimum effective potential when the radius of the bias rings is reduced. There seems to be a linear dependence between the bias current magnitude and the minimum effective potential level. A bias ring with a small radius must therefore support much larger currents and hence have a bigger cross-section than a bias ring with a larger radius.

It will now be shown how the circular potential minimum around a wire can be moved down along the wire by changing the bias currents. In Fig. 2.7 the circular minimum is seen around the wire at the top of the figure. The wire has a radius of $57.2 \mu\text{m}$ and the currents in the wire are -92.5 mA DC and -10 mA RF. The frequency is 800 kHz. The infinitesimally thin bias rings have a radius of 1 mm and are placed at $z = \pm 3$ mm. In Fig. 2.7 the lower ring carries an RF current of -2.5 A and the upper ring an RF current of 0 A. In Fig. 2.8 the circular minimum has been moved to the centre of the wire. The RF current is here 1.5 A in opposite directions in the two bias rings.

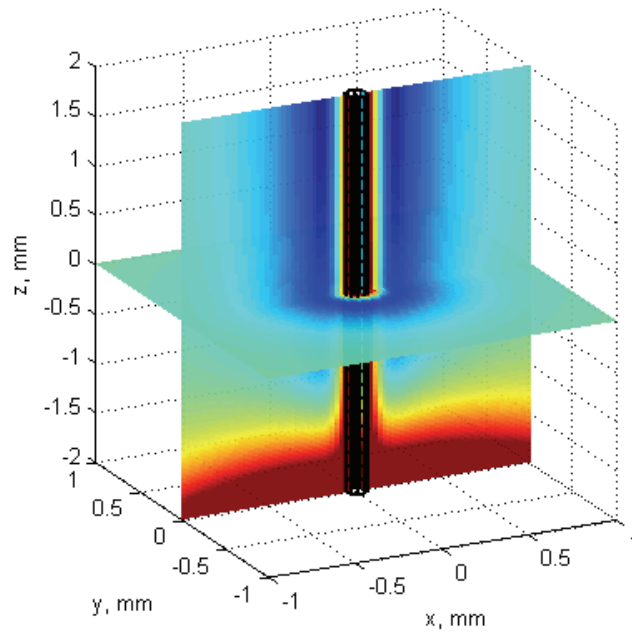


Fig. 2.7. Shifting of the circular potential minimum, (here seen around the top).

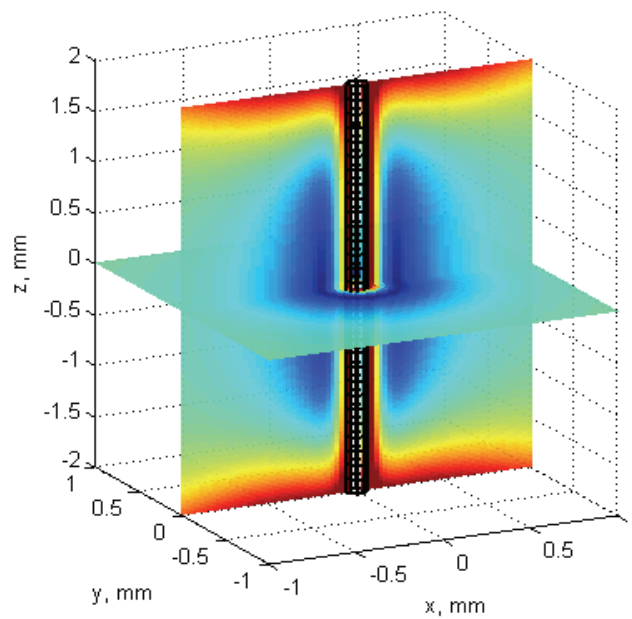


Fig. 2.8. Shifting of the circular potential minimum, (here seen in the middle).

Fig. 2.9 shows the potential surface $10e-29$ J for different RF ring currents. The wire currents are the same as for Fig. 2.7 and Fig. 2.8. The ring currents are as follows, where the isosurfaces are located from top to bottom and the lower and upper rings have the indices I and II respectively:

$$I_{RF,ring}^{I+II} = [-2.5 \ 0] \text{ A} \quad (\text{red}), \quad I_{RF,ring}^{I+II} = [-2.8 \ 0.4] \text{ A} \quad (\text{yellow}),$$

$$I_{RF,ring}^{I+II} = [-2.25 \ 1.0] \text{ A} \quad (\text{blue}), \quad I_{RF,ring}^{I+II} = [-1.5 \ 1.5] \text{ A} \quad (\text{green}),$$

$$I_{RF,ring}^{I+II} = [-1.0 \ 2.25] \text{ A} \quad (\text{blue}), \quad I_{RF,ring}^{I+II} = [-0.4 \ 2.8] \text{ A} \quad (\text{yellow})$$

and $I_{RF,ring}^{I+II} = [0 \ 2.5] \text{ A}$ (red). The bias rings are located outside of the plotted range at $z = \pm 3$ mm. Note that the potential surface for $10e-29$ J becomes progressively wider as it is moved away from the centre between the bias rings. The outermost potential surfaces in red actually extend out to the bias rings, but are shown truncated by the range of the plot. This happens in spite that the current in the bias ring on the opposite side has been greatly increased compared to the potential surface at the centre of the plot.

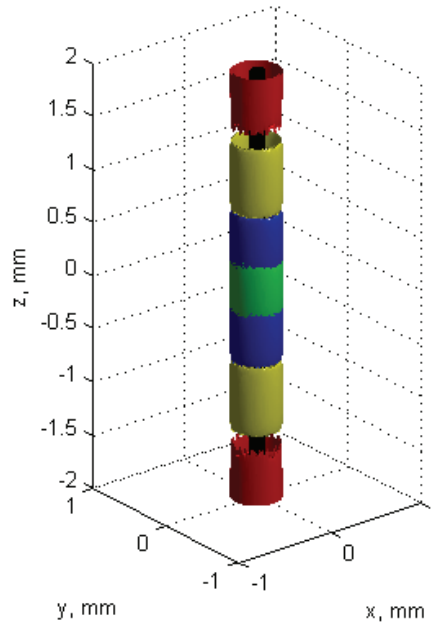


Fig. 2.9. The isosurface $U_{\text{eff}} = 10e-29$ J being moved up or down along a wire.

For the illustrated bias ring spacing of 6 mm, it is clear that the current in the bias ring that the circular minimum is moved away from must be increased in an almost exponential way to maintain a constant steepness in

the potential walls as the potential minimum is moved away from the centre between the bias rings and towards the other ring. If it is acceptable to allow the steepness of the trapping potential to decrease away from the centre between the bias rings this helps to reduce the need for very large currents in the bias rings.

If on the other hand it is desired to maintain a certain steepness of the potential walls of the circular minimum it may be necessary place bias rings at shorter intervals around the wire. If enough bias rings are present it becomes possible to use a pair of bias rings with one (or more) inactive bias ring(s) between them to pump the cloud of cold atoms along the wire. The inactive ring is used to gradually take over for the bias ring that the cold atoms are moved away from when the circular minimum has been moved past it. The RF current in the ring should be in-phase with the RF current in ring it takes over for. When the circular minimum then approaches the second active ring it is gradually turned off and superseded by the next ring along the wire. The RF current in the next ring should again be in-phase with the RF current in the ring it takes over for. This should eliminate the need for very large bias currents but requires that bias rings must be placed at relatively short intervals along the wire.

The described approach avoids a phase change (reversal) of the RF currents on either side of the circular potential minimum. Although the directions of the bias currents seem to be unimportant for atom pumping along a single wire, the phase difference should be 180° between the RF currents in the two active rings for transfer of cold atoms between two crossed wires. This will be explained in detail in Section 2.5. The use of two bias rings on one side of the circular minimum containing the cold atoms will create a second empty circular minimum between the two rings. This minimum will be merged with the potential minimum containing the cold atoms on the side toward which the cold atoms are being pumped. It is not clear whether this could negatively affect the cold atom condensate. One other thing is that the extra inactive bias rings may come physically very close to or in the way of crossing wires for example. All this needs to be considered in a practical realization. Careful simulations of atom pumping along the wires should therefore be made once a specific design has been decided on. This will show whether the chosen bias ring radius and spacing can be used.

2.4 The effective potential around two crossed wires

When two wires cross each other in two different planes close to each other the expression for the distance d , where the effective potential between the wires is zero, is changed. This is illustrated by the plot in Fig. 2.10 of the three dimensional surface $U_{\text{eff}} = 5\text{e-}29 \text{ J}$ for a geometry consisting of two crossed wires. The wires, each with a radius of $57.2 \mu\text{m}$, are represented by a wireframe mesh. The figure illustrates essentially the same as Fig. 3(b) published in [146], which shows a slightly different effective potential. There is in fact a double surface around both wires and the circular effective potential minimum around the wires lies in between these two surfaces. The figure shows that the potential surfaces are pulled towards each other at the crossing point of the wires.

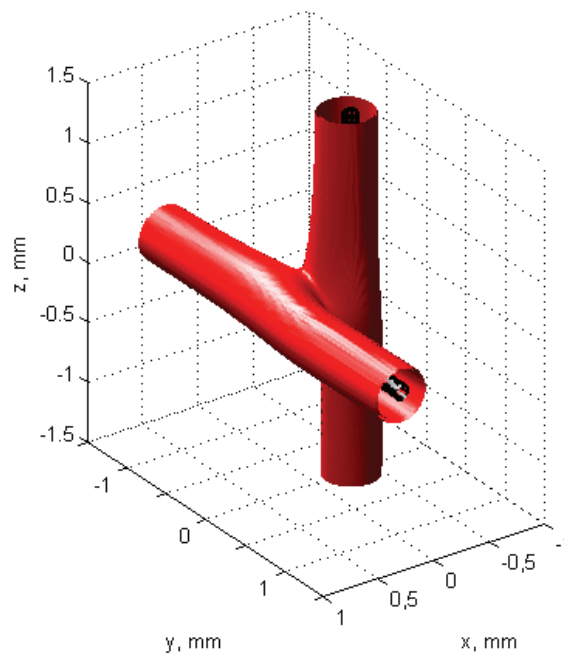


Fig. 2.10. Isosurface plot of the effective potential for $U_{\text{eff}} = 5\text{e-}29 \text{ J}$.

The distance d between the wires is also in this case constant for the same ratio of DC current to cyclic RF frequency. This can be easily checked by changing the DC current and cyclic RF frequency so that the ratio of the two is kept constant. It can be seen that the first term under the root sign in

equation (2.1) dominates strongly for $I_{RF} \ll I_{DC}$, except for input values close to resonance. The second term will therefore be neglected here initially. Its effect will be considered in Section 2.4.1. To find a new equation for the distance d one must start with the complete expression for $|\mathbf{B}_{DC}(\boldsymbol{\rho})|$, where the radius ρ is $\sqrt{x^2 + y^2}$ for a wire in the z -direction for example. It is here easiest to use the equations for the field components in Cartesian coordinates from [137] or [138]

$$\Delta_1^{(x)} = -\rho = \rho_z, \Delta_1^{(y)} = 0, r_1 = \sqrt{(x - \rho_z)^2 + y^2}, \quad (2.6)$$

$$\Delta_2^{(x)} = \rho = \rho_y, \Delta_2^{(z)} = 0, r_2 = \sqrt{(x - \rho_y)^2 + z^2}, \quad (2.7)$$

$$B_{x_{DC}}^{(1+2)}(x, y, z) = -\frac{\mu_0 I_{DC}^{(1)} \cdot y}{2\pi \left[(x - \rho_z)^2 + y^2 \right]} + \frac{\mu_0 I_{DC}^{(2)} \cdot z}{2\pi \left[(x - \rho_y)^2 + z^2 \right]}, \quad (2.8)$$

$$B_{y_{DC}}^{(1+2)}(x, y) = \frac{\mu_0 I_{DC}^{(1)} \cdot (x - \rho_z)}{2\pi \left[(x - \rho_z)^2 + y^2 \right]} + 0, \quad (2.9)$$

$$B_{z_{DC}}^{(1+2)}(x, z) = 0 - \frac{\mu_0 I_{DC}^{(2)} \cdot (x - \rho_y)}{2\pi \left[(x - \rho_y)^2 + z^2 \right]}. \quad (2.10)$$

The geometry of the two wires is shown in Fig. 2.11 in the xy -plane.

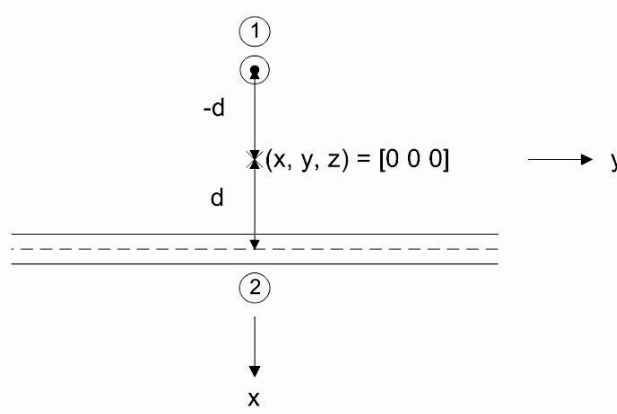


Fig. 2.11. Geometry of two crossed wires in the xy -plane. The wires are labelled 1 and 2. The origin is placed in the middle between the wires.

It is here sufficient to find the B-field as a function of the distance x between the two wires where they come closest to each other. Along this line $y = z = 0$ and $B_{x_{DC}}^{(1+2)}(x, y, z) = 0$ because the numerators become zero in both terms. The complete expression for $|\mathbf{B}_{DC}|$ is therefore as follows:

$$|\mathbf{B}_{DC}(x, \rho)| = \sqrt{\left(\frac{\mu_0 I_{DC}^{(1)} \cdot (x - \rho_z)}{2\pi[(x - \rho_z)^2]}\right)^2 + \left(\frac{-\mu_0 I_{DC}^{(2)} \cdot (x - \rho_y)}{2\pi[(x - \rho_y)^2]}\right)^2}, \quad (2.11)$$

$$|\mathbf{B}_{DC}(x, \rho)| = \sqrt{\frac{\mu_0^2 I_{DC1}^2 \cdot (x^2 - 2x\rho_z + \rho_z^2)}{4\pi^2(x^2 - 2x\rho_z + \rho_z^2)^2} + \frac{\mu_0^2 I_{DC2}^2 \cdot (x^2 - 2x\rho_y + \rho_y^2)}{4\pi^2(x^2 - 2x\rho_y + \rho_y^2)^2}}, \quad (2.12)$$

$$|\mathbf{B}_{DC}(x, \rho)| = \sqrt{\frac{\mu_0^2 I_{DC1}^2 \cdot (x^2 - 2x\rho_y + \rho_y^2) + \mu_0^2 I_{DC2}^2 \cdot (x^2 - 2x\rho_z + \rho_z^2)}{4\pi^2(x^2 - 2x\rho_z + \rho_z^2)(x^2 - 2x\rho_y + \rho_y^2)}}. \quad (2.13)$$

It is reasonable to define the DC currents to be of the same magnitude in both wires. Hence $I_{DC}^2 = I_{DC1}^2 = I_{DC2}^2$. Equation (2.13) can then be written

$$|\mathbf{B}_{DC}(x, \rho)| = \sqrt{\frac{2\mu_0^2 I_{DC}^2 x^2 + \mu_0^2 I_{DC}^2 (\rho_y^2 + \rho_z^2) - 2x\mu_0^2 I_{DC}^2 \cdot (\rho_y + \rho_z)}{4\pi^2(x^4 - 2x^3\rho_y + x^2\rho_y^2 - 2x^3\rho_z + 4x^2\rho_z\rho_y - 2x\rho_z\rho_y^2 + x^2\rho_z^2 - 2x\rho_z^2\rho_y + \rho_z^2\rho_y^2)}}. \quad (2.14)$$

When $\rho = \rho_y = -\rho_z$ is substituted into the equation above we get

$$|\mathbf{B}_{DC}(x, \rho)| = \sqrt{\frac{2\mu_0^2 I_{DC}^2 x^2 + \mu_0^2 I_{DC}^2 (\rho^2 + (-\rho)^2)}{4\pi^2(x^4 - 2x^3\rho + x^2\rho^2 + 2x^3\rho - 2x^2\rho^2 + 2x\rho^3 + x^2\rho^2 - 2x\rho^3 + \rho^4)}}, \quad (2.15)$$

$$|\mathbf{B}_{DC}(x, \rho)| = \sqrt{\frac{2\mu_0^2 I_{DC}^2 (x^2 + \rho^2)}{4\pi^2(x^4 - 2x^2\rho^2 + \rho^4)}} = \frac{\mu_0 I_{DC}}{2\pi} \sqrt{\frac{2(x^2 + \rho^2)}{(x^2 - \rho^2)^2}} = \left| \frac{\mu_0 I_{DC}}{2\pi(x^2 - \rho^2)} \sqrt{2(x^2 + \rho^2)} \right|. \quad (2.16)$$

The point where the effective potential is zero lies in the middle between the wires as shown in Fig. 2.10. By setting $x = 0$ an expression for $|\mathbf{B}_{DC}(\rho)|$ is found

$$|\mathbf{B}_{\text{DC}}(\rho)| = \frac{\mu_0 I_{\text{DC}}}{2\pi\rho^2} \sqrt{2\rho^2} = \frac{\mu_0 I_{\text{DC}}}{2\pi\rho} \sqrt{2} = \frac{\mu_0 I_{\text{DC}} \sqrt{2}}{2\pi\rho}. \quad (2.17)$$

This expression is seen to be the same as equation (2.3) for the single wire except for the factor $\sqrt{2}$.

If the second term in (2.1) is neglected the expression for the radius d where the effective potential is zero between two crossing wires becomes

$$d = \frac{\mu_B g_F \mu_0 \sqrt{2}}{2\pi\hbar} \left(\frac{I_{\text{DC}}}{\omega_{\text{RF}}} \right). \quad (2.18)$$

The dependence of d on $I_{\text{DC}}/\omega_{\text{RF}}$ computed according to (2.18) is shown in Fig. 2.22.

The magnetic field $|\mathbf{B}_{\text{DC}}(x, \rho)|$ in (2.16) is plotted in Fig. 2.23 in Section 2.6 for $\rho = d = 0.302$ mm, $I_{\text{DC}} = 92.5$ mA and $\omega_{\text{RF}} = 2\pi \cdot 8\text{e}5$ rad/s. Fig. 2.23 also shows the magnetic field $|\mathbf{B}_{\text{DC}}(y, \rho)|$ between two parallel wires, the expression for which will be derived in Section 2.6. The distance between the crossed or parallel wires is $2d$, where d is different for the crossed and parallel wires. At the centre between the wires the magnetic field has the value $8.66\text{e-}5$ T, which is equal to $\hbar\omega_{\text{RF}}/\mu_B g_F$. This assures that the effective potential is zero at the centre when only the first term under the root sign in equation (2.1) is taken into account. In sections 2.4.1 and 2.6.1 it will be explained why this is a reasonable simplification.

The expression in equation (2.16) is for infinitesimally thin wires. For wires with a finite radius the magnetic field outside of the wires is still given by (2.16). Inside of the wires the magnetic field is different however, and the graphs in Fig. 2.23 are therefore physically incorrect in the regions around the peaks, which lie inside the physical wires.

The graphs for the effective potential are of the same form as those for $|\mathbf{B}_{\text{DC}}|$, but with a different number range on the vertical axis and a value of zero at the centre between the wires. A plot of the effective potential in the yz -plane located at the centre between the crossed wires for $x = 0$ is shown in Fig. 2.12. The effective potential at the centre is zero as expected.

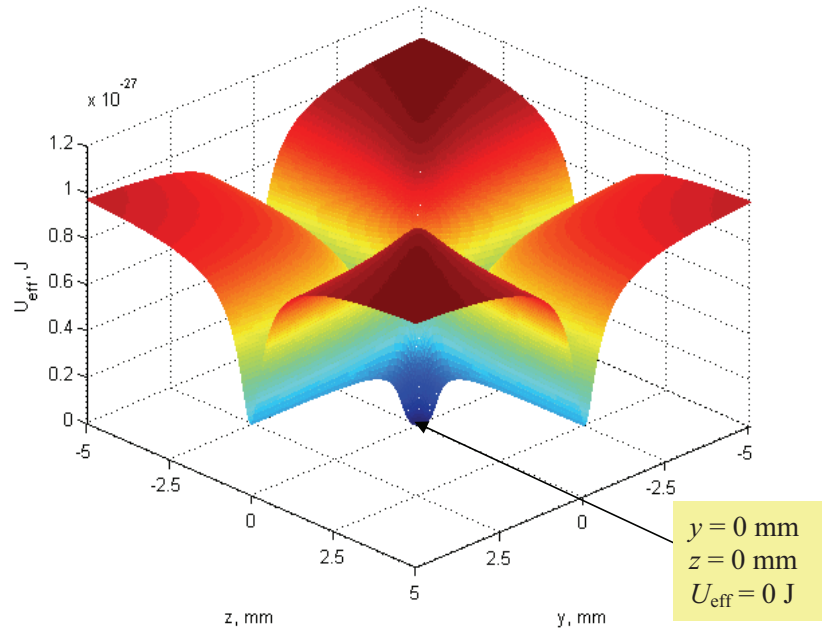


Fig. 2.12. The effective potential in the yz -plane for $x = 0$ for two crossed wires placed at the distance $2d = 0.604$ mm. The wires are without external bias.

The mesh plot in Fig. 2.12 gives only a 2D description of the effective potential. To make up for this a 3D slice plot is provided in Fig. 2.13. The highest potential levels are found just outside of the wire surfaces. The minimum of zero in the potential between the wires is also here evident. The depth of the trapping potential in this case is about $75.5 \mu\text{K}$. This is just a trifle less than for the single wire.

An isosurface plot of the area where the wires cross is shown in Fig. 2.14 for two effective potential levels. This plot clearly shows that the local potential minima inside the wires are completely isolated. The blue surface for $U_{\text{eff}} = 1\text{e-}29$ J can be seen to be a bit patchy in some places. This is because quite high data point resolution is necessary to display smooth isosurfaces around very small or narrow areas.

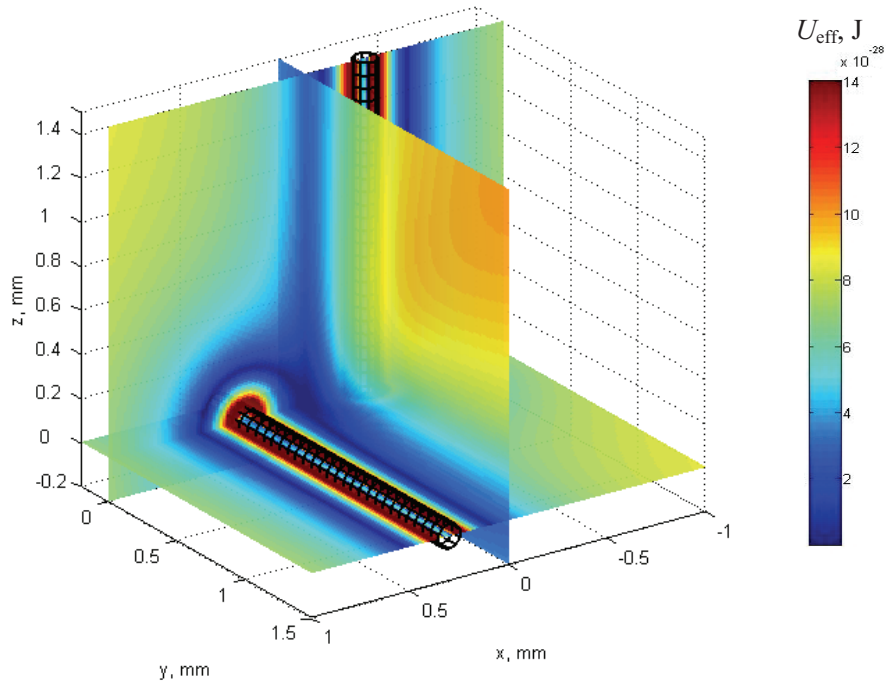


Fig. 2.13. Slice-plot of U_{eff} in the planes $x=0$, $y=0$ and $z=0$.

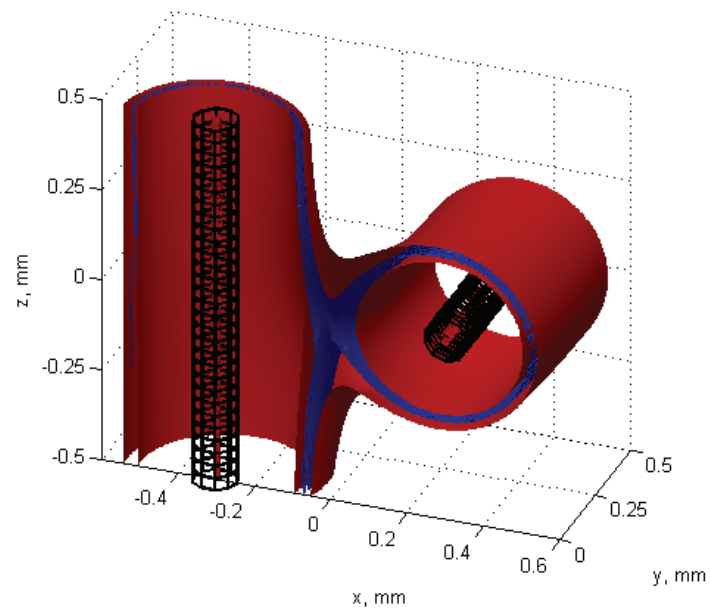


Fig. 2.14. Isosurface plot of $U_{\text{eff}} = 8.552 \times 10^{-29}$ J and $U_{\text{eff}} = 1 \times 10^{-29}$ J.

The touching of two minimum potential manifolds around two crossed wires has later become known as the quasi-synaptic effect [147], [148]. By using bias rings placed around the two wires to pump clouds of cold atoms along the wires controlled atom transfer from one wire to the other can be achieved. This effect is reminiscent of the synaptic effect which describes the transmission of signals between nerve cells in the brain and nervous system. The prospective transfer of atoms between two crossed wires is explained in detail in Section 2.5.

2.4.1 The effect of the RF current on U_{eff} for two crossed wires

Simulations have indicated that the amplitude of the RF current has little or no effect on the effective potential topology around the wires when certain conditions are met. One condition is that the RF current amplitude must be the same in both wires. A second condition is that the RF currents must either both be of the same sign as the DC current in each wire, or both be of opposite sign relative to the DC current in each wire. Different RF current amplitudes in the two wires, or RF current of the same sign as the DC current in one wire and RF current of opposite sign to the DC current in the other wire, will in other words cause distortion of the effective potential. A third condition is of course that the amplitude of the RF current can not approach zero without the frequency also being set to zero in equation (2.1). This amounts to removing the RF current altogether. The equation will otherwise become invalid in this case.

This experimental outcome verifies qualitatively that the equations allow the RF currents to flow in opposite directions in each half cycle without changing the topology of the effective potential. This behaviour is indeed necessary for combined DC and RF excitation of the wire structures to work. The practical consequence of this is that the RF currents in the different wires must have the same amplitude and be phase synchronized either in-phase or in counter-phase depending on the direction of the DC current in each wire. For two crossed wires the directions of the DC currents in the wires can be chosen freely. The only difference is that the elliptic curvature around the touching point at the centre, seen in Fig. 2.10, may slant in the orthogonal direction. The frequency of the RF current is essential to forming the minimum potential manifolds around the wires. The RF current amplitude I_{RF} must be chosen to be much smaller than the DC current amplitude, but not too small either. Otherwise the rotating wave approximation, on which equation (2.1) depends, is no longer applicable.

Computations based on the magnetic field equations have with this shown that there is a dependency between the phases of the RF currents and the directions of the DC currents when two crossed wires are viewed together as a system. This is complicated to prove mathematically because many different combinations of current signs would have to be considered separately. Instead, limited results will be derived for the case when the RF currents are of equal magnitude and have the same sign as the DC current in each wire. The DC currents are also taken to be of equal magnitude and it is assumed that the quasi-static approximation is valid. It will first be shown that $B_{\text{RF}}^{(\perp)}(\boldsymbol{\rho})$ is zero in the centre point between two crossed wires, resulting in equation (2.27). This means that the second term in equation (2.1) is zero for this point, regardless of the amplitude of the RF current for the conditions applied. This result is afterwards expanded to also apply along a line between the centres of the crossed wires, resulting in equation (2.33). The effective potential along that same line is given by equation (2.34).

The mentioned equations for $B_{\text{RF}}^{(\perp)}(\boldsymbol{\rho})$ will now be derived. Because this derivation is mathematically detailed and falls outside of the interest of most readers, it is recommended that readers who are not very interested in it should at this point just take a quick look at the result in equations (2.27), (2.33) and (2.34), and then move on to the next section.

The RF current I_{RF} is found in the second term under the root sign in equation (2.1). This term is $B_{\text{RF}}^{(\perp)}(\boldsymbol{\rho})$ multiplied by a constant. The equation for $B_{\text{RF}}^{(\perp)}(\boldsymbol{\rho})$, given by equation (2) in [138], has already been presented in Section 2.2. The RF field components can be calculated using the same formulas as the ones used for the DC field. A quasi-static approximation for the RF field is assumed. This means that equations (2.6)-(2.17) will also apply to the RF field components. We are now ready to evaluate the equation for $B_{\text{RF}}^{(\perp)}(\boldsymbol{\rho})$, which is repeated again for convenience.

$$B_{\text{RF}}^{(\perp)}(\boldsymbol{\rho}) = \sqrt{(\mathbf{B}_{\text{RF}}(\boldsymbol{\rho}))^2 - \left(\frac{\mathbf{B}_{\text{RF}}(\boldsymbol{\rho})\mathbf{B}_{\text{DC}}(\boldsymbol{\rho})}{|\mathbf{B}_{\text{DC}}(\boldsymbol{\rho})|} \right)^2} \quad (2.19)$$

$|\mathbf{B}_{\text{DC}}(\boldsymbol{\rho})|$ is given by equation (2.17). The same equation can be used for the RF field

$$|\mathbf{B}_{\text{RF}}(\boldsymbol{\rho})| = \frac{\mu_0 I_{\text{RF}} \sqrt{2}}{2\pi\rho}. \quad (2.20)$$

From (2.9) and (2.10) it follows that

$$\mathbf{B}_{\text{RF}}(x, \rho) \mathbf{B}_{\text{DC}}(x, \rho) = \frac{\mu_0 I_{\text{RF}}^{(1)} \cdot (x - \rho_z)}{2\pi [(x - \rho_z)^2]} \cdot \frac{\mu_0 I_{\text{DC}}^{(1)} \cdot (x - \rho_z)}{2\pi [(x - \rho_z)^2]} + \frac{-\mu_0 I_{\text{RF}}^{(2)} \cdot (x - \rho_y)}{2\pi [(x - \rho_y)^2]} \cdot \frac{-\mu_0 I_{\text{DC}}^{(2)} \cdot (x - \rho_y)}{2\pi [(x - \rho_y)^2]}, \quad (2.21)$$

$$\mathbf{B}_{\text{RF}}(x, \rho) \mathbf{B}_{\text{DC}}(x, \rho) = \frac{\mu_0^2 I_{\text{RF}}^{(1)} I_{\text{DC}}^{(1)} \cdot (x^2 - 2\rho_z x + \rho_z^2)}{4\pi^2 [(x - \rho_z)^4]} + \frac{\mu_0^2 I_{\text{RF}}^{(2)} I_{\text{DC}}^{(2)} \cdot (x^2 - 2\rho_y x + \rho_y^2)}{4\pi^2 [(x - \rho_y)^4]}, \quad (2.22)$$

$$\mathbf{B}_{\text{RF}}(x, \rho) \mathbf{B}_{\text{DC}}(x, \rho) = \frac{\mu_0^2 I_{\text{RF}}^{(1)} I_{\text{DC}}^{(1)} \cdot (x^2 - 2\rho_z x + \rho_z^2)}{4\pi^2 [(x^2 - 2\rho_z x + \rho_z^2)(x - \rho_z)^2]} + \frac{\mu_0^2 I_{\text{RF}}^{(2)} I_{\text{DC}}^{(2)} \cdot (x^2 - 2\rho_y x + \rho_y^2)}{4\pi^2 [(x^2 - 2\rho_y x + \rho_y^2)(x - \rho_y)^2]}, \quad (2.23)$$

$$\mathbf{B}_{\text{RF}}(x, \rho) \mathbf{B}_{\text{DC}}(x, \rho) = \frac{\mu_0^2 I_{\text{RF}}^{(1)} I_{\text{DC}}^{(1)}}{4\pi^2 (x - \rho_z)^2} + \frac{\mu_0^2 I_{\text{RF}}^{(2)} I_{\text{DC}}^{(2)}}{4\pi^2 (x - \rho_y)^2}. \quad (2.24)$$

For $x = 0$ this simplifies to

$$\mathbf{B}_{\text{RF}}(\rho) \mathbf{B}_{\text{DC}}(\rho) = \frac{\mu_0^2 I_{\text{RF}} I_{\text{DC}}}{2\pi^2 (\rho)^2}, \quad (2.25)$$

where it is assumed that the DC and RF currents go in the same direction in each wire, i.e. that $I_{\text{RF}} \cdot I_{\text{DC}}$ is positive, and that $|I_{\text{DC}}^{(1)}| = |I_{\text{DC}}^{(2)}|$ and $|I_{\text{RF}}^{(1)}| = |I_{\text{RF}}^{(2)}|$.

$B_{\text{RF}}^{(\perp)}(\rho)$ can now be calculated for $x = 0$ as

$$B_{\text{RF}}^{(\perp)}(\rho) = \sqrt{\left(\frac{\mu_0 I_{\text{RF}} \sqrt{2}}{2\pi \rho}\right)^2 - \left(\frac{\mu_0^2 I_{\text{RF}} I_{\text{DC}} \cdot \cancel{z} \cancel{\pi} \cancel{\rho}}{\cancel{z} \pi^2 (\rho)^2 \cdot \mu_0 I_{\text{DC}} \sqrt{2}}\right)^2} = \sqrt{\left(\frac{\mu_0 I_{\text{RF}} \sqrt{2}}{2\pi \rho}\right)^2 - \left(\frac{\mu_0 I_{\text{RF}}}{\pi \rho \sqrt{2}}\right)^2}, \quad (2.26)$$

$$B_{\text{RF}}^{(\perp)}(\rho) = \sqrt{\left(\frac{2\mu_0^2 I_{\text{RF}}^2}{4\pi^2 \rho^2} - \frac{\mu_0^2 I_{\text{RF}}^2}{2\pi^2 \rho^2}\right)} = \sqrt{\left(\frac{\mu_0^2 I_{\text{RF}}^2}{2\pi^2 \rho^2} - \frac{\mu_0^2 I_{\text{RF}}^2}{2\pi^2 \rho^2}\right)} = 0. \quad (2.27)$$

The second term under the root sign in (2.1) is therefore zero at the midpoint between the wires for $x = y = z = 0$, and does not change the distance d found in (2.18).

An analytical expression for the potential function as a function of the distance between the crossed wires at the point where they come closest to each other is now derived. We make use of (2.16) for $\mathbf{B}_{\text{DC}}(x, \rho)$. The same equation is used for $\mathbf{B}_{\text{RF}}(x, \rho)$ with I_{RF} substituted for I_{DC} . Equation (2.24) is used for $\mathbf{B}_{\text{RF}}(x, \rho)\mathbf{B}_{\text{DC}}(x, \rho)$.

When $\rho = \rho_y = -\rho_z$ is substituted into (2.24) we get:

$$\mathbf{B}_{\text{RF}}(x, \rho)\mathbf{B}_{\text{DC}}(x, \rho) = \frac{\mu_0^2 I_{\text{RF}}^{(1)} I_{\text{DC}}^{(1)}}{4\pi^2 (x+\rho)^2} + \frac{\mu_0^2 I_{\text{RF}}^{(2)} I_{\text{DC}}^{(2)}}{4\pi^2 (x-\rho)^2} = \frac{\mu_0^2 I_{\text{RF}}^{(1)} I_{\text{DC}}^{(1)} (x-\rho)^2 + \mu_0^2 I_{\text{RF}}^{(2)} I_{\text{DC}}^{(2)} (x+\rho)^2}{4\pi^2 (x+\rho)^2 (x-\rho)^2}, \quad (2.28)$$

$$\mathbf{B}_{\text{RF}}(x, \rho)\mathbf{B}_{\text{DC}}(x, \rho) = \frac{\mu_0^2 I_{\text{RF}} I_{\text{DC}} \left((x-\rho)^2 + (x+\rho)^2 \right)}{4\pi^2 (x+\rho)^2 (x-\rho)^2} = \frac{2\mu_0^2 I_{\text{RF}} I_{\text{DC}} (x^2 + \rho^2)}{4\pi^2 (x^4 - 2x^2 \rho^2 + \rho^4)}, \quad (2.29)$$

$$B_{\text{RF}}^{(\perp)}(x, \rho) = \sqrt{\left(\frac{\mu_0 I_{\text{RF}}}{2\pi} \frac{\sqrt{2(x^2 + \rho^2)}}{\sqrt{(x^2 - \rho^2)^2}} \right)^2 - \left(\frac{2\mu_0^2 I_{\text{RF}} I_{\text{DC}} (x^2 + \rho^2) \cdot 2\pi \sqrt{(x^2 - \rho^2)^2}}{4\pi^2 (x^4 - 2x^2 \rho^2 + \rho^4) \cdot \mu_0 I_{\text{DC}} \sqrt{2(x^2 + \rho^2)}} \right)^2}, \quad (2.30)$$

$$B_{\text{RF}}^{(\perp)}(x, \rho) = \sqrt{\frac{2\mu_0^2 I_{\text{RF}}^2 (x^2 + \rho^2)}{4\pi^2 (x^2 - \rho^2)^2} - \left(\frac{\mu_0 I_{\text{RF}} (x^2 + \rho^2) \cdot \sqrt{(x^2 - \rho^2)^2}}{\pi (x^4 - 2x^2 \rho^2 + \rho^4) \cdot \sqrt{2(x^2 + \rho^2)}} \right)^2}, \quad (2.31)$$

$$B_{\text{RF}}^{(\perp)}(x, \rho) = \sqrt{\frac{\mu_0^2 I_{\text{RF}}^2 (x^2 + \rho^2)}{2\pi^2 (x^4 - 2x^2 \rho^2 + \rho^4)} - \frac{\mu_0^2 I_{\text{RF}}^2 (x^2 + \rho^2)^{\cancel{2}} (x^4 - 2x^2 \rho^2 + \rho^4)}{2\pi^2 (x^4 - 2x^2 \rho^2 + \rho^4)^{\cancel{2}} (x^2 + \rho^2)}}, \quad (2.32)$$

$$B_{\text{RF}}^{(\perp)}(x, \rho) = \sqrt{\frac{\mu_0^2 I_{\text{RF}}^2 (x^2 + \rho^2)}{2\pi^2 (x^2 - \rho^2)^2} - \frac{\mu_0^2 I_{\text{RF}}^2 (x^2 + \rho^2)}{2\pi^2 (x^2 - \rho^2)^2}} = 0, \quad (2.33)$$

and

$$U_{\text{eff}}(x, \rho) = m_F \sqrt{\left[\frac{\mu_B g_F \mu_0 I_{\text{DC}}}{2\pi} \frac{\sqrt{2(x^2 + \rho^2)}}{\sqrt{(x^2 - \rho^2)^2}} - \hbar \omega_{\text{RF}} \right]^2}. \quad (2.34)$$

The second term under the root sign in (2.1) for the effective potential is hence zero along a line between the centre points on two crossed wires. It has been assumed that the DC and RF currents go in the same direction in each wire, i.e. $I_{\text{RF}} \cdot I_{\text{DC}}$ is positive, and that $|I_{\text{DC}}^{(1)}| = |I_{\text{DC}}^{(2)}|$ and $|I_{\text{RF}}^{(1)}| = |I_{\text{RF}}^{(2)}|$. If the currents in the two wires are of different magnitude equation (2.29) is no longer valid and it becomes more difficult to determine what the RF magnetic field normal to the local DC magnetic vector $B_{\text{RF}}^{(1)}(x, \rho)$ is.

It has nonetheless been shown that the equation for the distance d , where the minimum potential manifolds around the two wires touch, can be derived using only the first term under the root sign in (2.1) when certain conditions are placed on the currents in the crossing wires.

2.5 Prospective atom transfer between two crossed wires with bias rings

Two crossing wires placed at a distance of $2d$, where d is given by (2.18), lead to an effective potential minimum of zero as already explained. This was illustrated in Fig. 2.12 where the parameters were as follows: $d = 0.302$ mm, $I_{\text{DC} | z\text{-wire}} = I_{\text{DC} | y\text{-wire}} = -92.5$ mA, $I_{\text{RF} | z\text{-wire}} = I_{\text{RF} | y\text{-wire}} = -10$ mA and $f_{\text{RF}} = 800$ kHz. The radius of the wires in Fig. 2.12 was 57.2 μm , which corresponds to a maximum current density in the wires of about 1000 A/cm².

As a practical matter the number of decimals used in the calculations must be controlled in Matlab to be able to see the minimum of zero, for example using the plot marker. This can be done by using all available decimals in the distance d and by blanking out all additional decimals to the number of decimals in d plus one in the following four terms in $U_{\text{eff}}(\rho)$:

$$\left[\mu_B g_F |\mathbf{B}_{\text{DC}}(\rho)| \right], \left[\hbar \omega_{\text{RF}} \right], \left[(\mathbf{B}_{\text{RF}}(\rho))^2 \right] \text{ and } \left[\left(\frac{\mathbf{B}_{\text{RF}}(\rho) \mathbf{B}_{\text{DC}}(\rho)}{|\mathbf{B}_{\text{DC}}(\rho)|} \right)^2 \right].$$

The potential minimum of zero can be avoided by placing bias rings around the wires, as previously illustrated in Fig. 2.2(b). Simulations have shown that care must be taken when the signs of the currents in the rings are defined. For example the four current sign combinations in Table 2.1 do not remove the absolute zero in the effective potential for a given current I .

Table 2.1. Four current sign combinations that do not remove the minimum of zero for a given current I .

Combination 1 – 2	Combination 3 – 4
$I_{RF z\text{-wire rings}}^{(I, II)} = \pm I, \pm I$	$I_{RF z\text{-wire rings}}^{(I, II)} = \mp I, \pm I$
$I_{RF y\text{-wire rings}}^{(I, II)} = \pm I, \pm I$	$I_{RF y\text{-wire rings}}^{(I, II)} = \mp I, \pm I$

This is illustrated in Fig. 2.15 for $I_{RF|z\text{-wire rings}} = [-0.1 \ 0.1]$ A and $I_{RF|y\text{-wire rings}} = [-0.1 \ 0.1]$ A. The simulated infinitesimally thin rings have a radius of 1 mm and are placed 6 mm apart on each wire. The ring with a negative coordinate along the axis through the centre of the ring is indexed first. The wire currents and wire radii are the same as in Fig. 2.12. The four current combinations have that in common that the two element sign vectors for the currents in the rings around the z -wire and y -wire are identical.

Note that if one of the ring currents is changed slightly the absolute potential minimum of zero disappears. The ring current sign combinations can therefore be used so long as care is taken to avoid that the currents in all the four rings have the same amplitude at any one time.

The four remaining current sign combinations in Table 2.2 eliminate the absolute minimum of zero. The first two current combinations give the highest increase in the effective potential U_{eff} above zero, but the minimum potential channel between the crossed wires is also ruined at the same time.

Table 2.2. Four current sign combinations that remove the minimum of zero for a given current I .

Combination 1 – 2	Combination 3 – 4
$I_{RF z\text{-wire rings}}^{(I, II)} = \pm I, \pm I$	$I_{RF z\text{-wire rings}}^{(I, II)} = \mp I, \pm I$
$I_{RF y\text{-wire rings}}^{(I, II)} = \mp I, \mp I$	$I_{RF y\text{-wire rings}}^{(I, II)} = \pm I, \mp I$

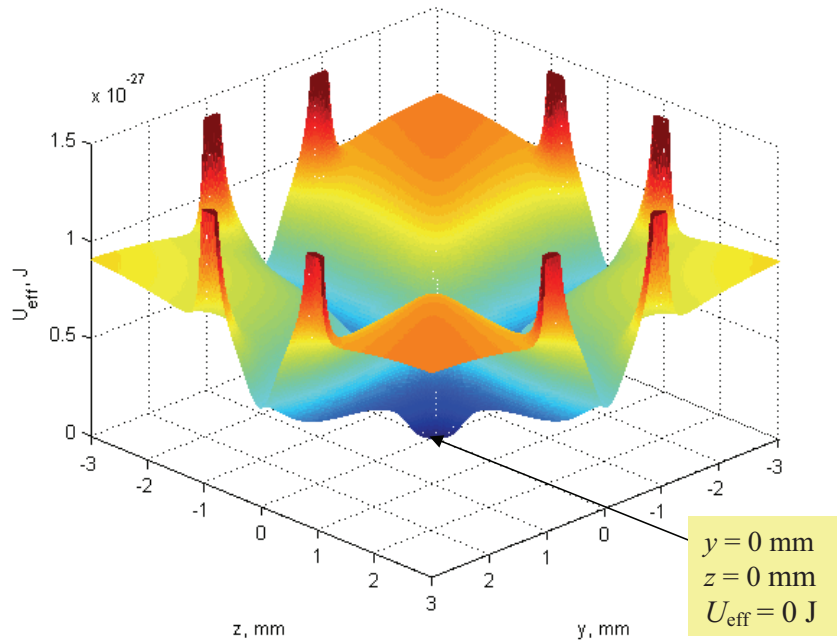


Fig. 2.15. The effective potential for two crossed wires when a combination of ring currents from Table 2.1 is used. The figure is in the plane $x = 0$.

The bias rings around the wires can also be used to transfer a cloud of cold atoms between the crossed wires. This is done by first creating a slope in the effective potential around the donor wire of cold atoms that extends down to a common minimum at the centre between the crossed wires. It appears that this downward slope can not be formed when bias current sign combinations from Table 2.2 are used. As already mentioned the first two combinations effectively ruin the minimum potential channel between the crossed wires by producing deeper minima along the wires on the sides facing away from the centre point between the wires. The possible current sign combinations, not detailed in the tables, where the currents in three of the bias rings are of the same sign and the current in the fourth ring is of the opposite sign are also not usable for transferring cold atoms between the crossed wires. Such asymmetric biasing would in any case pose a problem should the cold atoms be attempted transferred in the reverse direction.

The current sign combinations in Table 2.1 can all be used to create a downward slope around the donor wire of cold atoms. The first two combinations can produce a steep slope down to a common minimum at the centre point between the wires. However, the resulting minimum is strongly attached to the minimum potential manifolds around the wires.

This means that cold atoms can not be pumped along either of the wires unless the DC current is turned off completely in the other wire. As a result the transfer of atoms is more complicated compared to the use of the other two current sign combinations in Table 2.1, the use of which will be treated in a moment. A video animation of the expected cold atom transfer is provided in Fig. 2.16. For readers with access to an electronic version of the thesis this animation and other animations in this thesis can be seen by double clicking on the figure. The animation can also be shown by playing the avi-file with the name shown in the field at the bottom of the figure using an appropriate media player.

The animation in Fig. 2.16 has 15 frames. The wires, each with a radius of $57.2 \mu\text{m}$, are placed at a distance of $2d$ where $d = 3.02\text{e-}4 \text{ mm}$. The DC current in the wires is 92.5 mA when fully on, and the RF current is 10 mA at 0.8 MHz . The currents have been defined with a negative sign in both wires. The bias currents in the rings around the two wires in each of the 15 frames are:

$$I_{\text{RF}|z\text{-wire rings}}^{\text{I+II}} = \left\{ \begin{array}{l} [2.5 \ 0.5], [2 \ 1], [1.5 \ 1.45], [1.5 \ 1.5], [1.5 \ 1.5], \\ [1.5 \ 1.5], [1.5 \ 1.5], [1.5 \ 1.5], [2 \ 2], [2.5 \ 2.5], \\ [2.5 \ 2.5], [2 \ 2], [1.5 \ 1.5], [1 \ 1], [0.5 \ 0.5] \end{array} \right\} \text{A},$$

$$I_{\text{RF}|y\text{-wire rings}}^{\text{I+II}} = \left\{ \begin{array}{l} [0.5 \ 0.5], [1 \ 1], [1.5 \ 1.5], [2 \ 2], [2.5 \ 2.5], \\ [2 \ 2], [1.45 \ 1.5], [0.5 \ 0.5], [1.5 \ 1.5], [1.5 \ 1.5], \\ [1.5 \ 1.5], [1.5 \ 1.5], [1.5 \ 1.45], [2 \ 1], [2.5 \ 0.5] \end{array} \right\} \text{A}.$$

In the first three frames the cold atoms are being pumped down the z -wire to the centre of the wire. For this to be possible the DC current in the y -wire must be turned off. In frames 4 to 7 the DC current in the y -wire is gradually turned on in steps of 50%, 75%, 90% and 95% of its final value. Notice that the y -wire is relatively strongly biased while the DC current is being turned on. In frame 8 the DC current in the y -wire is fully on at 92.5 mA , and the y -wire bias has been reduced to 0.5 A to empty a small pocket on the back side of the z -wire. The reduced y -wire bias causes the potential minimum next to the y -wire to divide into two and slide out a bit along the y -wire. This is shown in Fig. 2.17(a). It may not be necessary to reduce the y -wire bias quite so much.

The atom transfer takes place mostly in frame 8 and in frame 9, which is shown in Fig. 2.17(b). In frame 9 the y -wire bias has been increased and a single sharp minimum is again found next to the y -wire. The small pocket

on the back side of the z -wire has reappeared, but is now empty. In frame 9 the DC current in the z -wire has been reduced to 95% of its original value. This has little effect, but may pull the pointed potential minimum a bit closer to the y -wire. In frames 10 to 12 the DC current in the z -wire is reduced in steps of 90%, 75% and 50% of its original value. In frames 13 to 15 the DC current in the z -wire is off and the cold atoms are pumped along the y -wire. The RF currents in the wires may also be turned off when the DC currents are turned off, but this is not strictly necessary if the RF current amplitude is small.

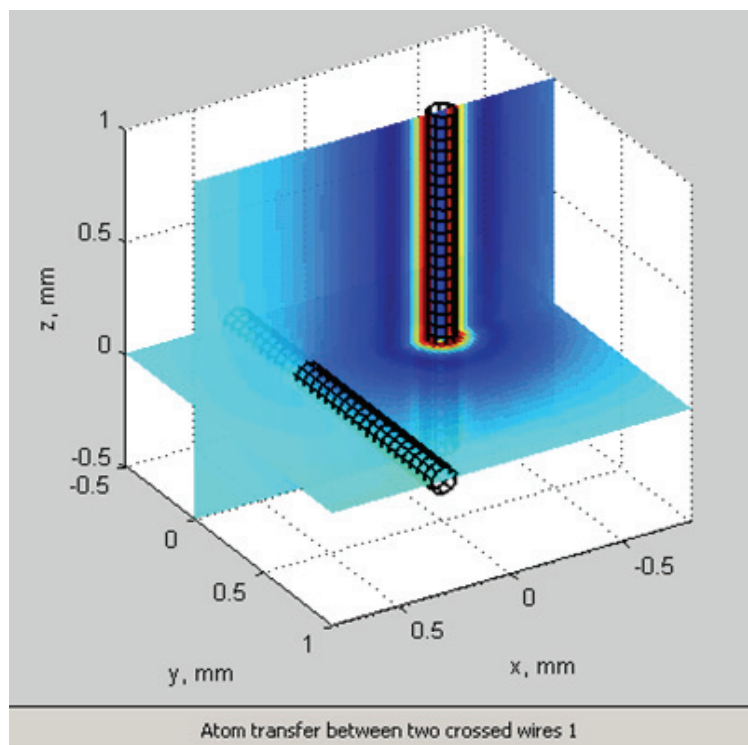


Fig. 2.16. Animation of atom transfer using bias currents of positive sign only.

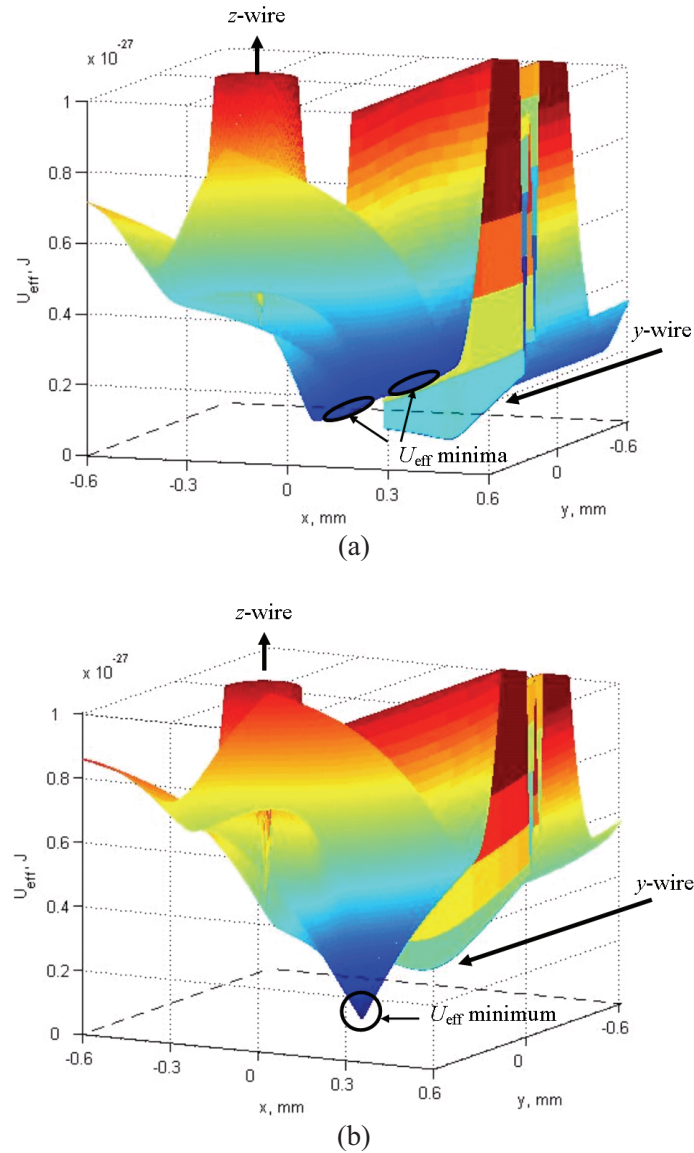


Fig. 2.17. Atom pumping with only positive bias. Frame 8 (a), and frame 9 (b).

The cold atom transfer example just described is included here only to give a complete account of the different possibilities and should be avoided if possible. The preferred way of transferring cold atoms between two crossed wires is with the use of the last two current sign combinations in Table 2.1.

These current sign combinations are, like the other combination pairs, the reverse of each other and yield the same result.

A video animation of the anticipated cold atom transfer is provided in Fig. 2.18. The video has 14 frames. The wire currents are -92.5 mA DC and -10 mA RF in both the wire in the z -direction and the wire in the y -direction. The frequency is also here 0.8 MHz. The bias currents in the rings in the 14 frames in the animation are:

$$I_{\text{RF}|z\text{-wire rings}}^{\text{I+II}} = \left\{ \begin{array}{l} [-2.5 \ 0], [-2.5 \ 0.5], [-2 \ 1], [-2 \ 1.5], [-2 \ 2], \\ [-1.5 \ 1.5], [-1.5 \ 1.5], [-0.7 \ 0.7], [-0.5 \ 0.5], \\ [0 \ 0], [0 \ 0], [0 \ 0], [0 \ 0], [0 \ 0] \end{array} \right\} \text{A},$$

$$I_{\text{RF}|y\text{-wire rings}}^{\text{I+II}} = \left\{ \begin{array}{l} [-0.05 \ 0.05], [-0.05 \ 0.05], [-0.05 \ 0.05], [-0.05 \ 0.05], \\ [-0.5 \ 0.5], [-0.75 \ 0.75], [-1.5 \ 1.55], [-2.1 \ 2.1], [-1.1 \ 1.1], \\ [-1.5 \ 1.5], [-1.5 \ 1.5], [-2 \ 1], [-2.5 \ 0.5], [-2.5 \ 0] \end{array} \right\} \text{A}.$$

In the first five frames the cold atoms are being pumped down the z -wire to the centre of the wire. In frames 6 and 7 a downward slope is created in the effective potential around the z -wire down to a common minimum at the centre between the crossed wires. This transfers the cold atoms from around the vertical wire to the common minimum between the wires. Plots of the effective potential in the xy -plane ($z = 0$) for frame 6 and frame 7 have been published as Fig. 7(a) and Fig. 7(b) in [146]. In the article it is described how two effective potential minima are first formed close to the centre between the wires in frame 6.

In frame 7 a common minimum is formed at the centre between the wires. At the same time a pair of low potential pockets is formed on the sides around the z -wire. This is not a problem since the cold atoms were first moved to the two potential minima in frame 6, which in frame 7 have merged to become the common minimum. Frame 7 from the animation in Fig. 2.18 is shown in Fig. 2.19(a).

The effective potential for frame 7 in the xz -plane for $y = 0$ is shown in Fig. 2.19(b). It is practically identical in shape to the effective potential in the xy -plane in Fig. 7(b) in [146]. This is not strange since the bias currents are about ± 1.5 A in all bias rings. The current in one of the bias rings has in fact been increased to 1.55 A to avoid an absolute zero in the potential at the common minimum.

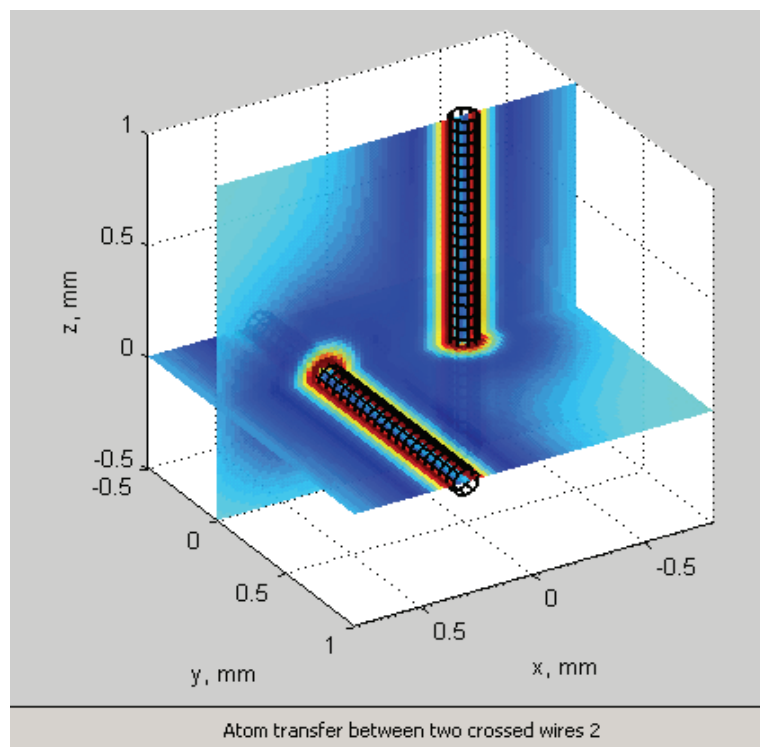


Fig. 2.18. Animation of cold atom transfer using bias currents of different signs.

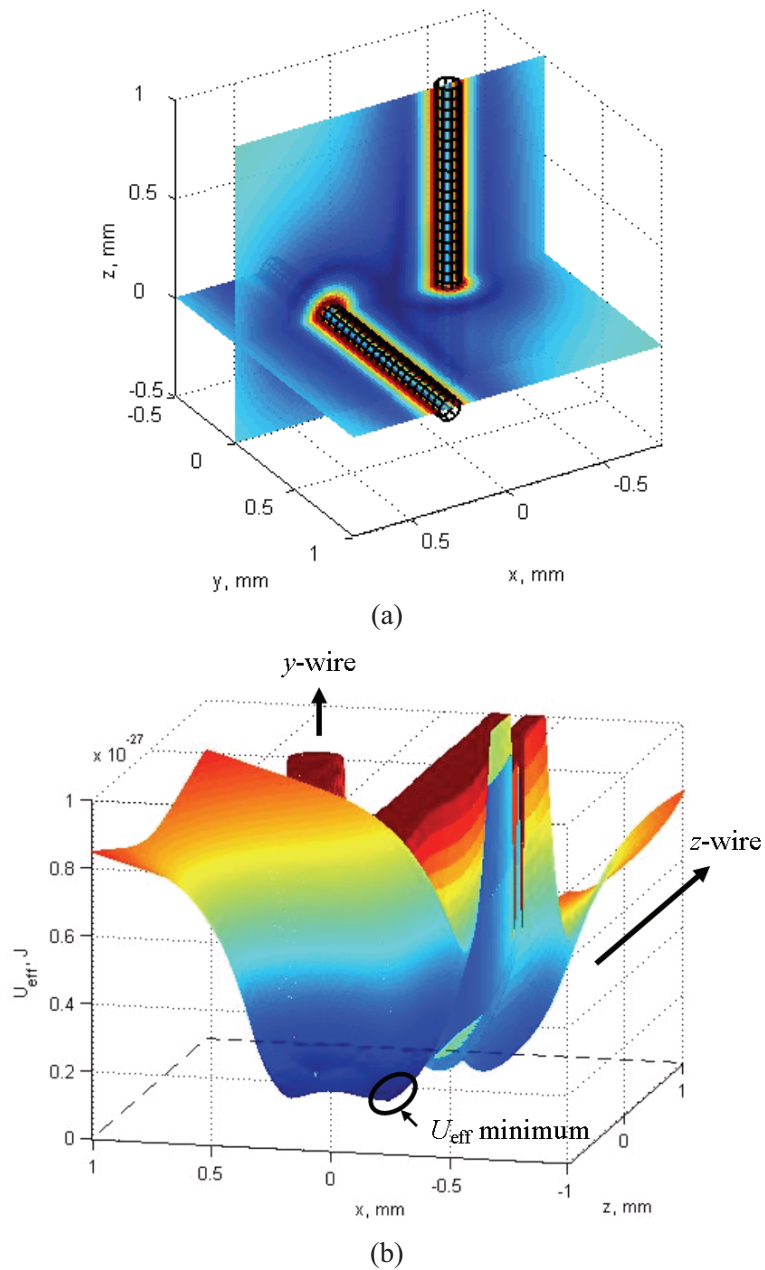


Fig. 2.19. Frame 7 in the animation (a), and U_{eff} in the xz -plane for frame 7 (b).

There are at this point two ways of completing the atom transfer. One possibility is to reduce the DC current in the donor wire, here the z -wire,

while keeping the cloud of cold atoms in the potential minimum around the acceptor wire, or y -wire in this case. The donor wire is then free to be used to transport a second cloud of cold atoms to a crossing wire somewhere else. The DC current should in that case also be reduced in the acceptor wire to increase the barrier between the cold atom streams. Alternatively the cold atoms can be pumped away along the acceptor wire right away without changing the DC current in the donor wire. This is more straightforward and, if tunnelling turns out to be a major problem, it may in fact be the only feasible way of completing the atom transfer.

In the animation in Fig. 2.18 the DC current is reduced in the donor wire in frames 8 to 11 in steps of 95 %, 90 %, 75 % and 50 % of its original value. In frame 8, which is shown in Fig. 2.20(a), the bias is reduced in the rings around the z -wire and increased in the rings around the y -wire. This creates potential minima on the sides around the acceptor wire without creating a competing potential minimum next to the centre point between the wires around the donor wire. As a result of this bias excitation two minima are formed along the side of the donor wire that faces toward the acceptor wire away from the crossing point of the wires. This is shown especially in Fig. 2.20(b) and can be seen in Fig. 2.20(a) as well. These minima along the donor wire are not a problem since the cold atoms are now in the minima around the acceptor wire and a barrier exists to prevent them from flowing back to the donor wire.

In frame 9 the DC current in the donor wire is reduced to 90 % of its original value. It is now difficult avoid two separate minimum potential manifolds, one associated with each wire. The bias has now instead been much reduced in the rings around the y -wire to maximize the height of the barrier between the minimum potential manifolds around the two wires. In frame 10 the DC current in the z -wire is reduced to 75 % of its original value. The minimum potential manifolds around the wires are now well separated and the barrier between them increases naturally without the need for careful adjustment of the bias currents.

In frame 11 the DC current in the z -wire has been reduced to 50 % of its original value. The barrier between the minimum potential manifolds around the wires is now so high that it is not necessary to turn down the DC current in the z -wire more. Graphs showing the barrier between the minimum potential manifolds along the x -axis between the crossed wires corresponding to frames 8 to 11 have been published in Fig. 8(a) in [146]. In the figure curve “1” is for frame 8 and curve “4” is for frame 11. The article [146] contains several figures that are complementary to the figures

shown here and provides an alternative introduction to atom transfer between two crossed wires.

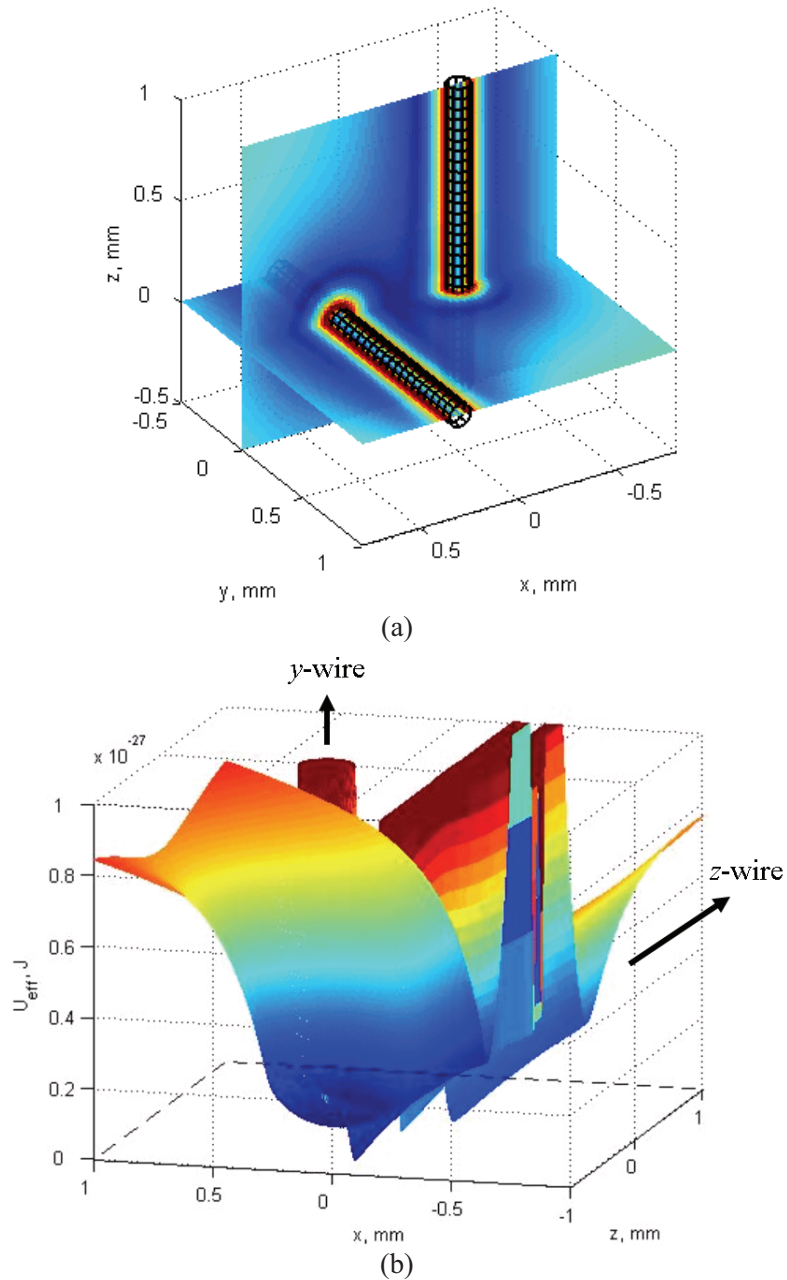


Fig. 2.20. Frame 8 in the animation (a), and U_{eff} in the xz -plane for frame 8 (b).

The cold atoms can alternatively be pumped away along the acceptor wire at once without turning down the DC current in the donor wire. To do this frame 8 – 14 in the animation in Fig. 2.18 can be replaced by four alternative frames with the following bias currents in the rings:

$$I_{\text{RF} | z\text{-wire rings}}^{\text{I+II, (8-11)}} = \{[-0.8 \ 0.8], [-0.5 \ 0.5], [-0.05 \ 0.05], [-0.05 \ 0.05]\} \text{ A},$$

$$I_{\text{RF} | y\text{-wire rings}}^{\text{I+II, (8-11)}} = \{[-2 \ 1.5], [-2 \ 1], [-2.5 \ 0.5], [-2.5 \ 0]\} \text{ A}.$$

The DC current in the z-wire is kept at -92.5 mA. The DC current in the y-wire and the RF currents in both wires are the same as before. The atom transfer takes place essentially in frames 6 and 7, which are not changed. The bias currents in the four frames have a lot in common with the bias currents in the frames they replace in Fig. 2.18. The last two frames are for example practically identical. Because there is little new to see the alternative completion of the atom transfer will not be given additional illustration here.

A question that can be asked is whether the barrier height in frame 9 is adequate to prevent cold atoms from tunnelling back into the slightly shallower minimum around the donor wire. The conditions for such tunnelling are present temporarily in frame 9 and partly in frame 10. See e.g. Fig. 8(a) in [146]. It is not clear to what extent this may be a problem. The situation is in any case avoided by pumping the cold atoms away from the wire junction without first reducing the DC current in the donor wire. This is more straightforward but a bit of flexibility is lost. The donor wire is tied up for longer and it becomes less convenient to temporarily store the cold atoms around the acceptor wire. However, unless the wires are busy buses for cold atoms in a quantum computer, this will not make much difference.

It may at the end be worth mentioning that the account given above of current sign combinations that can or can not be used to transfer cold atoms between two crossed wires is very sensitive to the signs of the field components for the bias rings around the horizontal y-wire. In the course of exploring inter-wire atom transfer sign errors were at first made in the rotation of the field components for rings around a wire in the y-direction. This led to some wrong conclusions initially about which combinations of current signs that could be used. The rotation of the field components for the bias rings was described in Section 1.7.3.

2.6 The effective potential around two parallel wires

We begin by once again seeking a new equation for the distance d that makes the effective potential zero at the centre point between the wires. Although it is possible to use the equation for B_ϕ in cylindrical coordinates for the two wires, the equations for the field components in Cartesian coordinates from [137] or [138] will be used here. This will make the derivation comparable to the previous case of two crossed wires.

The field components are as follows:

$$\Delta_1^{(x)} = 0, \Delta_1^{(y)} = -\rho = \rho_1, r_1 = \sqrt{x^2 + (y - \rho_1)^2}, \quad (2.35)$$

$$\Delta_2^{(x)} = 0, \Delta_2^{(z)} = \rho = \rho_2, r_2 = \sqrt{x^2 + (y - \rho_2)^2}, \quad (2.36)$$

$$B_{x_{DC}}^{(1+2)}(x, y) = -\frac{\mu_0 I_{DC}^{(1)} \cdot (y - \rho_1)}{2\pi [x^2 + (y - \rho_1)^2]} - \frac{\mu_0 I_{DC}^{(2)} \cdot (y - \rho_2)}{2\pi [x^2 + (y - \rho_2)^2]}, \quad (2.37)$$

$$B_{y_{DC}}^{(1+2)}(x, y) = \frac{\mu_0 I_{DC}^{(1)} \cdot x}{2\pi [x^2 + (y - \rho_1)^2]} + \frac{\mu_0 I_{DC}^{(2)} \cdot x}{2\pi [x^2 + (y - \rho_2)^2]}, \quad (2.38)$$

$$B_{z_{DC}}^{(1+2)} = 0. \quad (2.39)$$

The geometry of two parallel wires is shown in Fig. 2.21 in the yz -plane.

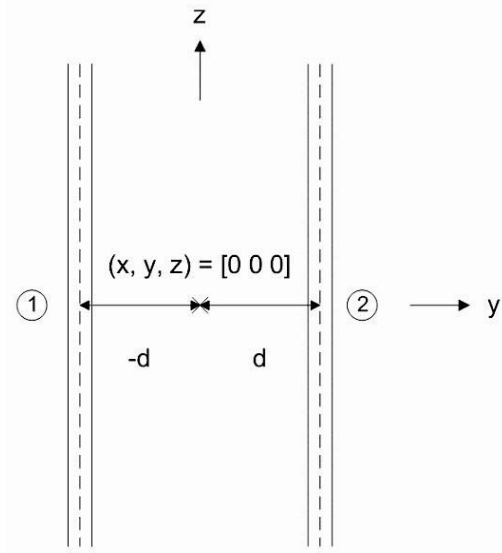


Fig. 2.21. Geometry of two parallel wires in the yz -plane. The wires are labelled 1 and 2. The origin is placed between the wires.

The line between the centres of the two wires lies in the y -direction. One can therefore set $x = 0$ in the equations above, since the fields in the x or z directions are of no interest in the following derivation. When $x = 0$ the field components in $B_{yDC}^{(1+2)}(x, y)$ disappear since x appears as a factor in the numerator of both terms. The equation for $|\mathbf{B}_{DC}(y, \rho)|$ thus becomes

$$|\mathbf{B}_{DC}(y, \rho)| = \sqrt{\left(\frac{-\mu_0 I_{DC}^{(1)} \cdot (y - \rho_1)}{2\pi(y - \rho_1)^2} - \frac{\mu_0 I_{DC}^{(2)} \cdot (y - \rho_2)}{2\pi(y - \rho_2)^2} \right)^2}, \quad (2.40)$$

$$|\mathbf{B}_{DC}(y, \rho)| = \sqrt{\left(\frac{-\mu_0 I_{DC}^{(1)} \cdot (y - \rho_2) - \mu_0 I_{DC}^{(2)} \cdot (y - \rho_1)}{2\pi(y - \rho_1)(y - \rho_2)} \right)^2}, \quad (2.41)$$

$$|\mathbf{B}_{DC}(y, \rho)| = \sqrt{\frac{\mu_0^2 I_{DC1}^2 (y - \rho_2)^2 + \mu_0^2 I_{DC2}^2 (y - \rho_1)^2 + 2\mu_0^2 I_{DC1} I_{DC2} (y - \rho_1)(y - \rho_2)}{4\pi^2 (y - \rho_1)^2 (y - \rho_2)^2}}. \quad (2.42)$$

We substitute $\rho_1 = -\rho_2 = -\rho$ and rewrite the expression for $|\mathbf{B}_{DC}(y, \rho)|$.

$$|\mathbf{B}_{\text{DC}}(y, \rho)| = \sqrt{\frac{\mu_0^2 I_{\text{DC1}}^2 (y - \rho)^2 + \mu_0^2 I_{\text{DC2}}^2 (y + \rho)^2 + 2\mu_0^2 I_{\text{DC1}} I_{\text{DC2}} (y + \rho)(y - \rho)}{4\pi^2 (y + \rho)^2 (y - \rho)^2}}, \quad (2.43)$$

$$|\mathbf{B}_{\text{DC}}(y, \rho)| = \sqrt{\frac{\mu_0^2 (I_{\text{DC1}}^2 y^2 - 2I_{\text{DC1}}^2 y\rho + I_{\text{DC1}}^2 \rho^2 + I_{\text{DC2}}^2 y^2 + 2I_{\text{DC2}}^2 y\rho + I_{\text{DC2}}^2 \rho^2 + 2I_{\text{DC1}} I_{\text{DC2}} y^2 - 2I_{\text{DC1}} I_{\text{DC2}} \rho^2)}{4\pi^2 (y^4 - 2y^3\rho + y^2\rho^2 + 2y^3\rho - 4y^2\rho^2 + 2y\rho^3 + y^2\rho^2 - 2y\rho^3 + \rho^4)}}, \quad (2.44)$$

$$|\mathbf{B}_{\text{DC}}(y, \rho)| = \mu_0 \sqrt{\frac{(I_{\text{DC1}}^2 + I_{\text{DC2}}^2 + 2I_{\text{DC1}} I_{\text{DC2}}) y^2 + 2(I_{\text{DC2}}^2 - I_{\text{DC1}}^2) y\rho + (I_{\text{DC1}}^2 + I_{\text{DC2}}^2 - 2I_{\text{DC1}} I_{\text{DC2}}) \rho^2}{4\pi^2 (y^2 - \rho^2)^2}}. \quad (2.45)$$

At this point we set $y = 0$ to obtain the eventual expression for $|\mathbf{B}_{\text{DC}}(\rho)|$

$$|\mathbf{B}_{\text{DC}}(y=0, \rho)| = \left| \frac{\mu_0 \rho \sqrt{(I_{\text{DC1}}^2 + I_{\text{DC2}}^2 - 2I_{\text{DC1}} I_{\text{DC2}})}}{2\pi\rho^2} \right| = \left| \frac{\mu_0 \sqrt{(I_{\text{DC1}}^2 + I_{\text{DC2}}^2 - 2I_{\text{DC1}} I_{\text{DC2}})}}{2\pi\rho} \right|. \quad (2.46)$$

This leads to the following equation for d

$$d = \frac{\mu_B g_F \mu_0}{2\pi\hbar} \left(\frac{\sqrt{(I_{\text{DC1}}^2 + I_{\text{DC2}}^2 - 2I_{\text{DC1}} I_{\text{DC2}})}}{\omega_{\text{RF}}} \right). \quad (2.47)$$

It may seem a bit cumbersome to put in specific values for the two DC currents in (2.47) to find d . In this case it is relevant to choose $I_{\text{DC2}} = I_{\text{DC1}}$ or $I_{\text{DC2}} = -I_{\text{DC1}}$, since different currents in the two wires most certainly will move a zero in the effective potential away from the centre point between the wires. If we choose $I_{\text{DC2}} = I_{\text{DC1}}$ the term in the root sign becomes

$$\sqrt{(I_{\text{DC1}}^2 + I_{\text{DC2}}^2 - 2I_{\text{DC1}} I_{\text{DC2}})} = I_{\text{DC}} \sqrt{2-2} = 0. \quad (2.48)$$

It is clear that $|\mathbf{B}_{\text{DC}}| = 0$ for two parallel wires at the centre point between the wires ($x = y = 0$) independent of d when $I_{\text{DC2}} = I_{\text{DC1}}$. In this case $U_{\text{eff}} \neq 0$. To be precise U_{eff} becomes $U_{\text{eff}}(\rho) = m_F \hbar \omega_{\text{RF}}$ if only the first term under the root sign in (2.1) is considered. The use of different currents in the two wires may cause the effective potential to become zero at the centre between the wires, but this leads to asymmetry and is not expected to be a viable solution.

If one chooses $I_{\text{DC2}} = -I_{\text{DC1}}$ this problem is avoided. The term under the root sign becomes

$$\sqrt{(I_{\text{DC1}}^2 + I_{\text{DC2}}^2 - 2I_{\text{DC1}} I_{\text{DC2}})} = \sqrt{I_{\text{DC}}^2 (2 - 2(-1))} = 2I_{\text{DC}}, \quad (2.49)$$

and the expression for d becomes

$$d = \frac{\mu_B g_F \mu_0}{\pi \hbar} \left(\frac{|I_{DC}|}{\omega_{RF}} \right). \quad (2.50)$$

The currents in two parallel wires should therefore be equal and of opposite sign. The dependence of d on I/ω_{RF} computed according to (2.50) is plotted in Fig. 2.22.

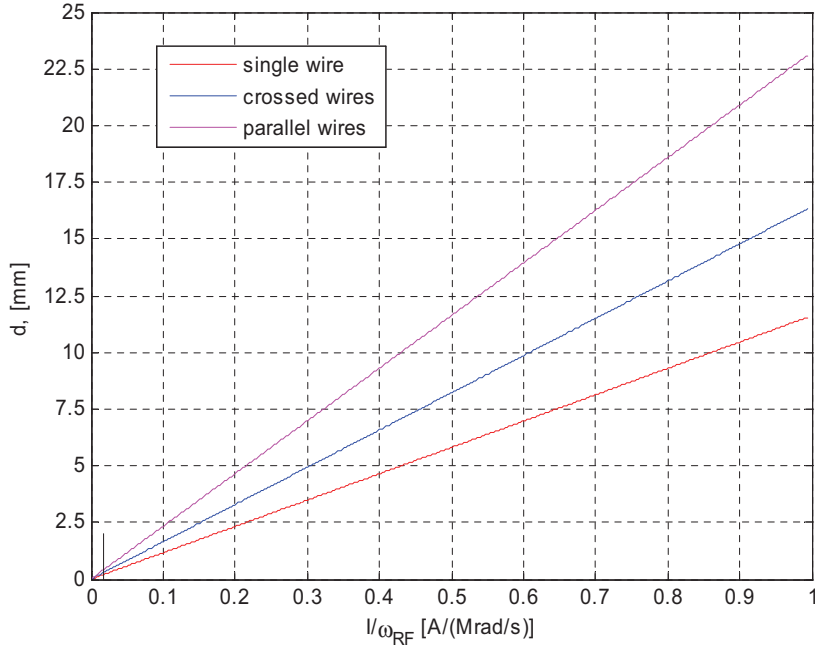


Fig. 2.22. Distance d for which the effective potential is zero for a single wire and for two crossed and two parallel wires. A mark has been placed at $I/\omega_{RF} = 0.0925/(2\pi \cdot 0.8) = 0.0184$.

Equation (2.45) for $|\mathbf{B}_{DC}(y, \rho)|$ is plotted in Fig. 2.23 for $\rho = d = 0.427$ mm, $I_{DC} = 92.5$ mA and $\omega_{RF} = 2\pi \cdot 8e5$ rad/s (blue curve). The total distance between the parallel wires is $2d$. It is seen that $|\mathbf{B}_{DC}|$ falls to $\hbar\omega_{RF}/(\mu_B g_F) = 1.055e-34 \cdot 2\pi \cdot 8e5 / (9.274e-24 \cdot 0.66) = 8.66e-5$ T at the centre between the wires for both graphs. This corresponds to $U_{\text{eff}} = 0$ J.

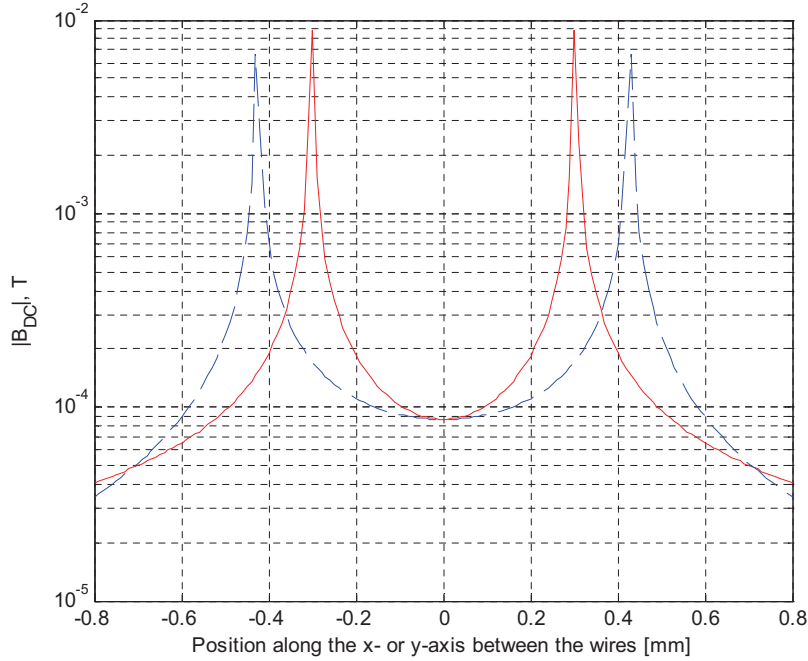


Fig. 2.23. $\mathbf{B}_{\text{DC}}(x, \rho = 3.02\text{e-}4)$ calculated from (2.16) (solid red graph), and $\mathbf{B}_{\text{DC}}(y, \rho = 4.27\text{e-}4)$ calculated from (2.45) (dashed blue graph).

The effective potential around two parallel wires is shown in Fig. 2.24. The slice-plot in (a) shows the two planes $x = 0$ and $z = 0$, and the plot in (b) shows the isosurface $U_{\text{eff}} = 3.5\text{e-}29$ J. In Fig. 2.24 $d = 0.427$ mm, $I_{\text{DC} | z\text{-wire}1} = -I_{\text{DC} | z\text{-wire}2} = -92.5$ mA, $I_{\text{RF} | z\text{-wire}1} = -I_{\text{RF} | z\text{-wire}2} = -10$ mA, and $f_{\text{RF}} = 800$ kHz. The wire with index 1 is at $y = -d$ and the wire with index 2 is at $y = d$. The radius of each wire is 57.2 μm . The isosurface for $U_{\text{eff}} = 0$ J clearly forms a figure of eight manifold around the two parallel wires. To plot this isosurface is however problematic. This is because isosurfaces calculated in Matlab require increased data point resolution when the volume that they enclose becomes smaller. The isosurface for $U_{\text{eff}} = 0$ J is a single manifold around the two wires that does not enclose a volume in the same way. Very high data point resolution would therefore be required if it is possible to plot this isosurface at all.

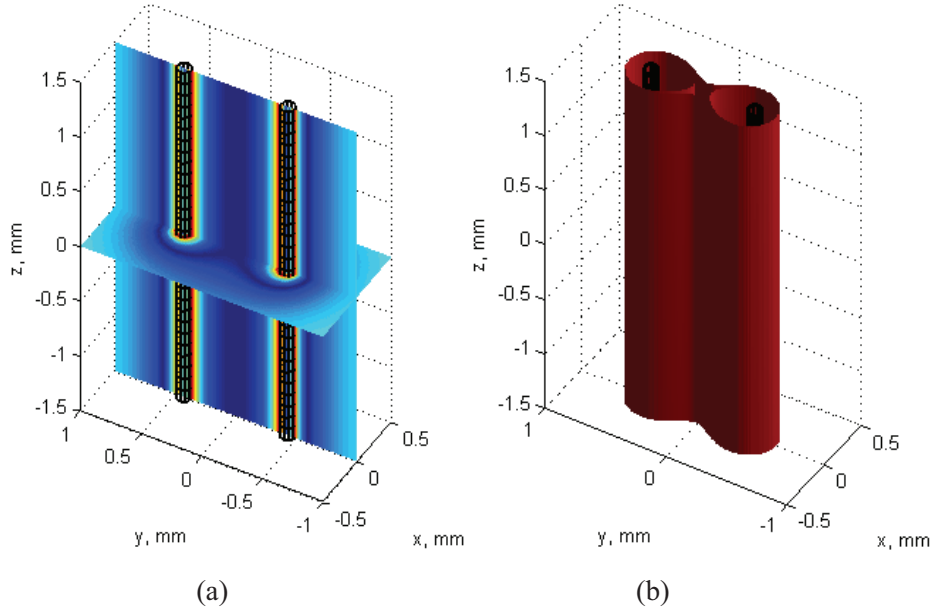


Fig. 2.24. Effective potential plots for two parallel wires. Slice-plot where the dark blue colour represents the effective potential minimum (a), and isosurface-plot for $U_{\text{eff}} = 3.5 \times 10^{-29}$ J (b).

The depth of the trapping potential for the parallel wires in Fig. 2.24 is $76.7 \mu\text{K}$, which is about the same as for a single wire.

2.6.1 The effect of the RF current on U_{eff} for two parallel wires

In the case of two parallel wires simulations suggest that the situation is similar to how it is for two crossed wires. Again the RF current amplitude must be the same in both wires and the RF currents must either both be of the same sign as the DC current in each wire, or both be of opposite sign relative to the DC current in each wire, to not have distortion of the effective potential. As already explained the DC currents must be in opposite directions in two parallel wires. The RF currents must consequently always be in counter-phase in the two wires. This result can be generalized for an array of parallel wires. In this case DC currents must be in alternating directions in neighbouring wires and RF currents must be in counter-phase in neighbouring wires.

This behaviour is again awkward to prove mathematically. A limited result will be derived for the case when the RF currents are of equal

magnitude and have the same sign as the DC current in each wire. The DC currents are also taken to be of equal magnitude in each wire. It will first be shown that $B_{\text{RF}}^{(\perp)}(\boldsymbol{\rho})$ is zero in the centre point between two parallel wires, resulting in equation (2.58). This result is then expanded to apply along a line between the centres of the parallel wires, resulting in equation (2.69). The effective potential along that same line is given by equation (2.70).

As was the case of two crossed wires, this derivation may be too detailed and tedious for many readers. In this case it is recommended to here just take a quick look at the result in equations (2.58), (2.69) and (2.70), and then move on to the next section.

The mentioned equations for $B_{\text{RF}}^{(\perp)}(\boldsymbol{\rho})$ will now be derived. The RF field components are also for this case calculated using the same formulas as the ones used for the DC field. A quasi-static approximation for the RF field is assumed. This means that equations (2.35)-(2.50) also apply to the RF field components.

We begin by finding an expression for $B_{\text{RF}}^{(\perp)}(\boldsymbol{\rho})$ and assume that $I_{\text{DC}2} = -I_{\text{DC}1}$. $B_{\text{RF}}^{(\perp)}(\boldsymbol{\rho})$ is defined in equation (2.19). $|\mathbf{B}_{\text{DC}}(\boldsymbol{\rho})|$ is now given by equation (2.46) and (2.49). The same equation can also be used for the RF field so that

$$|\mathbf{B}_{\text{RF}}(\boldsymbol{\rho})| = \left| \frac{\mu_0 I_{\text{RF}}}{\pi \rho} \right|. \quad (2.51)$$

From equation (2.37) for $x = 0$.

$$\mathbf{B}_{\text{RF}}(y, \rho) \mathbf{B}_{\text{DC}}(y, \rho) = \left(-\frac{\mu_0 I_{\text{RF}}^{(1)} \cdot (y - \rho_1)}{2\pi(y - \rho_1)^2} - \frac{\mu_0 I_{\text{RF}}^{(2)} \cdot (y - \rho_2)}{2\pi(y - \rho_2)^2} \right) \cdot \left(-\frac{\mu_0 I_{\text{DC}}^{(1)} \cdot (y - \rho_1)}{2\pi(y - \rho_1)^2} - \frac{\mu_0 I_{\text{DC}}^{(2)} \cdot (y - \rho_2)}{2\pi(y - \rho_2)^2} \right). \quad (2.52)$$

Note that $\rho_1 = -\rho_2$. Equation (2.38) is not used since the terms in $B_{y\text{DC}}^{(1+2)}(x, y)$ disappear for $x = 0$. The sign of ρ is important in the numerators in (2.52). Setting $\rho_1 = \rho_2 = \rho$ leads to the erroneous result that $\mathbf{B}_{\text{RF}}(y, \rho) \mathbf{B}_{\text{DC}}(y, \rho) = 0$.

$$\mathbf{B}_{\text{RF}}(y, \rho) \mathbf{B}_{\text{DC}}(y, \rho) = \left(-\frac{\mu_0 I_{\text{RF}}^{(1)} \cdot (y - \cancel{\rho_1})}{2\pi(y - \rho_1)^2} - \frac{\mu_0 I_{\text{RF}}^{(2)} \cdot (y - \cancel{\rho_2})}{2\pi(y - \rho_2)^2} \right) \cdot \left(-\frac{\mu_0 I_{\text{DC}}^{(1)} \cdot (y - \cancel{\rho_1})}{2\pi(y - \rho_1)^2} - \frac{\mu_0 I_{\text{DC}}^{(2)} \cdot (y - \cancel{\rho_2})}{2\pi(y - \rho_2)^2} \right), \quad (2.53)$$

$$\mathbf{B}_{\text{RF}}(y, \rho) \mathbf{B}_{\text{DC}}(y, \rho) = \left(\frac{\mu_0^2 I_{\text{RF}}^{(1)} I_{\text{DC}}^{(1)}}{4\pi^2 (y - \rho_1)^2} + \frac{\mu_0^2 I_{\text{RF}}^{(1)} I_{\text{DC}}^{(2)}}{4\pi^2 (y - \rho_1)(y - \rho_2)} + \frac{\mu_0^2 I_{\text{RF}}^{(2)} I_{\text{DC}}^{(1)}}{4\pi^2 (y - \rho_1)(y - \rho_2)} + \frac{\mu_0^2 I_{\text{RF}}^{(2)} I_{\text{DC}}^{(2)}}{4\pi^2 (y - \rho_2)^2} \right). \quad (2.54)$$

We now set $y = 0$ analogous to the derivation of (2.46). (By assuming that both the RF currents and DC currents in the two wires are anti-symmetric, only the result for $y = 0$ is of interest in the calculation of ρ .)

$$\mathbf{B}_{\text{RF}}(\rho) \mathbf{B}_{\text{DC}}(\rho) = \left(\frac{\mu_0^2 I_{\text{RF}}^{(1)} I_{\text{DC}}^{(1)}}{4\pi^2 \rho_1^2} + \frac{\mu_0^2 I_{\text{RF}}^{(1)} I_{\text{DC}}^{(2)}}{4\pi^2 \rho_1 \rho_2} + \frac{\mu_0^2 I_{\text{RF}}^{(2)} I_{\text{DC}}^{(1)}}{4\pi^2 \rho_1 \rho_2} + \frac{\mu_0^2 I_{\text{RF}}^{(2)} I_{\text{DC}}^{(2)}}{4\pi^2 \rho_2^2} \right), \quad (2.55)$$

$$\mathbf{B}_{\text{RF}}(\rho) \mathbf{B}_{\text{DC}}(\rho) = \left(\frac{\mu_0^2 I_{\text{RF}}^{(1)} (I_{\text{DC}}^{(1)} - I_{\text{DC}}^{(2)}) + \mu_0^2 I_{\text{RF}}^{(2)} (-I_{\text{DC}}^{(1)} + I_{\text{DC}}^{(2)})}{4\pi^2 \rho^2} \right). \quad (2.56)$$

With $I_{\text{DC}} = I_{\text{DC}2} = -I_{\text{DC}1}$ and $I_{\text{RF}} = I_{\text{RF}2} = -I_{\text{RF}1}$

$$\mathbf{B}_{\text{RF}}(\rho) \mathbf{B}_{\text{DC}}(\rho) = \frac{2\mu_0^2 I_{\text{RF}} I_{\text{DC}} + 2\mu_0^2 I_{\text{RF}} I_{\text{DC}}}{4\pi^2 \rho^2} = \frac{\mu_0^2 I_{\text{RF}} I_{\text{DC}}}{\pi^2 \rho^2}. \quad (2.57)$$

$B_{\text{RF}}^{(\perp)}(\rho)$ can now be found as

$$B_{\text{RF}}^{(\perp)}(\rho) = \sqrt{\left(\frac{\mu_0 I_{\text{RF}}}{\pi \rho} \right)^2 - \left(\frac{\mu_0^{\cancel{2}} I_{\text{RF}} I_{\text{DC}} \cdot \cancel{\pi} \cancel{\rho}}{\pi^{\cancel{2}} \rho^{\cancel{2}} \cdot \mu_0^{\cancel{2}} I_{\text{DC}}} \right)^2} = \sqrt{\left(\frac{\mu_0 I_{\text{RF}}}{\pi \rho} \right)^2 - \left(\frac{\mu_0 I_{\text{RF}}}{\pi \rho} \right)^2} = 0. \quad (2.58)$$

The second term under the root sign in (2.1) is also in this case zero at the midpoint between the wires and the expression for d in equation (2.50) remains unchanged.

An analytical expression for the potential function as a function of distance between the parallel wires is now derived. We make use of equation (2.45) for $\mathbf{B}_{\text{DC}}(y, \rho)$. The same equation is used for $\mathbf{B}_{\text{RF}}(y, \rho)$ with I_{RF} substituted for I_{DC} . Equation (2.54) is used for $\mathbf{B}_{\text{RF}}(y, \rho) \mathbf{B}_{\text{DC}}(y, \rho)$. With $I_{\text{DC}} = I_{\text{DC}2} = -I_{\text{DC}1}$ and $I_{\text{RF}} = I_{\text{RF}2} = -I_{\text{RF}1}$ equation (2.45) becomes

$$|\mathbf{B}_{\text{DC}}(y, \rho)| = \mu_0 \sqrt{\frac{(2I_{\text{DC}}^2 - 2I_{\text{DC}}^2)y^2 + 2(I_{\text{DC}}^2 - I_{\text{DC}}^2)y\rho + (2I_{\text{DC}}^2 + 2I_{\text{DC}}^2)\rho^2}{4\pi^2 (y^2 - \rho^2)^2}} = \frac{2\mu_0 I_{\text{DC}} \rho}{2\pi (y^2 - \rho^2)}, \quad (2.59)$$

and equation (2.54) becomes

$$\mathbf{B}_{\text{RF}}(y, \rho) \mathbf{B}_{\text{DC}}(y, \rho) = \left(\frac{\mu_0^2 I_{\text{RF}} I_{\text{DC}}}{4\pi^2 (y+\rho)^2} - \frac{\mu_0^2 I_{\text{RF}} I_{\text{DC}}}{4\pi^2 (y+\rho)(y-\rho)} - \frac{\mu_0^2 I_{\text{RF}} I_{\text{DC}}}{4\pi^2 (y+\rho)(y-\rho)} + \frac{\mu_0^2 I_{\text{RF}} I_{\text{DC}}}{4\pi^2 (y-\rho)^2} \right), \quad (2.60)$$

$$\mathbf{B}_{\text{RF}}(y, \rho) \mathbf{B}_{\text{DC}}(y, \rho) = \left(\frac{\mu_0^2 I_{\text{RF}} I_{\text{DC}}}{4\pi^2 (y+\rho)^2} - \frac{2\mu_0^2 I_{\text{RF}} I_{\text{DC}}}{4\pi^2 (y+\rho)(y-\rho)} + \frac{\mu_0^2 I_{\text{RF}} I_{\text{DC}}}{4\pi^2 (y-\rho)^2} \right), \quad (2.61)$$

$$\mathbf{B}_{\text{RF}}(y, \rho) \mathbf{B}_{\text{DC}}(y, \rho) = \left(\frac{\mu_0^2 I_{\text{RF}} I_{\text{DC}} (y^2 - 2y\rho + \rho^2) + \mu_0^2 I_{\text{RF}} I_{\text{DC}} (y^2 + 2y\rho + \rho^2) - 2\mu_0^2 I_{\text{RF}} I_{\text{DC}} (y^2 - \rho^2)}{4\pi^2 (y+\rho)^2 (y-\rho)^2} \right), \quad (2.62)$$

$$\mathbf{B}_{\text{RF}}(y, \rho) \mathbf{B}_{\text{DC}}(y, \rho) = \left(\frac{2\mu_0^2 I_{\text{RF}} I_{\text{DC}} y^2 + 2\mu_0^2 I_{\text{RF}} I_{\text{DC}} \rho^2 - 2\mu_0^2 I_{\text{RF}} I_{\text{DC}} (y^2 - \rho^2)}{4\pi^2 (y+\rho)^2 (y-\rho)^2} \right) = \frac{\mu_0^2 I_{\text{RF}} I_{\text{DC}} \rho^2}{\pi^2 (y+\rho)^2 (y-\rho)^2}, \quad (2.63)$$

$$\mathbf{B}_{\text{RF}}(y, \rho) \mathbf{B}_{\text{DC}}(y, \rho) = \frac{\mu_0^2 I_{\text{RF}} I_{\text{DC}} \rho^2}{\pi^2 (y^2 + 2y\rho + \rho^2)(y^2 - 2y\rho + \rho^2)} = \frac{\mu_0^2 I_{\text{RF}} I_{\text{DC}} \rho^2}{\pi^2 (y^4 - 2y^2 \rho^2 + \rho^4)}. \quad (2.64)$$

When this result is substituted into the equation for $B_{\text{RF}}^{(\perp)}(y, \rho)$ we get

$$B_{\text{RF}}^{(\perp)}(y, \rho) = \sqrt{\left(\frac{2\mu_0 I_{\text{RF}} \rho}{2\pi (y^2 - \rho^2)} \right)^2 - \left(\frac{\mu_0^2 I_{\text{RF}} I_{\text{DC}} \rho^2 \cdot \cancel{\pi} (y^2 - \rho^2)}{\pi^2 (y^4 - 2y^2 \rho^2 + \rho^4) \cdot \cancel{\mu_0} I_{\text{DC}} \cancel{\rho}} \right)^2}, \quad (2.65)$$

$$B_{\text{RF}}^{(\perp)}(y, \rho) = \sqrt{\left(\frac{2\mu_0 I_{\text{RF}} \rho}{2\pi (y^2 - \rho^2)} \right)^2 - \left(\frac{\mu_0 I_{\text{RF}} \rho \cdot (y^2 - \rho^2)}{\pi (y^4 - 2y^2 \rho^2 + \rho^4)} \right)^2}, \quad (2.66)$$

$$B_{\text{RF}}^{(\perp)}(y, \rho) = \sqrt{\frac{4\mu_0^2 I_{\text{RF}}^2 \rho^2}{4\pi^2 (y^2 - \rho^2)^2} - \frac{\mu_0^2 I_{\text{RF}}^2 \rho^2 (y^2 - \rho^2)^2}{\pi^2 (y^4 - 2y^2 \rho^2 + \rho^4)^2}}, \quad (2.67)$$

$$B_{\text{RF}}^{(\perp)}(y, \rho) = \sqrt{\frac{4\mu_0^2 I_{\text{RF}}^2 \rho^2 (y^4 - 2y^2 \rho^2 + \rho^4) - 4\mu_0^2 I_{\text{RF}}^2 \rho^2 (y^2 - \rho^2)^2}{4\pi^2 (y^4 - 2y^2 \rho^2 + \rho^4)^2}}, \quad (2.68)$$

$$B_{\text{RF}}^{(\perp)}(y, \rho) = \sqrt{\frac{4\mu_0^2 I_{\text{RF}}^2 \rho^2 (y^4 - 2y^2 \rho^2 + \rho^4) - 4\mu_0^2 I_{\text{RF}}^2 \rho^2 (y^4 - 2y^2 \rho^2 + \rho^4)}{4\pi^2 (y^4 - 2y^2 \rho^2 + \rho^4)^2}} = 0, \quad (2.69)$$

$$U_{\text{eff}}(y, \rho) = m_F \sqrt{\left[\frac{\mu_B g_F 2\mu_0 I_{\text{DC}} \rho}{2\pi (y^2 - \rho^2)} - \hbar \omega_{\text{RF}} \right]^2}. \quad (2.70)$$

The second term under the root sign in (2.1) for the effective potential is zero along a line between two parallel wires when $I_{\text{DC}} = I_{\text{DC}2} = -I_{\text{DC}1}$ and $I_{\text{RF}} = I_{\text{RF}2} = -I_{\text{RF}1}$. If the currents in the two wires are of different magnitude equation (2.59) is no longer valid and the RF magnetic field normal to the local DC magnetic vector $B_{\text{RF}}^{(\perp)}(y, \rho)$ is most likely no longer zero.

2.7 Prospective atom transfer between two parallel wires with bias rings

The possibility of pumping cold atoms between two parallel wires using bias rings has been briefly explored. This has turned out to be more difficult than in the case of two crossed wires. Because the proposed technique appears somewhat inconvenient, the description given here will be kept short.

A common minimum can be created at the centre between the parallel wires using bias rings placed around pairs of parallel wires. However, low potential regions begin to appear to the side of the wires unless a pair of perpendicularly placed bias rings is used in addition to the pair of bias rings around the parallel wires. This extra pair of bias rings may be placed around a second pair of parallel wires pointing in the orthogonal direction. This is the geometry of a four-wire cell, which will be described in Section 2.8. Here however, only the additional bias rings are of interest.

The obtainable common minimum is illustrated in Fig. 2.25. The figure shows a pair of parallel wires like the ones in Fig. 2.24, but with the centre of the wires moved to $x = -0.302$ mm. A pair of bias rings of radius $r = 1.0$ mm and with RF currents $I_{\text{RF} | z\text{-wire rings}} = [-1.5 \ 1.5]$ A have been placed around both wires at $z = \pm 3$ mm. A pair of perpendicular bias rings, also of radius $r = 1.0$ mm, with RF currents $I_{\text{RF} | y\text{-axis rings}} = [-0.3 \ 0.3]$ A have been placed at $y = \pm 3$ mm, with the centres of the rings offset to $x = 0.302$ mm. The wire currents are the same as in Fig. 2.24.

The creation of such a common minimum may be useful in some situations and cold atoms can be transported along the wires in the common minimum. It appears however that bias rings centred between the parallel wires can not be used to transfer atoms from around one wire to around the other wire. The extra pair of perpendicularly placed bias rings does not change this. The root of the problem seems to be that one pair of bias rings is centred on the common minimum and prevent it from being moved sideways towards one of the parallel wires. If the DC current in one of the wires is subsequently reduced, the cloud of cold atoms in the common minimum will be divided into two and practically no transfer of cold atoms will take place between the wires. It can therefore be put in question whether the creation of a common minimum between the wires is useful enough to justify the presence of the two pairs of bias rings.

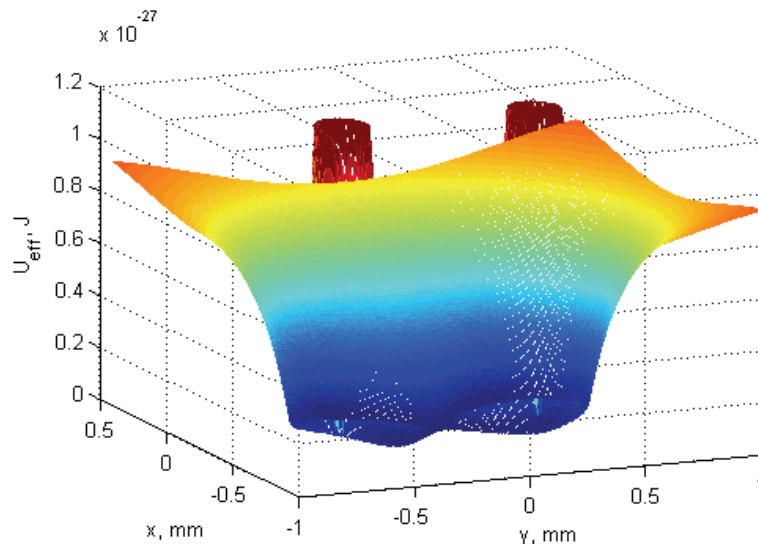


Fig. 2.25. U_{eff} around two parallel wires with a pair of bias rings placed around both wires as well as a pair of perpendicularly placed bias rings. The potential slice is for $z = 0$ mm.

If one is prepared to use a pair of bias rings around each of the two parallel wires, which may be spaced differently along each of the wires, it seems to be possible to transfer cold atoms from around one wire to the other wire.

The anticipated cold atom transfer is illustrated by the video animation in Fig. 2.26. In the figure, bias rings with a radius of 0.65 mm have been placed around each of the two parallel wires in Fig. 2.24. The bias rings are

centred at $z = \pm 3$ mm along the wire with a negative y -coordinate and at $z = \pm 3.5$ mm along the wire with a positive y -coordinate. The wire currents are the same as in Fig. 2.24. The video consists of 18 frames. The bias currents in the rings in the 18 animated frames are:

$$I_{\text{RF}|z\text{-wire rings}}^{\text{I+II}} = \left\{ \begin{array}{l} [2 \ 0], [2 \ 0], [2 \ 0], [2 \ 0], [2.2 \ 0], \\ [2 \ -0.5], [2 \ -1], [1.5 \ -1.5], [1 \ -1], \\ [0.5 \ -0.5], [0.5 \ -0.5], [0.5 \ -0.5], \\ [0.5 \ -0.5], [0.5 \ -0.5], [0.5 \ -0.5], \\ [0.5 \ -0.5], [0.5 \ -0.5], [0.5 \ -0.5] \end{array} \right\} A,$$

$$I_{\text{RF}|z\text{-wire rings}}^{\text{III+IV}} = \left\{ \begin{array}{l} [0 \ 0], [0 \ -0.6 \cdot k], [0 \ -1.2 \cdot k], [0 \ -1.7 \cdot k], [0 \ -2.2 \cdot k], \\ [0.5 \cdot k \ -2 \cdot k], [1 \cdot k \ -2 \cdot k], [1.5 \cdot k \ -1.5 \cdot k], [1.75 \cdot k \ -1.75 \cdot k], \\ [2 \cdot k \ -2 \cdot k], \\ [1.5 \cdot k \ -2 \cdot k], [0.9 \cdot k \ -2 \cdot k], [0.3 \cdot k \ -2 \cdot k], [0 \ -2.2 \cdot k] \end{array} \right\} A,$$

where $k = 1.546$. The constant k is a factor found by optimization which is used to increase the current in the pair of bias rings that are spaced 7 mm apart so that the strength of the field at the centre between the bias rings is equivalent to the field from the bias rings that are spaced 6 mm apart. The bias rings at the lower end of the figure have the indices I and III.

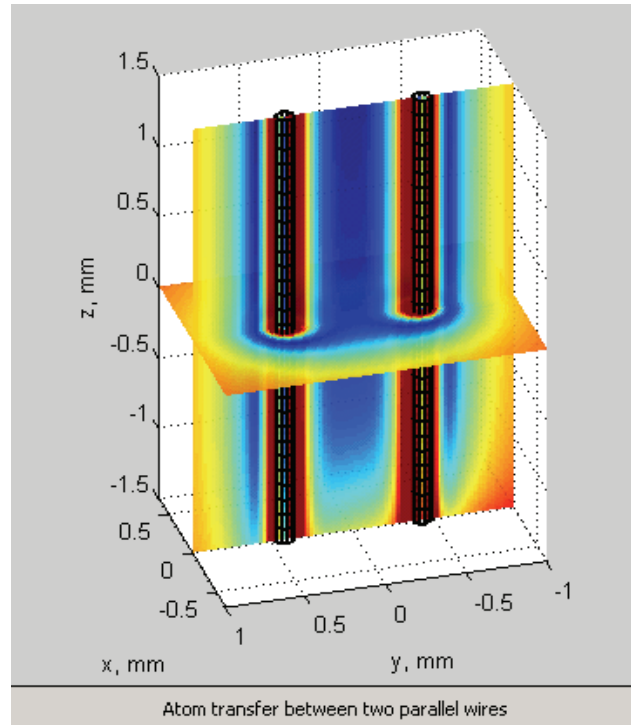


Fig. 2.26. Animation of cold atom transfer between two parallel wires.

In the first four frames the cold atoms are being moved down within the common minimum between the parallel wires toward the centre of the figure. In frame 5 a slope is created around the wire with a negative y -coordinate toward the common minimum between the wires. The effective potential in frame 5 is shown in Fig. 2.27 for $z = 0$. In frames 6 – 8 bias current transitions are done. The common minimum between the wires is kept, but the downward slope around the wire with a negative y -coordinate is impaired.

In frames 9 and 10 the common minimum is pulled toward the wire with a positive y -coordinate. This is shown by the graphs for the respective frames in Fig. 2.28. The graph for frame 5 is included but it lies underneath the graph for frame 8 for the most part. The same is the case for the graphs for frame 6 and 7 and they have therefore been left out. In frame 11 – 14 the DC current in the wire with a negative y -coordinate is reduced to 95 %, 90 %, 75 % and 50 % respectively of its original value. This splits the potential surfaces around the two wires but retains the cold atoms in the minimum around the wire with a positive y -coordinate. In frames 15 – 18

the cold atoms are moved down along the same wire. The minimum would have been moved all the way down if the bias current had been completely turned off in the lower bias ring around the other wire.

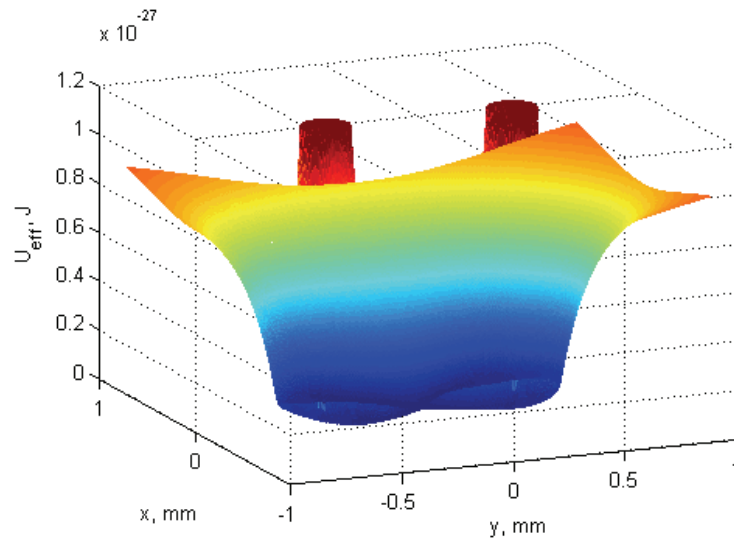


Fig. 2.27. The effective potential around two parallel wires corresponding to frame 5 in the animation in Fig. 2.26.

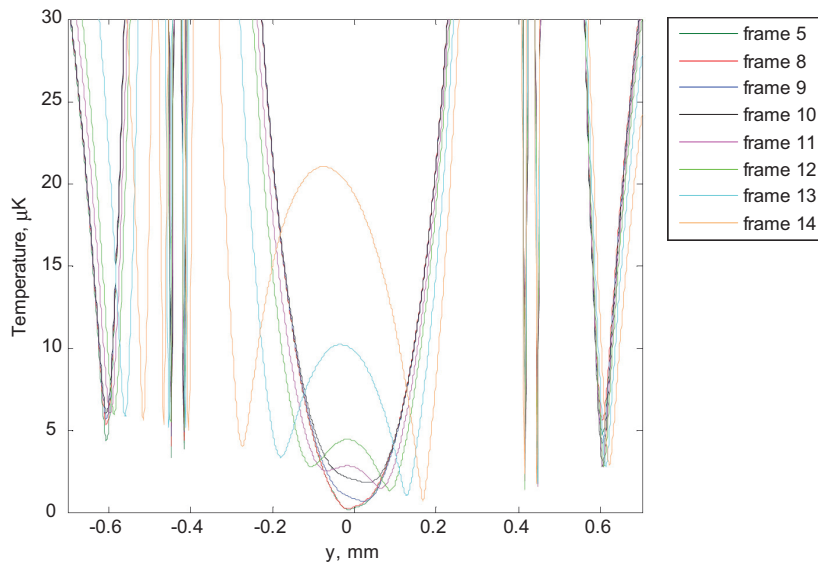


Fig. 2.28. The effective potential between two parallel wires for several of the frames in the animation in Fig. 2.26.

Although it seems feasible to transfer atoms directly between two parallel wires this requires a pair of relatively small bias rings around each of the two wires. Small bias rings have been found to be less efficient than larger bias rings as explained in Section 2.3, and the currents in the bias rings must therefore be relatively much larger. It may therefore be just as practical to place a crossing wire next to the parallel wires and transfer atoms from around one parallel wire to the other by doing two atom transfers between crossed wires.

2.8 The four-wire cell

If two pairs of parallel wires are placed so that they cross in two different planes a four-wire cell is created. The geometry of the four-wire cell is shown in Fig. 2.29. To a first approximation d_x can be taken to be the distance d for two crossed wires from equation (2.18), and d_y the distance d for two parallel wires from equation (2.50).

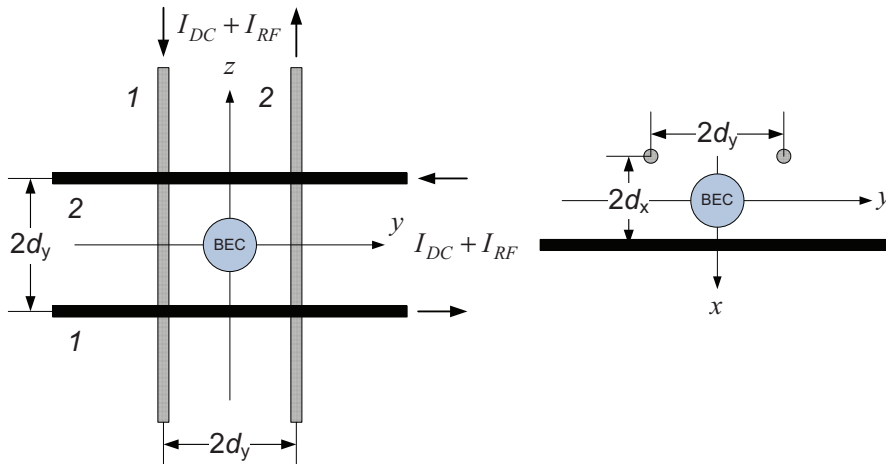


Fig. 2.29. The four-wire cell viewed from the side and from above.

The nature of the effective potential is however so that any change in geometry or currents affects the overall potential, at least for wires that are relatively close to each other. Therefore the equations derived for two crossed wires in Section 2.4, or for two parallel wires in Section 2.6, are no longer accurate in the case of the four-wire cell. This is illustrated by the plot of the isosurface $U_{\text{eff}} = 8\text{e-}29$ J in Fig. 2.30, where one of the wires in

the four-wire cell has been removed by setting the DC and RF currents to zero. The figure shows that just by adding a crossing wire the effective potential between two parallel wires is influenced considerably, even at some distance from the crossing wire.

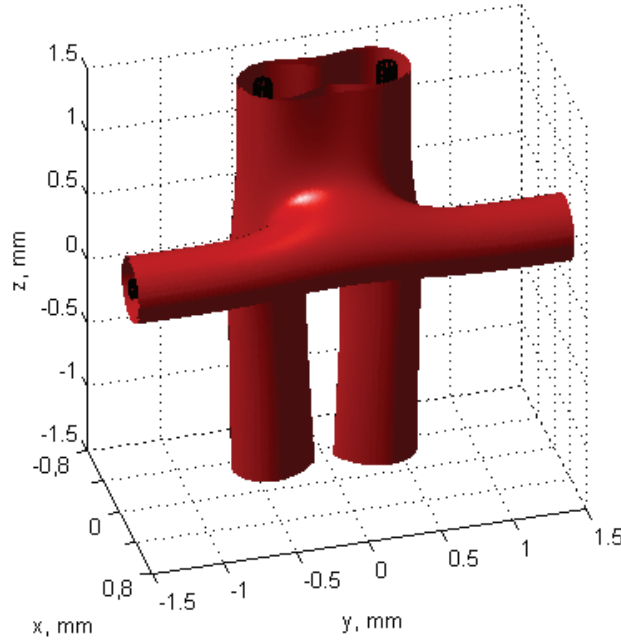


Fig. 2.30. The potential surface $U_{\text{eff}} = 8\text{e-}29$ J for two parallel wires and a third crossing wire. The currents in the two vertical wires are: $I_{\text{DC}|z\text{-wire}}^{(1,2)} = [-92.5, 92.5]$ mA, and $I_{\text{RF}|z\text{-wire}}^{(1,2)} = [-10, 10]$ mA. The currents in the horizontal wire are: $I_{\text{DC}|y\text{-wire}}^{(2)} = 92.5$ mA, and $I_{\text{RF}|y\text{-wire}}^{(2)} = 10$ mA. The frequency is $f_{\text{RF}} = 0.8$ MHz. The distance $d_x = 0.302$ mm and the distance $d_y = 0.427$ mm. The radius of the wires is 57.2 μm .

To adjust for the dependence of the effective potential on the contributions from each wire in the design, the most practical solution is to resort to optimization. The four-wire cell and the multi-wire structures described later in this Chapter have therefore all been optimized to better bring to light what their realizable potential is. It may still be possible to find analytical equations for a limited number of wires, but this approach has not been pursued. This is because the math becomes complicated while the

result is of limited benefit. New equations will have to be found for every variant of the geometry and the equations may not become practical to use.

Optimizations have instead been done by running simple scripts in Matlab. The optimization scripts are mostly based on the use of the built in function “fminbnd”, which accepts a function argument. The function searches for the value of a specified variable of the argument function that minimizes the overall function value. A starting value and upper and lower bounds for the variable that is solved for are supplied beforehand. The argument function, which in this case is the potential function U_{eff} for the relevant geometry, is evaluated only in a single geometric point, which is either at the centre between two crossed wires or at the centre between two parallel wires. The function “fminbnd” is called for every variable that is optimized from within a while-loop. The while-loop is repeated a certain number of times to allow each variable to be determined with the remaining variables that are being optimized updated. This allows the optimized variables to converge on a consistent solution. The number of iterations of the while-loop has been set high to make absolutely sure that the solutions for the different optimized variables have converged. Running the optimization scripts is in fact done in minutes, but checking the result by computing the potential in 3D for the complete structure may take an hour or more depending on the number of wires, the resolution and the necessary plot range.

The optimization script for the four-wire cell is for example as follows:

```
options = optimset('TolX',1e-18,'FunValCheck','off');
x1z=-3.020987525871509e-4;
dy1=-4.272321530847429e-4;

% Set upper and lower bounds on the controller
lb_x1z = -5e-4;
ub_x1z = -0.2e-4;
lb_dy1 = -7e-4;
ub_dy1 = -0.5e-4;

wire_geom=0;
k=1;
while k <= 20
    Ueff_fun=@(x1z) abs(Total_U_eff(wire_geom,dy1,x1z,0,dy1,dy1));
    x1z = fminbnd(@(x1z) abs(Total_U_eff(wire_geom,dy1,x1z,0,dy1,dy1)),lb_x1z,ub_x1z,options);
    Ueff_fun=@(dy1) abs(Total_U_eff(wire_geom,dy1,x1z,x1z,0,dy1));
    dy1 = fminbnd(@(dy1) abs(Total_U_eff(wire_geom,dy1,x1z,x1z,0,dy1)),lb_dy1,ub_dy1,options);
    k=k+1;
end
fprintf('x1z =%0.15e \n\n',x1z)
fprintf('dy1 =%0.15e \n\n',dy1)
```

x/z is here the distance $-d_x$ and dy/l the distance $-d_y$ in Fig. 2.29. Upper and lower bounds are first defined for the two variables. The argument function, which is here named “Total_U_eff”, returns the value of the effective potential. The wire geometry is specified as an input argument where “wire_geom = 0” corresponds to the four-wire cell. The next two input arguments are the two variables being optimized. The last three input arguments are the x - y - and z -coordinates of the point where the argument function is minimized. Finally the optimized variables are printed out. The negative sign for both x/z and dy/l is a result of the position of the geometric origin.

The isosurface $U_{\text{eff}} = 8\text{e-}29$ J for the optimized four-wire cell is shown in Fig. 2.31. The minimum potential manifold is close to the shown isosurface. Closer to the wires and in the middle between the crossing wires the potential is higher. The wire currents are $I_{\text{DC}|z\text{-wire}}^{(1,2)} = [-92.5, 92.5]$ mA and $I_{\text{DC}|y\text{-wire}}^{(1,2)} = [-92.5, 92.5]$ mA. The RF currents are 10 mA, and have the same sign as the DC current in each wire. The frequency is 0.8 MHz as before. The optimized distances are $d_x = -x/z = 0.267$ mm and $d_y = -dy/l = 0.370$ mm. The effective potential has been minimized in the point $(x, y, z) = (0, dy/l, dy/l)$ for x/z and in the point $(x, y, z) = (x/z, 0, dy/l)$ for dy/l . As previously explained the RF currents must be of equal magnitude and either all be of the same sign as the DC current in each wire, or all be of opposite sign with respect to the DC current in each wire.

The described optimization approach has been successful especially for smaller geometries involving a limited number of optimized variables. If the intention is to fabricate the four-wire cell using conductors on top of and under a micro machined substrate, the distance between the crossed wires should be fixed at the chosen substrate thickness plus one conductor height. In this case the two variables to optimize are the distance d_y and the DC wire current. This optimization has been done for the four micro-wire cell which is described in the next Chapter.

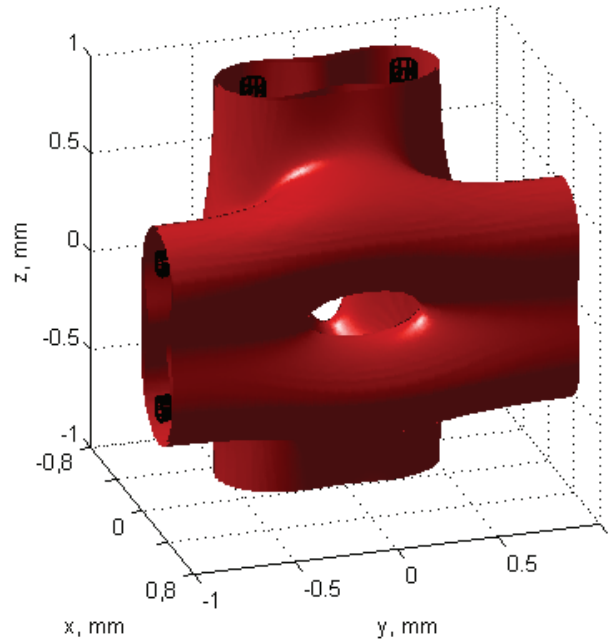


Fig. 2.31. The potential surface $U_{\text{eff}} = 8\text{e-}29$ J for four crossing wires. The distances between the crossing and parallel wires have been optimized.

The optimized four-wire cell is shown in a complementary slice-plot in Fig. 2.32. The purpose of the optimization has been to obtain minima in the effective potential between the crossed wires in the four wire-crossing-points and between the parallel wires behind the crossing wires. In Fig. 2.32 a near circular potential minimum can be seen in the yz -plane around the centre of the cell. This 2D potential minimum is of practically uniform depth for the optimized cell. The minimum also has additional small loops outwards between the parallel wires on each side.

The footprint of the potential minimum can be discerned from the darkest blue regions in Fig. 2.32. Without optimization the 2D potential minimum is not of perfectly uniform depth. Instead eight slightly deeper minima are found along the periphery on both sides of the four wire-crossing-points. Thus the 2D potential minimum in the yz -plane can be used to check the quality of the optimization.

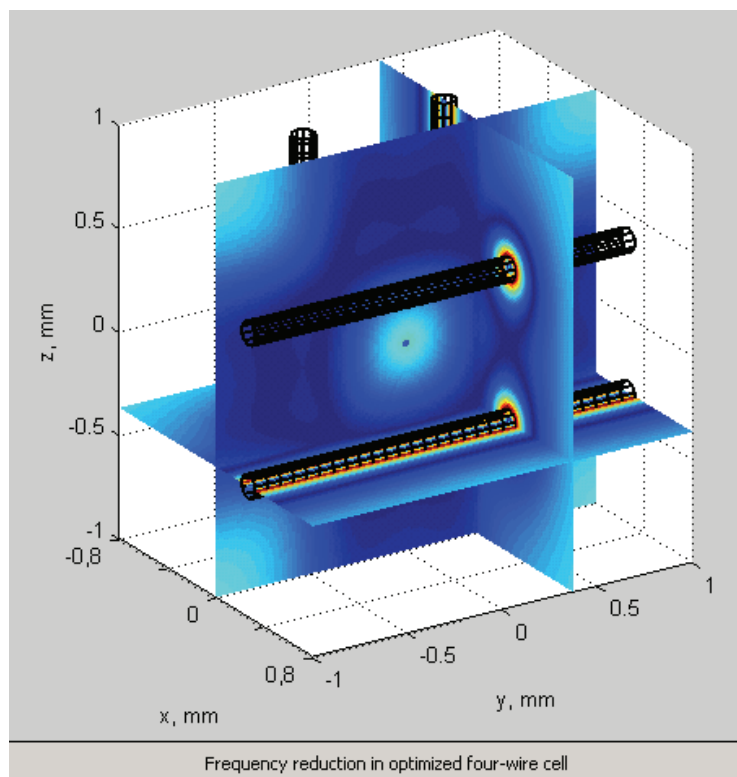


Fig. 2.32. Animation showing the frequency being reduced in the four-wire cell.

Fig. 2.32 is also a video animation showing the transformation of the effective potential as the RF frequency is reduced from 0.8 MHz to zero in steps of 0.1 MHz. The video shows that as the frequency is reduced the local potential maximum at the centre remains isolated in 3D while the surrounding minimum around the wires implodes into the centre. This effect may allow the study of collision and entanglement between strong- and weak-field-seeking atoms. But this is a bit speculative.

When the four-wire cell is excited by only the DC currents it becomes a trap for weak-field-seeking atoms. The effective potential is now as shown in Fig. 2.33. Unfortunately there is an absolute zero in the effective potential at the centre of the trap as a result of the symmetry of the geometry. This will lead to Majorana spin-flip transitions. One solution is to place bias rings around either single wires or pairs of parallel wires outside the cell. If one can live with a slight degradation of the trapping potential it should also be possible to alter the DC or RF currents very slightly in the wires to avoid the zero in the B-field.

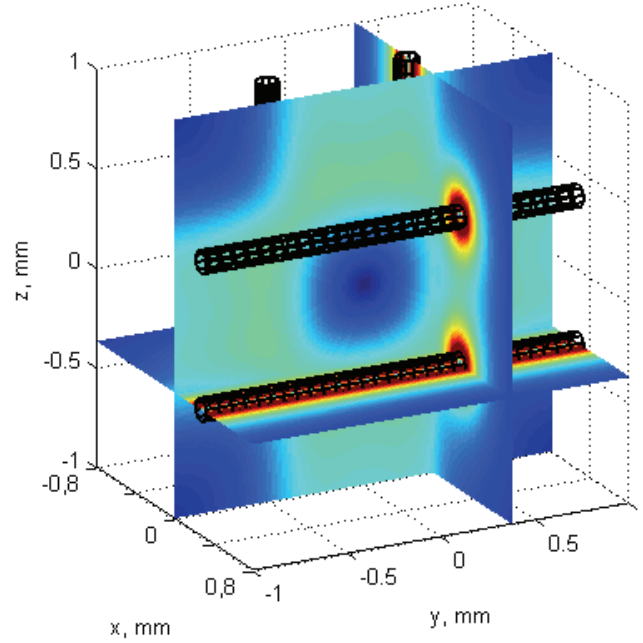


Fig. 2.33. Slice-plot showing the four-wire cell excited by only the DC currents.

To quantify precisely the depth of the four-wire cell trap, graphs have been calculated of the effective potential along the x -axis in Fig. 2.34 and along the z -axis in Fig. 2.35. The x -axis goes through the centre of the cell and extends out between the parallel wires on both sides. The z -axis goes through the centre of the cell vertically. The axes are identical to those shown in Fig. 2.33. The temperature has been calculated as $T = U_{eff}/k_B$, where $k_B = 1.3807e-23$ J/K is Boltzmann's constant.

In the two figures the red graphs are for $f_{RF} = 0.8$ MHz, the green graphs for $f_{RF} = 0.6$ MHz, the blue graphs for $f_{RF} = 0.4$ MHz, the magenta graphs for $f_{RF} = 0.2$ MHz, and the black graphs are for zero frequency. The potential along the y -axis is identical to the potential along the z -axis in Fig. 2.35, as dictated by the geometric symmetry of the cell. Note that in the calculation of the effective potential the magnetic quantum number has been set to $m_F = 2$ for all graphs. If the potential maximum at the centre of the cell is used to catch and hold ground state atoms with $m_F = 1$, the effective potential shown by the graphs must be divided by two according to equation (2.1), when the ground state atoms are considered.

In the case of DC + RF excitation no absolute zero in the effective potential has been found. However, the graphs of the potential in Fig. 2.34 and Fig. 2.35 suggest that a somewhat deformed spherical minimum exists around the centre of the cell at least for frequencies below 0.6 MHz. This minimum could well lie at zero potential for the four-wire cell. To be able to see a minimum of zero directly, a point on the zero minimum manifolds would have to coincide exactly with a mesh point with full numeric precision. It is therefore in this case difficult to establish whether the minimum is exactly zero or a small value except by painstaking equation analysis. This has not been pursued further.

One other matter to consider is that as the RF frequency becomes low the RF current will at some point begin to behave more like a DC current. Unfortunately the DC currents can not be allowed to change much at all. It may be possible to gradually reduce the RF current amplitude for low frequencies so that the RF current amplitude becomes zero as the frequency approaches zero. This transition is difficult to explore analytically especially since equation (2.1) is not sensitive to the amplitude of the RF current.

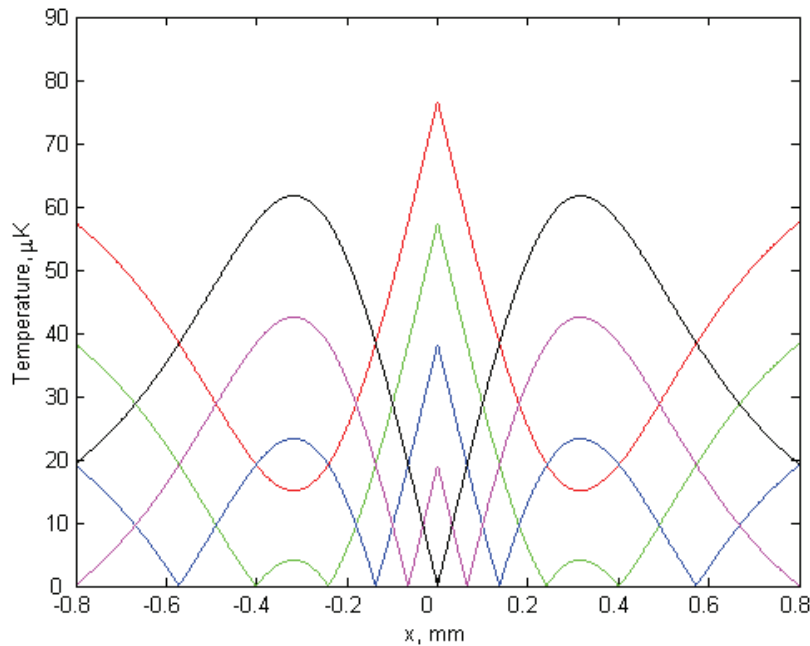


Fig. 2.34. The potential along the x -axis through the centre of the four-wire cell.

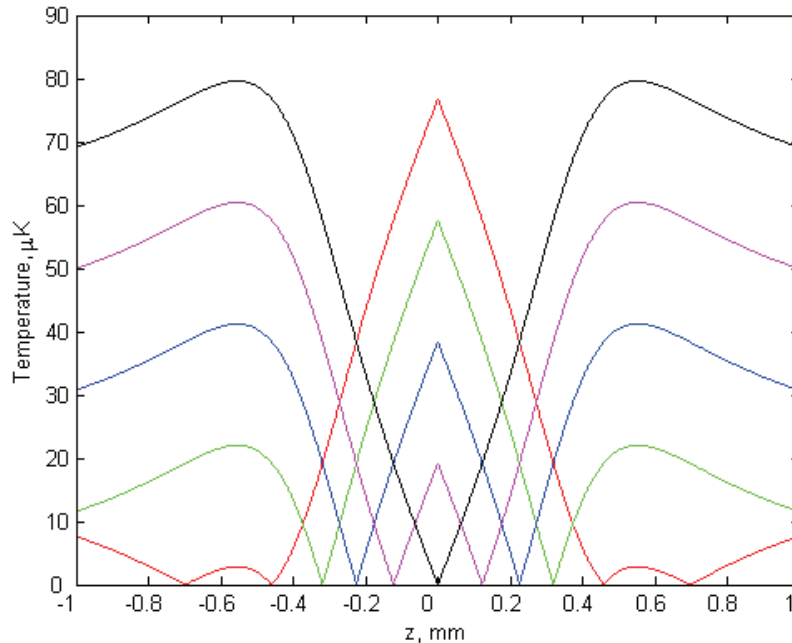


Fig. 2.35. The potential along the z -axis through the centre of the four-wire cell.

Loading of the four-wire cell can be contemplated in several different ways. One possibility is to load the four-wire cell trap with weak-field-seeking atoms by pumping the atoms in along one of the four wires with the other wires inactive. Wires can be made inactive by reducing their DC currents to for example 50 % of their critical values. This will retract the minimum potential manifolds around the wires so much that they don't come anywhere near the minimum potential manifolds around wires that carry DC currents at their critical levels.

When the cold atoms have been moved to one of the four sides in the cell, the DC currents can be slowly increased back to their critical values again in the other three wires. The potential minimum either at the centre or around the centre of the cell should then have been loaded with the low-field-seeking atoms. This technique is most realistic for geometries consisting of a single cell or only a pair of cells since it is difficult to transport atoms to more than one cell at a time along any one of the wires. In practise all the cells in the geometry must be turned on at the same time since they share some of the wires.

A different technique would be to load the four-wire cell with strong-field-seeking atoms by filling the volume containing the trap with a cold

atom condensate. Then the DC and RF currents in the wires can then be slowly turned on and some ground state atoms would then presumably be trapped in the local potential maximum at the centre of the cell. It is not clear whether this technique of loading the cell with ground state atoms can be combined with loading of the cell with weak-field-seeking atoms along one of the wires. The weak-field-seeking atoms would in this case have to be pumped toward a corner of the cell with all four wires carrying DC currents at their critical levels.

Loading of the cell structures has not been explored in simulations because the procedure will be more elaborate than in the case of transferring atoms between crossed wires for example. Eventual results would also be less suitable for easy illustration here. Before more effort is invested in exploring different loading techniques it would be best to have experimental confirmation of especially the four-wire cell's ability to trap different sorts of cold atoms.

Another way of loading cells with cold atoms would be to send the atoms into the centre of the cell through a hollow core optical fibre. Atom transport through hollow core optical fibres has already been demonstrated in [86]. The optical fibres should not affect the magnetic field generated potential, and the fibres could be inserted between the parallel wires, (along the x -axis in Fig. 2.33), or from any direction between the layers of parallel wires. This loading technique would be suitable for geometries with an arbitrary number of cells. Several multi-cell geometries will be described in the following sections of this Chapter. This method of loading the trap can be implemented experimentally without further theoretical consideration.

2.8.1 The four-wire cell and a quadrupolar trap

One possible use of the four-wire cell, which has been described already, is in the exploration of collision and entanglement between strong- and weak-field-seeking atoms. Another possible application, which has been briefly looked at, is to use the four-wire cell in place of a pair of closely spaced bias loops in a quadrupolar trap.

However, because there is an absolute zero in the magnetic field at the centre of the four-wire cell when it is excited by only DC currents, the problem of Majorana spin-flip transitions persists also for the quadrupolar trap when it is combined with the four-wire cell. This makes the use of the four-wire cell less attractive compared to a pair of bias rings, since the bias rings may be used to eliminate the minimum of zero. Because the four-wire

cell is a new concept in combination with a quadrupolar trap, the possible use of the four-wire cell will nevertheless be given a short introduction here.

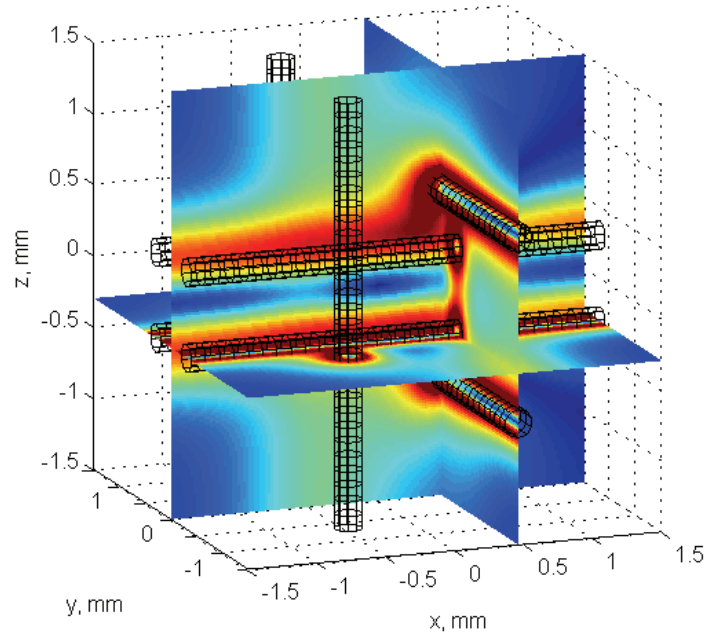
The four-wire cell can be placed either on the outside or on the inside of the four Ioffe-bars in a quadrupolar trap. The effective potential for the four-wire cell placed on the outside of the Ioffe-bars is shown in Fig. 2.36, where only DC excitation has been used. Because the opening between the wires in the four-wire cell described above is very small, a scaled variant of the four-wire cell has been used.

The scaling of the four-wire cell has been done provisionally in the following way. First the distance between the four Ioffe-bars, each with a radius of 0.1 mm, has been set to 0.6 mm. The DC current in the Ioffe-bars has been set to 150 mA. To keep the wires away from the Ioffe-bars the distance d_y , which is half the distance between two parallel wires, has been set to $d_y = 0.65$ mm. The distance d between two parallel wires is given by equation (2.50) for the case of $I_{DC2} = -I_{DC1}$. This equation can be used to find the necessary DC current in the wires of the four-wire cell as follows:

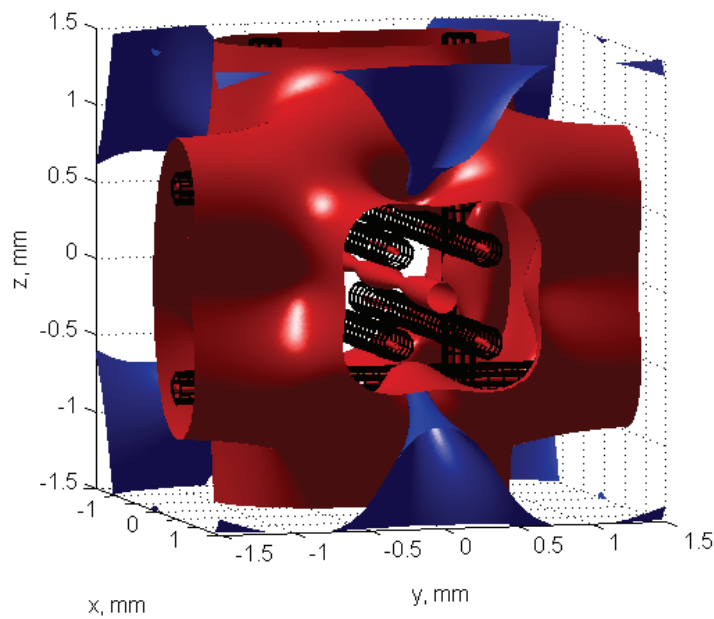
$$|I_{DC}| = \frac{d\omega_{RF}\pi\hbar}{\mu_B g_F \mu_0} = \frac{6.5 \cdot 10^{-4} \text{ m} \cdot 5.027 \cdot 10^6 \text{ rad/s} \cdot \pi \cdot 1.05 \cdot 10^{-34} \text{ Js}}{9.27 \cdot 10^{-24} \text{ J/T} \cdot 0.66 \cdot 4\pi \cdot 10^{-7} \text{ H/m}} = \underline{\underline{140.73 \text{ mA}}}, \quad (2.71)$$

where the frequency has been kept at 0.8 MHz. The distance d_x can be found as $d_x = d_y / \sqrt{2} = 0.65 \text{ mm} / \sqrt{2} = 0.46 \text{ mm}$. The radius of the wires in the four-wire cell has been increased to 0.1 mm. To obtain the best possible result two of the three variables d_x , d_y , or $|I_{DC}|$ should be optimized. Optimization has not been done in this case since this is not necessary to obtain an overview.

Two additional minima are located on both sides of the potential minimum at the centre in Fig. 2.36(a). An Isosurface plot of the potential levels $U_{\text{eff}} = 2\text{e-}28 \text{ J}$ and $U_{\text{eff}} = 8\text{e-}28 \text{ J}$ is provided in Fig. 2.36(b). The channel between the Ioffe-bars through the four-wire cell can be seen in the middle. Just outside of the bars a red lump can be seen on the right side. It contains one of the two additional minima on the inside.



(a)



(b)

Fig. 2.36. The four-wire cell placed on the outside of the Ioffe-bars. (a) A slice-plot view, and (b) the isosurfaces $U_{\text{eff}} = 2e-28$ J (blue) and $U_{\text{eff}} = 8e-28$ J (red).

The effective potential for the four-wire cell placed on the inside of the Ioffe-bars is shown in Fig. 2.37. The same four-wire cell as in Fig. 2.31 has here been used. The DC currents in the wires are also the same and only DC excitation has been applied. The only difference is that the wire radius has been increased to 0.1 mm. The four Ioffe-bars, each with a radius of 0.1 mm, have been placed 1.6 mm apart. The DC current in the Ioffe-bars has been increased to 500 mA in the figure. A branching out of the minimum potential is seen along the channel to the right of the minimum at the centre. The current has therefore been increased in the bars in an attempt to isolate the end points on the branches from the minimum potential channel through the cell.

Graphs of effective potential through the length of the quadrupolar trap, i.e. along the x -axis, for the simulated geometries in Fig. 2.36 and Fig. 2.37 are shown in Fig. 2.38. Note that the graphs are not directly comparable due to the different geometries and DC currents in the four-wire cells. The current in the Ioffe-bars has no effect on the graphs in Fig. 2.38 since the field is zero in the middle between the bars.

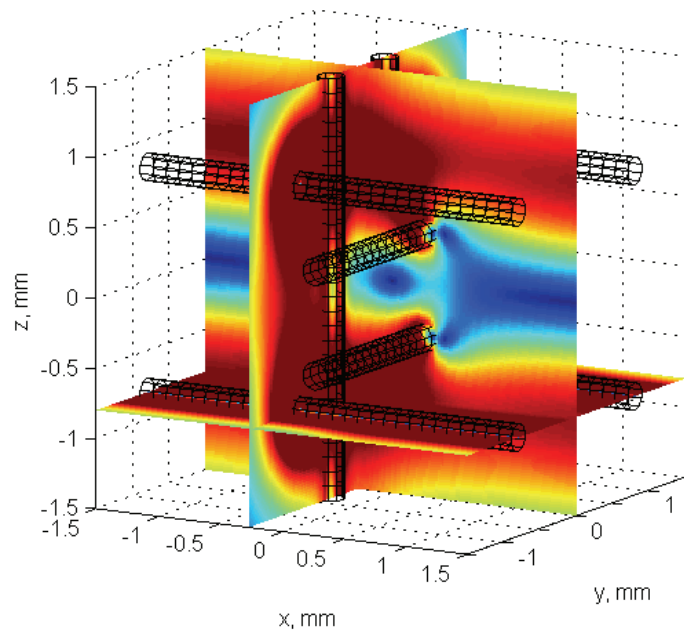


Fig. 2.37. The four-wire cell placed on the inside of the Ioffe-bars.

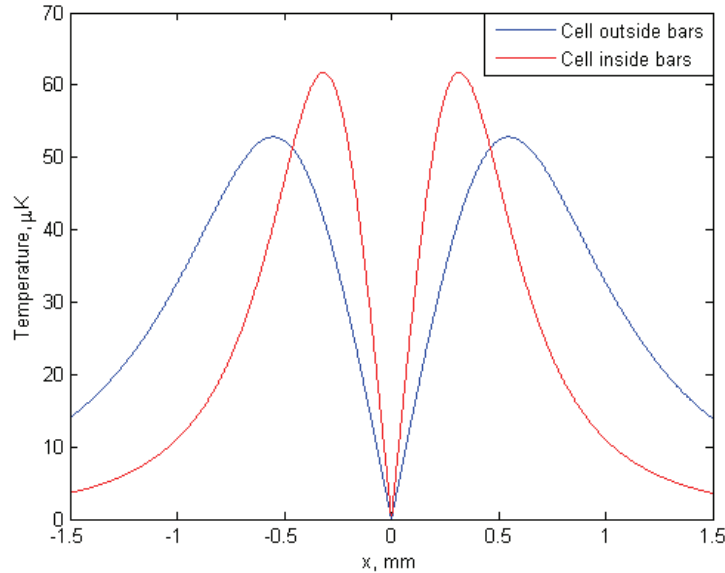


Fig. 2.38. Potential graphs along the x -axis for the geometries in Fig. 2.36 (blue), and Fig. 2.37 (red).

As one might expect the quadrupolar trap becomes tighter with the four-wire cell on the inside of the Ioffe-bars. This follows from that the four-wire cell is physically smaller in this case. An absolute zero in the potential is seen at the centre of the trap. Majorana spin-flip transitions must therefore be prevented either by changing one or more of the currents slightly or by applying an external bias field.

The branching out of the minimum potential in the channel for the four-wire cell on the inside of the Ioffe-bars happens in the orthogonal plane on the opposite side if the DC currents in the Ioffe-bars are reversed. For Ioffe-bar currents of 150 mA the branching of the minimum is illustrated by the blue isosurface in Fig. 2.39. This feature is a serious drawback with placing the four-wire cell on the inside of the bars.

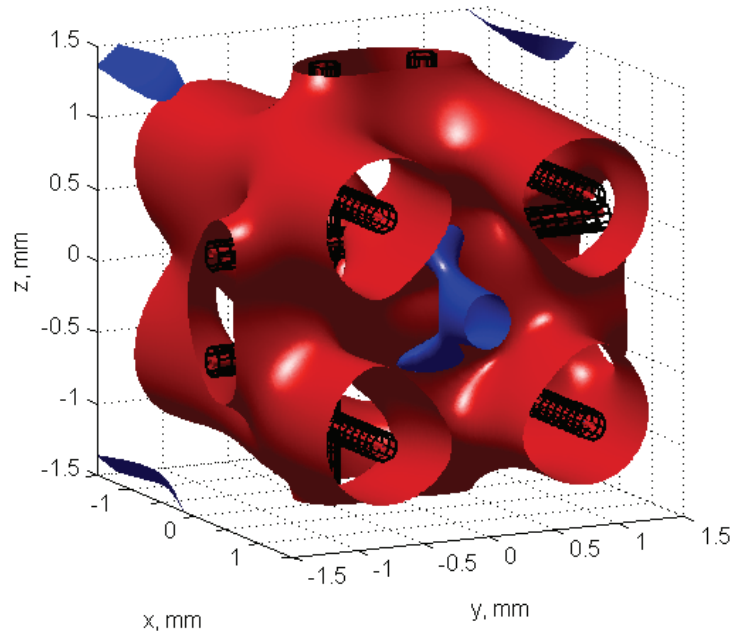


Fig. 2.39. U_{eff} for the geometry in Fig. 2.37 with reduced Ioffe-bar currents. The isosurfaces are $U_{\text{eff}} = 2\text{e-}28$ J (blue) and $U_{\text{eff}} = 8\text{e-}28$ J (red).

Another way of looking at these results is that it should be possible to load the four-wire cell with weak-field-seeking atom condensate by pumping it along the minimum between four Ioffe-bars placed either on the inside or on the outside of the four-wire cell. This is however probably not the most practical way of loading the four-wire cell.

The combined DC and RF excitation of the four-wire cell with Ioffe-bars present has also been briefly explored. As an example the effective potential for the geometry in Fig. 2.36, where the four-wire cell is on the outside of the Ioffe-bars, is shown in Fig. 2.40. The DC currents in the four-wire cell are the same as in Fig. 2.36. The RF current amplitude is 20 mA and the frequency is 0.8 MHz. The DC current in the four Ioffe-bars is 150 mA. The topology of the effective potential exhibits a complicated pattern in three dimensions in this case. The effective potential pattern through the centre of the trap nevertheless shows some similarity to that of an ordinary Ioffe-Pritchard trap excited by both DC and RF currents.

It is interesting to note that only DC currents have been used in the Ioffe-bars in Fig. 2.40. Separate simulations have shown that there is no visible difference to the figure if small RF currents are added in the Ioffe-bars.

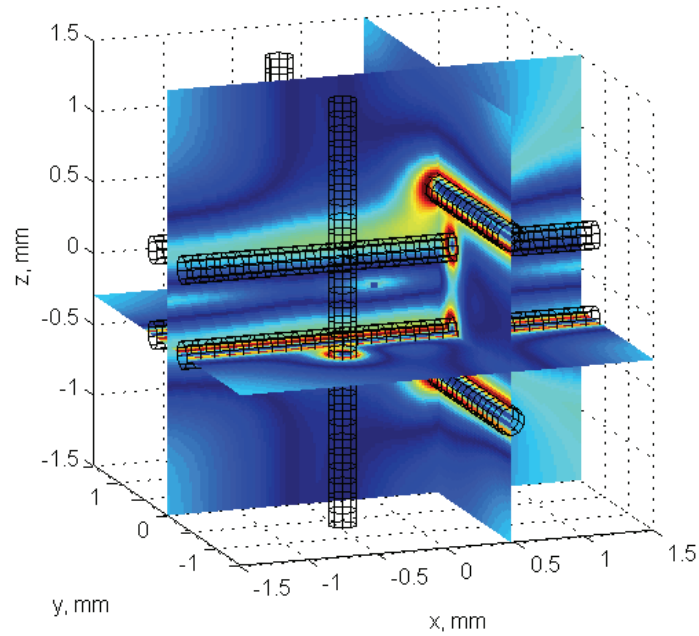


Fig. 2.40. U_{eff} for the geometry in Fig. 2.36 with both DC and RF excitation.

To sum up it should be possible to use the four-wire cell as an alternative to a pair of closely spaced bias rings in a quadrupolar trap. The four-wire cell can be placed either on the outside or on the inside of the Ioffe-bars. The trap becomes tighter when the four-wire cell is placed on the inside of the Ioffe-bars, but a branching of the potential minimum on one side is a major drawback. If the four-wire cell is used with only DC excitation steps must be taken to prevent Majorana spin-flip transitions.

2.9 Single-layered cell-grids

Arrays of multiple cells can be created by adding more parallel wires in both wire-planes. The simplest multi-cell geometry, which consists of 3 x 3 crossed wires, is shown in Fig. 2.41.

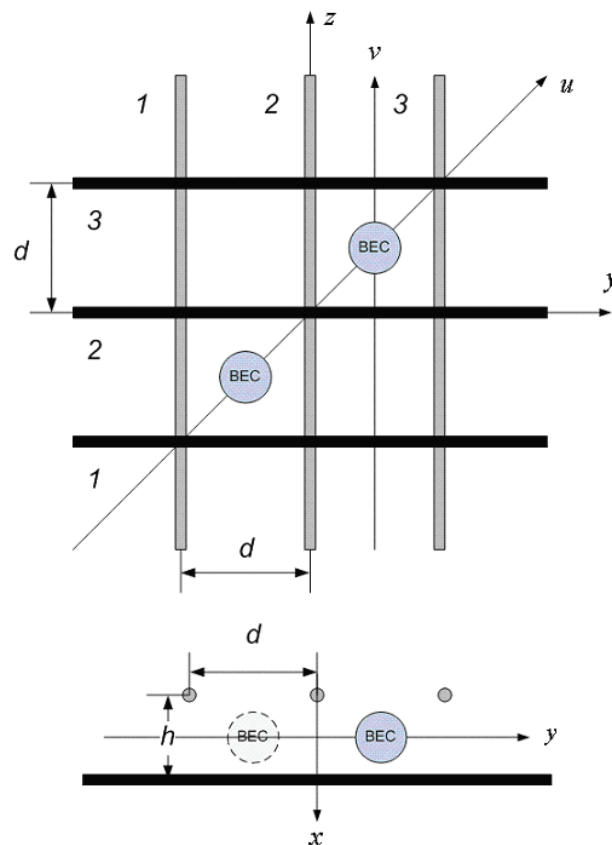


Fig. 2.41. 3 x 3 crossed wires viewed from the side and from above.

The 3 x 3 wire geometry exhibits either two local potential maxima or two potential minima diagonally depending on whether DC + RF excitation or just DC excitation is applied to the wires. The two potential maxima or two potential minima represent potential wells for strong-field-seeking or weak-field-seeking atoms respectively. The two potential wells can subsequently be merged to form a single potential well at the centre of the geometry by reducing the DC currents in the two centre wires. This particular geometry

is therefore interesting for the study of entanglement of BEC matter placed in the two potential wells. If such entanglement of BEC matter takes place, the structure may be used as a matter-wave beam splitter as part of an interferometer [107]. However, a closer study or practical experiments will be needed to properly assess the usefulness of the structure for this purpose.

The 3 x 3 wire geometry also requires optimization to maximize the height of the trapping barrier. In this case three out of the four variables $d_x = h/2$, $d_y = d/2$, $|I_{DC, c-w}|$ or $|I_{DC, p-w}|$ should be optimized. Here $|I_{DC, c-w}|$ is the current in the two centre wires and $|I_{DC, p-w}|$ is the current in the four peripheral wires. The DC currents must be in opposite directions in adjacent parallel wires in each wire-plane.

A 3 x 3 wire geometry of comparable size to the four-wire cell described in Section 2.8 has been studied as an example. The variables $xIz = -d_x$, $dyI = -d_y$, and $IZ2 = |I_{DC, p-w}|$ have been optimized. The DC current in the centre wires $|IZ1| = |I_{DC, c-w}|$ has been kept at 92.5 mA. The optimization technique is otherwise the same as in the case of the four-wire cell. The optimized variables are shown in Table 2.3 together with their values. The table also lists the point where the function for the effective potential has been minimized.

Table 2.3. Defining variables for the three-by-three wire geometry. Three variables have been optimized. The variable $IZ1$ is also listed.

Variable	Value	U_{eff} minimized in point (x, y, z)
$IZ1$	-92.5 mA	Not optimized
$IZ2$	82.1 mA	$0, 2*dyI, 2*dyI$
dyI	-0.346 mm	$xIz, dyI, 0$
xIz	-0.243 mm	$0, 0, 0$

The remaining variables used in the simulation are found from the variables in Table 2.3 from symmetry. They become as follows:

$IZ3 = IZ2$, $IYn = IZn$ for $n = 1 - 3$, $dzI = dyI$ and $xIy = -xIz$. In the case of the DC currents the numbers in the variable names refer to the wires numbered in the positive y -direction or from bottom to top in the following order {3 1 2}.

When combined DC and RF excitation is used two local maxima or peaks in the effective potential appear in one of the two diagonal directions. The signs of the DC currents in the wires in one of the wire-planes determine along which diagonal the peaks appear. A plot of the effective potential in

the yz -plane, which is located at the centre between the two wire-planes at $x = 0$, is shown in Fig. 2.42. The DC wire currents in the figure are $I_{\text{DC}|z\text{-wire}}^{(1-3)} = [82.1, -92.5, 82.1]$ mA and $I_{\text{DC}|y\text{-wire}}^{(1-3)} = [82.1, -92.5, 82.1]$ mA. The RF currents are $I_{\text{RF}|z\text{-wire}}^{(1-3)} = [10, -10, 10]$ mA and $I_{\text{RF}|y\text{-wire}}^{(1-3)} = [10, -10, 10]$ mA. $f_{\text{RF}} = 0.8$ MHz. The distance $d = -2 \cdot dy l = -2 \cdot dz l = 0.692$ mm and the distance $h = -2 \cdot xl z = 0.486$ mm. The radius of the wires is 57.2 μm .

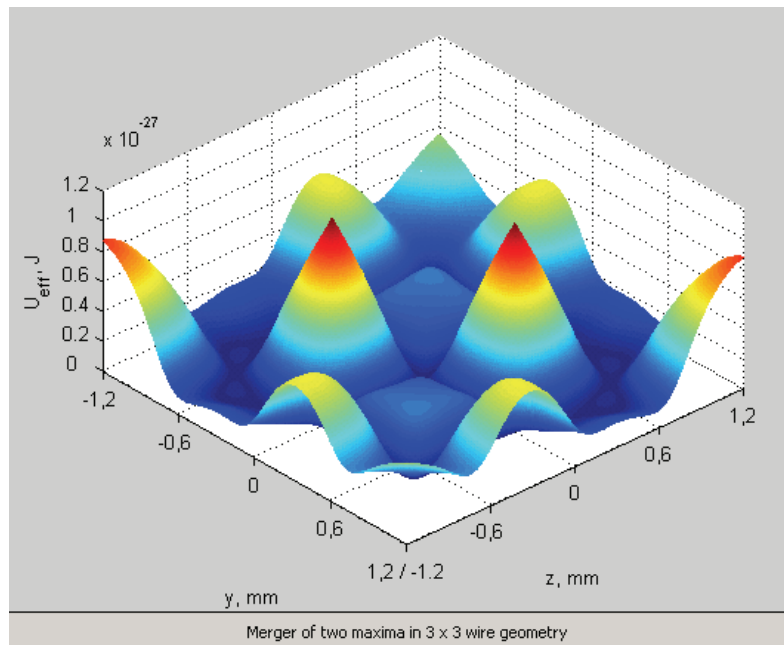


Fig. 2.42. Animation showing merger of two potential maxima.

Fig. 2.42 is also an animation which shows the merger of the two peaks into a single maximum at the centre of the geometry. This is accomplished by reducing the DC current in the centre wires. The DC currents in the centre wires in the nine frames in the animation are: $|I_{\text{DC},c-w}^{(2)}| = [92.5, 69.4, 46.3, 23.1, 9.25, 23.1, 46.3, 69.4, 92.5]$ mA. The DC current is negative in the centre wire in both the z -direction and the y -direction.

The mid-frame in the animation is shown in Fig. 2.43. The effective potential here forms a single maximum at the centre. What this 2D plot

does not reveal is the shape of the potential in the perpendicular x -direction. A 3D figure of the effective potential is therefore provided in Fig. 2.44. This figure shows that the effective potential is much higher around the centre wires in the x -direction. This greatly reduces the height of the potential barrier in this direction.

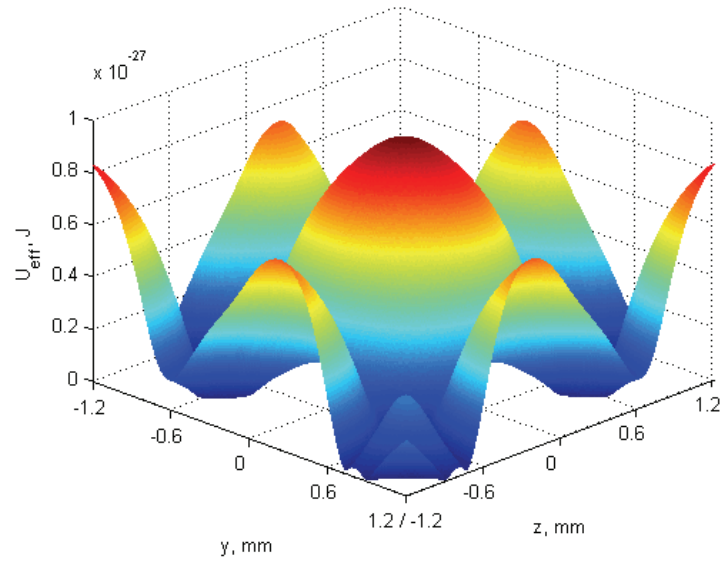


Fig. 2.43. The merged potential maximum in the yz -plane.

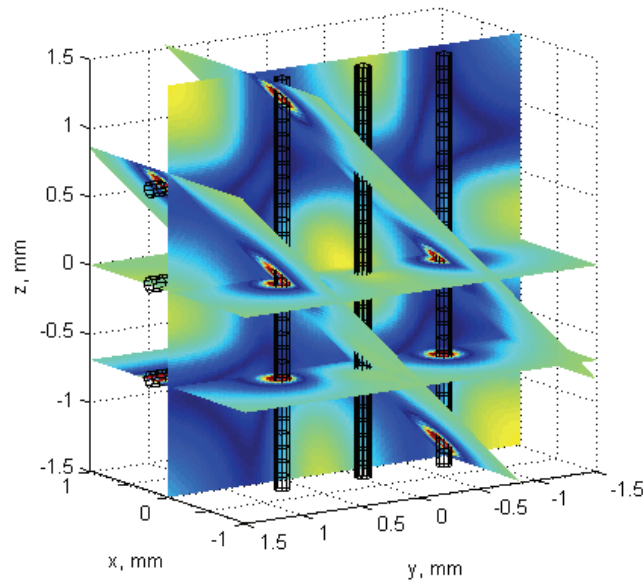


Fig. 2.44. The merged potential maximum in a 3D perspective.

In order to quantify the magnitude of the trapping potential, graphs of the effective potential have been calculated along the lines labelled u and v in Fig. 2.41 as well as in the x -direction through the point where the lines u and v intersect and in the x -direction through the mid-point of the geometry. These graphs are shown in Fig. 2.45 to Fig. 2.48.

The graphs show the temperature potential in Kelvin, which is simply the effective potential divided by Boltzmann's constant. The red graphs correspond to the initial situation in Fig. 2.42 with two peaks diagonally and the black graphs correspond to a single maximum at the centre of the geometry. The dotted blue graphs, the dashed green graphs and the dash-dotted magenta graphs correspond to frames 2 – 4 in the animation in Fig. 2.42, and indicate the transition in going from the red to the black graphs.

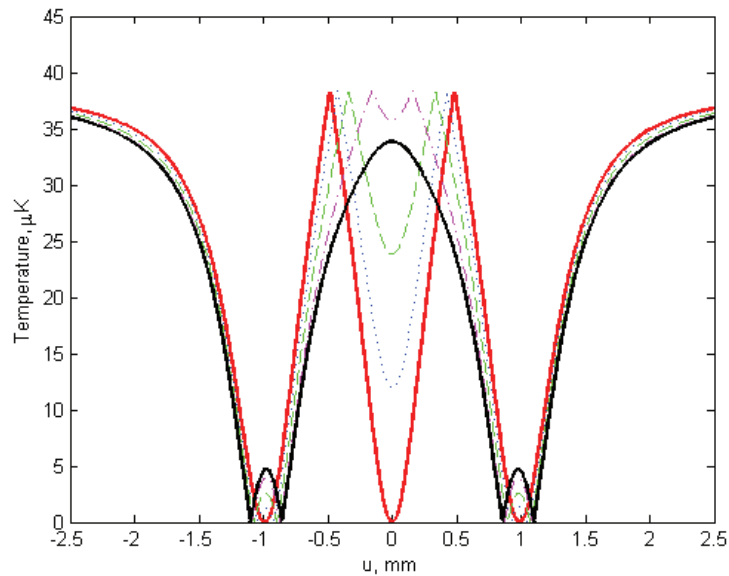


Fig. 2.45. The effective potential along the line u in Fig. 2.41 for $x = 0$.

Because the peaks in the effective potential in Fig. 2.45 – Fig. 2.48 attract strong-field-seeking atoms, the graphs have been calculated using the magnetic quantum number for strong-field-seeking atoms, i.e. $m_F = 1$ in equation (2.1). Note that the positions of the peaks of the red graph are minutely displaced from the centres of the two diagonal cells. This is thought to be caused by the diagonal symmetry of the effective potential pattern for the geometry as a whole. The structure has been optimized for the initial situation of two peaks in the effective potential. When the DC currents in the centre wires are reduced the match in the minima next to the

merging peaks at the centre gets progressively worse. This explains the small lobes next to the single maximum in Fig. 2.45.

The potential along the line v in Fig. 2.41 is shown in Fig. 2.46. For the red graph a small maximum can be seen in the cells without the peaks. These small maxima are not thought to pose a problem. In any case there is little that can be done to minimize them since they are part of the overall effective potential pattern. The black graph only slices through the single central maximum near the edge and is therefore of limited interest.

Fig. 2.47 shows that the potential barrier is smaller in the x -direction for the red graph than it was in the v - and u -directions. The difference here is about $10 \mu\text{K}$. Again the black graph slices through the single central maximum in the periphery and provides little extra information.

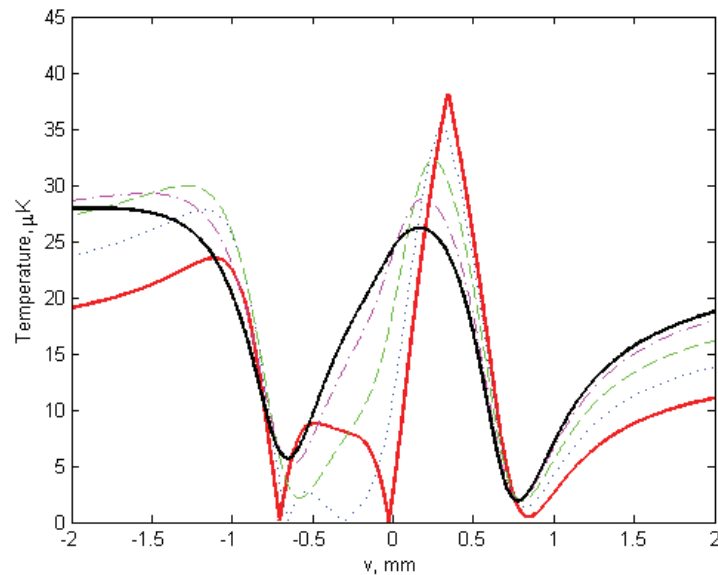


Fig. 2.46. The effective potential along the line v in Fig. 2.41 for $x = 0$.

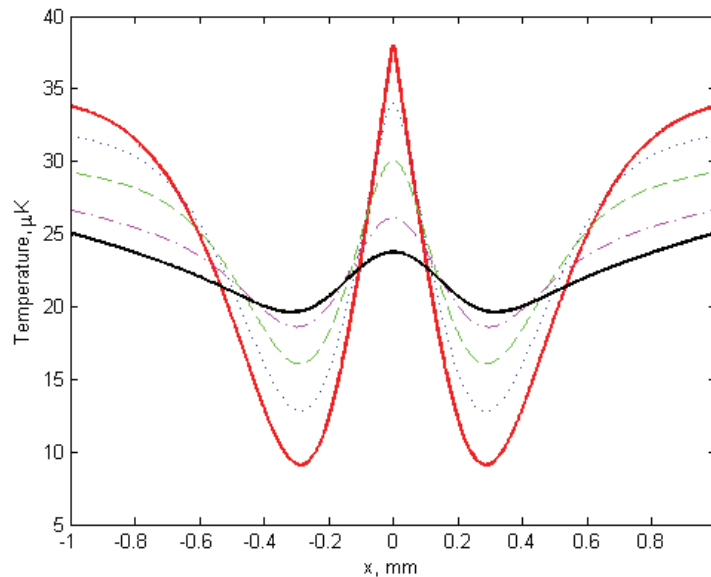


Fig. 2.47. The effective potential in the x -direction through the point where the lines u and v intersect in Fig. 2.41.

The main weakness of this design can be seen in the plot of the potential in the x -direction through the point where the centre wires intersect in Fig. 2.48. Because the DC current has been reduced to 10 % of its value before the merger of the two peaks started, the potential does not drop very much around and outside of the centre wires. The potential barrier for the black graph measured from the centre-point to the dips around the wires is only about 9.6 μK . One should in fact instead look at the potential to the side of the centre wires as shown in Fig. 2.44. Here the potential appears to be higher than in the minimum around the centre wires, and so the potential barrier would be even lower. This makes it difficult to trap strong-field-seeking atoms in the merged potential maximum at the centre unless something is done to make the potential barrier larger. It may for example not be necessary to reduce the DC current quite down to 10 % for the two peaks to have merged completely.

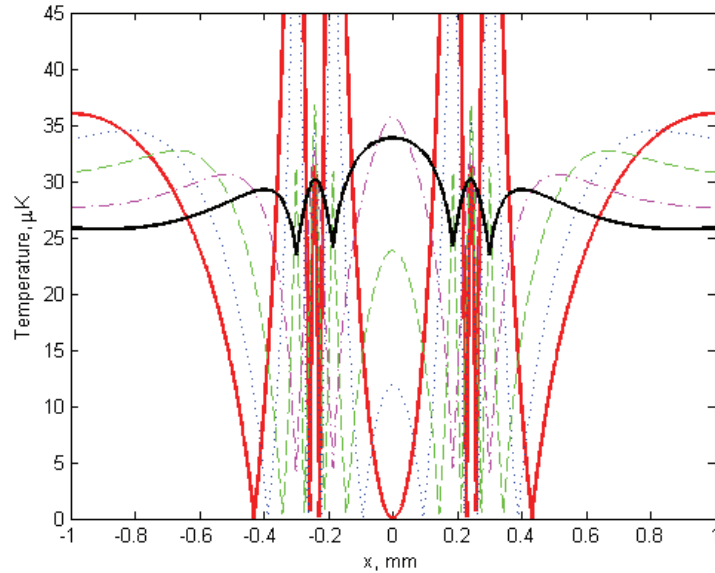


Fig. 2.48. The effective potential in the x -direction through the point where the centre wires intersect in Fig. 2.41.

In the next Chapter a micrometre-sized 3×3 wire structure will be shown. Here the potential barrier is considerably higher. The height of the barrier depends on the distance from the wire surfaces to the atom condensates that is chosen when the scaling of the trap is done. The current magnitude in the wires may also be very important in this context.

When the 3×3 wire geometry in Fig. 2.41 is excited only by DC currents two potential minima appear along one of the diagonals instead of the peaks. This is illustrated in Fig. 2.49. The small potential maxima along the other diagonal in Fig. 2.42 are still there however, and have not been turned into shallow minima. So the potential landscape is not exactly inverted. Since the potential minima attract weak-field-seeking atoms $m_F = 2$ must now be used in equation (2.1).

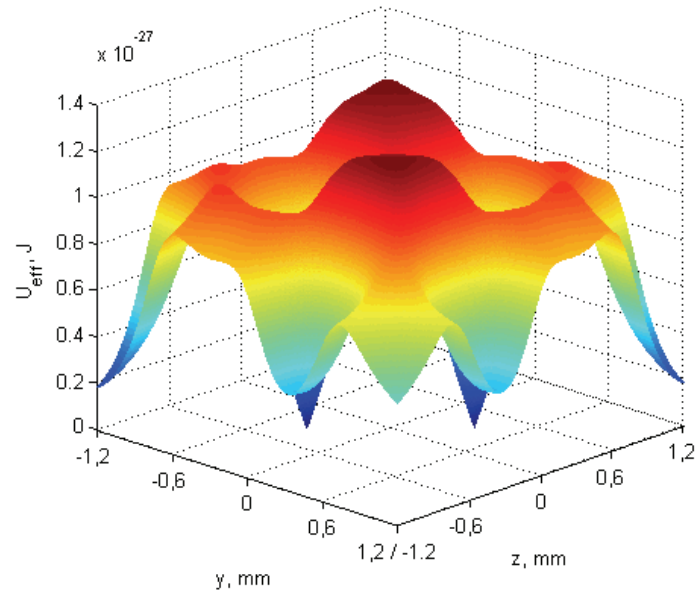


Fig. 2.49. Potential minima in the yz -plane with only DC excitation.

Graphs of the effective potential have also in this case been calculated along the lines u and v and in the x -direction through the points where the lines u and v intersect and where the centre wires intersect. The graphs have been calculated using the magnetic quantum number for weak-field-seeking atoms ($m_F = 2$). The blue graph along the line u in Fig. 2.50 shows the two potential wells. The two minima are also here minutely offset from the centres of the two diagonal cells. The reason for this may be the diagonal symmetry seen in the overall effective potential. The two minima have so far not been seen to be absolute zeros in the potential. However, because the exact positions of the minima are not known it is difficult to confirm this definitely.

The dotted red graphs, the dashed green graphs and the dash-dotted magenta graphs indicate the potential when the DC current in the two centre wires has been reduced to 75 %, 50 % and 25 % respectively of its original value, just as in the figures for combined DC and RF excitation. Note that the potential barrier in Fig. 2.50 – Fig. 2.53 is twice as high as in the case of combined DC and RF excitation. This is for the most part due to the use of different magnetic quantum numbers. In Fig. 2.53 the height of the potential barrier measured between the mid-point on the black graph and one of the small peaks next to the wires is about $21.2 \mu\text{K}$. This is much better than in the case of combined DC and RF excitation in Fig. 2.48.

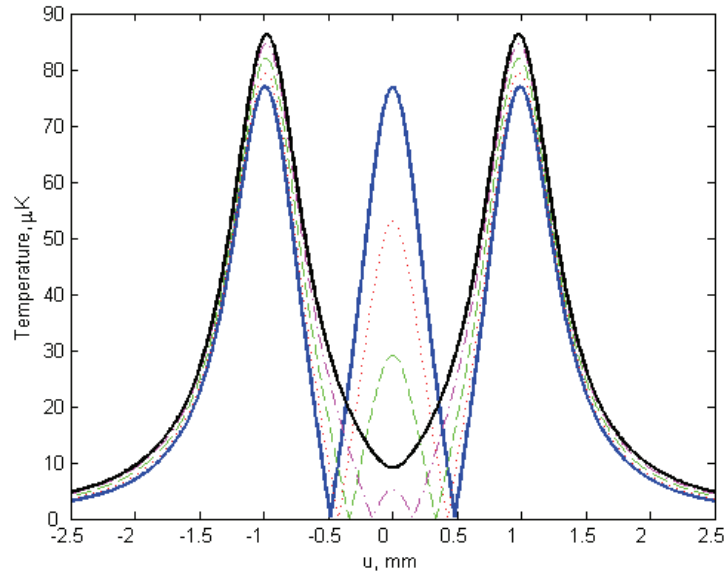


Fig. 2.50. The effective potential with only DC excitation along the line u shown in Fig. 2.41 for $x = 0$.

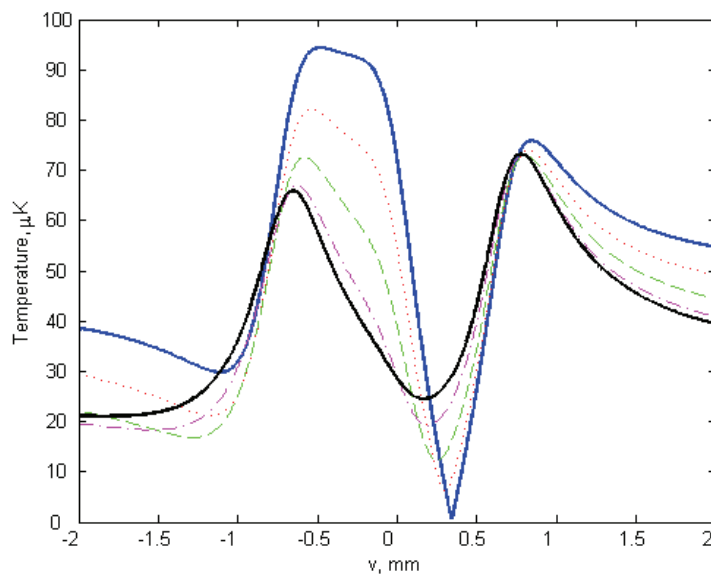


Fig. 2.51. The effective potential with only DC excitation along the line v shown in Fig. 2.41 for $x = 0$.

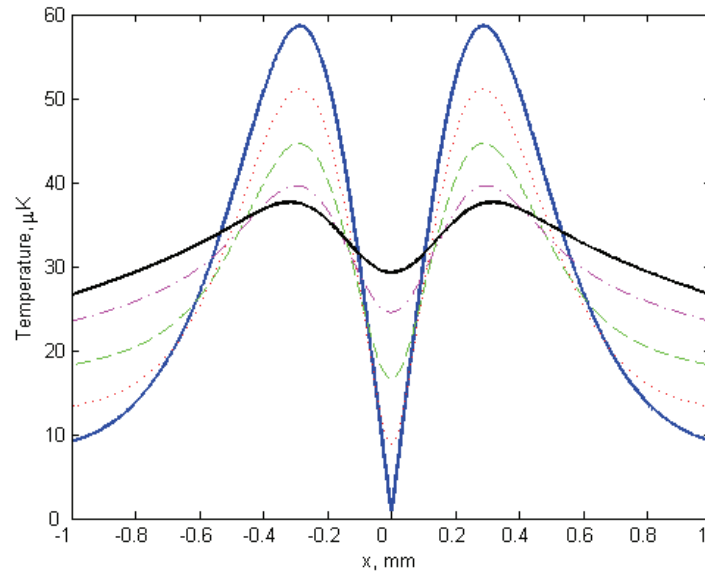


Fig. 2.52. The effective potential with only DC excitation in the x -direction through the point where the lines u and v intersect in Fig. 2.41.

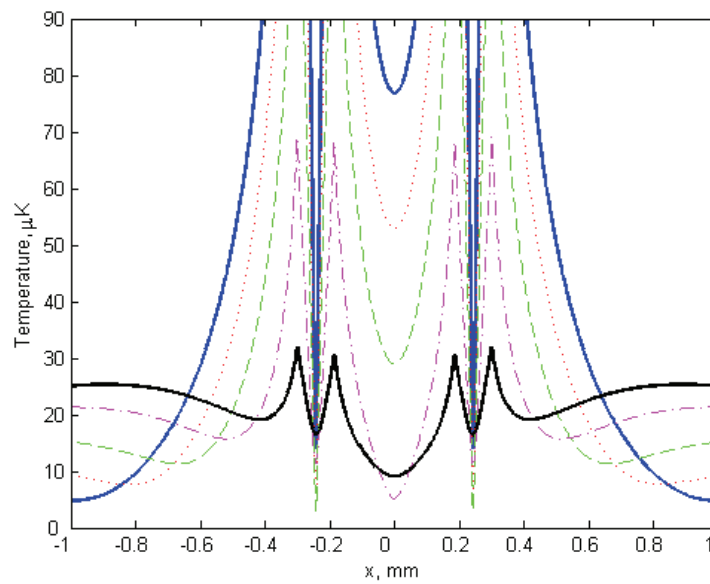


Fig. 2.53. The effective potential with only DC excitation in the x -direction through the point where the centre wires intersect in Fig. 2.41.

Another geometry that has been studied is that of 6 x 6 intersecting wires. The geometry, which is shown in Fig. 2.54, is obtained by simply adding three extra parallel wires in each of the two wire-planes in Fig. 2.41.

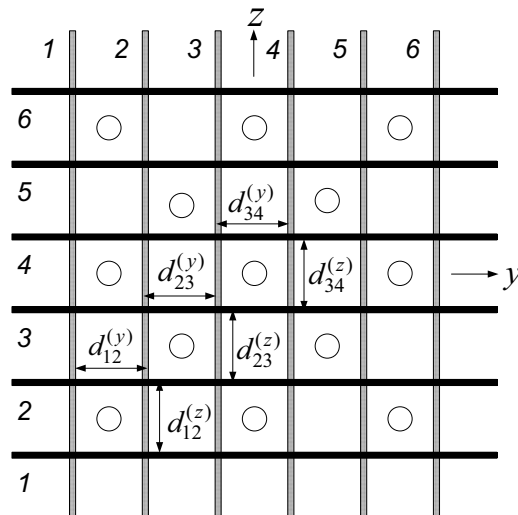


Fig. 2.54. Cell-grid consisting of 6 x 6 wires. Local potential maxima are indicated with circles.

The effective potential for the 6 x 6 wire structure is shown in the yz -plane in Fig. 2.55. The yz -plane in the figure lies at the centre between the two wire-planes. The effective potential is seen to have peaks in a chequered pattern, with a peak in every other cell position. A reversed pattern with peaks in the cell positions without peaks in Fig. 2.55 can also be created if the directions of the DC currents in the wires in one of the wire-planes are reversed.

A different perspective on the pattern of peaks is given by the plot of the effective potential level $9e-29$ J in Fig. 2.56. The peaks in the effective potential are here located in the openings between the wires. It is also clear that the potential surfaces close around pairs of wires where they emerge from the grid in an extension of the potential pattern seen within the grid.

Altogether six variables have been optimized for the 6 x 6 wire cell-grid in Fig. 2.55 and Fig. 2.56. The variables are listed in Table 2.4 along with their values and the point where the effective potential function has been minimized. The optimization technique is the same as for the four-wire cell and the 3 x 3 wire geometry. The variables $IZ3$ and $IZ5$ are the DC current magnitudes in the second outermost and the outermost wires in each wire-

plane. The variables $dy1$, $dy3$ and $dy5$ are the distances from the symmetry line of each wire-plane to the innermost, second outermost and outermost wire pairs respectively. $x1z = h/2$ sets the distance between the wire-planes.

Table 2.4. Optimized variables for the cell-grid in Fig. 2.54. A total of six variables have been optimized. The variable $IZ1$ is also shown.

Variable	Value	U_{eff} minimized in point (x, y, z)
$(IZ1)$	-92.5 mA	Not optimized
$IZ3$	93.0 mA	0, $dy3$, $dy1$
$IZ5$	-82.6 mA	0, $dy5$, $dy1$
$dy1$	-0.343 mm	$x1z$, 0, $dy1$
$dy3$	-1.03 mm	$x1z$, $(dy3-0.5*(dy3-dy1))$, $dy1$
$dy5$	-1.73 mm	$x1z$, $(dy5-0.5*(dy5-dy3))$, $dy1$
$x1z$	-0.247 mm	0, $dy1$, $dy1$

All of the other DC currents and distances used in the simulation can be found from the variables in Table 2.4. The remaining DC currents become $IZn = -IZ(n-1)$ for $n = \{2, 4, 6\}$ and $IYn = IZn$ for $n = 1 - 6$. The remaining distances are found as $dyn = -dy(n-1)$ for $n = \{2, 4, 6\}$ and $dzn = dyn$ for $n = 1 - 6$. $x1y = -x1z$. The wires have here been numbered in the positive y -direction or from bottom to top in the order $\{5\ 3\ 1\ 2\ 4\ 6\}$.

In Fig. 2.54 the wires are numbered sequentially from left to right and from bottom to top. Relative to this figure the DC currents in the six wires in each wire-plane become as follows:

$$I_{\text{DC}|z\text{-wire}}^{(1-6)} = [-82.6, 93.0, -92.5, 92.5, -93.0, 82.6] \text{ mA and}$$

$$I_{\text{DC}|y\text{-wire}}^{(1-6)} = [-82.6, 93.0, -92.5, 92.5, -93.0, 82.6] \text{ mA.}$$

The RF currents are $I_{\text{RF}|z\text{-wire}}^{(1-6)} = [-10, 10, -10, 10, -10, 10] \text{ mA and}$

$$I_{\text{RF}|y\text{-wire}}^{(1-6)} = [-10, 10, -10, 10, -10, 10] \text{ mA. } f_{\text{RF}} = 0.8 \text{ MHz.}$$

The distances shown in Fig. 2.54 are found as $d_{12} = |dy5| - |dy3| = 0.701 \text{ mm}$, $d_{23} = |dy3| - |dy1| = 0.684 \text{ mm}$ and $d_{34} = 2 \cdot |dy1| = 0.687 \text{ mm}$. The distance between the two wire-planes becomes $h = 2 \cdot |x1z| = 0.493 \text{ mm}$.

The inter-wire spacing resulting from the optimization is seen to differ by less than 2.5 %. It is therefore a good question whether uniform inter-wire spacing could work just as well. With the simple optimization technique

used the best result is however obtained by including all three distances $dy1$, $dy3$ and $dy5$ in the optimization instead of just the distance $dy1$. The optimization of both the inter-wire distances and the currents in the two outermost wires in each wire-plane thus appears to guide the optimization script toward a better solution.

In a practical realization it may be convenient to use a substrate with a specific thickness. In this case the DC current magnitude in the innermost wires in each wire-plane $|Iz|$ should be optimized instead of xIz .

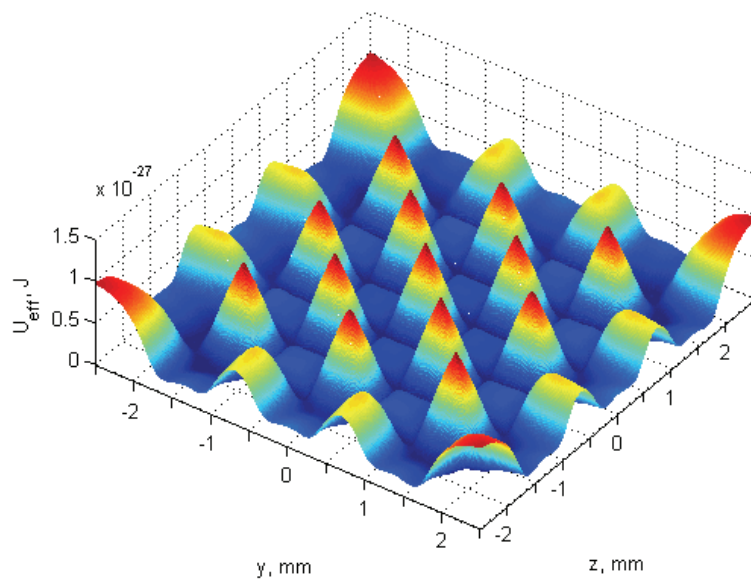


Fig. 2.55. The effective potential generated by DC and RF currents in a 6 x 6 wire structure. In the figure $x = 0$.

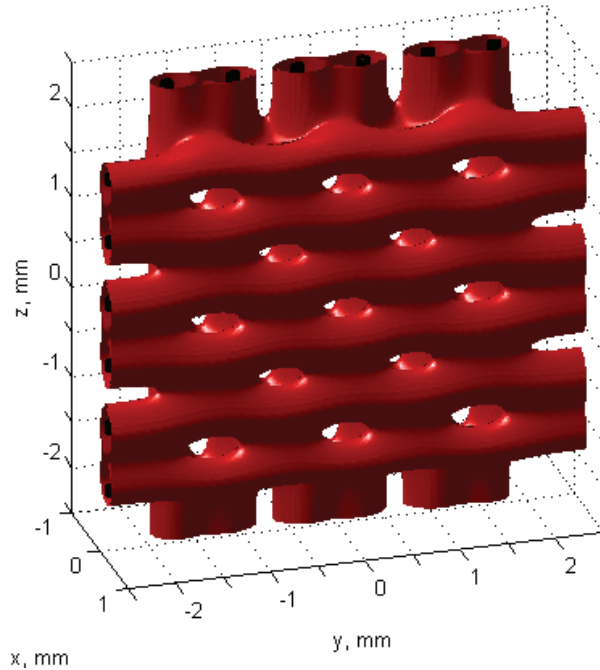


Fig. 2.56. The isosurface $U_{\text{eff}} = 9\text{e-}29$ J for the 6 x 6 wire structure with DC and RF excitation.

If only the DC currents are applied to the 6 x 6 wire structure in Fig. 2.55 and Fig. 2.56, the effective potential in the yz -plane becomes as shown in Fig. 2.57. The figure shows as expected a larger pattern of the same kind as previously shown in Fig. 2.49 for the 3 x 3 wire geometry. There are not thought to be any absolute zeros in the effective potential in Fig. 2.57. Cross-interference between the cells and a not quite perfect optimization seems to raise the potential minima above zero and thus limit the possibility of Majorana spin-flip transitions. It is however difficult to be absolutely certain of this since the effective potential is close to zero especially in the cell at the centre.

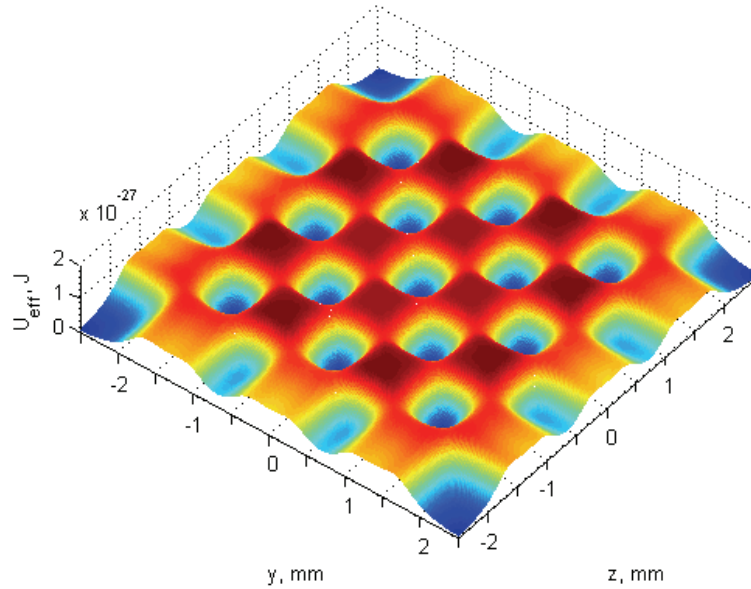


Fig. 2.57. The effective potential generated by DC currents in the 6 x 6 wire structure.

The 6 x 6 wire structure forms a multi-cell grid that could find use in the making of a quantum register with increased noise immunity. As seen in Fig. 2.55 and in Fig. 2.57 only half the cell positions have a peak or minimum in the effective potential which makes them usable. This cell-grid and the multi-layered cell-grids in Section 2.10 have an effective potential pattern that should be made use of as it is in an eventual application. For example, the 6 x 6 wire structure is not well suited for merging BEC condensates in adjacent potential peaks or minima. This is because each wire is shared between several cells. Attempts to merge two peaks or minima distort the effective potential in other cells so that only a few of the cells become usable. The only operation that can be controlled electrically for all cells is to turn the potential maxima into potential minima by reducing the frequency and turning down the RF currents.

2.10 Multi-layered cell-grids

Cell-grids such as those described in the previous section can be stacked in multiple layers. This may find application in the making of volume compact quantum registers. The stacking of cell-grids is straightforward in principle. The only thing to keep in mind is that the DC current should be reversed in corresponding parallel wires in neighbouring layers just like in the case of adjacent parallel wires in each wire-plane. This was at first not thought to be necessary but is in fact important to keep the layers from interfering with each other.

As an example, the effective potential surface $U_{\text{eff}} = 9\text{e-}29$ J for two stacked 6 x 6 wire cell-grids is depicted in Fig. 2.58. The difficulty here lies in the optimization of inter-wire distances and the DC wire currents. This two-layer geometry requires that both cell-grid layers be considered together for the optimization to be successful. The complete geometry consists of two inner wire rows and two outer wire rows which are significantly different in terms of surrounding topology.

The variables that have been optimized for this geometry are shown in Table 2.5. The table also lists their values and the point where the effective potential function has been minimized. The variables $IZ3$, $IZ5$, $dy1$, $dy3$ and $dy5$ pertain to the inner wire rows and the variables $IY3$, $IY5$, $dz1$, $dz3$ and $dz5$ are associated with the outer wire rows. The distances between the wire rows have been optimized through the variables $x1z$, $x2z$ and $x3z$. $2 \cdot |x1z|$ is here the distance between the outer wire rows and the closest of the inner wire rows and $x3z - x1z$ is the distance between the two inner wire rows. The variable $x2z$ has also been optimized but it is not independent and could equally well have been calculated as $x2z = 2 \cdot x1z - x3z$.

Similar to the case of the 6 x 6 wire geometry the distance from the symmetry line of each wire row to the innermost wires is $dy1$ or $dz1$. The distance from the symmetry line to the second outermost wires is $dy3$ or $dz3$ and the distance from the symmetry line to the outermost wires is $dy5$ or $dz5$. The distances $dy1$, $dy3$ and $dy5$ here apply to the two inner wire-planes and the distances $dz1$, $dz3$ and $dz5$ apply to the outer wire-planes.

The DC current magnitude in the innermost wires in each wire plane is similarly $|IZ1|$ or $|IY1|$. The DC current magnitudes in the second outermost and outermost wires are $|IZ3|$ or $|IY3|$ and $|IZ5|$ or $|IY5|$ respectively. The variables $IZ1$, $IZ3$ and $IZ5$ here apply to the two inner wire-planes and the variables $IY1$, $IY3$ and $IY5$ apply to the two outer wire-planes.

Table 2.5. Optimized variables for the cell-grid structure in Fig. 2.58. A total of fourteen variables have been optimized. The variable $IZ1$ is also listed.

Variable	Value	U_{eff} minimized in point (x, y, z)
$(IZ1)$	-92.5 mA	Not optimized
$IZ3$	94.4 mA	$(-x3z-0.5*(-x3z-x1z)), dy3, dz1$
$IZ5$	-76.7 mA	$(-x3z-0.5*(-x3z-x1z)), dy5, dz1$
$IY1$	-98.1 mA	Scaled only with $IY3$ and $IY5$
$IY3$	99.6 mA	$0, dy1, dz3$
$IY5$	-82.4 mA	$0, dy1, dz5$
$dy1$	-0.354 mm	$x1z, 0, dy1$
$dy3$	-1.08 mm	$x1z, (dy3-0.5*(dy3-dy1)), dy1$
$dy5$	-1.78 mm	$x1z, (dy5-0.5*(dy5-dy3)), dy1$
$dz1$	-0.357 mm	$-x1z, dy1, 0$
$dz3$	-1.07 mm	$-x1z, dy1, (dz3-0.5*(dz3-dz1))$
$dz5$	-1.78 mm	$-x1z, dy1, (dz5-0.5*(dz5-dz3))$
$x1z$	-0.262 mm	$0, dy1, dy1$
$x2z$	-1.32 mm	$(-x3z+0.5*(x2z+x3z)), dy1, dz1$
$x3z$	0.795 mm	$(-x1z+0.5*(x3z+x1z)), dy1, dz1$

The other DC currents and distances used in the simulation are found from symmetry from the variables in Table 2.5. The remaining DC currents become $IZn = -IZ(n-1)$ for $n = \{2, 4, 6\}$ and $IYn = -IY(n-1)$ for $n = \{2, 4, 6\}$ for the cell-grid in front in Fig. 2.58 (g1). $IZn = -IY(n-6)$ for $n = 7 - 12$ and $IYn = -IZ(n-6)$ for $n = 7 - 12$ for the cell-grid to the rear in Fig. 2.58 (g2).

The remaining distances are found as $dyn = -dy(n-1)$ for $n = \{2, 4, 6\}$ and $dz n = -dz(n-1)$ for $n = \{2, 4, 6\}$ for the cell-grid in front in Fig. 2.58 (g1). $dyn = dz(n-6)$ for $n = 7 - 12$ and $dz n = dy(n-6)$ for $n = 7 - 12$ for the cell-grid to the rear in Fig. 2.58 (g2). $x1y = -x1z$. The variable $x3z$ is used to find $x2y$, which is equal to $-x3z$. The wires have here been numbered in the positive y -direction or from bottom to top in the order $\{5\ 3\ 1\ 2\ 4\ 6\}$ for cell-grid one (g1) and in the order $\{11\ 9\ 7\ 8\ 10\ 12\}$ for cell-grid two (g2).

The wire currents in the four wire-planes can be summed up as follows:

$$I_{\text{DC}|z\text{-wire}, g1}^{(1-6)} = [-76.7, 94.4, -92.5, 92.5, -94.4, 76.7] \text{ mA},$$

$$I_{\text{DC}|y\text{-wire}, g1}^{(1-6)} = [-82.4, 99.6, -98.1, 98.1, -99.6, 82.4] \text{ mA},$$

$$I_{\text{DC}|z\text{-wire}, g2}^{(1-6)} = [82.4, -99.6, 98.1, -98.1, 99.6, -82.4] \text{ mA},$$

$$I_{\text{DC}|y\text{-wire},g2}^{(1-6)} = [76.7, -94.4, 92.5, -92.5, 94.4, -76.7] \text{ mA},$$

where g1 refers to the cell-grid in front in Fig. 2.58 and g2 refers to the cell-grid to the rear. The wires are here numbered from left to right and from bottom to top. The RF currents are 10 mA of the same sign as the DC current in each wire. The frequency is $f_{\text{RF}} = 0.8 \text{ MHz}$.

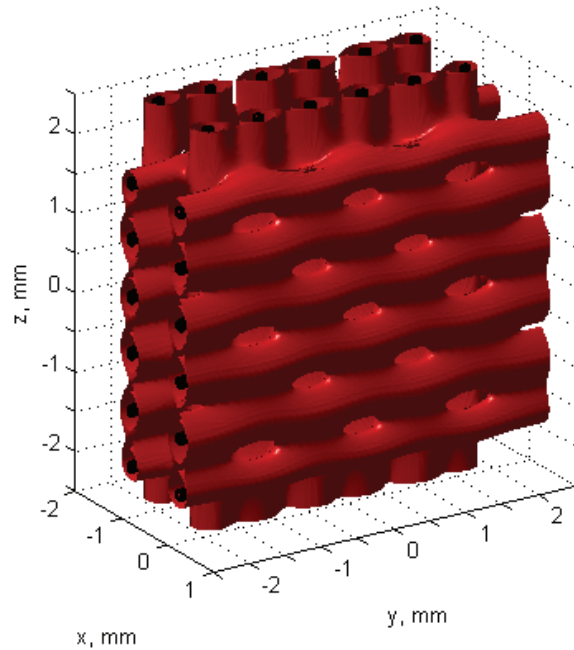


Fig. 2.58. The isosurface $U_{\text{eff}} = 9\text{e-}29 \text{ J}$ for a 24 wire structure with DC and RF excitation.

The distances $dz5$ and $dy5$ have become as good as identical. This is an intended result of a modification to the optimization script. Inside the while-loop, after the calls to the function “fminbnd” for all variables, the optimized currents $IY1$, $IY3$ and $IY5$ have been scaled up or down with each iteration of the while-loop depending on whether $dz5$ is greater than or equal to $dy5$ or smaller than $dy5$ respectively. The scaling factor is 1.02 or 0.98 to begin with. With the onset of toggling between up-scaling and down-scaling the increment or decrement is halved every time a toggle occurs until the scaling factor becomes less than $1 \pm 1\text{e-}10$, after which the scaling is stopped. The Matlab code for current scaling in the optimization script is as follows:

Definitions before the while-loop:

```
increase_factor=1.02;
decrease_factor=0.98;
prev_factor=increase_factor;
```

Code appended inside the while-loop:

```
if dz5>=dy5    % Note that dz5 and dy5 are both negative
  if prev_factor==decrease_factor
    increase_factor=increase_factor-0.5*(increase_factor-1);
  end
  if increase_factor>=(1+1e-10)
    IY1=IY1*increase_factor;
    IY3=IY3*increase_factor;
    IY5=IY5*increase_factor;
    prev_factor=increase_factor;
  else
    disp('Currents have converged');
  end
else
  if prev_factor==increase_factor
    decrease_factor=decrease_factor+0.5*(1-decrease_factor);
  end
  if decrease_factor<=(1-1e-10)
    IY1=IY1*decrease_factor;
    IY3=IY3*decrease_factor;
    IY5=IY5*decrease_factor;
    prev_factor=decrease_factor;
  else
    disp('Currents have converged');
  end
end
end
```

The while-loop has here been repeated 200 times compared to just 20 times for the four-wire cell because of the greater number of variables. It is possible to scale either $IY1$, $IY3$ and $IY5$ or $IZ1$, $IZ3$ and $IZ5$ in this way but not both. The while-loop should be iterated enough times for the scaling of the currents to converge on its specified accuracy. This modification helps to stabilize the optimization script and prevents the spacing between wires in the outer and inner wire rows from differing more than necessary.

It is seen that the distances dy_n and dz_n for $n = \{1, 3, 5\}$ differ by at most just over one percent, which is very little. Furthermore the difference between $dy3$ and $dz3$ calculated as $dy3 = dz3 = 3 \cdot dy1$ or $dy5$ and $dz5$ calculated as $dy5 = dz5 = 5 \cdot dy1$ and the optimized values for the same variables is at most about one and a half percent. It therefore looks as if the same inter-wire spacing can be used for both the inner and outer wire rows. A uniform inter-wire spacing based on the optimization of just one distance should also be possible.

Unfortunately, because of the rather simple optimization technique used, the best solution is not found by optimizing only the currents $IZ3$, $IZ5$, $IY1$, $IY3$, $IY5$, the distance $dy1$ or $dz1$ and the distances $x1z$ and $x3z$. The optimization script must be allowed to adjust both the distances between the wires and the currents in most of the wires to converge on a good solution. Otherwise it is not able to detect, for example, if the current magnitude for the variables $IY1$, $IY3$ and $IY5$ has become too high or too low relative to the current magnitude for the variables $IZ3$ and $IZ5$. It thus becomes more difficult to take into account dependencies between variables when uniform inter-wire spacing is used.

Three cell grids can also be stacked as shown in Fig. 2.59 and Fig. 2.60. Fig. 2.59 shows the effective potential surface $U_{\text{eff}} = 9\text{e-}29$ J and Fig. 2.60 the effective potential in slices placed at $x = 0$, $x = -x2z$, $y = 0$, $y = -dy5$, $z = dy5$ and $z = 0$.

For the cell grid in the middle the wire rows lie symmetrically inside the geometry and can therefore share one set of optimized variables. In Fig. 2.59 and Fig. 2.60 the variables $IZ3$, $IZ5$, $dy1$, $dy3$ and $dy5$, have been optimized for these wire rows. The DC current magnitude in the innermost wires has been kept at $|IZ1| = 92.5$ mA. The distance variables $dy1$, $dy3$ and $dy5$ have the same definition as in the case of the two stacked wire grids in Fig. 2.58. The letters y or Z and the numbers in the variable names may be interpreted as follows. For distance variables “ y ” refers to y -axis displacement and for current variables “ Z ” is the pointing direction of the wire for which the current is defined. The numbers refer to the wires in each row numbered in the positive y -direction or from bottom to top in the following order $\{5\ 3\ 1\ 2\ 4\ 6\}$.

A separate set of variables has been optimized for the two outermost wire rows in the geometry. These are $IZ7$, $IZ9$, $IZ11$, $dy7$, $dy9$ and $dy11$. The numbers 7-12 here relate to the wires in the cell-grid (g2) seen in the foreground in Fig. 2.59. The wires in the cell-grid in the middle (g1) have the numbers 1-6 and the wires in the cell-grid at the back (g3) have the numbers 13-18. However, for this cell-grid (g3) the variables are found from the cell-grid in front (g2) from symmetry.

In the same manner as for the two stacked wire grids in Fig. 2.58, the currents $IZ7$, $IZ9$ and $IZ11$ have been scaled up or down with each iteration of the while-loop depending on whether $dy11$ is greater than or equal to $dy5$ or smaller than $dy5$ respectively. (The expression “if $dz5 \geq dy5$ ” in the code excerpt on page 167 is simply replaced with “if $dy11 \geq dy5$ ” and the variables $IY1$, $IY3$ and $IY5$ are replaced with $IZ7$, $IZ9$ and $IZ11$ respectively.

Since $dy11$ and $dy5$ are also here both negative numbers no other changes are necessary.) As already mentioned only one set of currents may be scaled in this way. Otherwise the optimization will not converge.

The relevant variables for the two second outermost wire rows in the geometry have been optimized only in part. The DC currents in the second outermost ($IY9$) and outermost ($IY11$) wires have been optimized, while the DC current in the innermost wires ($IY7$) has been set equal to $IZ1$. The distance variables have been set equal to those for the cell-grid at the centre, i.e. $dz7 = dy1$, $dz9 = dy3$ and $dz11 = dy5$. Attempts to include $dz7$, $dz9$, $dz11$ and $IY7$ among the optimized variables have caused the optimization script to latch on to a bad solution for some of the variables, and this effectively ruins the entire optimization.

The distances between the wire rows have been optimized through the variables $x1z$, $x2z$ and $x3z$. The variable $x1z$ is the distance from the symmetry plane ($x = 0$) through the centre of the geometry to the wire row pointing in the z -direction in cell-grid one (g1). $x2z$ and $x3z$ are the distances from the symmetry plane to the wire rows pointing in the z -direction in cell-grids two and three respectively. All the variables that have been optimized are listed in Table 2.6 together with their values and the point where the effective potential function has been minimized.

Table 2.6. Defining variables for the cell-grid structure in Fig. 2.59. Altogether 16 variables have been optimized. The variables $IZ1$, $IY7$, $dz7$, $dz9$ and $dz11$ have also been listed to give a more complete picture.

Variable	Value	U_{eff} minimized in point (x, y, z)
$(IZ1)$	-92.5 mA	Not optimized
$IZ3$	93.0 mA	0, $dy3$, $dy1$
$IZ5$	-79.3 mA	0, $dy5$, $dy1$
$IZ7$	96.1 mA	Scaled only with $IZ9$ and $IZ11$
$IZ9$	-95.9 mA	$(-x3z+0.5*(x2z+x3z))$, $dy9$, $dz7$
$IZ11$	83.7 mA	$(-x3z+0.5*(x2z+x3z))$, $dy11$, $dz7$
$(IY7)$	Set equal to $-IZ1$	Not optimized
$IY9$	-93.3 mA	$(-x3z+0.5*(x2z+x3z))$, $dy7$, $dz9$
$IY11$	85.4 mA	$(-x3z+0.5*(x2z+x3z))$, $dy7$, $dz11$
$dy1$	-0.348 mm	$x1z$, 0, $dy1$
$dy3$	-1.04 mm	$x1z$, $(dy3-0.5*(dy3-dy1))$, $dy1$
$dy5$	-1.73 mm	$x1z$, $(dy5-0.5*(dy5-dy3))$, $dy1$
$dy7$	-0.348 mm	$x2z$, 0, $dz7$

$dy9$	-1.05 mm	$x2z, (dy9-0.5*(dy9-dy7)), dz7$
$dy11$	-1.73 mm	$x2z, (dy11-0.5*(dy11-dy9)), dz7$
$(dz7)$	Set equal to $dy1$	Not optimized
$(dz9)$	Set equal to $dy3$	Not optimized
$(dz11)$	Set equal to $dy5$	Not optimized
$x1z$	-0.261 mm	$0, dy1, dy1$
$x2z$	-1.30 mm	$(-x3z+0.5*(x2z+x3z)), dy7, dz7$
$x3z$	0.784 mm	$(-x1z+0.5*(x3z+x1z)), dy7, dz7$

The remaining DC currents and distances are found from the optimized variables in Table 2.6 by making use of symmetry. The remaining DC currents are found as follows: $Izn = -IZ(n-1)$ for $n = \{2, 4, 6, 8, 10, 12\}$, $IYn = Izn$ for $n = 1 - 6$. $IY8 = -IY7$, $IY10 = -IY9$ and $IY12 = -IY11$. $Izn = IY(n-6)$ for $n = 13 - 18$ and $IYn = IZ(n-6)$ for $n = 13 - 18$.

The remaining distances are found as: $dyn = -dy(n-1)$ for $n = \{2, 4, 6, 8, 10, 12\}$ and $dz n = dyn$ for $n = 1 - 6$. $dz8 = -dz7$, $dz10 = -dz9$ and $dz12 = -dz11$. $dyn = dz(n-6)$ for $n = 13 - 18$ and $dz n = dy(n-6)$ for $n = 13 - 18$. The distances from the symmetry plane ($x = 0$) to the wire rows pointing in the y -direction are found from symmetry to be $x1y = -x1z$, $x2y = -x3z$ and $x3y = -x2z$.

The wire currents in the six wire-planes can be summarized as follows:

$$I_{DC|z-wire, g1}^{(1-6)} = [-79.3, 93.0, -92.5, 92.5, -93.0, 79.3] \text{ mA},$$

$$I_{DC|y-wire, g1}^{(1-6)} = [-79.3, 93.0, -92.5, 92.5, -93.0, 79.3] \text{ mA},$$

$$I_{DC|z-wire, g2}^{(1-6)} = [83.7, -95.9, 96.1, -96.1, 95.9, -83.7] \text{ mA},$$

$$I_{DC|y-wire, g2}^{(1-6)} = [85.4, -93.3, 92.5, -92.5, 93.3, -85.4] \text{ mA},$$

$$I_{DC|z-wire, g3}^{(1-6)} = [85.4, -93.3, 92.5, -92.5, 93.3, -85.4] \text{ mA},$$

$$I_{DC|y-wire, g3}^{(1-6)} = [83.7, -95.9, 96.1, -96.1, 95.9, -83.7] \text{ mA},$$

where $g1$ refers to the cell-grid in the middle in Fig. 2.59, $g2$ refers to the cell-grid seen in front (where the x -values are negative) and $g3$ to the cell-grid at the back. The wires are here numbered sequentially in the positive y -direction or from bottom to top. The RF currents are 10 mA of the same sign as the DC current in each wire. The frequency is $f_{RF} = 0.8$ MHz.

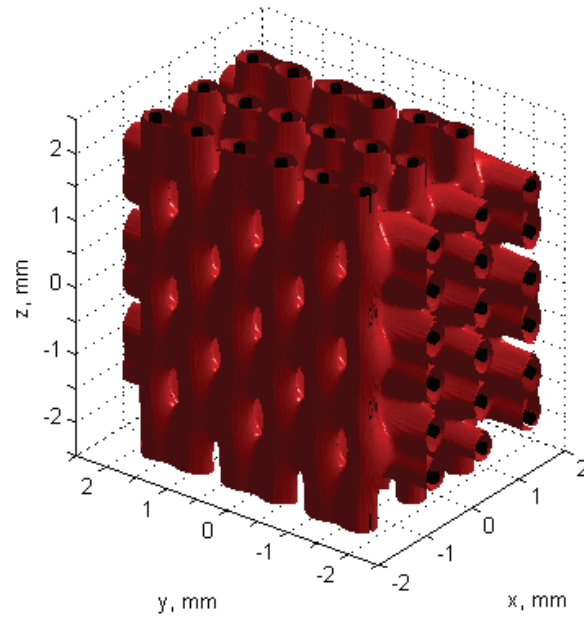


Fig. 2.59. The isosurface $U_{\text{eff}} = 9e-29$ J for a 36 wire structure with DC and RF excitation.

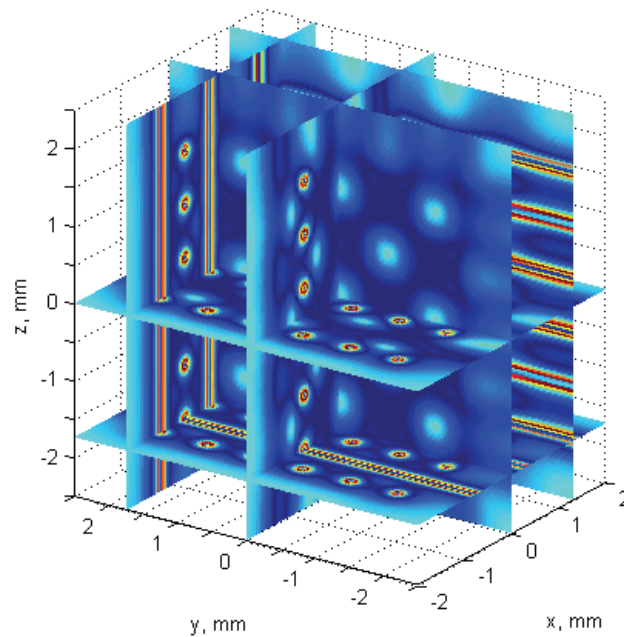


Fig. 2.60. The effective potential generated by DC and RF currents in the 36 wire structure.

The slice of the effective potential for $y = 0$ in Fig. 2.60 is shown separately in Fig. 2.61. In this figure it can be seen that the potential barrier is increased in the x -direction between the parallel wires for cells surrounded by other cells within the geometry. For cells along the periphery the depth of the minimum is reduced in the outward facing direction.

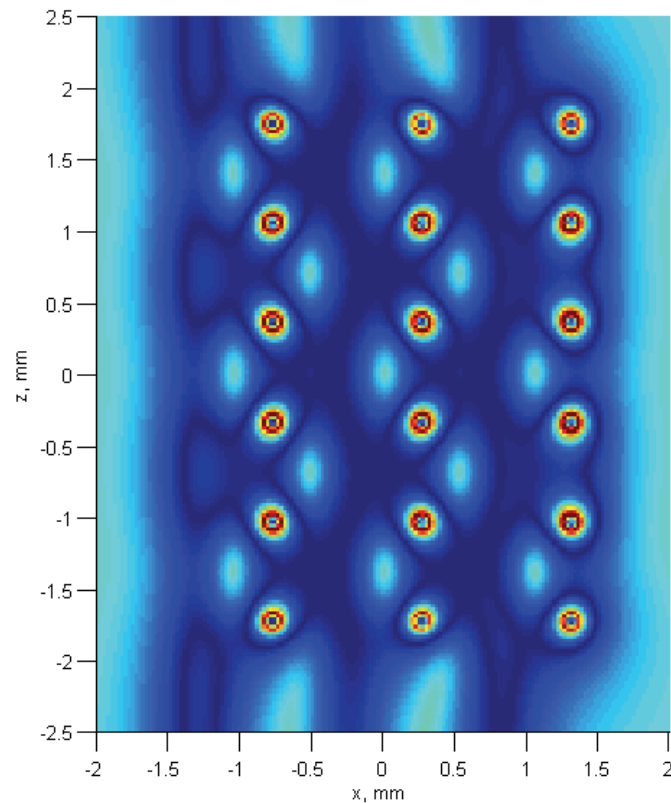


Fig. 2.61. The effective potential slice for $y = 0$ in Fig. 2.60 shown by itself.

Within the potential minimum meandering down between the two rows of wires in the y -direction on the right side of Fig. 2.61 several lighter blue patches are visible. This may suggest that the optimization is not as good as it could have been. One may suspect that x^2z and the variables for the outer wire layers have ended up with sub-optimal values. For the time being it is difficult to see what can be done about this, if the optimized pattern can be improved at all. The lighter blue bumps appear away from the points where the effective potential function is minimized and can not be seen in graphs along the axes either. The same lighter patches are also present in the slice

of the effective potential for $z = 0$, which is a mirror image of Fig. 2.61 with the y -axis replacing the z -axis.

In the case of especially the multi-layered cell-grids the optimization scheme based on the function “fminbnd” has been found to be simplistic and consequently unstable. If too many variables are optimized or a wrong combination of variables is chosen for optimization the optimization script will give a bad solution for one or more of the variables. If a variable fails to converge this is simply overlooked and the optimization continues for the other variables. In this case the upper or lower bound is often returned for the variable that has not converged. It is therefore necessary to visually check the solution for the optimized variables afterwards by computing the effective potential for the whole structure.

The major limitations of the optimization scheme used are that all variables are optimized one at a time (mostly) and that the optimization is done by only considering a single geometric point for each variable. In addition there is no mechanism for restarting or correcting the optimization for a variable if it has first come away from an optimal solution.

To allow the optimization script to adjust for the inter-dependence of the DC current level in the wires between different wire-rows it has been necessary to optimize both the distances between parallel wires and the DC currents in the wires to obtain a consistently good solution. Extra variables have in this way been introduced to stabilize the optimization and to improve the solution for the optimized variables. The disadvantage of this is that the geometric complexity increases needlessly. A better and more powerful optimization technique can hopefully be found later. The main goal has here been to explore the possibilities of the different wire geometries. The efforts made within the topic of optimization have therefore been limited.

The stacked layers of cell grids can also display potential minima in the cells when the wires are excited by only the DC currents, just as in the case of a single cell grid. This is illustrated in Fig. 2.62 for the geometry in Fig. 2.59 – Fig. 2.61. If only cell grids with potential minima are needed it is expected that optimization of the geometry is less important. The potential minima should then form for a wide range of currents similar to the potential minimum between the Ioffe-bars in an Ioffe-Pritchard trap.

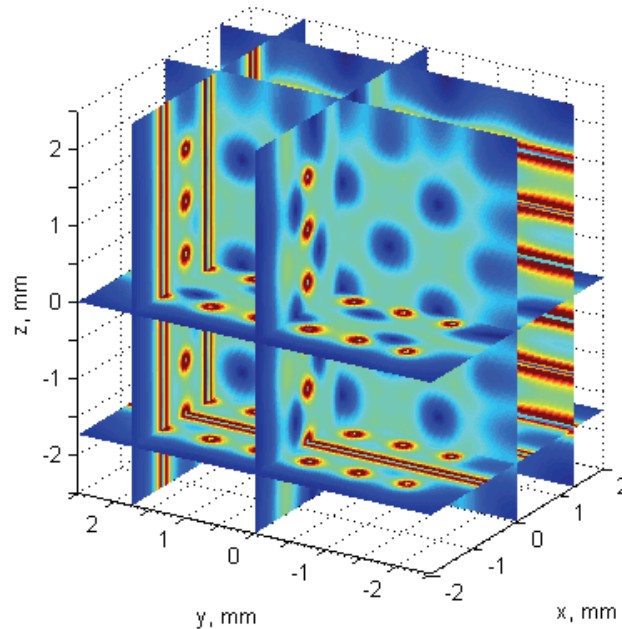


Fig. 2.62. The effective potential generated by just the DC currents in the 36 wire structure.

The possibility of transferring atoms between two crossed wires near the centre of the 36 wire geometry in Fig. 2.59 has been looked at briefly. For this the DC current magnitude in all other wires was reduced to 50 %. Although atom transfer between the crossed wires seems to be possible the fact that the crossing point of the wires is no longer right at the centre between the bias rings causes much trouble. To compensate for the displacement ($dy1$ or $dz1$) of the crossed wires from the mid-point between the bias rings the bias currents must be increased many-fold in the bias rings that are farthest away. Such very high currents are not possible in practise.

The very high bias-currents also distort the effective potential topology elsewhere within the geometry so that trapped atoms can not be held in cells located anywhere near the bias rings. This makes the practical utilization of the structure as a whole very low. In the case of atom transfer between crossed wires that are displaced even further from the mid-point between the bias rings, the currents in the bias rings would become hopelessly large. Atom transfer between crossed wires inside large cell-grids is accordingly not practical in any sense.

2.11 Conclusion

In this Chapter a one-wire atom guide and several traps for cold matter consisting of parallel and crossing wires have been developed. The traps include a four-wire cell with a potential peak or well at its centre, a 3 x 3 wire structure with a double peak or well potential and cell-grids containing multiple traps.

Analytical equations have been derived for the distance d to the cylindrical minimum-potential manifold around a single wire and between two crossed and two parallel wires. These equations define the one-wire guide and the systems of two crossed and two parallel wires. The equations have in addition been used to find initial values for the distances between the wires in the optimization routine for the traps and cell-grids. It has also been shown analytically that the RF current amplitude does not change the effective potential along a line between two crossed or two parallel wires if the DC and RF current magnitudes are the same in both wires. The equations for the distance d , where the minimum potential manifolds around the wires touch, can in this case be derived using only the first term under the root sign in equation (2.1).

Computations of the effective potential in Matlab have yielded a series of interesting results. For the one-wire guide it has been shown that there exists a cylindrical minimum-potential manifold around a wire excited by DC and RF currents. A minimum of zero of the effective potential is removed by placing a pair of bias rings around the wire. The currents in the bias rings should be RF currents, at least predominantly. Small DC current offsets may be used in addition. The bias rings can also be used to move the resulting circular potential minimum up or down along the wire by changing the magnitudes of the RF currents in the bias rings.

For a system of two crossed wires it has been shown the minimum potential surfaces around the wires touch for certain critical values of the DC currents in the two wires. It is often most convenient to use the same DC current magnitude in the two wires, but different combinations are possible. The RF currents should be of the same magnitude and frequency to avoid distortion. RF currents of different frequencies can not be studied at present because equation (2.1) is no longer valid. Simulations have been performed in Matlab which indicate that clouds of cold atoms can be transferred between the wires at the touching point of the minimum potential surfaces by changing the magnitudes of the RF currents in the bias rings around the wires.

In a system of two parallel wires the minimum potential surfaces around the wires also touch for certain critical values of the DC currents. The DC currents should in this case be in opposite directions in the two wires. It may be possible to transfer clouds of cold atoms directly between two parallel wires, but because this appears to require a pair of bias rings around each of the wires it is most likely not worthwhile to do in practice.

A four-wire cell trap made from two pairs of parallel wires which cross in different planes has been designed and simulated. The structure has been optimized using a Matlab routine based on the function ‘fminbnd’. The four-wire cell can be used to trap both weak- and strong-field-seeking atoms and may also allow a study of collision and entanglement between the two types of atoms. If only DC excitation is applied the four-wire cell becomes a trap for weak-field-seeking atoms. In this case a zero potential minimum is known to exist at the centre. The four-wire cell trap as presented here is not quite complete and ready to use. Measures must be taken to mask the sharp minimum potential regions. Otherwise weak-field-seeking atoms will be lost to Majorana transitions there. The sharp minima are in part supported by perfect accuracy in distances and currents as well as a precise optimization. To raise the minimum potential level different steps may be taken. One can reduce the accuracy in currents and wire positions (which will certainly happen in practice to some extent), introduce distortion in the form of a small RF phase shift in the wires or use bias rings around the wires. The relative advantages of the different options have so far not been studied.

A geometry consisting of three-by-three crossed wires forms a two-peak or two-well potential that is prospective for the study of entanglement of BEC matter placed in the potential peaks or wells. The structure could be used as a matter-wave beam splitter, but further work and experiments are necessary to determine the applicability of the structure for this purpose.

Multiple parallel wires that cross in two wire-planes make a grid of cells that can trap either strong- or weak-field-seeking atoms. Potential minima are found at the centre of the cells when the wires carry only DC currents. Cell-grids of this kind may find use as part of a quantum register. Multiple cell-grids can be stacked which enables them to be 3D integrated. Several distances and currents must be optimized in the cell-grids so that potential minima form in the right places in between the different cells. The optimization of stacked cell-grids poses a challenge. The optimization technique that has been applied has shown itself to be too simple and this limits the quality of the solution for the optimized variables. The emphasis has however here been on determining the realizable potential of the

different wire structures and not on the development of different optimization techniques.

The wire grids will most likely also require steps to be taken to raise the level of the potential minimum. Reduced accuracy in currents and distances, the introduction of small RF phase shifts and the use of a small external bias are again possible options. The external bias should in this case be applied in the direction perpendicular to the wire-planes. The bias field should preferably also be made uniform.

Chapter 3

Micrometre and Nanometre Scale Structures

3.1 Introduction

In this Chapter many of the wire geometries described in Chapter 2 will be scaled down to micrometre and nanometre sizes. The downscaling can be done with little effort using the equations derived in Chapter 2. When the dimensions become very small wires must however be replaced by micro-wires or carbon nanotubes (CN's). Each reference to a wire in Chapter 2 may thus be extended to apply to a conductor of any type.

The Chapter begins by showing how scaling to micrometre size may be done. Two examples of micron sized structures are then provided, a four-micro-wire cell and a three-by-three micro-wire structure. The two structures have been optimized to come close to a future practical realization on a micro-machined substrate. To make a final design either analytical equations for the magnetic field for a conductor with a rectangular cross-section or a suitable simulation program is needed. It may also be necessary to consider substrate effects.

The Chapter continues by describing scaling to nanometre size. When the dimensions become very small physical effects, such as the Casimir-Polder force, must be taken into account. The Casimir-Polder force limits how close to the conductors the cold atom clouds can be placed. This in turn reduces the depth of the atom trap unless currents can be increased through the use of bundled nanotubes.

Many of the structures from Chapter 2 are subsequently demonstrated on a nanometre scale. First the anticipated cold atom transfer between two crossed nanotubes is detailed. An optimized four-nanotube cell is then described. It can be compared with the micrometre- and millimetre-sized

four-wire cells described earlier. Nanotubes can also be used to make cell-grids, and an optimized nanotube cell-grid is defined. Finally it is shown how nanotube cell-grids can be stacked, just as in the case of millimetre sized wire-grids.

3.2 Scaling to micrometre size

When structures are scaled down to micrometre size it becomes important to keep cold atom condensates at a certain minimum distance from the conductor surfaces to avoid thermally-induced spin-flip transitions. Resistive noise in the conductors, caused by a finite conductivity, leads to electromagnetic-field fluctuations that can be strong enough to drive spin transitions, which in turn lead to trapping losses [118], [149], [150].

In the case of a micrometre sized structure the cold atoms should be kept at least 30 – 40 μm away from the conductor surfaces at all times. This minimum distance depends to some extent on the quality of the micro-wires. It is important that the surfaces of the micro-wires are smooth and that the conductivity is good to reduce the problem of thermally-induced spin transitions.

The minimum distance from the centre of the conductor to the (circular) potential minimum around it is the distance given above plus one conductor radius. The effective potential minimum comes closest to the surface of a single conductor with no other current carrying conductors nearby. The presence of additional crossing or parallel current carrying conductors has the effect of pulling the potential minimum away from the conductors in the area between the conductors.

We begin the scaling of the geometry by estimating the DC current in a single conductor for a distance $d = 35 \mu\text{m}$ from the effective potential minimum to the centre of the conductor and for a RF frequency of 0.8 MHz. The RF frequency of 0.8 MHz is chosen as a starting point since it is expected to lead to sensible conductor currents. It is principally the size of the geometry and the currents that are scaled, although the RF frequency may also have to be changed to adjust the DC currents and the trapping distance from the conductors.

The depth of the trap increases with increasing DC currents and RF frequency. The trap can consequently be made deeper by increasing the DC currents. The correct relation between the RF frequency and the Larmor frequency is taken into account by equation (2.1) for the effective potential.

We assume to begin with that the necessary radius of the micro-wires is close to the 5 μm margin in the distance and skip a detailed consideration of the conductor radius for now. We use (2.4) and get

$$I_{DC} = \frac{d \cdot \omega_{RF} \cdot 2\pi\hbar}{\mu_B g_F \mu_0} = \frac{35 \cdot 10^{-6} \text{m} \cdot 2\pi \cdot 0.8 \cdot 10^6 \frac{\text{rad}}{\text{s}} \cdot 2\pi \cdot 1.05 \cdot 10^{-34} \text{Js}}{9.27 \cdot 10^{-24} \frac{\text{J}}{\text{T}} \cdot 0.66 \cdot 4\pi \cdot 10^{-7} \frac{\text{H}}{\text{m}}} = \underline{15.16 \text{ mA}}. \quad (3.1)$$

By comparing equations (2.4) and (2.18) we see that the distance d is $\sqrt{2}$ times greater for two crossed conductors. This gives the minimum distance between two crossed conductors of $\sqrt{2} \cdot 2d = 2\sqrt{2} \cdot 35 \mu\text{m} = 99.0 \mu\text{m}$. In an integrated realization this distance is equal to the substrate thickness plus one conductor thickness.

To make a design using circular conductors that lies close up to an integrated realization the substrate thickness is set to 100 μm , a common dimension, and the thickness of conductors with a quadratic cross-section is set to 10 μm . This gives a new distance $d = 110 \mu\text{m} / 2\sqrt{2} = 38.89 \mu\text{m}$ for a single conductor. The new DC current is

$$I_{DC} = \frac{d \cdot \omega_{RF} \cdot 2\pi\hbar}{\mu_B g_F \mu_0} = \frac{38.89 \cdot 10^{-6} \text{m} \cdot 2\pi \cdot 0.8 \cdot 10^6 \frac{\text{rad}}{\text{s}} \cdot 2\pi \cdot 1.05 \cdot 10^{-34} \text{Js}}{9.27 \cdot 10^{-24} \frac{\text{J}}{\text{T}} \cdot 0.66 \cdot 4\pi \cdot 10^{-7} \frac{\text{H}}{\text{m}}} = \underline{16.84 \text{ mA}}. \quad (3.2)$$

We now estimate the necessary circular conductor radius. The maximum current density is defined to be 1 MA/cm² in the conductors. The amplitude of the RF current, which can be adjusted freely to some extent, is set to 5 mA. This gives a minimum circular conductor radius of

$$a_{\min} = \sqrt{\frac{I_{w,DC} + I_{w,AC}}{\pi \cdot I_{\max}}} = \sqrt{\frac{(0.01684 + 0.005) \text{A}}{\pi \cdot (10^6 \cdot 10^4) \text{A/m}^2}} = \underline{0.834 \cdot 10^{-6} \text{m}}. \quad (3.3)$$

If a maximum current density of 1 kA/cm² had been used instead, as in the case of the millimetre sized geometry, the conductor radius would be

$$a_{\min} = \sqrt{\frac{I_{w,DC} + I_{w,AC}}{\pi \cdot I_{\max}}} = \sqrt{\frac{(0.01684 + 0.005) \text{A}}{\pi \cdot (10^3 \cdot 10^4) \text{A/m}^2}} = \underline{26.37 \cdot 10^{-6} \text{m}}. \quad (3.4)$$

Since this conductor radius is more than a quarter of the substrate thickness this is unrealistic in practise. The conductor cross-section has already been chosen to be 100 μm^2 above. This is equivalent to a circular conductor radius of 5.64 μm . This radius is acceptable since the distance d permits a

maximum conductor radius of 8.89 μm before the effective potential minimum comes closer than 30 μm to the conductor surface.

The maximum current density in the conductors becomes

$$I_{\max} = \frac{I_{w,DC} + I_{w,AC}}{\pi \cdot a^2} = \frac{(0.01684 + 0.005)\text{A}}{\pi \cdot (5.64 \cdot 10^{-6} \text{ m})^2} = \underline{2.185 \cdot 10^8 \text{ A/m}^2} = \underline{21.85 \text{ kA/cm}^2}. \quad (3.5)$$

This current density is well below what the conductors are expected to withstand. The current density is nevertheless increased from the very safe levels in the millimetre-sized structures in Chapter 2.

To finish the scaling we calculate the half-distance d between two parallel conductors using equation (2.50) to be

$$d = \frac{\mu_B g_F \mu_0}{\pi \hbar} \left(\frac{|I_{DC}|}{\omega_{RF}} \right) = \frac{9.27 \cdot 10^{-24} \frac{\text{J}}{\text{T}} \cdot 0.66 \cdot 4\pi \cdot 10^{-7} \frac{\text{H}}{\text{m}}}{\pi \cdot 1.05 \cdot 10^{-34} \text{ Js}} \left(\frac{16.84 \cdot 10^{-3} \text{ A}}{2\pi \cdot 0.8 \cdot 10^6 \frac{\text{rad}}{\text{s}}} \right) = \underline{77.78 \mu\text{m}}. \quad (3.6)$$

The distance $2d$ between two crossed conductors stays fixed at 110 μm . We are now ready to look at two examples of micron sized structures.

3.3 A four micro-wire cell

The geometry of the cell is the same as previously shown in Fig. 2.29. Micro-wires are here used instead of wires and distances will be given in micrometres. Just as in the case of the four-wire cell in Chapter 2 the four micro-wire cell should be optimized. The DC current and the half-distances d between two crossed and two parallel conductors found in Section 3.2 are used as initial values in the optimization routine. The optimization routine used is the same as for the four-wire cell in Chapter 2, except that the current $|IZI|$ is optimized instead of xIz . The variable $|IZI|$ is the DC current in the conductor labelled “1” that is parallel with the z -axis in Fig. 2.29. The remaining DC currents are defined as $IZ2 = -IZ1$ and $IYn = IZn$, for $n = 1 - 2$.

The variable $dy1$, which is the y -axis displacement of conductor “1” parallel with the z -axis, is also optimized. The optimized values are $|IZI| = -19.0 \text{ mA}$ and $dy1 = -76.2 \mu\text{m}$. The effective potential has been minimized in the point $(x, y, z) = (0, dy1, dy1)$ for $|IZI|$ and in the point $(x, y, z) = (xIz, 0, dy1)$ for $dy1$. The variable $xIz = -55 \mu\text{m}$ is the x -axis displacement of the

(row of) conductors parallel with the z -axis. The remaining variables are defined as $dy_2 = -dy_1$, $dz_n = dyn$ for $n = 1 - 2$ and $x_1y = -x_1z$. In Fig. 2.29 $2d_x = -x_1z + x_1y$ and $2d_y = -dy_1 + dy_2$. The RF currents are 5 mA of the same sign as the DC current in each conductor. The RF frequency is 0.8 MHz and the radius of the micro-wires is $5.64 \mu\text{m}$.

The plot in Fig. 3.1 shows three slices through the four micro-wire cell where the effective potential minimum around the micro-wires can be seen clearly. The dark blue figure-of-eight pattern around the micro-wires pointing in the y -direction suggests that the optimization has been successful. The potential maximum at the centre of the cell is not shown in the figure. Instead the yz -plane slice through the centre of the cell is shown in a mesh-plot in Fig. 3.2. The dark blue pattern around the peak at the centre is of practically uniform depth if the optimization has been successful. The minimum also makes small loops out between the parallel wires as explained previously for the four-wire cell in Chapter 2.

When only DC currents are used the four micro-wire cell has a potential minimum at the centre as shown in Fig. 3.3. The figure is very similar to Fig. 2.33 for the four-wire cell.

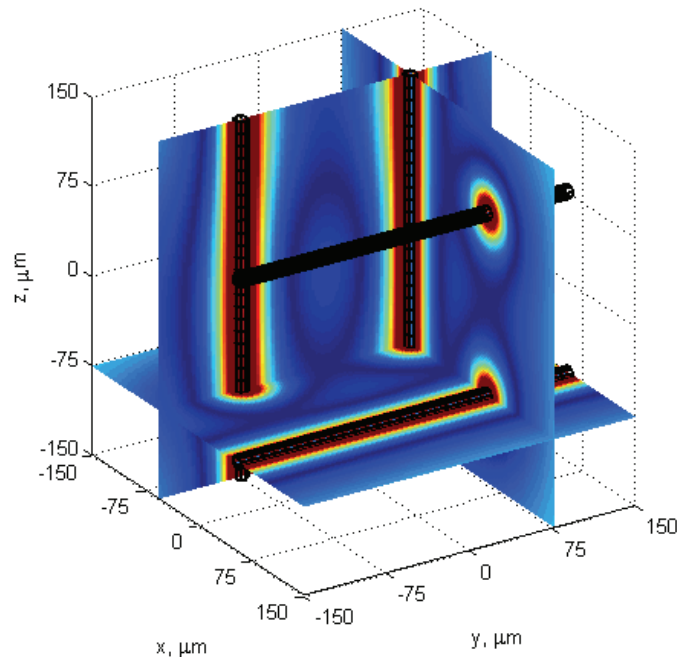


Fig. 3.1. The effective potential in the planes $x = x_1z$, $y = dy_2$ and $z = dz_1$.

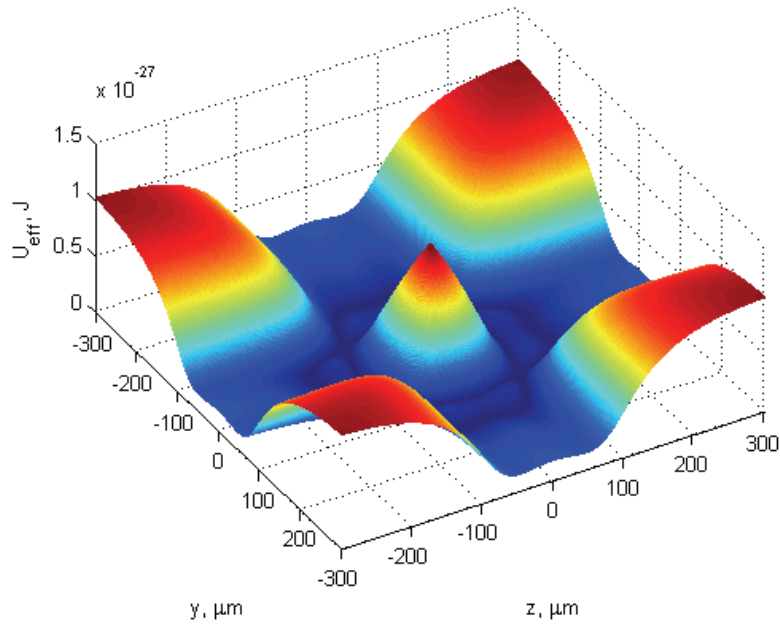


Fig. 3.2. Plot of the effective potential in the yz -plane for $x = 0$ in Fig. 3.1.

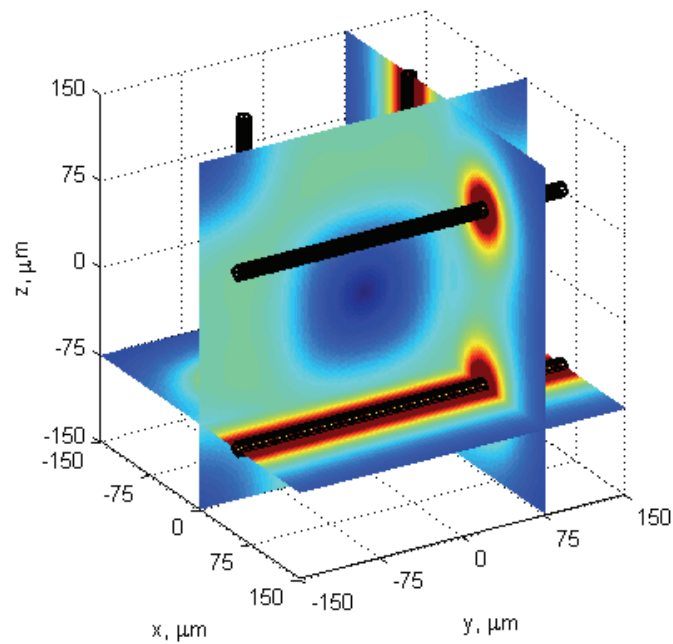


Fig. 3.3. The four micro-wire cell when excited by only the DC currents.

Graphs showing the depth of the four micro-wire cell trap have been calculated along the x -axis in Fig. 3.4 and along the z -axis in Fig. 3.5, just as was done for the four wire cell in Chapter 2. The axes are the same as shown in Fig. 3.3. The temperature has been calculated as $T = U_{eff} / k_B$, where $k_B = 1.3807 \times 10^{-23}$ J/K is Boltzmann's constant. In the two figures the red graphs are for $f_{RF} = 0.8$ MHz, the green graphs are for $f_{RF} = 0.6$ MHz, the blue graphs are for $f_{RF} = 0.4$ MHz, the magenta graphs are for $f_{RF} = 0.2$ MHz, and the black graphs are for zero frequency. The potential along the y -axis is identical to the potential along the z -axis in Fig. 3.5 as made necessary by symmetry.

A magnetic quantum number of $m_F = 2$ has been used for all graphs. If the potential maximum at the centre of the cell is used to catch and hold ground state atoms with $m_F = 1$, the effective potential shown by the graphs must be divided by two according to equation (2.1) when the ground state atoms are considered. The potential maximum at the centre is approximately equal to $m_F \cdot \hbar \cdot \omega_{RF} / k_B$, and is entirely caused by the RF dressing effect.

The graphs in Fig. 3.4 and Fig. 3.5 are spot alike those for the four-wire cell in Fig. 2.34 and Fig. 2.35. The only difference is in the distance readings. The explanation for this is that the depth of the trap does not change unless the frequency is changed. The frequency is 0.8 MHz in both cases.

The effective potential is zero at the centre of the trap when it is excited by only the DC currents. For RF excitation it is difficult to establish whether the deformed spherical minimum around the centre of the cell lies at zero potential. The situation is thus exactly the same as for the four-wire cell.

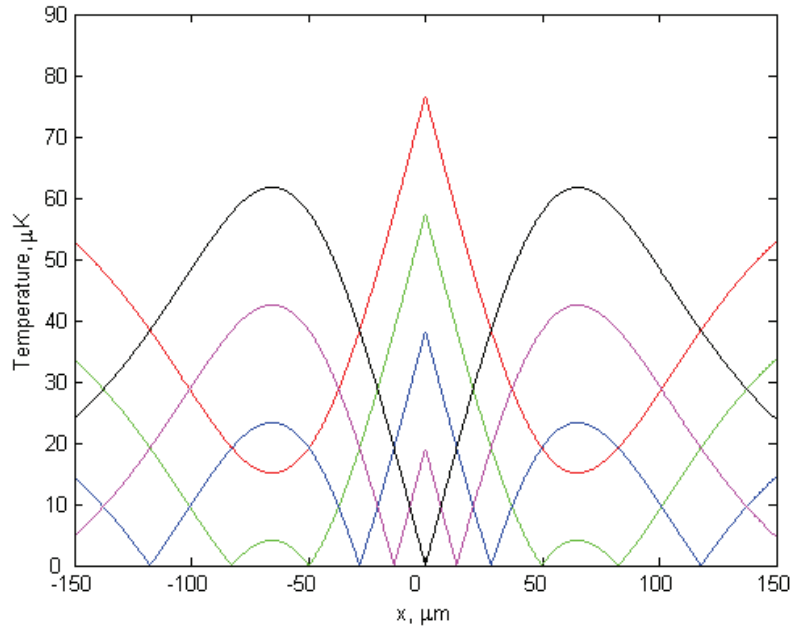


Fig. 3.4. Potential along the x -axis through the centre of the four micro-wire cell.

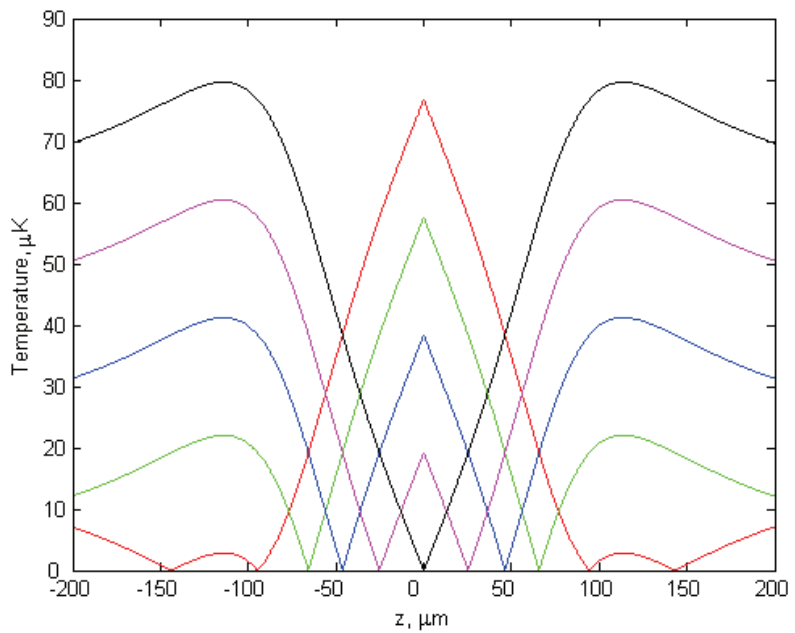


Fig. 3.5. Potential along the z -axis through the centre of the four micro-wire cell.

3.4 A 3 x 3 micro-wire geometry

The three-by-three micro-wire geometry is shown in Fig. 2.41. The usage of the structure does not change depending on whether wires, micro-wires or nanotubes are used as conductors. The big difference lies in the size of the atom clouds in the two wells and the distance between them. Downscaling generally leads to a study of fewer atoms in smaller wells placed closer together.

As an adaptation toward a future experimental realization of the structure on a micro-machined substrate, the distance x/z has been kept constant. With reference to Fig. 2.41 $x/z = -h/2$. The variables optimized are $dy1$, $Iz1 = -|I_{DC, c-w}|$ and $Iz2 = |I_{DC, p-w}|$. Here $|I_{DC, c-w}|$ is the current in the two micro-wires at the centre and $|I_{DC, p-w}|$ is the current in the four peripheral micro-wires. The DC currents must still be in opposite direction in adjacent parallel micro-wires in each wire-plane.

The optimized variables are detailed in Table 3.1. The table also lists the points where the function for the effective potential U_{eff} has been minimized. The geometric origin lies in the middle between the two micro-wires at the centre for this structure. The remaining variables can be found as follows: $Iz3 = Iz2$, $Iyn = Izn$ for $n = 1 - 3$, $dz1 = dy1$ and $xly = -x/z$. In the case of the DC currents the numbers in the variable names refer to the micro-wires numbered in the positive y -direction or from bottom to top in the sequence $\{3\ 1\ 2\}$. With reference to Fig. 2.41 $d = -2 \cdot dy1 = -2 \cdot dz1$. The RF currents are 5 mA of the same sign as the DC current in each micro-wire. The RF frequency is 0.8 MHz as before and the micro-wire radius is 5.64 μm .

Table 3.1. Defining variables for the three-by-three micro-wire geometry. Three variables have been optimized. The variable x/z is also listed.

Variable	Value	U_{eff} minimized in point (x, y, z)
x/z	-55.0 μm	Not optimized
$dy1$	-78.2 μm	$x/z, dy1, 0$
$Iz1$	-20.9 mA	0, 0, 0
$Iz2$	18.6 mA	0, $2 \cdot dy1, 2 \cdot dy1$

The merger of the two potential peaks into a single maximum at the centre of the 3 x 3 micro-wire geometry is illustrated by the animation in Fig. 3.6. The DC currents in the centre micro-wires in the nine frames are:

$|I_{\text{DC}, c-w}^{(2)}| = [20.9, 15.7, 10.5, 5.23, 2.09, 5.23, 10.5, 15.7, 20.9]$ mA. The DC current is negative in the micro-wire at the centre in both the z -direction and the y -direction. The animation shows that the two potential maxima remain isolated in 3D as they are brought together to form a single maximum.

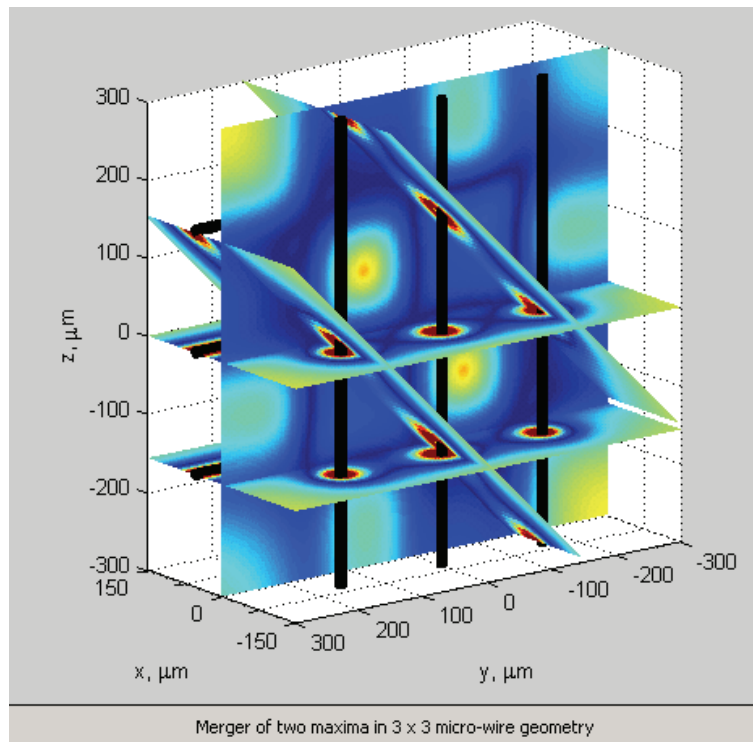


Fig. 3.6. Animation showing the merger of two potential maxima in 3D.

The single maximum in frame 5 of the animation is lesser well defined in the x -direction between the two micro-wires at the centre. The reason for this is the low DC currents in the centre micro-wires that allow the two potential peaks to merge into a single maximum. The single maximum is shown in Fig. 3.7 for those who are unable to play the animation. The plot in Fig. 3.7 can be compared with Fig. 2.44 for the three-by-three wire structure. The most striking difference is that the relative thickness of the conductors is much smaller in the micro-wire version. The current density is accordingly also much higher as was pointed out when the scaling to micrometre size was done.

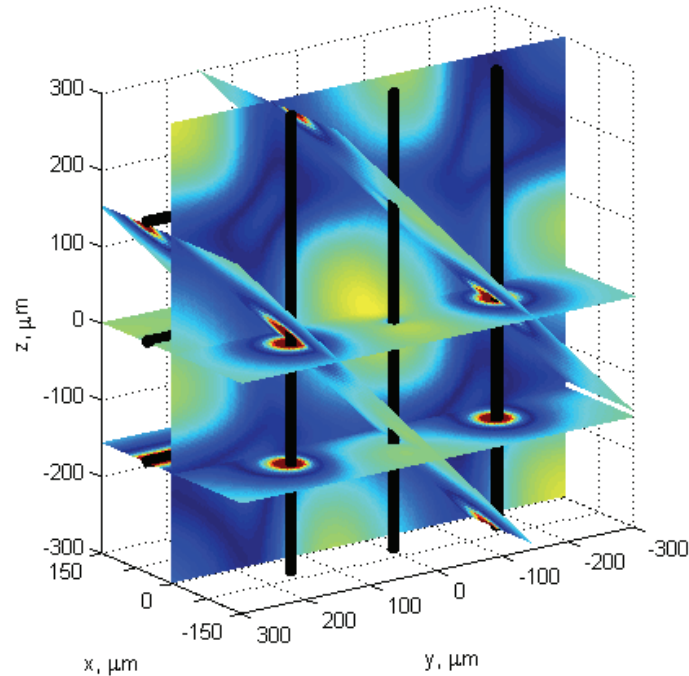


Fig. 3.7. The merged potential maximum in frame 5 of the animation.

Just as was done for the three-by-three wire geometry in Section 2.9 graphs of the effective potential have been calculated along the lines labelled u and v in Fig. 2.41 as well as in the x -direction through the point where the lines u and v intersect and in the x -direction through the centre of the geometry. The graphs are shown in Fig. 3.8 to Fig. 3.11. The temperature in degrees Kelvin is simply the effective potential divided by Boltzmann's constant.

The red graphs correspond to the initial situation with two peaks in Fig. 3.6. The black graphs show the single maximum at the centre (frame 5 in the animation). The dotted blue graphs, the dashed green graphs and the dash-dotted magenta graphs correspond to frames 2 – 4 in the animation in Fig. 3.6. The potential peaks in Fig. 3.8 – Fig. 3.11 attract strong-field-seeking atoms and the graphs have therefore been scaled to correspond to the magnetic quantum number for strong-field-seeking atoms, i.e. the case where $m_F = 1$ in equation (2.1).

The graphs in Fig. 3.8 – Fig. 3.11 can be seen to be almost identical to the corresponding graphs for the three-by-three wire structure in Fig. 2.45 – Fig. 2.48. Small differences can however be found for some of the curves. The only graph that comes out significantly different is the black graph for

the single maximum in Fig. 3.11. This graph dips much further down next to the centre micro-wires when compared to the black graph in Fig. 2.48. The difference is a dip of $22.3 \mu\text{K}$ from the maximum at $x = 0$ in Fig. 3.11 compared to a dip of $9.6 \mu\text{K}$ in Fig. 2.48. The maximum at $x = 0$ is $33.85 \mu\text{K}$ in both cases. The explanation for this is thought to lie in the distance that the atom condensates are kept away from the conductors relative to the size of the conductors and the current density in the conductors.

A nanometre sized version of the three-by-three conductor structure has previously been described in [151]. There the atom condensates must be kept relatively far away from the conductor surfaces on account of the Casimir-Polder force. At the same time the maximum current that can be sent through the nanotubes is limited. As a result the dip next to the nanotubes at the centre from the maximum at $x = 0$ of $11.2 \mu\text{K}$ is only about $6.9 \mu\text{K}$. Since the potential barrier may be even lower to the side of the nanotubes, the three-by-three nanotube geometry will not be given further consideration in this thesis. The use of bundled nanotubes with increased currents may improve the situation, but this lies beyond the scope of this work.

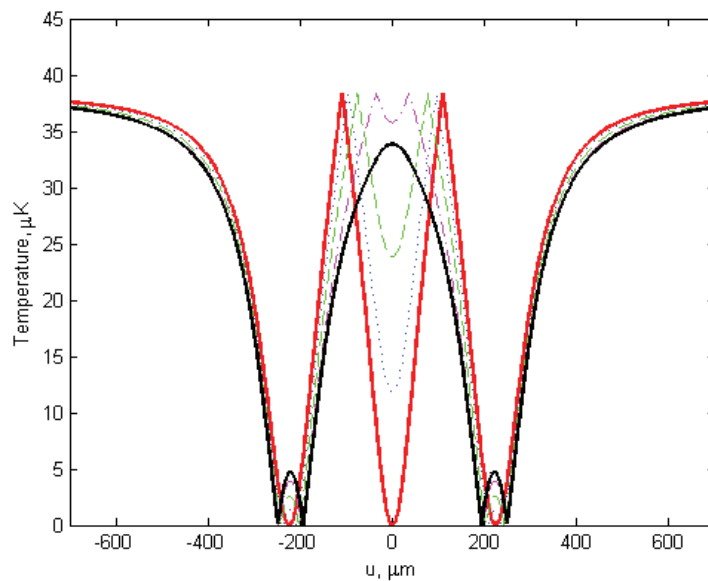


Fig. 3.8. The effective potential along the line u in Fig. 2.41 for $x = 0$.

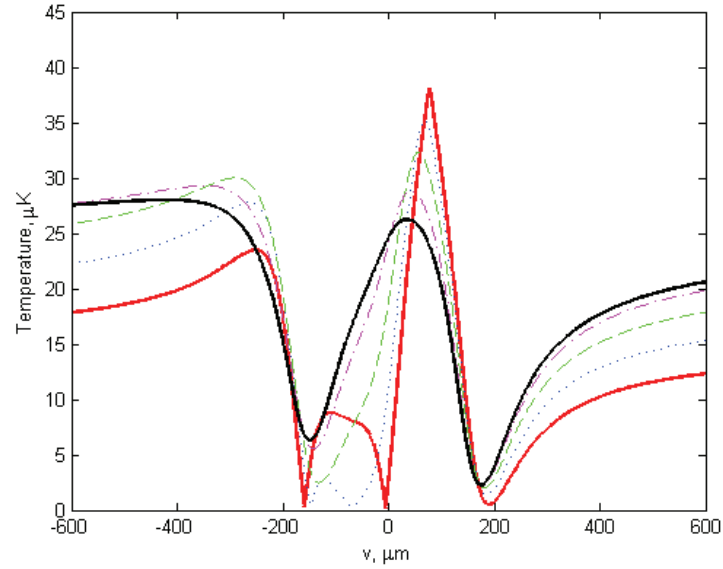


Fig. 3.9. The effective potential along the line v in Fig. 2.41 for $x = 0$.

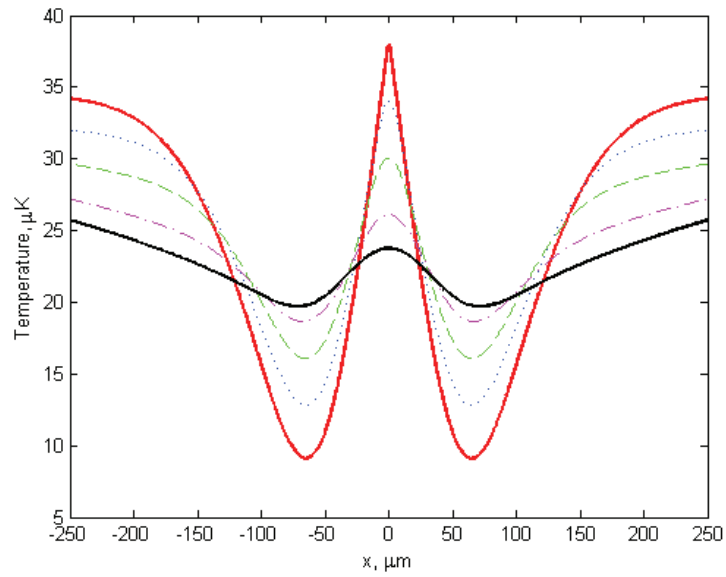


Fig. 3.10. The effective potential in the x -direction through the point where the lines u and v intersect in Fig. 2.41.

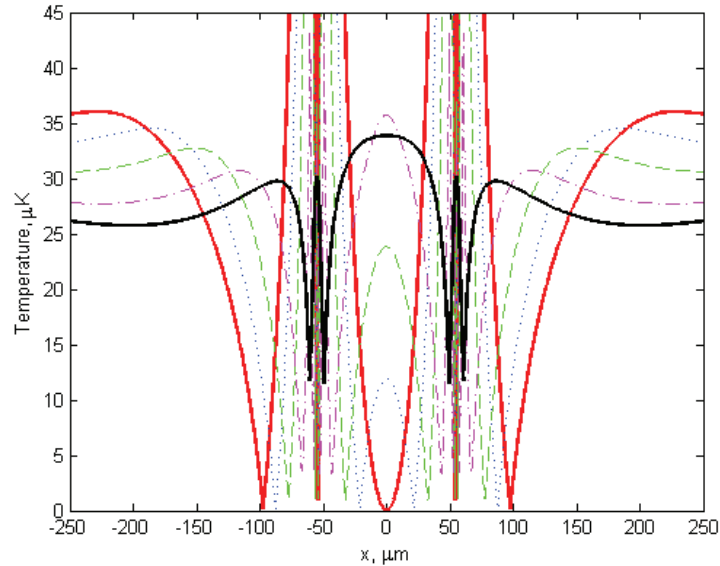


Fig. 3.11. The effective potential in the x -direction through the point where the centre wires intersect in Fig. 2.41.

When the three-by-three micro-wire structure is excited by only the DC currents it exhibits two potential wells along one of the diagonals. The diagonal that the potential wells appear along can be changed by reversing the DC currents in the micro-wires in one of the micro-wire rows. The two potential wells are depicted in 3D in Fig. 3.12.

By using the same DC currents as in the animation in Fig. 3.6 the two potential wells can be brought together to form a single well at the centre of the geometry. The resulting minimum in the effective potential is shown in Fig. 3.13. It is also here apparent that the potential barrier in the x -direction between the micro-wires at the centre is much lower than in other directions. However, as will be explained in a moment, the potential barrier is here in fact much higher than for the single maximum in Fig. 3.7.

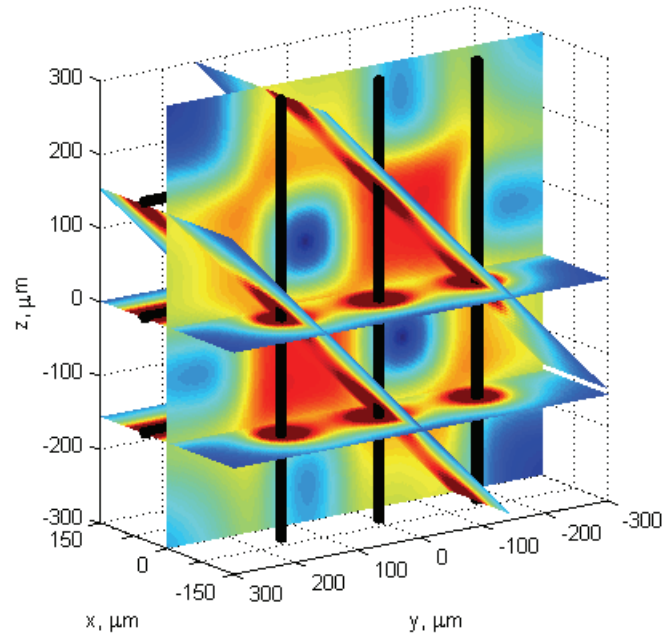


Fig. 3.12. The double-well effective potential with only DC excitation.

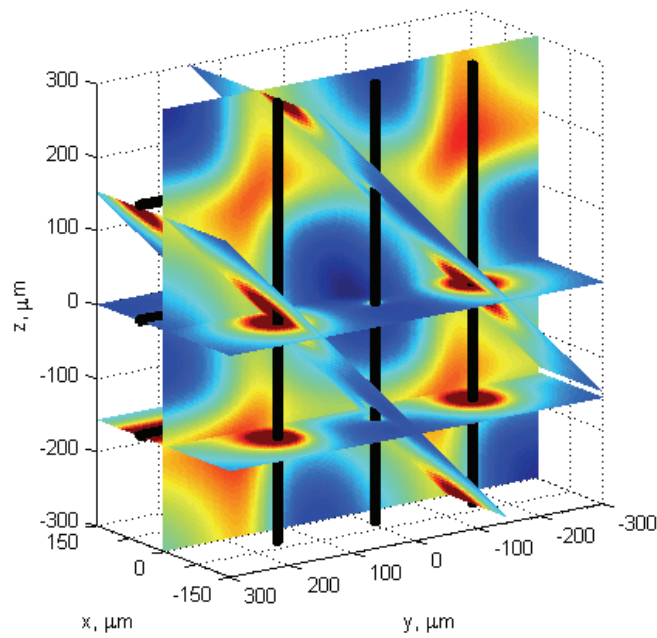


Fig. 3.13. The merged potential minimum with only DC excitation.

Graphs of the effective potential have once again been calculated along the lines u and v in Fig. 2.41 and in the x -direction through the points where the lines u and v intersect and where the centre micro-wires intersect. The graphs have all been calculated using the magnetic quantum number for weak-field-seeking atoms ($m_F = 2$).

The blue graph along the line u in Fig. 3.14 shows the two initial potential wells. The dotted red graphs, the dashed green graphs and the dash-dotted magenta graphs indicate the potential when the DC current in the two centre micro-wires has been reduced to 75 %, 50 % and 25 % respectively of its starting value. The black graphs show the potential when the DC current in the centre micro-wires has been reduced to 10 % of its starting value, corresponding to frame 5 in the animation in Fig. 3.6 without the RF currents.

The graphs in Fig. 3.14 – Fig. 3.17 are almost identical to the graphs for the three-by-three wire geometry in Fig. 2.50 – Fig. 2.53. Only a few very small differences can be seen except for the magenta and black graphs in Fig. 3.17, which are significantly different. The two graphs pull up much further close to the centre micro-wires compared to in Fig. 2.53.

In Fig. 3.17 the height of the potential barrier measured between the mid-point on the black graph and one of the small peaks next to the wires is about 59.9 μK , which is much better than the barrier of 22.3 μK for combined DC and RF excitation in Fig. 3.11. Much of the difference can be explained by the use of different magnetic quantum numbers, but not all. The barriers appear to be higher in general in the case of potential wells for weak-field-seeking atoms.

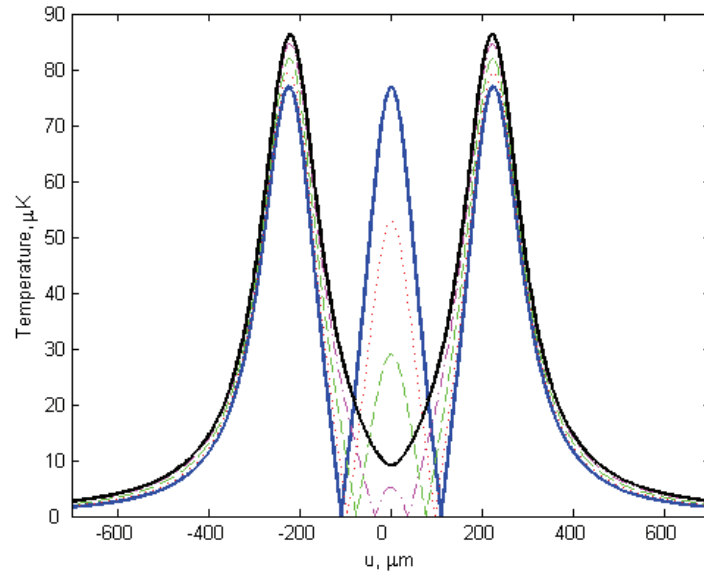


Fig. 3.14. The effective potential with only DC excitation along the line u shown in Fig. 2.41 for $x = 0$.

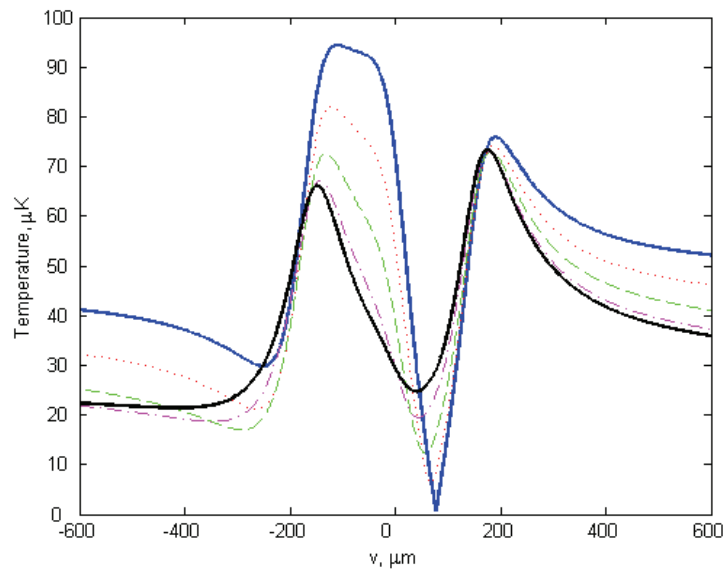


Fig. 3.15. The effective potential with only DC excitation along the line v shown in Fig. 2.41 for $x = 0$.

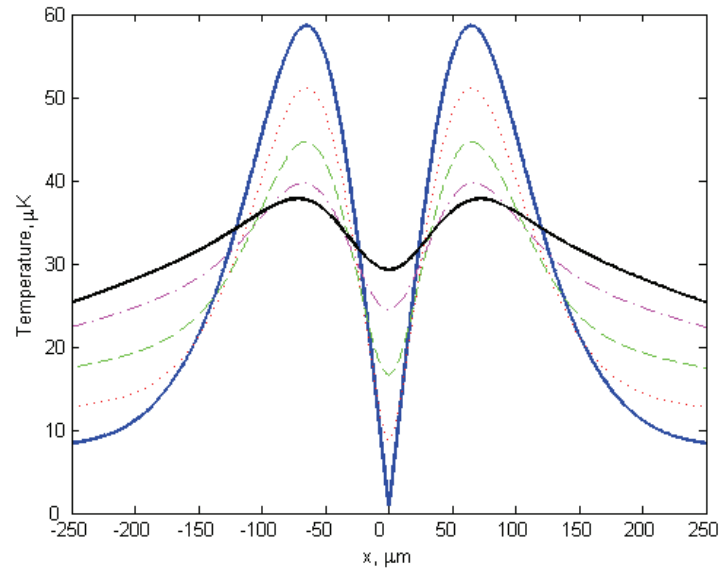


Fig. 3.16. The effective potential with only DC excitation in the x -direction through the point where the lines u and v intersect in Fig. 2.41.

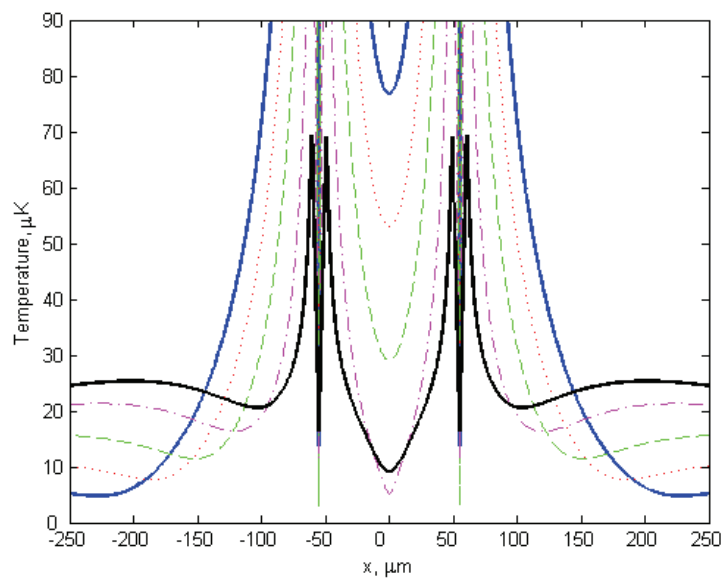


Fig. 3.17. The effective potential with only DC excitation in the x -direction through the point where the centre wires intersect in Fig. 2.41.

3.5 Scaling to nanometre size

When structures are scaled down to nanometre size cold atom condensates must be kept at a minimum distance from the conductor surfaces to prevent atom-surface interaction. There are two mechanisms that play a part when the dimensions are on a nanometre scale. The first is thermally-induced spin-flip transitions. Thermal excitation of atoms generates noise currents that lead to fluctuating magnetic fields close to the body surface [118]. The magnetic field fluctuations can in turn drive atomic spin transitions that lead to trapping loss.

The second mechanism is the Casimir-Polder force. An atom in its ground state placed sufficiently close to a dielectric body experiences a (generally attractive) dispersion force due to the presence of the dielectric material [152] – [154]. The Casimir-Polder potential adds to the effective potential generated by the DC and RF currents in the conductors. Close to the conductor surface the effective potential is repulsive for ground state atoms. The combined potential, consisting of the Casimir-Polder potential and the effective potential, forms a potential barrier around the conductors. If this barrier becomes too narrow, atoms can tunnel through it and get stuck at the conductor surfaces.

The experimental study of carbon nanotubes has recently attracted a lot of research interest [155]. Carbon nanotubes (CN's) appear to have several advantages as conductors in miniaturized magnetic traps. Because CN's consist of only a small amount of dielectric matter the Casimir-Polder force is minimized. The noise currents should also be much reduced compared to in a dielectric bulk material because of the small amount of matter in the nanotubes. However, neither thermal spin-flips nor the Casimir-Polder force can be overlooked when the dimensions are very small. The Casimir-Polder force is thought to play a bigger role than thermal spin-flips at short distances from the nanotube surface. Another attractive feature of CN's is that they have extremely homogeneous surfaces, something which helps to prevent disturbances in the effective potential topology of the trap.

Numerical estimation of the Casimir-Polder force is a complex operation mathematically. It has been performed in [118] for a single nanotube assuming a relatively simple trap geometry. In [118] the minimum feasible trapping distance is found to be about 100 nm. This minimum distance, measured from the nanotube surface to the surrounding effective potential minimum, will be used in the following to demonstrate scaling to nanometre size.

In the article conclusion in [118] it is suggested that multi-walled nanotubes will permit higher current densities that can create a magnetic trapping potential comparable to the Casimir-Polder potential even for smaller distances. It turns out that it is easy to make a deep potential minimum closer to the conductor surface for a fixed DC conductor current simply by increasing the RF frequency. As the RF frequency is increased, the depth of the trapping potential is increased and the trapping distance d is reduced by the same factor. However, as is evident from the first two figures in [118], the reduction in the spin-flip lifetime and the increase in the Casimir-Polder force are extremely steep close to a conductor surface. This makes it a risky business to try to reduce the minimum trapping distance by increasing the conductor currents and the RF frequency with it. A careful calculation of the Casimir-Polder force seems to be necessary to determine whether the trapping distance can be further reduced.

Ideally the Casimir-Polder potential should have been calculated for each of the nanometre sized structures in the remainder of this Chapter and then added to the effective potential. This would have resulted in a new total effective potential. This is a large undertaking that should be done before the eventual fabrication of nanometre sized prototypes. The graphs for the spin-flip lifetime and tunnelling time in [118] give little hope that the minimum feasible trapping distance can be set to much less than 100 nm, independent of the Casimir-Polder potential.

To achieve the maximum trap depth a DC current should first be chosen so that the total current in the nanotubes is just below the maximum allowable current (e.g. 20 μA). The trapping potential can also be made deeper still through the use of multi-walled or bundled nanotubes, which permit even larger currents. If the trapping distance d continues to be below its minimum value, it must be increased by reducing the initial RF frequency. This simultaneously reduces the depth of the trap proportionally to the reduction in frequency.

In the following single-walled (9, 0) carbon nanotubes with a radius of 3.52 Å ($3.52 \cdot 10^{-10}$ m) will be assumed used. Carbon nanotubes of this type have been considered in [118], and it is convenient to use the same nanotubes here. The physical properties of a CN are determined by the way in which the graphite sheet is rolled. The winding angle with respect to the hexagonal carbon lattice is usually described by two integer numbers (a , b). When $2a + b = 3n$, where n is again an integer, a CN shows metallic behaviour. Otherwise it is semi-conducting. (9, 0) carbon nanotubes ($n = 6$) accordingly show metallic behaviour. The choice of which nanotube to use is in any case not very critical for the atom traps in this Chapter. Because

the radius of a carbon nanotube is very small it will be neglected to begin with when the distance d from the centre of the nanotube to the surrounding potential minimum is estimated.

The largest sustainable current before saturation effects become important in the above mentioned nanotubes is 20 μA [118]. To keep the total current below 20 μA we choose a DC current of 15 μA and an RF current of 4 μA . With the distance d and the DC current I_{DC} having been determined, the frequency can be calculated from the relation between d , I_{DC} and ω_{RF} in equation (2.4) to be

$$\omega_{\text{RF}} = \frac{\mu_B g_F \mu_0}{2\pi\hbar} \left(\frac{I_{\text{DC}}}{d} \right) = \frac{9.27 \cdot 10^{-24} \frac{\text{J}}{\text{T}} \cdot 0.66 \cdot 4\pi \cdot 10^{-7} \frac{\text{H}}{\text{m}}}{2\pi \cdot 1.05 \cdot 10^{-34} \text{ Js}} \left(\frac{15 \cdot 10^{-6} \text{ A}}{100 \cdot 10^{-9} \text{ m}} \right) = 1.74 \cdot 10^6 \frac{\text{rad}}{\text{s}}, \quad (3.7)$$

$$f_{\text{RF}} = \frac{\omega_{\text{RF}}}{2\pi} = \underline{277123 \text{ Hz}}. \quad (3.8)$$

For convenience, but also to obtain a small margin in the distance, the frequency is rounded down to 0.27 MHz. Equation (2.4) is then used to find the new distance d to the circular minimum around a single nanotube:

$$d = \frac{\mu_B g_F \mu_0}{2\pi\hbar} \left(\frac{I_{\text{DC}}}{\omega_{\text{RF}}} \right) = \frac{9.27 \cdot 10^{-24} \frac{\text{J}}{\text{T}} \cdot 0.66 \cdot 4\pi \cdot 10^{-7} \frac{\text{H}}{\text{m}}}{2\pi \cdot 1.05 \cdot 10^{-34} \text{ Js}} \left(\frac{15 \cdot 10^{-6} \text{ A}}{2\pi \cdot 270 \cdot 10^3 \text{ rad/s}} \right) = \underline{102.6 \text{ nm}}. \quad (3.9)$$

The equation for the distance d for a single wire/conductor should always be used since the minimum potential surface comes closest to a wire/conductor on sides facing away from other crossing or parallel conductors. The distances d for two crossed or for two parallel conductors are always larger than the shortest distance from the centres of the conductors to the surrounding minimum potential manifold.

Examination of equations (2.4) and (2.18) shows that the distance d is $\sqrt{2}$ times greater for two crossed conductors. This gives the distance $d = \sqrt{2} \cdot 102.6 \text{ nm} = 145.15 \text{ nm}$ for two crossed nanotubes. The total distance between two crossed nanotubes is accordingly $2d = 290.3 \text{ nm}$.

To complete the calculations we obtain the half-distance d between two parallel nanotubes using equation (2.50) to be

$$d = \frac{\mu_B g_F \mu_0}{\pi\hbar} \left(\frac{|I_{\text{DC}}|}{\omega_{\text{RF}}} \right) = \frac{9.27 \cdot 10^{-24} \frac{\text{J}}{\text{T}} \cdot 0.66 \cdot 4\pi \cdot 10^{-7} \frac{\text{H}}{\text{m}}}{\pi \cdot 1.05 \cdot 10^{-34} \text{ Js}} \left(\frac{15 \cdot 10^{-6} \text{ A}}{2\pi \cdot 270 \cdot 10^3 \text{ rad/s}} \right) = \underline{205.3 \text{ nm}}. \quad (3.10)$$

The half-distances d between two crossing or parallel nanotubes are only valid in the case of two crossing or two parallel nanotubes without any

other nearby conductors. When additional parallel or crossing conductors are present the currents and distances should be found by optimization.

The frequency we have ended up with in this design of 0.27 MHz is roughly one third of the starting out frequency of 0.8 MHz. If the current carrying capacity of the conductors could be increased by a factor of about three, through the use of multi-walled or bundled nanotubes, the RF frequency could have been kept at 0.8 MHz. The minimum trapping distance d would then have been the same but the depth of the trapping potential would have increased almost threefold. The trapping distance d does not change so long as the ratio of the DC current to the angular frequency stays the same.

If the minimum trapping distance were to be increased to $d = 150$ nm for the single-walled nanotubes with DC currents of $15 \mu\text{A}$, the new RF frequency would become 0.185 MHz. This would reduce the depth of the trapping potential by a factor of 0.684 compared to the design presented above with $f_{\text{RF}} = 0.27$ MHz. Unless the DC currents can be increased an increase in the minimum trapping distance will thus severely reduce the depth of the trapping potential.

In the remaining sections of this Chapter several nanometre sized structures will be introduced. The expected atom transfer between two crossed nanotubes will be described first in Section 3.6. A four nanotube cell is then presented in Section 3.7. In sections 3.8 and 3.9 a nanotube cell-grid and stacked nanotube cell-grids are exemplified.

3.6 Atom transfer between two crossed CN's with bias rings

The scaling down to nanometre size of the wire structures in Chapter 2 has little effect on the shape of the effective potential. The biggest difference may be that minima in the effective potential are not seen inside the nanotubes. The cross-sectional area of the nanotubes is however very small. Since the data resolution is limited possible potential minima inside the nanotubes would most likely not be visible in any case.

The isosurface $U_{\text{eff}} = 5\text{e-}29$ J is shown for two crossed nanotubes without bias in Fig. 3.18. The currents in the nanotubes are $-15 \mu\text{A}$ DC and $-4 \mu\text{A}$ RF in both nanotubes. The frequency is 0.27 MHz and the distance between the nanotubes is $2d = 290.3$ nm. The nanotube radius is 3.52 \AA ($3.52 \cdot 10^{-10}$ m). The figure shows clearly that there is a double surface

around both nanotubes. The effective potential minimum of zero, i.e the isosurface $U_{\text{eff}} = 0$ J, is to be found in between these two surfaces.

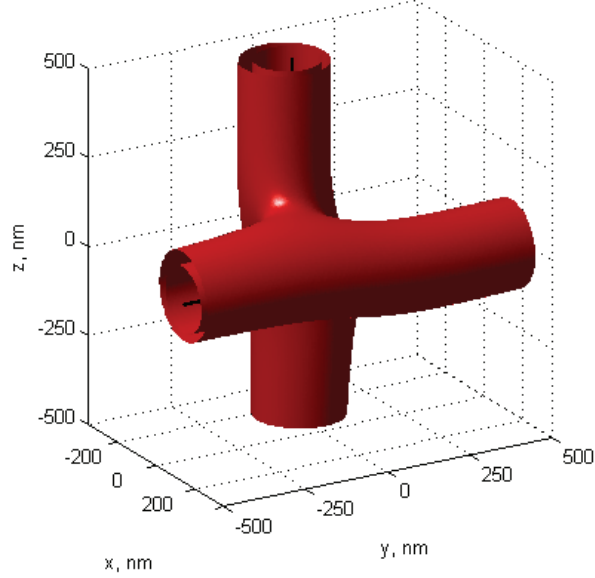


Fig. 3.18. The potential manifold $U_{\text{eff}} = 5e-29$ J for two crossing nanotubes.

To enable a transfer of cold atoms between the crossed nanotubes in Fig. 3.18 a pair of bias rings is placed around each nanotube. The radius of the bias rings is 380 nm and they are centred at $z = \pm 1 \mu\text{m}$ and at $y = \pm 1 \mu\text{m}$ around the nanotube in the z -direction and y -direction respectively. Only the use of the last two current sign combinations in Table 2.1 for the currents in the bias rings will be shown.

A 14 frame video showing the anticipated transfer of cold atoms is supplied in Fig. 3.19. The nanotube currents are $-15 \mu\text{A}$ DC and $-4 \mu\text{A}$ RF just as in Fig. 3.18. The frequency is $f_{\text{RF}} = 0.27$ MHz and radius of the nanotubes $R_{\text{CN}} = 3.52 \text{ \AA}$. The currents in the bias rings in the 14 frames are:

$$I_{\text{RF}|z\text{-cond. rings}}^{\text{I+II}} = \left\{ \begin{array}{l} [-350 \ 0], [-350 \ 70], [-280 \ 140], [-280 \ 210], \\ [-280 \ 280], [-210 \ 210], [-210 \ 210], [-150 \ 150], \\ [-60 \ 60], [0 \ 0], [0 \ 0], [0 \ 0], [0 \ 0], [0 \ 0] \end{array} \right\} \mu\text{A},$$

$$I_{\text{RF}|y\text{-cond. rings}}^{\text{I+II}} = \left\{ \begin{array}{l} [-10 \ 10], [-10 \ 10], [-10 \ 10], [-10 \ 10], [-70 \ 70], \\ [-110 \ 110], [-210 \ 220], [-290 \ 290], [-150 \ 150], \\ [-210 \ 210], [-210 \ 210], [-280 \ 140], [-350 \ 70], [-350 \ 0] \end{array} \right\} \mu\text{A}.$$

In the first five frames of the animation cold atoms are being pumped down along the nanotube in the z -direction toward the centre of the nanotube. In frames 6 and 7 a downward slope is created in the effective potential around the nanotube in the z -direction down to a common minimum at the centre between the crossing nanotubes. This transfers the cold atoms from around the nanotube in the z -direction to the common minimum between the nanotubes.

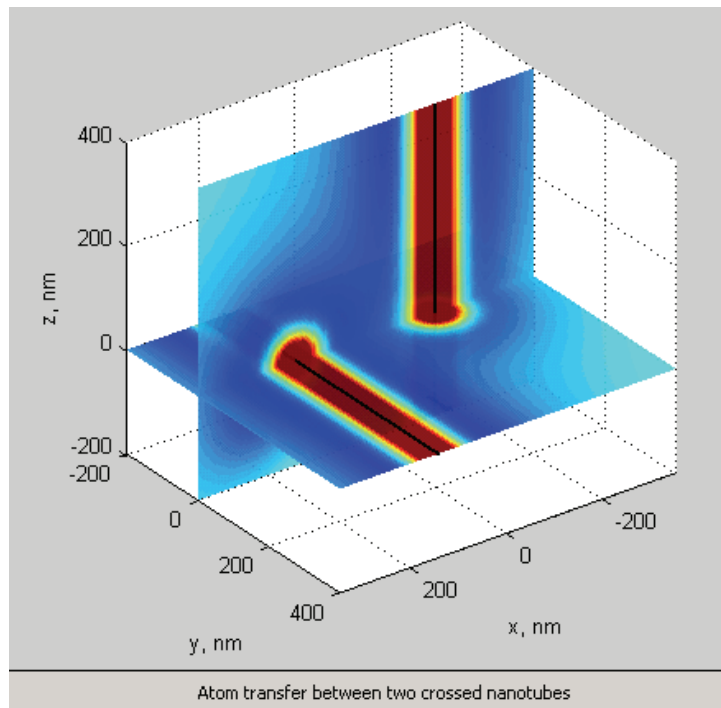


Fig. 3.19. Animation of cold atom transfer using bias currents of different signs.

Frame 6 in the animation is shown in Fig. 3.20(a). The effective potential in the xy -plane ($z = 0$) in frame 6 is shown in Fig. 3.20(b). The figure shows that two effective potential minima have formed close to the centre between the nanotubes. The cold atom condensate around the nanotube in the z -direction is expected to accumulate in the two minima.

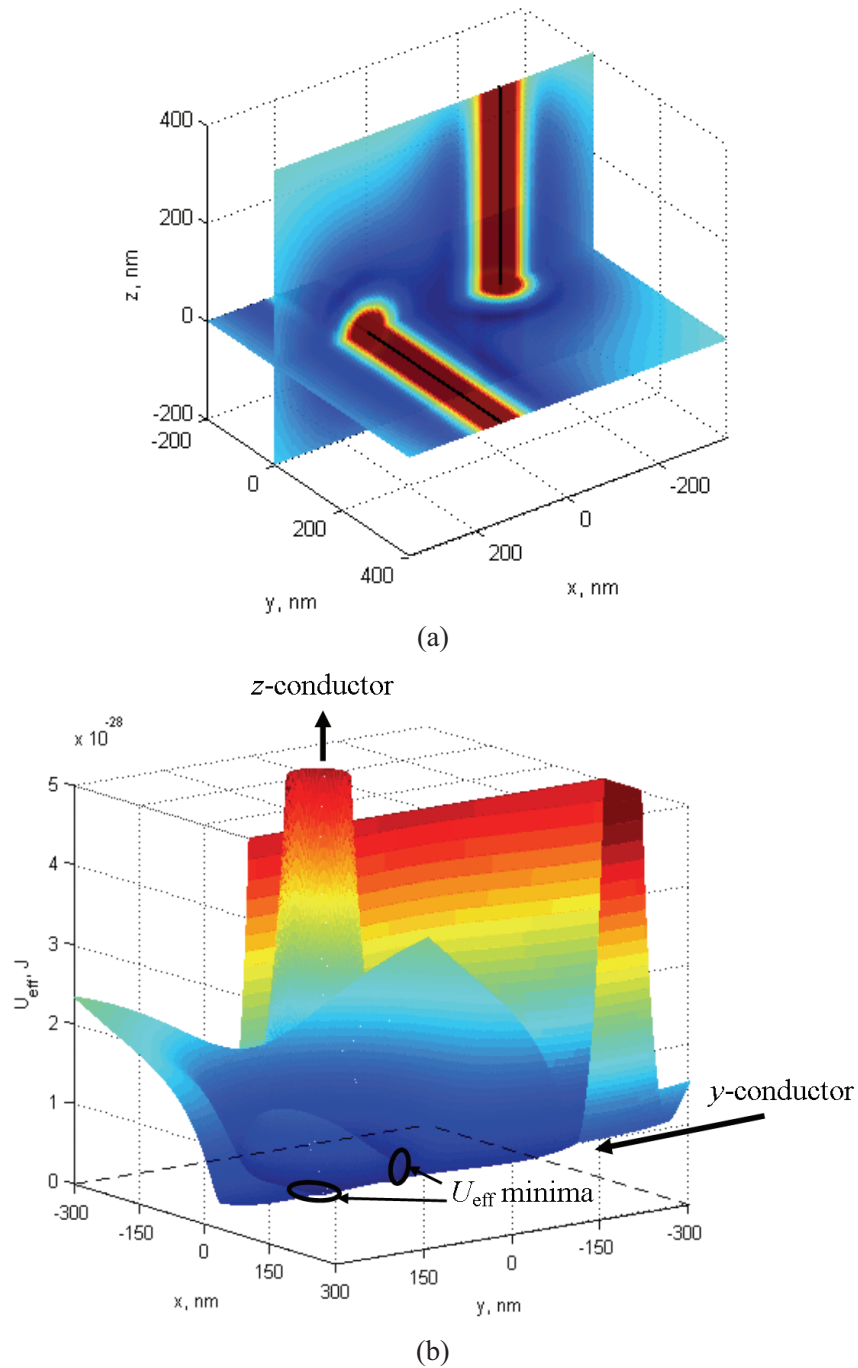


Fig. 3.20. Frame 6 in the animation (a), and U_{eff} in the xy -plane in frame 6 (b).

Fig. 3.21 shows the effective potential in the xy -plane ($z = 0$) in frame 7. The figure shows that a common minimum has formed at the centre between the nanotubes. At the same time a pair of low potential regions has formed on the sides around the nanotube in the z -direction. Since these regions are isolated from the two effective potential minima in frame 6 during the transition from frame 6 to frame 7, all of the cold atom matter should end up in the common minimum at the centre.

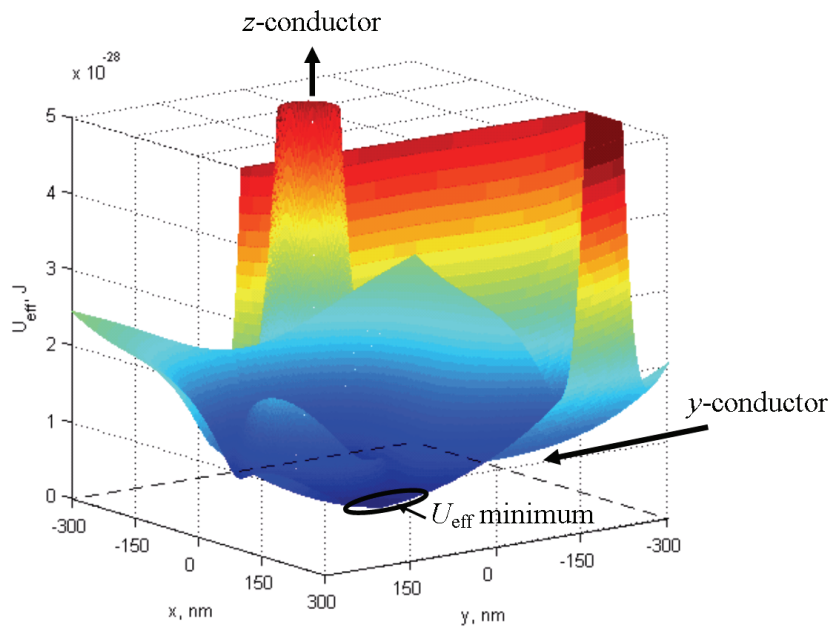


Fig. 3.21. U_{eff} in the xy -plane in frame 7 in the animation.

Fig. 3.22 gives additional information about the value of the effective potential along the x -axis ($y = z = 0$) for frame 6 in Fig. 3.20(b) and for frame 7 in Fig. 3.21. The red curve (*) corresponds to frame 6 and the blue curve (o) to frame 7. The low potential regions next to the nanotube in the z -direction do not show up along the x -axis and the graphs do not therefore give a complete picture. Note that the current in one of the bias rings has been increased to $220 \mu\text{A}$ in frame 7 to avoid an absolute zero in the potential at the common minimum.

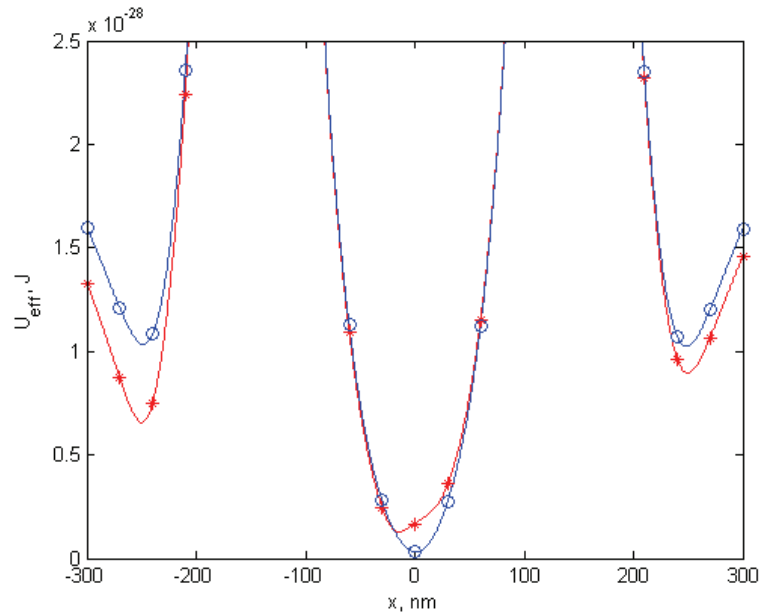


Fig. 3.22. The effective potential along the x -axis in frame 6 and frame 7.

The RF bias currents that have been used are relatively high. The reason for this is in part to demonstrate the atom transfer more clearly. It may not be necessary to use quite so high bias currents in practise. The bias currents may also be reduced by bringing the bias rings closer together and perhaps by increasing the radius of the rings a bit. The equations for infinitesimally thin current rings have been used here for the simulation. The question of how to implement the bias rings has so far not been addressed. Hopefully it will be possible to use bundled nanotubes.

The atom transfer can henceforth be completed in two ways. The cloud of cold atoms can be kept in the potential minimum around the nanotube in the y -direction, (the nanotube that accepts cold atoms), while the DC current is reduced in the nanotube in the z -direction, (the nanotube that donates cold atoms). This amounts to splitting the common minimum in such a way as to keep most of the cold atoms in the minimum around the acceptor nanotube. The alternative is to pump the cloud of cold atoms away from the crossing point along the acceptor nanotube without attempting to split the common minimum between the nanotubes first. This is more straightforward but ties up the donor nanotube a bit longer.

In the animation in Fig. 3.19 the approach of splitting the common minimum has been taken. In frames 8 to 11 the DC current is reduced in the donor nanotube in steps of 95 %, 90 %, 75 % and 50 % of its original

value. The effective potential along the x -axis is illustrated by the four graphs in Fig. 3.23. In the figure the blue graph (1, \cdot) is for frame 8, the red graph (2, \circ) is for frame 9, the magenta graph (3, $*$) is for frame 10 and the black graph (4, \diamond) is for frame 11.

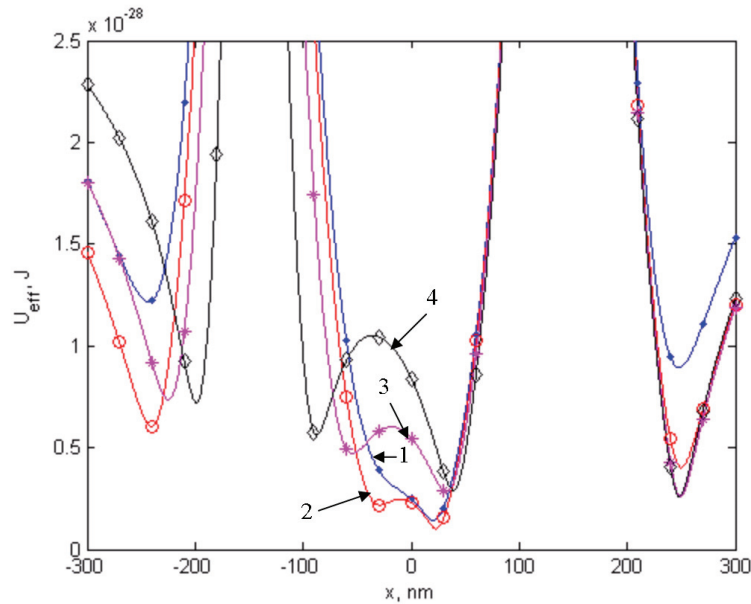


Fig. 3.23. The effective potential along the x -axis in frames 8 – 11.

In frame 8 the potential minimum has been deepened next to the acceptor nanotube while avoiding a split of the common minimum. The effective potential in the xy -plane in frame 8 is shown in Fig. 3.24. In frame 9 the DC current in the donor nanotube has been reduced to 90 % and a second minimum begins to appear, as shown in the insert in Fig. 3.24. Note that the insert only shows the effective potential in the area just around the common minimum.

In frames 10 and 11 the potential barrier between the two minima increases with the reduction of the DC current in the donor nanotube. Frame 11 of the animation is shown in Fig. 3.25. The cold atom cloud is now in the minimum around the nanotube in the y -direction. The nanotube in the z -direction can from this point onwards be considered to be inactive since the potential barrier between the potential minima around the two nanotubes is comfortably large.

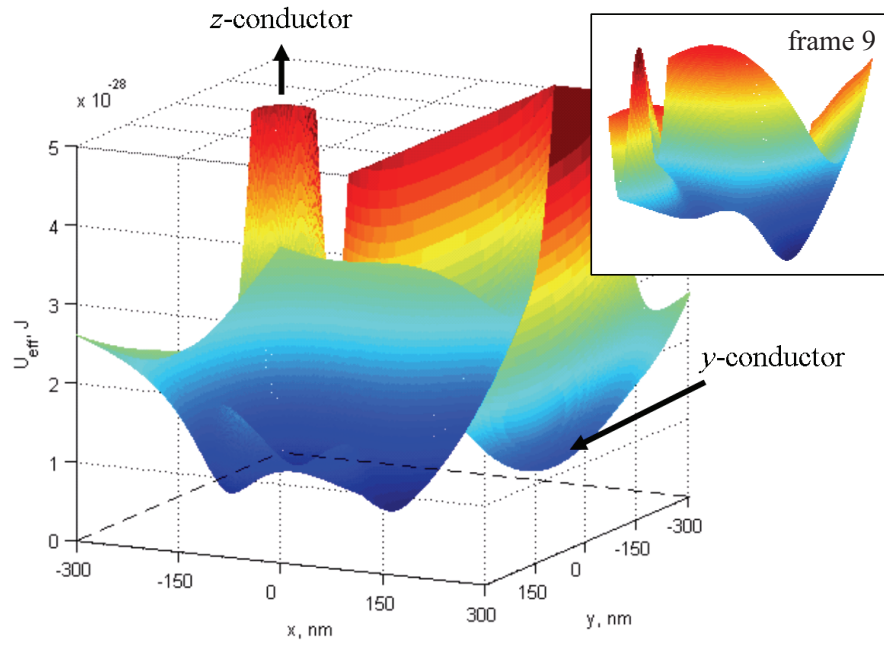


Fig. 3.24. U_{eff} in the xy -plane in frame 8 of the animation in Fig. 3.19.

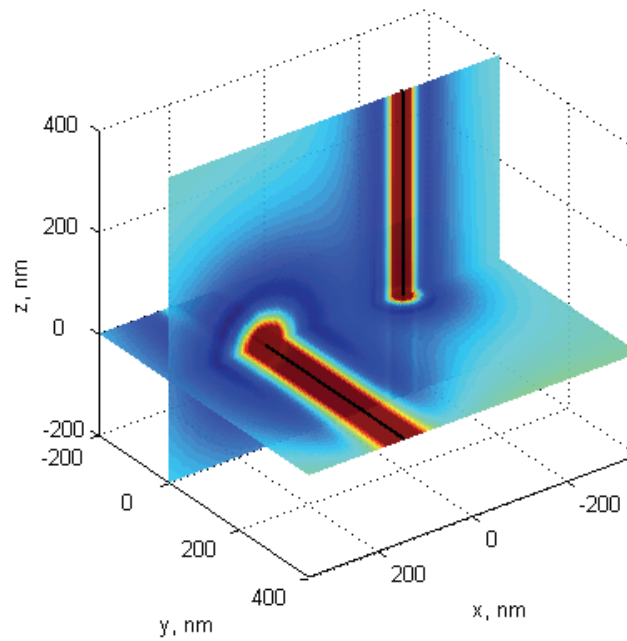


Fig. 3.25. Frame 11 in the animation in Fig. 3.19. Here $I_{\text{DC}, z\text{-wire}} = 0.5 \cdot IZ1$.

The RF currents have not been altered in either nanotube in the sequence of frames. The cold atoms can finally be pumped along the acceptor nanotube and the atom transfer is complete. This was shown in frame 12 – 14 in Fig. 3.19.

The cold atoms can also be pumped away along the acceptor nanotube at once without turning down the DC current in the donor nanotube. This can be done by replacing frame 8 – 14 in the animation in Fig. 3.19 by four alternative frames with the following bias currents:

$$I_{\text{RF}|z\text{-cond. rings}}^{\text{I+II}} = \{[-110 \ 110], [-70 \ 70], [-10 \ 10], [-10 \ 10]\} \mu\text{A},$$

$$I_{\text{RF}|y\text{-cond. rings}}^{\text{I+II}} = \{[-280 \ 210], [-280 \ 140], [-350 \ 70], [-350 \ 0]\} \mu\text{A},$$

The DC current in the nanotube in the z -direction is kept at $-15 \mu\text{A}$. The DC current in the nanotube in the y -direction and the RF currents in both nanotubes are the same as before. Because the bias currents in the four new frames are similar to the bias currents in frames they replace in Fig. 3.19 there is not much more to show. The four frames will therefore not be illustrated further.

The decision on how to complete the atom transfer depends on whether the barrier height in frame 9 of $\sim 1 \mu\text{K}$ is adequate to prevent cold atoms from tunnelling back into the slightly shallower minimum around the donor nanotube. The height of the barrier between the potential minima around the nanotubes as the common minimum is split is shown in Fig. 3.23. The sequence of frames in Fig. 3.19 has been arrived at as a best effort and there is no guarantee that the result is good enough to be viable in practise.

The approach of splitting the common minimum may have advantages in a quantum computer [156], since it allows cold atoms to be stored around the acceptor nanotube temporarily. It would also free up the donor nanotube faster so that it can be used to transport a second cloud of cold atoms somewhere else. The key word here is faster, since it will otherwise take time to move the cold atoms sufficiently far from the crossing point to disconnect the minimum potential surfaces around the nanotubes. In the end one may not have a choice in this matter. The alternative of pumping away the cloud of cold atoms at once is both simpler and more robust against tunnelling and should work just as well in most cases. The easiest solution may here turn out to also be the best solution.

3.7 A four carbon nanotube cell

The geometry of the cell is as shown in Fig. 2.29. The four nanotube cell should also be optimized. The optimization routine used is the same as for the four-wire cell in Chapter 2, and the variables x/z and $dy1$ are optimized. The DC current and the half-distances d between two crossed and two parallel conductors from Section 3.5 are used as initial values in the optimization routine. The DC currents in the nanotubes are $I/Z1 = -15 \mu\text{A}$, $I/Z2 = 15 \mu\text{A}$, $I/Y1 = -15 \mu\text{A}$ and $I/Y2 = 15 \mu\text{A}$.

The optimized values are $x/z = -128.4 \text{ nm}$ and $dy1 = -177.8 \text{ nm}$. The effective potential has been minimized in the point $(x, y, z) = (0, dy1, dy1)$ for x/z and in the point $(x, y, z) = (x/z, 0, dy1)$ for $dy1$. The variables x/z and $dy1$ are the x -axis displacement of the (row of) conductors pointing in the z -direction and the y -axis displacement of conductor “1”, which also points in the z -direction, respectively. The remaining variables are defined as $dy2 = -dy1$, $dzn = dyn$ for $n = 1 - 2$ and $x/y = -x/z$. The RF currents are $4 \mu\text{A}$ of the same sign as the DC current in each conductor. The RF frequency is 0.27 MHz and the radius of the nanotubes is 3.52 \AA .

The effective potential manifold $U_{\text{eff}} = 5e-29 \text{ J}$ is shown in Fig. 3.26. The figure clearly shows a double surface around the nanotubes. The potential minimum is located between the two surfaces. The shape of the potential appears a bit chubbier in Fig. 3.26 compared to in Fig. 2.31 for the four-wire cell. This is because the potential level shown is higher relative to the depth of the trap. Fig. 3.27 shows the effective potential in three slices through the cell at $x = 0$, $y = dy2$ and $z = dz1$. The dark blue figure-of-eight pattern around the nanotubes in the y -direction indicates that the optimization has been successful. A 3D isolated potential maximum is again seen at the centre of the cell.

When only DC currents are used the four nanotube cell has a potential minimum at the centre as shown in Fig. 3.28. The figure is similar to Fig. 3.3 for the four micro-wire cell. The effective potential is very high and increases sharply towards the nanotube walls inside the brown circles. The current density in the nanotubes is clearly very high for their small size.

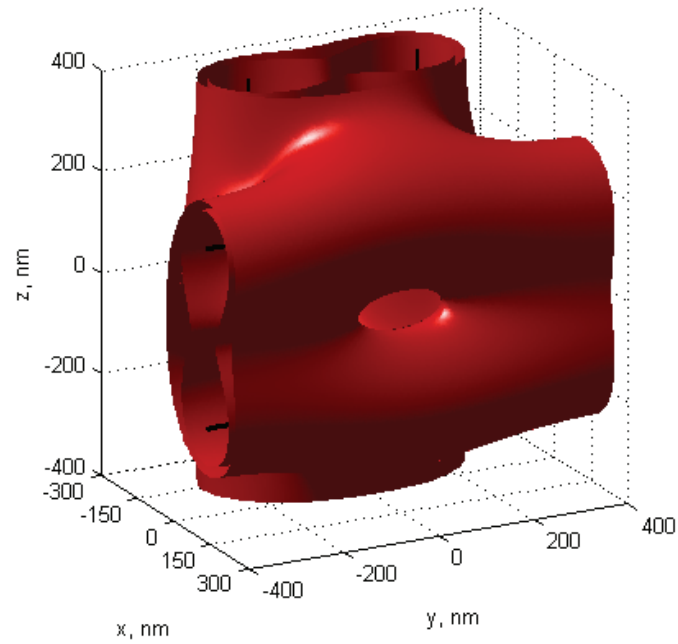


Fig. 3.26. The potential surface $U_{\text{eff}} = 5e-29 \text{ J}$ in a four carbon nanotube cell.

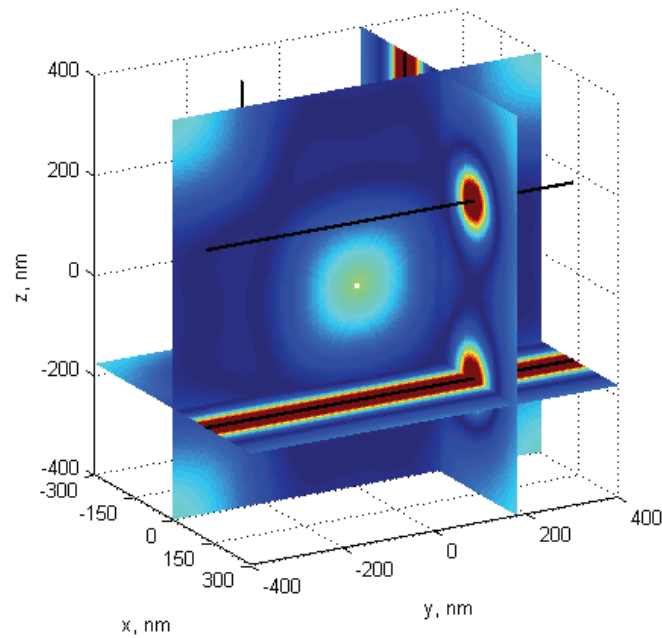


Fig. 3.27. Slice-plot showing the four-CN cell excited by DC and RF currents.

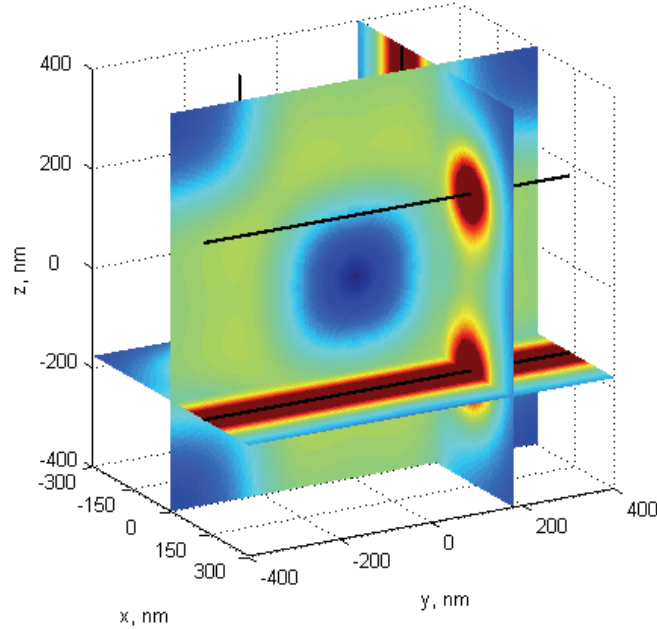


Fig. 3.28. Slice-plot showing the four-CN cell excited by only the DC currents.

The depth of the four nanotube cell trap is described by the graphs along the x -axis in Fig. 3.29 and along the z -axis in Fig. 3.30. The axes are the same as in Fig. 3.28. The temperature of the potential is $T = U_{eff} / k_B$. The potential along the y -axis is identical to the potential along the z -axis in Fig. 3.30. In the two figures the red graphs are for $f_{RF} = 0.27$ MHz, the green graphs for $f_{RF} = 0.18$ MHz, the blue graphs for $f_{RF} = 0.09$ MHz and the black graphs for zero frequency.

A magnetic quantum number of $m_F = 2$ has been used for all graphs. If the potential maximum at the centre of the cell is used to catch and hold ground state atoms with $m_F = 1$, the effective potential shown by the graphs must be divided by two according to equation (2.1), when the ground state atoms are considered. The potential maximum at the centre, which is due to the RF dressing effect, is approximately equal to $m_F \cdot \hbar \cdot \omega_{RF} / k_B$. The effective potential is zero at the centre of the trap when it is excited by only the DC currents. For DC + RF excitation it is difficult to establish whether or not the minimum around the centre of the cell is at zero potential.

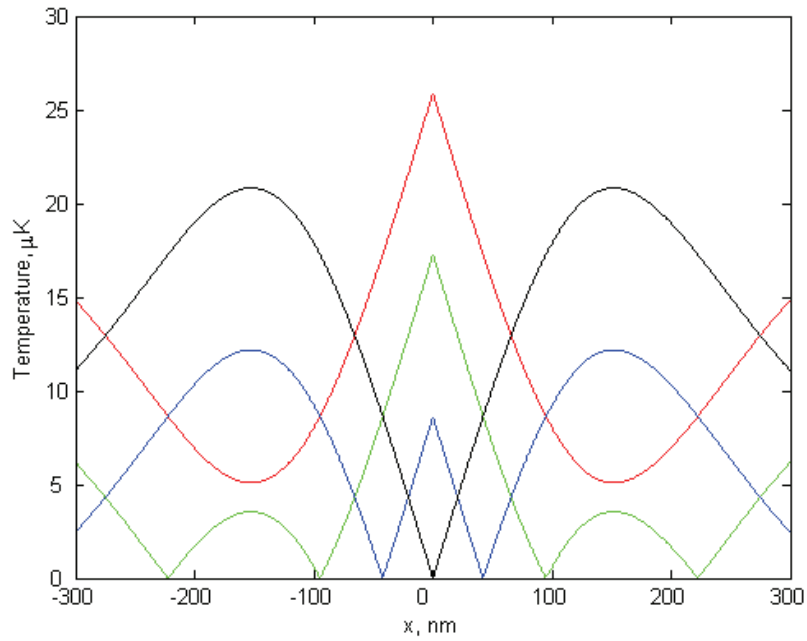


Fig. 3.29. Potential along the x -axis through the centre of the four nanotube cell.

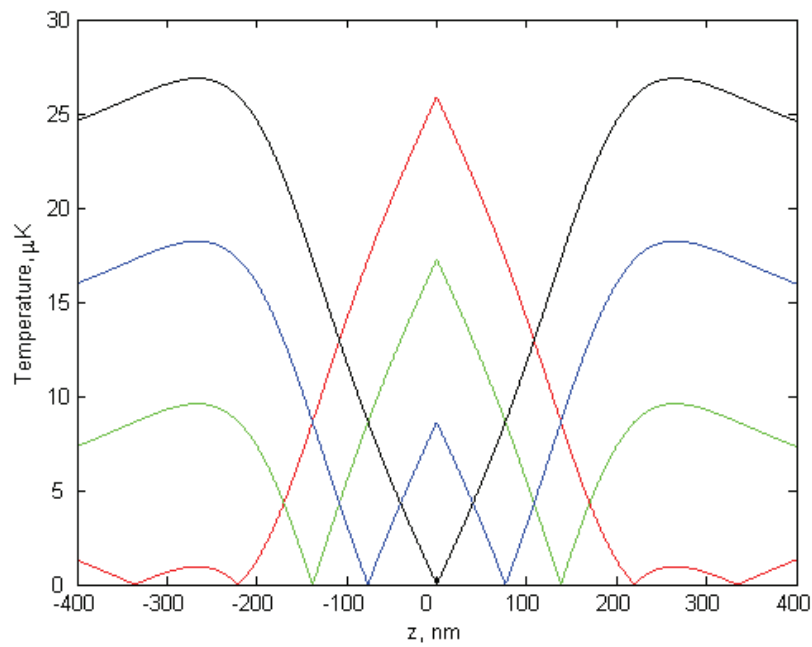


Fig. 3.30. Potential along the z -axis through the centre of the four nanotube cell.

The graphs in Fig. 3.29 and Fig. 3.30 show that the depth of the trap is proportional to the RF frequency. When the RF frequency is 0.27 MHz the depth of the trap is reduced to approximately one third of what it is when the RF frequency is 0.8 MHz. An early but mistaken attempt at scaling in which DC currents of 15 μA , RF currents of 4 μA and an RF frequency of 0.8 MHz were used, resulted in a minimum distance d for a single nanotube of 34.6 nm. When optimized this design gave the same trap depth as the millimetre and micrometre sized cell traps. Such a small trapping distance d is clearly not feasible in practise.

3.8 A single-layered CN cell-grid

A 3 x 3 crossed nanotube design has been described in [151]. The trapping barrier has however turned out to be very low in the x -direction close to the centre conductors when the two effective potential peaks or wells have been merged. The 3 x 3 nanotube geometry is therefore not expected to be good enough to be worth implementing in practise unless multi-walled or bundled nanotubes can be used. The assessment of such nanotubes is however judged to be beyond the scope of this work. The 3 x 3 nanotube geometry will accordingly not be given further description here.

A 6 x 6 crossed nanotube cell-grid has been studied. The geometry is as shown for the wire version in Fig. 2.54. Fig. 3.31(a) shows the effective potential in five slices for $x = 0$, $y = \{dy2, 0.5 \cdot (dy6 - dy4)\}$ and $z = \{0.5 \cdot (dz5 - dz3), dz1\}$. The figure gives a view of where the potential minimum and the potential maxima can be found inside the geometry.

A mesh-plot of the effective potential in the yz -plane has been published in Fig. 5 in [151]. Fig. 6 in [151] shows the effective potential in the same plane when the geometry is driven by only the DC currents. Apart from the different distance measurements, and that the height of the peaks or wells is reduced to about one third, the figures closely resemble the corresponding figures for the 6 x 6 wire geometry in Fig. 2.55 and Fig. 2.57. The chequered pattern of peaks can be reversed by changing the direction of the currents in one of the nanotube rows.

The effective potential in the slice for $y = dy2$ shown in Fig. 3.31(b) confirms visually that the optimization of the structure has been successful. Inspection of the resulting effective potential in this way seems to be the only way to check the quality of the optimized solution.

Six variables have been optimized for the 6 x 6 nanotube cell-grid. The variables are listed in Table 3.2 together with their values and the point where the effective potential function has been minimized. The optimization technique is the same as for the four-wire cell in Section 2.8. The variables $IZ3$ and $IZ5$ are the DC current magnitudes in the second outermost and outermost nanotubes in each conductor-plane. $dy1$, $dy3$, and $dy5$ are the distances from the symmetry line of each conductor-plane to the innermost, second outermost and outermost nanotubes respectively. The variable $xIz = h/2$ sets the distance between the two nanotube rows.

Table 3.2. Optimized variables for the nanotube cell-grid in Fig. 3.31. A total of six variables have been optimized. The variable $IZ1$ is listed in addition.

Variable	Value	U_{eff} minimized in point (x, y, z)
$(IZ1)$	-15.0 μA	Not optimized
$IZ3$	15.1 μA	0, $dy3$, $dy1$
$IZ5$	-13.4 μA	0, $dy5$, $dy1$
$dy1$	-164.9 nm	xIz , 0, $dy1$
$dy3$	-493.5 nm	xIz , $(dy3-0.5*(dy3-dy1))$, $dy1$
$dy5$	-830.6 nm	xIz , $(dy5-0.5*(dy5-dy3))$, $dy1$
xIz	-118.5 nm	0, $dy1$, $dy1$

All other DC currents and distances used in the simulation are determined from the variables in Table 3.2. The DC currents in remaining nanotubes become $IZn = -IZ(n-1)$ for $n = \{2, 4, 6\}$ and $IYn = IZn$ for $n = 1 - 6$. The remaining distances can be found as $dyn = -dy(n-1)$ for $n = \{2, 4, 6\}$ and $dzn = dyn$ for $n = 1 - 6$. $xIy = -xIz$. The nanotubes have here been numbered in the positive y -direction or from bottom to top as $\{5\ 3\ 1\ 2\ 4\ 6\}$.

In Fig. 2.54 the conductors are numbered from 1 – 6 in ascending order. Relative to Fig. 2.54 the currents in the nanotubes become as follows:

$$I_{\text{DC}|z\text{-tube}}^{(1-6)} = [-13.4, 15.1, -15.0, 15.0, -15.1, 13.4] \mu\text{A} \text{ and}$$

$$I_{\text{DC}|y\text{-tube}}^{(1-6)} = [-13.4, 15.1, -15.0, 15.0, -15.1, 13.4] \mu\text{A}.$$

The RF currents are $I_{\text{RF}|z\text{-tube}}^{(1-6)} = [-4, 4, -4, 4, -4, 4] \mu\text{A}$ and

$$I_{\text{RF}|y\text{-tube}}^{(1-6)} = [-4, 4, -4, 4, -4, 4] \mu\text{A}. \text{ The frequency is } f_{\text{RF}} = 0.27 \text{ MHz}.$$

The distances shown in Fig. 2.54 become $d_{12} = |dy5|-|dy3| = 337.0 \text{ nm}$, $d_{23} = |dy3|-|dy1| = 328.6 \text{ nm}$ and $d_{34} = 2\cdot|dy1| = 329.9 \text{ nm}$. $h = 2\cdot|xIz| =$

237.0 nm. The inter-nanotube spacing differs by less than 2.6 %. This suggests that uniform inter-wire spacing could work if a more robust optimization scheme can be found.

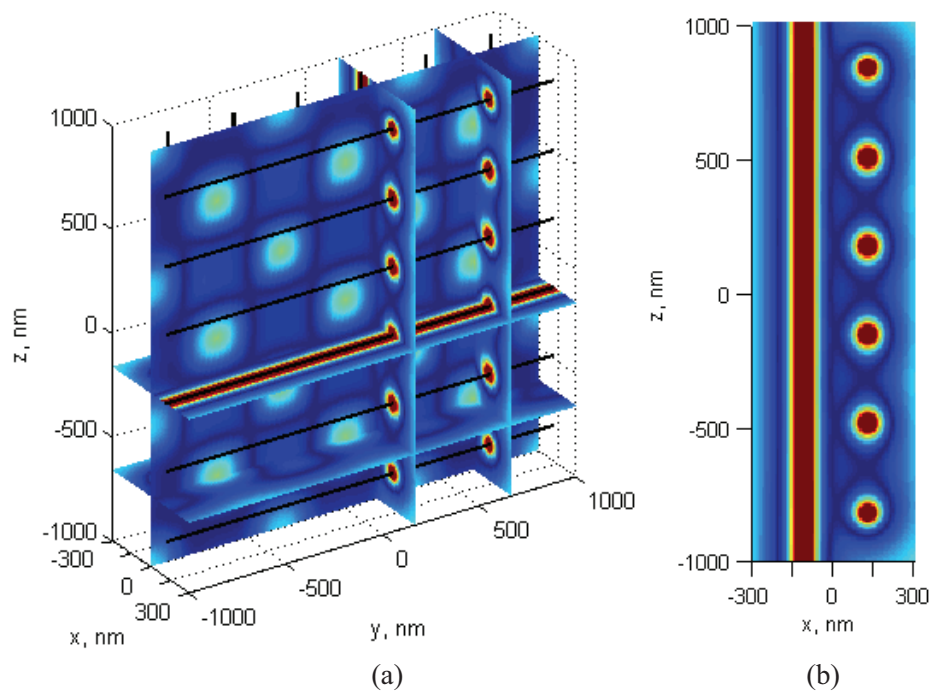


Fig. 3.31. The DC + RF generated potential in a 6 x 6 CN grid (a), and the slice for $y = dy/2$ shown by itself (b).

The application of the nanotube cell-grid is similar to that of the corresponding wire structure in Chapter 2. That is as part of a quantum register with increased noise immunity. The downscaling changes primarily the size of the atom clouds that can be held for processing. The effective potential pattern in the nanotube cell-grid can be considered to be rigid and should be used as it is in an eventual application. It is however possible to turn the potential maxima into potential minima in all cells simultaneously by reducing the frequency and by turning down the RF currents.

3.9 Multi-layered CN cell-grids

Nanotube cell-grids are stackable in the same way as the wire cell-grids in Chapter 2. To show this an example of two stacked cell-grids will be given first, followed by an example of three stacked cell-grids. 6 x 6 nanotube cell-grids similar to the one in Section 3.8 will be used.

The effective potential for two stacked 6 x 6 CN cell-grids is shown in five slices for $x = -x_3z$, $y = \{dy_2, 0.5 \cdot (dy_6 - dy_4)\}$ and $z = \{dz_5, 0\}$ in Fig. 3.32. This type of plot is useful to give an overview of the potential inside larger geometries. As explained in Chapter 2, the difficulty here lies in the optimization of the distances between the conductors and the critical DC currents. The two cell-grids must be considered together for the optimization to be successful. The geometry consists of two inner and two outer nanotube rows. These require separate sets of optimized variables.

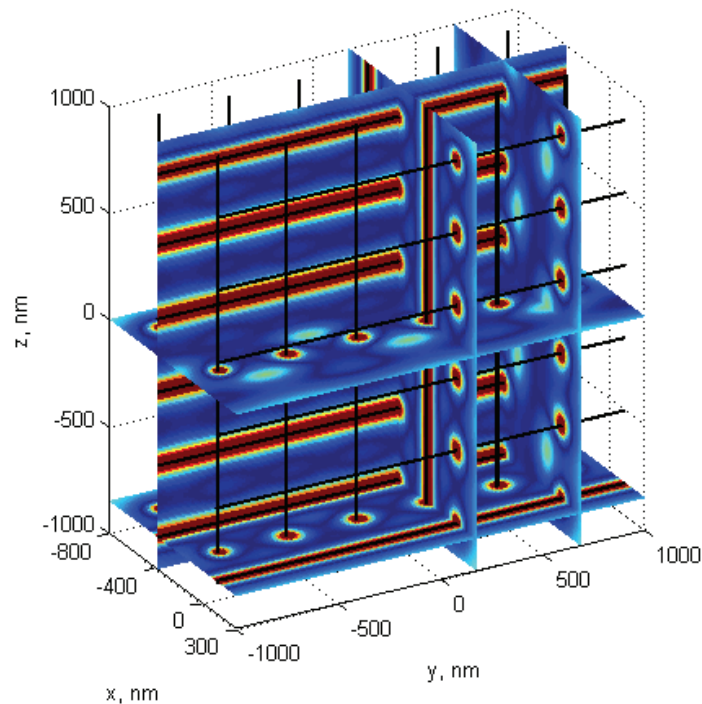


Fig. 3.32. The effective potential generated by DC and RF currents in a 24 CN structure.

All variables that have been optimized are listed in Table 3.3 together with their values and the point where the effective potential function has been minimized. The variables $dy1$, $dy3$, $dy5$, $IZ3$ and $IZ5$ are connected with the inner conductor rows and the variables $dz1$, $dz3$, $dz5$, $IY1$, $IY3$ and $IY5$ pertain to the outer conductor rows. The distances between the conductor rows have been optimized through the variables $x1z$, $x2z$ and $x3z$. $2 \cdot |x1z|$ is the distance between the outer conductor rows and the closest of the inner conductor rows. The distance between the two inner conductor rows is $x3z - x1z$. The variable $x2z$ has also been optimized but it is not independent for this geometry and can be found as $x2z = 2 \cdot x1z - x3z$.

Table 3.3. Optimized variables for the nanotube cell-grid structure in Fig. 3.32. A total of fourteen variables have been optimized. The variable $IZ1$ is also listed.

Variable	Value	U_{eff} minimized in point (x, y, z)
($IZ1$)	-15.0 μA	Not optimized
$IZ3$	15.1 μA	$(-x3z-0.5*(-x3z-x1z)), dy3, dz1$
$IZ5$	-12.2 μA	$(-x3z-0.5*(-x3z-x1z)), dy5, dz1$
$IY1$	-15.8 μA	Scaled only with $IY3$ and $IY5$
$IY3$	16.1 μA	0, $dy1, dz3$
$IY5$	-13.3 μA	0, $dy1, dz5$
$dy1$	-171.5 nm	$x1z, 0, dy1$
$dy3$	-514.4 nm	$x1z, (dy3-0.5*(dy3-dy1)), dy1$
$dy5$	-849.4 nm	$x1z, (dy5-0.5*(dy5-dy3)), dy1$
$dz1$	-169.5 nm	$-x1z, dy1, 0$
$dz3$	-509.4 nm	$-x1z, dy1, (dz3-0.5*(dz3-dz1))$
$dz5$	-849.4 nm	$-x1z, dy1, (dz5-0.5*(dz5-dz3))$
$x1z$	-125.2 nm	0, $dy1, dy1$
$x2z$	-630.4 nm	$(-x3z+0.5*(x2z+x3z)), dy1, dz1$
$x3z$	380.0 nm	$(-x1z+0.5*(x3z+x1z)), dy1, dz1$

The other DC currents and distances in the simulation are found from symmetry from the variables in Table 3.3. The remaining DC currents are $IZn = -IZ(n-1)$ for $n = \{2, 4, 6\}$ and $IYn = -IY(n-1)$ for $n = \{2, 4, 6\}$ for the cell-grid in front in Fig. 3.32 (g1). $IZn = -IY(n-6)$ for $n = 7 - 12$ and $IYn = -IZ(n-6)$ for $n = 7 - 12$ for the cell-grid to the rear in Fig. 3.32 (g2).

The remaining distances become $dyn = -dy(n-1)$ for $n = \{2, 4, 6\}$ and $dzn = -dz(n-1)$ for $n = \{2, 4, 6\}$ for the cell-grid in front in Fig. 3.32 (g1). $dyn = dz(n-6)$ for $n = 7 - 12$ and $dzn = dy(n-6)$ for $n = 7 - 12$ for the cell-

grid to the rear in Fig. 3.32 (g2). The variable $x1y = -x1z$. The variable $x3z$ has been optimized to find $x2y$, which is equal to $-x3z$.

For the two inner nanotube rows $dy1$ is the distance from the symmetry line of each nanotube row to the innermost nanotubes, $dy3$ is the distance from the symmetry line to the second outermost nanotubes and $dy5$ is the distance from the symmetry line to the outermost nanotubes. For the two outer nanotube rows the corresponding distances are $dz1$, $dz3$ and $dz5$.

The distances $dz5$ and $dy5$ have again become as good as identical. The reason for this is that the currents $IY1$, $IY3$ and $IY5$ have been scaled in the optimization in the same way as described in Section 2.10 for the multi-layered wire grids.

The distances dyn and dzn for $n = \{1, 3, 5\}$ can be seen to differ by at most 1.2 %. Furthermore the difference between $dy3$ and $dz3$ calculated as $dy3 = dz3 = 3 \cdot dy1$ or $dy5$ and $dz5$ calculated as $dy5 = dz5 = 5 \cdot dy1$ and the optimized values for the same variables is at most about one percent. It therefore seems that the same inter-conductor spacing can be used for both the inner and outer conductor rows. A uniform conductor spacing based on the optimization of just one distance should also be possible.

The currents in the four nanotube rows can be summed up as follows:

$$I_{\text{DC}|z\text{-tube}, g1}^{(1-6)} = [-12.2, 15.1, -15.0, 15.0, -15.1, 12.2] \mu\text{A},$$

$$I_{\text{DC}|y\text{-tube}, g1}^{(1-6)} = [-13.3, 16.1, -15.8, 15.8, -16.1, 13.3] \mu\text{A},$$

$$I_{\text{DC}|z\text{-tube}, g2}^{(1-6)} = [13.3, -16.1, 15.8, -15.8, 16.1, -13.3] \mu\text{A},$$

$$I_{\text{DC}|y\text{-tube}, g2}^{(1-6)} = [12.2, -15.1, 15.0, -15.0, 15.1, -12.2] \mu\text{A},$$

where $g1$ refers to the cell-grid in front in Fig. 3.32 and $g2$ refers to the cell-grid to the rear. The nanotubes are here numbered in the positive y -direction and from bottom to top. The RF currents are $4 \mu\text{A}$ of the same sign as the DC current in each nanotube. The frequency is $f_{\text{RF}} = 0.27 \text{ MHz}$.

Fig. 3.33 shows the effective potential in the xz -plane in two slices for $y = 0$ and $y = dy2$ separately. The slice for $y = 0$ in Fig. 3.33(a) shows that local potential maxima are found both within each grid and between the grids. The local maxima at the centre of the geometry are seen to be fully surrounded by a deep potential minimum.

The slice for $y = dy2$ in Fig. 3.33(b) can be used to assess the quality of the optimization. For the most part the effective potential minimum seems

to be exactly where it should be. Notice however that there is no strong potential minimum between the uppermost and lowermost nanotubes in the y -direction where $x \approx -380$ nm and the nanotube in the z -direction in the outer nanotube row. It is in this case difficult to point to any one variable as having been optimized badly. The simplicity of the optimization scheme itself seems to be the source of the problems as discussed in Chapter 2. It is thought that a different and better optimization approach is necessary to yield further improvement.

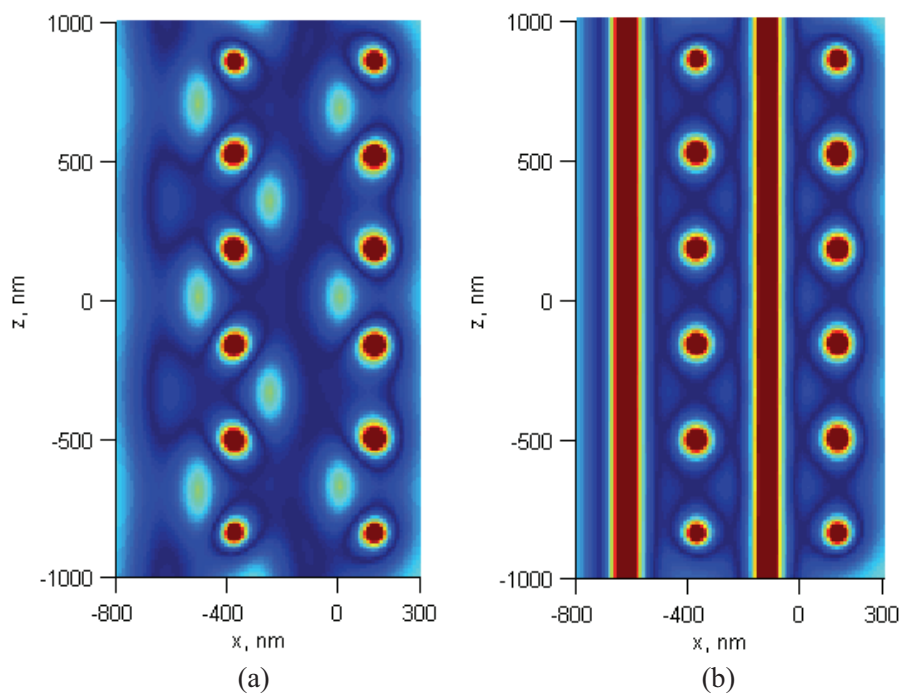


Fig. 3.33. The effective potential in slices for $y = 0$ (a) and $y = dy/2$ (b).

When three nanotube cell-grids are stacked the effective potential pattern becomes as shown in Fig. 3.34 and Fig. 3.35. Fig. 3.34 shows the potential surface $U_{\text{eff}} = 5e-29$ J and Fig. 3.35 shows the effective potential inside the structure in slices for $x = \{x/2z, 0\}$, $y = \{0, dy/6\}$ and $z = \{dz/5, 0\}$. The geometry of the nanotubes has been drawn in both figures.

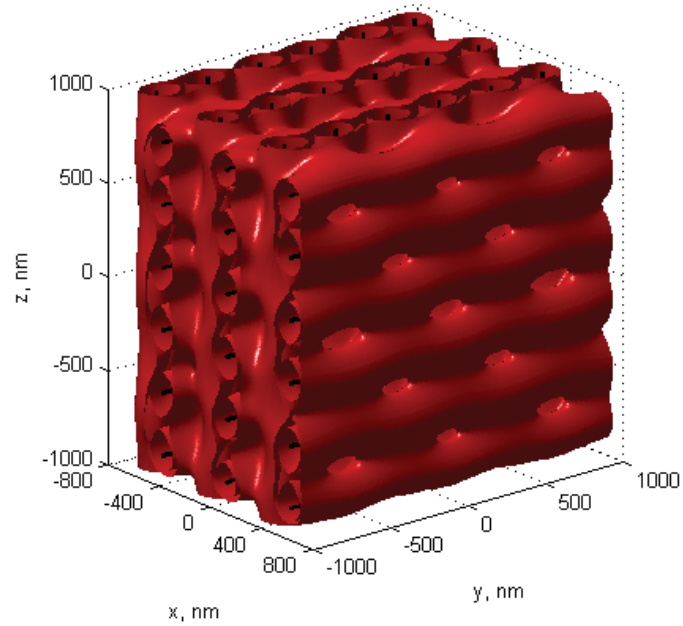


Fig. 3.34. The isosurface $U_{\text{eff}} = 5\text{e-}29$ J for a 36 CN structure with DC and RF excitation.

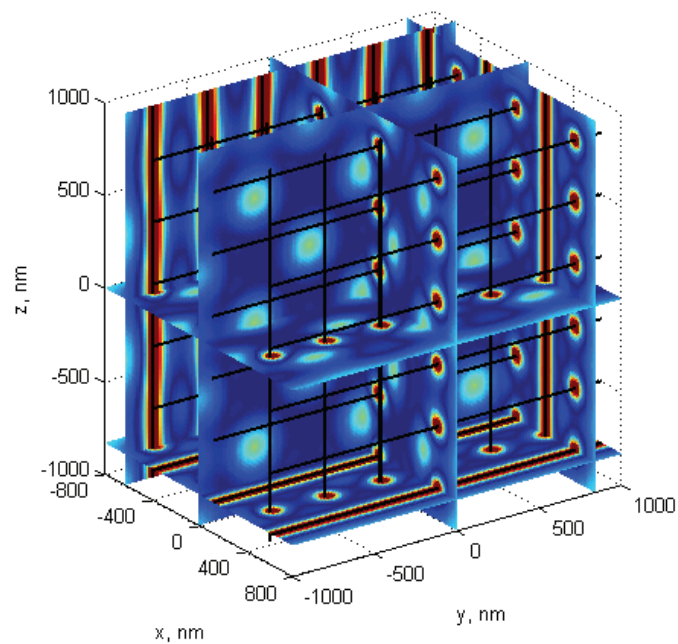


Fig. 3.35. The effective potential generated by DC and RF currents in the 36 nanotube structure.

The nanotube rows in the cell-grid in the middle lie symmetrically inside the geometry and can consequently share one set of optimized variables. The optimized variables are $IZ3$, $IZ5$, $dy1$, $dy3$ and $dy5$. The letters y or Z and the numbers in the variable names have the following meaning. For distance variables “ y ” refers to y -axis displacement and for current variables “ Z ” is the pointing direction of the nanotube. The numbers refer to the nanotubes in each row numbered in the positive y -direction or from bottom to top in the order $\{5\ 3\ 1\ 2\ 4\ 6\}$.

The variables $IZ7$, $IZ9$, $IZ11$, $dy7$, $dy9$ and $dy11$ have been optimized for the two outermost nanotube rows in the geometry. The numbers 7 – 12 here relate to the nanotubes in the grid at the back (g2) in Fig. 3.34. The nanotubes in the grid in the middle (g1) have the numbers 1 – 6 and the nanotubes in the grid at the front (g3) have the numbers 13 – 18. But for this grid (g3) the variables are found from the grid in the back (g2) from symmetry. Just as for the multi-layered wire-grids in Section 2.10 the currents $IZ7$, $IZ9$ and $IZ11$ have been scaled up or down with each iteration of the while-loop depending on whether $dy11$ is greater than or equal to $dy5$, or smaller than $dy5$, respectively.

The relevant variables for the two second outermost wire rows in the geometry have only been optimized in part. The DC currents in the second outermost ($IY9$) and outermost nanotubes ($IY11$) have been optimized, while the DC current in the innermost nanotubes ($IY7$) has been set equal to $IZ1$. The distance variables have been set equal to those for the nanotube grid at the centre, i.e. $dz7 = dy1$, $dz9 = dy3$ and $dz11 = dy5$. Attempts to include $dz7$, $dz9$, $dz11$ and $IY7$ among the optimized variables have caused the optimization script to latch on to a bad solution for some of the variables, which causes the optimization to fail.

The distances between the nanotube rows have been optimized through the variables $x1z$, $x2z$ and $x3z$. As before $x1z$ is the distance from the symmetry plane ($x = 0$) through the centre of the geometry to the nanotube row pointing in the z -direction in cell-grid one. $x2z$ and $x3z$ are the distances from the symmetry plane to the nanotube rows pointing in the z -direction in cell-grids two and three respectively. All the optimized variables are shown in Table 3.4 together with their values and the point where the effective potential function has been minimized.

Table 3.4. Defining variables for the nanotube cell-grid structure in Fig. 3.34. Altogether 16 variables have been optimized. The variables $IZ1$, $IY7$, $dz7$, $dz9$ and $dz11$ have also been listed to give a clearer picture.

Variable	Value	U_{eff} minimized in point (x, y, z)
$(IZ1)$	-15.0 μA	Not optimized
$IZ3$	15.1 μA	0, $dy3$, $dy1$
$IZ5$	-12.9 μA	0, $dy5$, $dy1$
$IZ7$	15.6 μA	Scaled only with $IZ9$ and $IZ11$
$IZ9$	-15.6 μA	$(-x3z+0.5*(x2z+x3z))$, $dy9$, $dz7$
$IZ11$	13.6 μA	$(-x3z+0.5*(x2z+x3z))$, $dy11$, $dz7$
$(IY7)$	Set equal to $-IZ1$	Not optimized
$IY9$	-15.1 μA	$(-x3z+0.5*(x2z+x3z))$, $dy7$, $dz9$
$IY11$	13.9 μA	$(-x3z+0.5*(x2z+x3z))$, $dy7$, $dz11$
$dy1$	-166.9 nm	$x1z$, 0, $dy1$
$dy3$	-500.8 nm	$x1z$, $(dy3-0.5*(dy3-dy1))$, $dy1$
$dy5$	-833.3 nm	$x1z$, $(dy5-0.5*(dy5-dy3))$, $dy1$
$dy7$	-167.4 nm	$x2z$, 0, $dz7$
$dy9$	-502.4 nm	$x2z$, $(dy9-0.5*(dy9-dy7))$, $dz7$
$dy11$	-833.3 nm	$x2z$, $(dy11-0.5*(dy11-dy9))$, $dz7$
$(dz7)$	Set equal to $dy1$	Not optimized
$(dz9)$	Set equal to $dy3$	Not optimized
$(dz11)$	Set equal to $dy5$	Not optimized
$x1z$	-125.2 nm	0, $dy1$, $dy1$
$x2z$	-624.6 nm	$(-x3z+0.5*(x2z+x3z))$, $dy7$, $dz7$
$x3z$	376.8 nm	$(-x1z+0.5*(x3z+x1z))$, $dy7$, $dz7$

The remaining DC currents and distances used in the simulation are found from the optimized variables in Table 3.4 by exploiting symmetry. The DC currents become as follows: $IZn = -IZ(n-1)$ for $n = \{2, 4, 6, 8, 10, 12\}$ and $IYn = IZn$ for $n = 1 - 6$. $IY8 = -IY7$, $IY10 = -IY9$ and $IY12 = -IY11$. $IZn = IY(n-6)$ for $n = 13 - 18$ and $IYn = IZ(n-6)$ for $n = 13 - 18$.

The remaining distances can be found as: $dyn = -dy(n-1)$ for $n = \{2, 4, 6, 8, 10, 12\}$ and $dzn = dyn$ for $n = 1 - 6$. $dz8 = -dz7$, $dz10 = -dz9$ and $dz12 = -dz11$. $dyn = dz(n-6)$ for $n = 13 - 18$ and $dzn = dy(n-6)$ for $n = 13 - 18$. The distances from the symmetry plane ($x = 0$) to the nanotube rows pointing in the y -direction are $x1y = -x1z$, $x2y = -x3z$ and $x3y = -x2z$.

The wire currents in the six nanotube-planes can be summed up as follows:

$$I_{\text{DC}|z\text{-tube}, g1}^{(1-6)} = [-12.9, 15.1, -15.0, 15.0, -15.1, 12.9] \mu\text{A},$$

$$I_{\text{DC}|y\text{-tube}, g1}^{(1-6)} = [-12.9, 15.1, -15.0, 15.0, -15.1, 12.9] \mu\text{A},$$

$$I_{\text{DC}|z\text{-tube}, g2}^{(1-6)} = [13.6, -15.6, 15.6, -15.6, 15.6, -13.6] \mu\text{A},$$

$$I_{\text{DC}|y\text{-tube}, g2}^{(1-6)} = [13.9, -15.1, 15.0, -15.0, 15.1, -13.9] \mu\text{A},$$

$$I_{\text{DC}|z\text{-tube}, g3}^{(1-6)} = [13.9, -15.1, 15.0, -15.0, 15.1, -13.9] \mu\text{A},$$

$$I_{\text{DC}|y\text{-tube}, g3}^{(1-6)} = [13.6, -15.6, 15.6, -15.6, 15.6, -13.6] \mu\text{A},$$

where g1 refers to the cell-grid in the middle in Fig. 3.34, g2 refers to the cell-grid at the back (where the x -values are negative) and g3 to the cell-grid in front. The nanotubes are here numbered sequentially in the positive y -direction or from bottom to top. The RF currents are $4 \mu\text{A}$ of the same sign as the DC current in each nanotube. The frequency is $f_{\text{RF}} = 0.27 \text{ MHz}$.

The success of the optimization can be judged by looking at the effective potential in the slice for $y = dy2$ in Fig. 3.36. The potential minimum can be seen to be just about right everywhere in the slice. Notice that the minimum comes closest to the surface of the nanotubes on the right hand corners. The effective potential slice for $y = dy4$ is essentially identical to the slice for $y = dy2$. In the slice for $y = dy6$, which is partly visible in Fig. 3.35, the pattern of the potential minimum begins to change because the cell structure is discontinued. There seems to be little that can be done about that considering how the structure is optimized.

The slice of the effective potential for $y = 0$ is shown again in Fig. 3.37. The figure shows that the potential barrier is increased in the x -direction between the parallel nanotubes for cells surrounded by other cells within the structure. For cells along the periphery the depth of the minimum is impaired in the outward facing direction. Fig. 3.37 is very similar to Fig. 2.61 for the corresponding wire geometry.

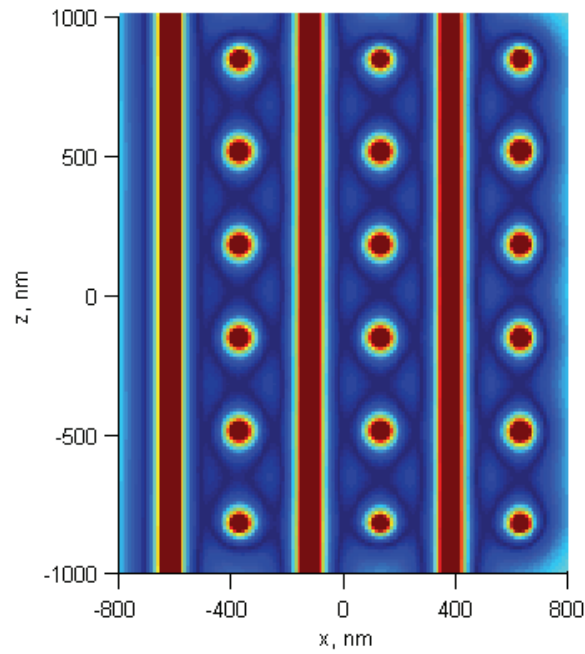


Fig. 3.36. The effective potential slice for $y = dy2$ in the 36 nanotube structure.

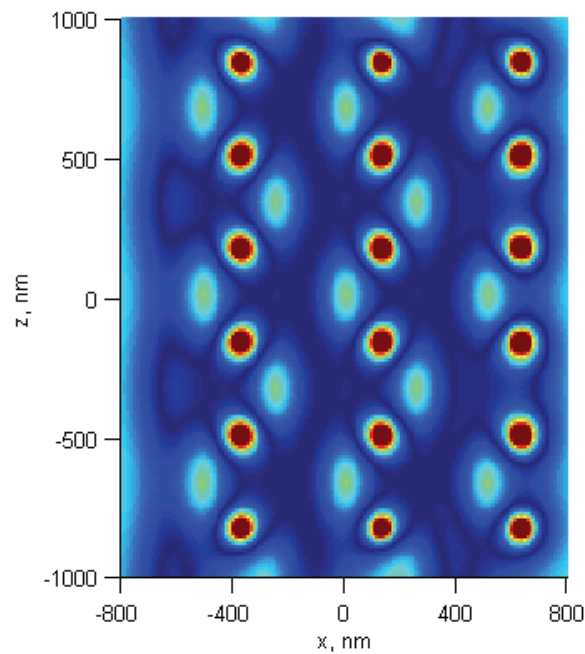


Fig. 3.37. The effective potential slice for $y = 0$ in Fig. 3.35 by itself.

When the nanotubes are excited by only the DC currents, potential minima are found at the centre of the cells (See e.g. Fig. 2.62). This will not be illustrated further here. In order to quantify the benefit of cells being surrounded by other cells in terms of increased height of the potential barrier between the cells, graphs of the effective potential have been calculated along the x -axis ($y = z = 0$) and along the z -axis ($x = y = 0$) through the 36 CN structure. The graphs are shown in Fig. 3.38(a) and (b) respectively. The red curves are for DC + RF excitation with $f_{\text{RF}} = 0.27$ MHz and the black curves are for DC excitation only. The dotted green and blue curves outline the effective potential for the in-between frequencies of $f_{\text{RF}} = 0.18$ MHz and $f_{\text{RF}} = 0.09$ MHz respectively.

The red curves appear to show that the potential minimum is divided in two between the cells. In the nanotube crossing points there are however only single minima both for the x -positions where the peaks are and for x -positions between the two minima between the cells in Fig. 3.38(a). The two minima between the cells are therefore part of the same minimum. There is thus a single minimum between the cells only in the points specified in the optimization.

Several limitations of the optimization technique were discussed in Section 2.10 in Chapter 2. Since the same optimization technique has been used throughout this Chapter the same things will apply also here. We therefore refer readers to the account given in Chapter 2 for additional information on this topic.

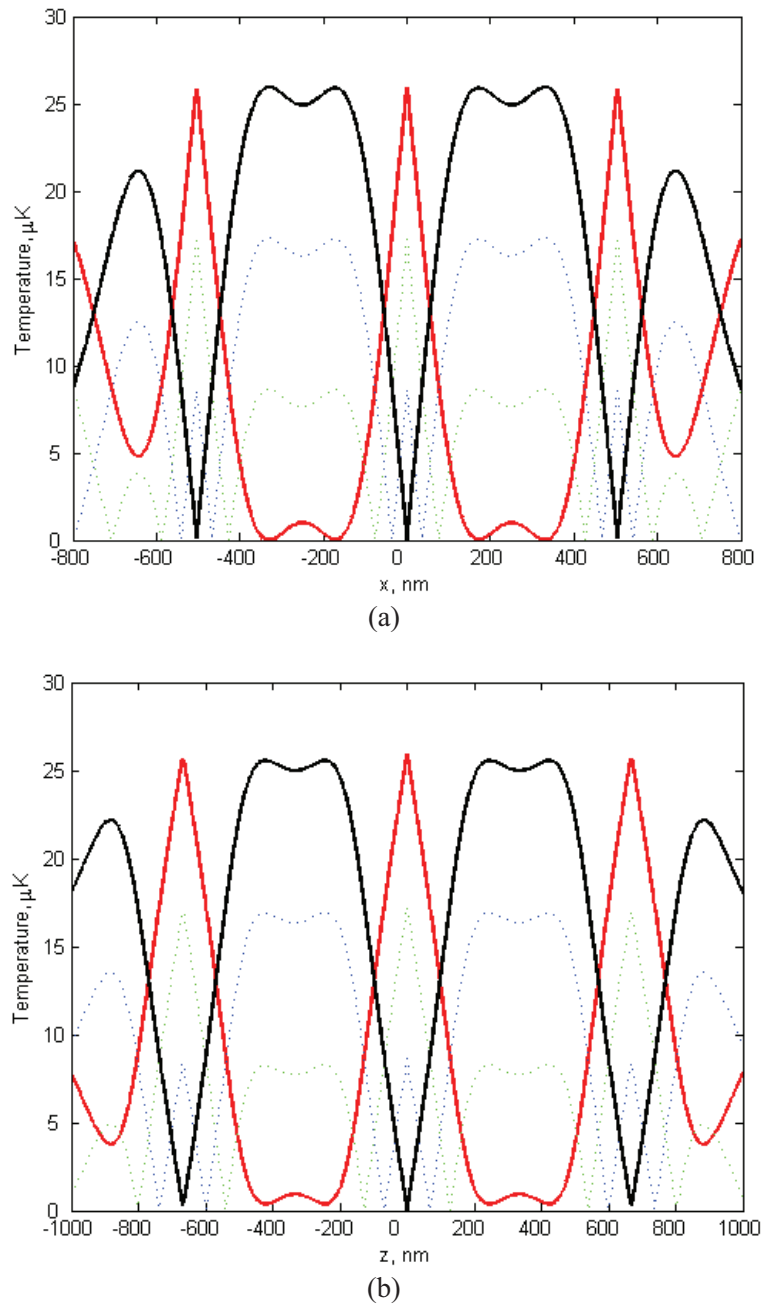


Fig. 3.38. Graphs along the x -axis (a) and z -axis (b) through the 36 CN structure.

3.10 Conclusion

In this Chapter the down-scaling of some of the wire structures from Chapter 2 to micrometre and nanometre size has been described and exemplified. The effects of thermally induced spin-flip transitions and the Casimir-Polder force have also been explained.

When scaling to micrometre size, the cold atom clouds must be kept at a certain minimum distance from the conductors to minimize thermally induced spin-flip transitions. The conductors should also be dimensioned to avoid extreme current densities. If conductors become very hot because of high currents and a finite conductivity, the problem of thermally induced magnetic field fluctuations will get worse.

Two examples have been given of micron sized structures, a four micro-wire cell and a 3 x 3 micro-wire geometry. Both geometries have been adapted toward a future realization on a micro-machined substrate for testing. The shape and depth of the trapping potentials have been found to be the same as for the corresponding wire structures in Chapter 2. The reduced dimensions make the atom traps suited for smaller atom clouds.

Scaling to nanometre size causes two loss mechanisms to play a part. In addition to thermally induced spin-flip transitions the effect of the Casimir-Polder force must be taken into account. The Casimir-Polder force is a generally attractive dispersion force caused by the presence of a dielectric material. The Casimir-Polder force creates a potential which adds to the effective potential created by the DC and RF currents in the conductors. The effect of the Casimir-Polder force is minimized by the use of carbon nanotubes as conductors. The minimum feasible trapping distance is expected to be no less than 100 nm from the surface of a carbon nanotube.

The prospective transfer of cold atoms between two crossed nanotubes has been illustrated. The situation is here much the same as for atom transfer between two crossed wires, which was covered in Section 2.5. The atom transfer may be completed in two ways, by splitting the common minimum or by pumping the cold atoms away from the junction right away. It is an open question whether both of these options are feasible in practise. The bias currents used here have also been too high for the bias rings to be implemented with ordinary carbon nanotubes. It may be possible to use smaller bias currents in practise and the bias rings may then be implemented using multi-walled or bundled nanotubes.

A four carbon nanotube cell trap has been designed and studied. The depth of the trapping potential became only about one third of what it was for the millimetre and micrometre sized four-conductor cell traps

considered previously in Sections 2.8 and 3.3. The depth of the four-nanotube cell trap is proportional to the RF frequency. For a given geometry size the RF frequency corresponds to a certain DC current level in the conductors. If the RF frequency is increased then the DC current level must also increase to maintain the same DC current to angular frequency ratio. The depth of the trap is accordingly also proportional to the DC current level in the conductors. It is the maximum conductor current that effectively limits the depth of the trap. The Larmor frequency is accounted for by the equation for the effective potential in (2.1) and does not have to be considered specifically for the traps and guides designed so far.

Several examples of grid structures composed of nanotubes have also been shown. Apart from the reduced trap depths the shape of the effective potential is practically identical to that of the corresponding wire-grids in Chapter 2. What is most noticeable is how narrow the nanotubes are relative to typical wires and micro-wires.

The optimization of the multi-layered cell-grids continues to pose a challenge in the same way as for the corresponding wire realizations in Chapter 2. The attained optimisation result is quite good for the most part, but there is still room for improvements. Further improvement of the optimization is expected to require the use of a better optimization scheme.

Chapter 4

Millimetre Sized Quadrupolar Traps

4.1 Introduction

A quadrupolar trap, which is similar to the Ioffe-Pritchard trap except for ring currents in opposite directions, is in this Chapter investigated in the RF dressing regime through simulations. The RF dressed Ioffe-Pritchard trap has previously been studied experimentally in [106], [157], and been found capable of trapping both strong- and weak-field-seeking atoms. There is however little published literature on the subject and the simulations presented here are intended to provide additional information in the case of the quadrupolar trap with ring currents in opposite directions.

The effect of reducing the spacing between the bias rings of a trap excited by only DC currents is afterwards also considered. This has been done to explore the possibility of making successively smaller magnetic traps that can be used to compress clouds of BECs for experimental study.

The Chapter begins with a presentation of results for a quadrupolar trap with bias rings with a circular cross-section. In Section 4.2 results from simulations in Amperes are first compared with results computed in Matlab based on the field equations in Section 1.7. Several figures from the numeric simulations of the trap in Amperes have been published to date in [138], [158]. Additional figures and graph data from the Amperes simulations are presented here and compared with equivalent results from Matlab to confirm the validity of the results.

The magnetic fields computed in Matlab assume infinitesimally thin bias rings. However, analogously to the case of fields around bars with a finite radius in Section 1.7.2, it is expected that the computed fields are very similar if not identical outside of the volume of the physical rings. The Amperes software is described in appendix A.

Section 4.2 continues by exploring the effect of different combinations of DC and RF currents in the Ioffe-bars and bias rings without making changes to the geometry. Several initial simulations indicated the presence of deeper potential minima within the circular potential minimum around the local maximum at the centre of the trap. In order to explore why these minima appear and to determine their relative depths, as well as to find out whether the trap is capable of exhibiting similar minima in other places around the central maximum, a number of additional simulations have been made. Because the possible current combinations are endless only a few current combinations which have led to significant changes in the effective potential pattern will be focused on.

In Section 4.3 a similar Ioffe-bar geometry with bias rings with a square cross-section is simulated in Amperes for different gap sizes between the rings. The results from Amperes are also here in part compared to results computed in Matlab by assuming infinitesimally thin bias rings.

4.2 The effect of different excitations of a quadrupolar trap

The geometry of the trap is shown in Fig. 4.1. The four Ioffe-bars, each with a diameter of $d = 1$ mm, are placed with a distance $D = 4$ mm between them. The bias rings, which have been simulated in Amperes, have a cross-sectional radius of $r = 0.5$ mm, an average radius of $R = 5$ mm from the centre of the trap, and are spaced 10 mm apart.

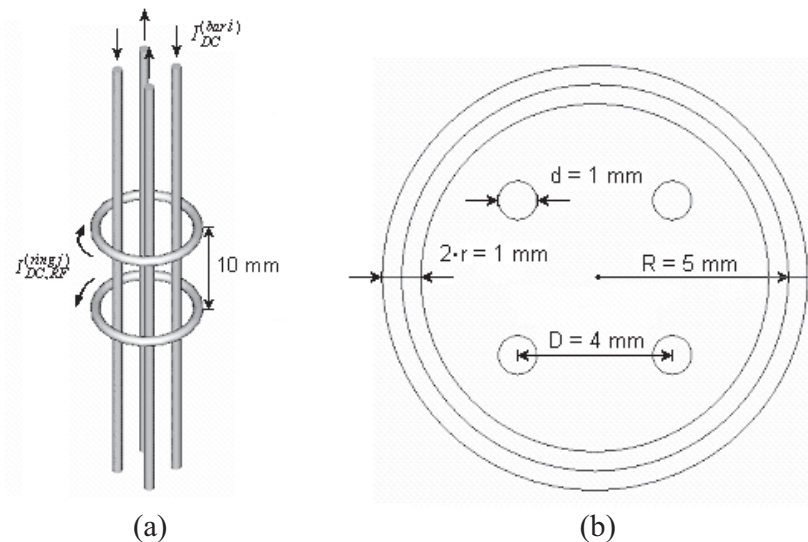


Fig. 4.1. Quadrupolar trap geometry. (a) 3D view, (b) view from above.

Before looking at the magnetic field from the complete trap it is instructive to first look at the field generated by the Ioffe-bars alone. The B-field for the Ioffe-bars, which has been calculated in Matlab, is shown in Fig. 4.2. The unit of the B-field magnitude B_m in Fig. 4.2(b) is Tesla.

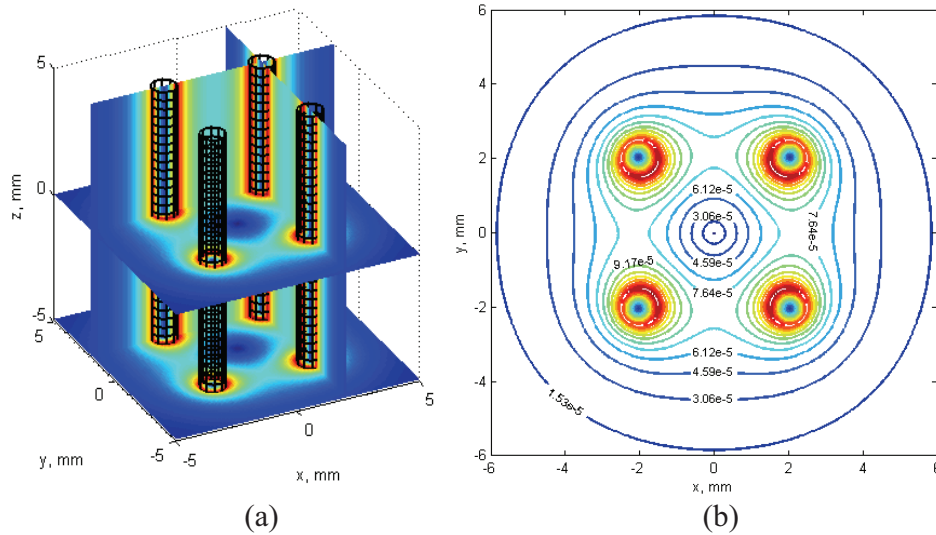


Fig. 4.2. B_m for Ioffe-bars. $|I_{DC, \text{bar}}| = 0.5$ A. (a) 3D view, (b) contour plot.

A second figure also computed in Matlab, which shows B_m for DC ring currents of $|I_{DC, \text{ring}}| = 0.5$ A, is shown in Fig. 4.3. Note that the ring geometry, which is represented by a wireframe mesh in the figure, is the ring geometry simulated in Amperes. The calculated B-field surfaces in Fig. 4.3 are for infinitesimally thin rings. The difference is however quite small as will become clear in a moment.

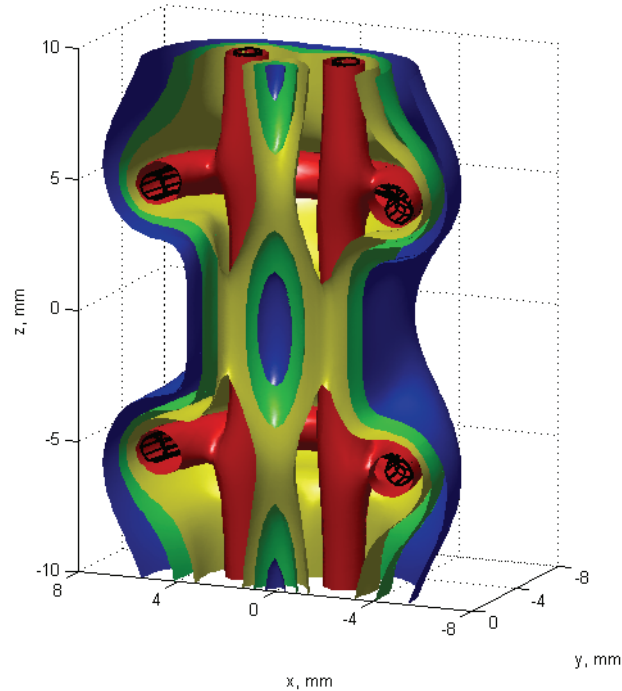


Fig. 4.3. Isosurface plot of B_m for $|I_{DC, \text{bar}}| = 0.5 \text{ A}$ and $|I_{DC, \text{ring}}| = 0.5 \text{ A}$. The four surfaces are $B_m = 3\text{e-}5 \text{ T}$ (blue), $B_m = 5\text{e-}5 \text{ T}$ (green), $B_m = 7\text{e-}5 \text{ T}$ (yellow) and $B_m = 1.3\text{e-}4 \text{ T}$ (red).

A more precise description of the magnetic field is given by contour plots. Three contour plots of the B-field from Amperes and Matlab are shown side by side in Fig. 4.4 for easy comparison. The currents in the bars and ring are the same as in Fig. 4.3, that is $|I_{DC, \text{bar}}| = 0.5 \text{ A}$ and $|I_{DC, \text{ring}}| = 0.5 \text{ A}$. The ring currents are in opposite directions in the two rings.

The plot in Fig. 4.4(a) has the x -axis pointing downwards and is therefore rotated 90° compared to Fig. 4.4(b). It should be mentioned that the contour levels are not exactly identical. In the Matlab figures Fig. 4.4(b, f) and (d) the upper bound on the data for calculating the contour levels has been set to $2.5\text{e-}4 \text{ T}$ and $3.2\text{e-}4 \text{ T}$ respectively. This leads to white circles where the infinitesimally thin rings intersect the plane of the plot. Inside the white circles the calculated B-field magnitude increases sharply toward the infinitesimally thin rings. The correct form of the field inside the rings is seen in the plots from Amperes (Fig. 4.4(c) and (e)). Note that there are 35 contour levels in Fig. 4.4(d, f) compared to 30 contour levels in Fig. 4.4(b) and in the Amperes figures.

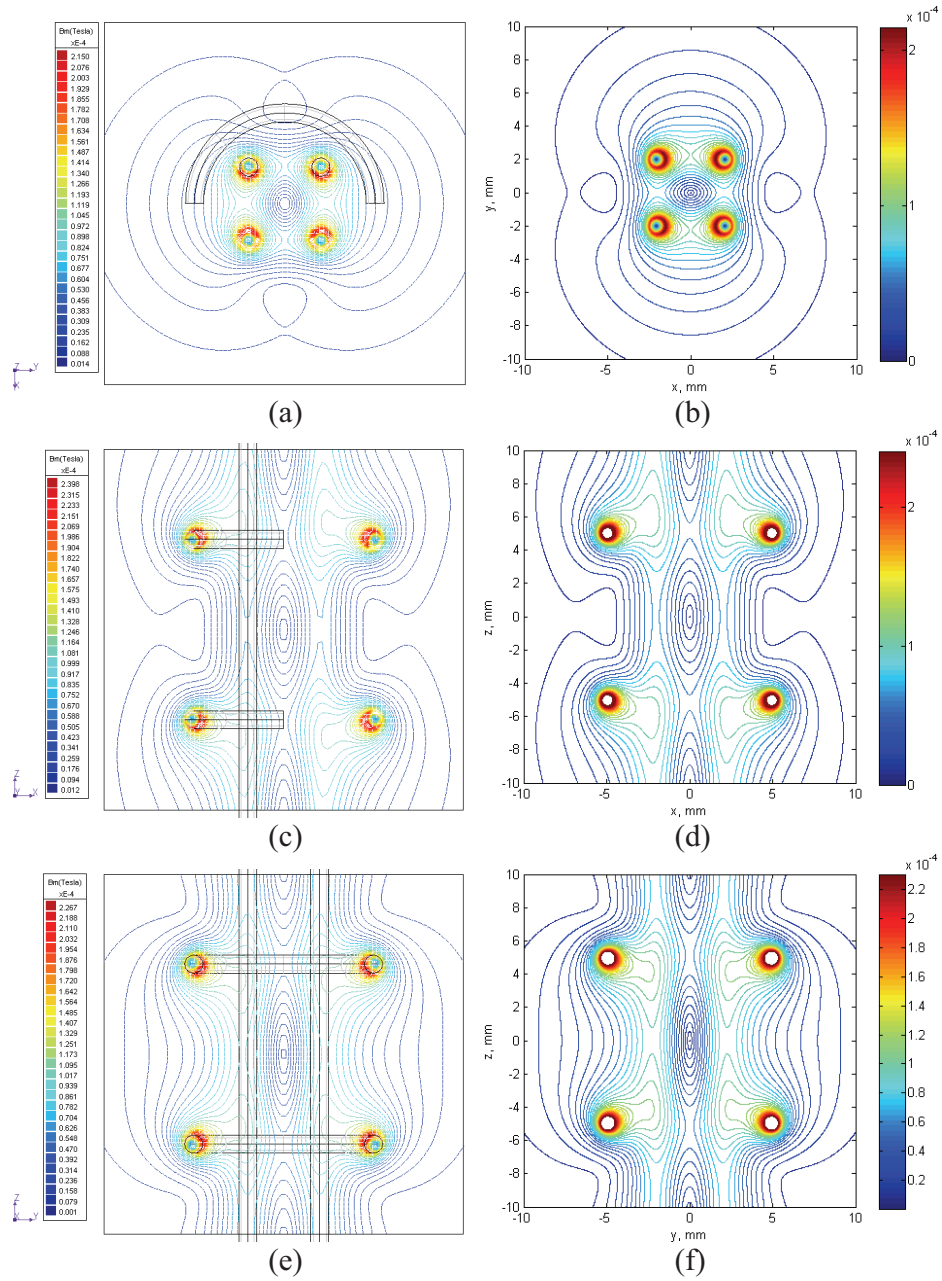


Fig. 4.4. Contour plots of B_m [T]. (a, b) xy -plane for $z = 0$ mm, (c, d) xz -plane for $y = 0$ mm and (e, f) yz -plane for $x = 0$ mm.

The magnetic fields along the z -axis, x -axis and y -axis are shown compared in Fig. 4.5 – Fig. 4.7 for Amperes simulations and Matlab computations. Ioffe-bar currents (DC) of 0.5 A and 1 A have been used. The ring currents (DC) were 0.5 A in opposite directions in the two rings. As can be seen, the Matlab calculations and Amperes simulations give practically identical results for the B-field along the axes through the centre of the quadrupolar trap.

In Fig. 4.5 it is apparent that the magnitude of the bar currents does not affect the magnetic field along the centre of the trap in the direction of the bars. This is not surprising since the B-field from the bars does not have a B_z -component. Along the x - and y -axes the trapping field changes with the magnitude of the bar currents. The change is however by a different factor along the x - and y -axes.

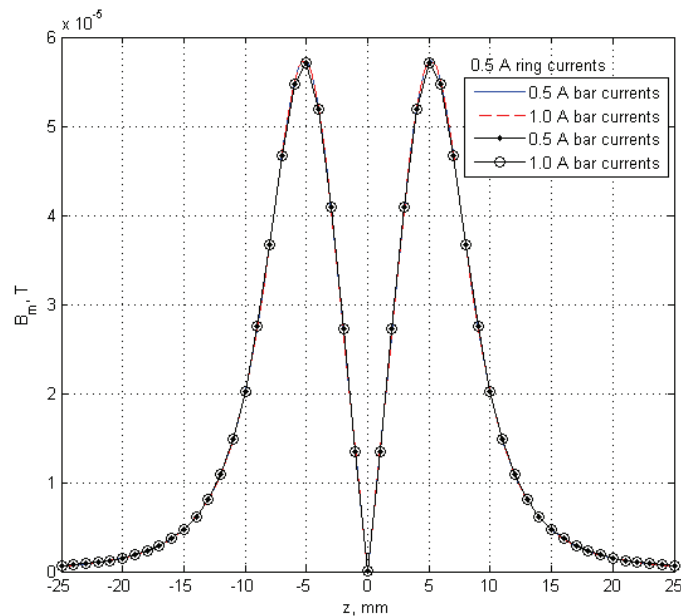


Fig. 4.5. Comparison of z -axis trapping fields for calculated results from Matlab, (solid and dashed lines), and simulated results from Amperes, (graphs with symbols).

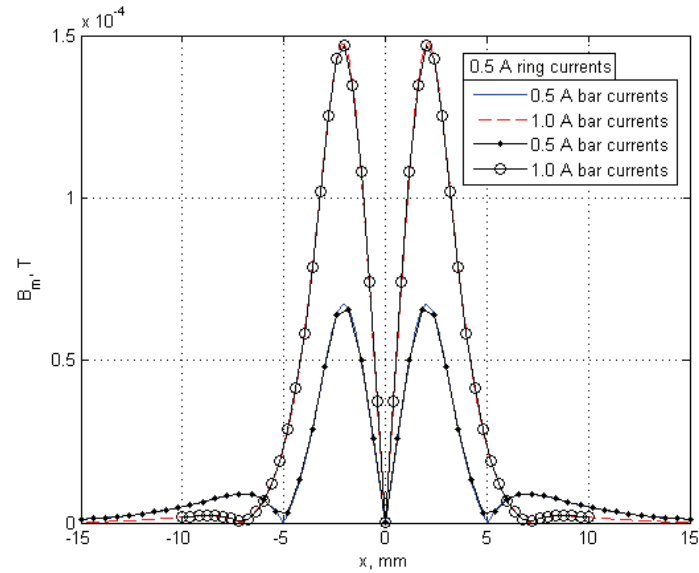


Fig. 4.6. Comparison of x -axis trapping fields for calculated results from Matlab, (solid and dashed lines), and simulated results from Amperes, (graphs with symbols).

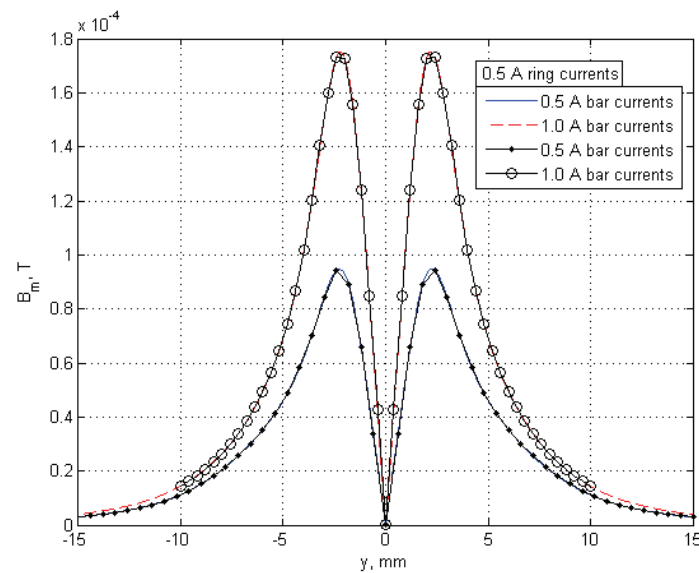


Fig. 4.7. Comparison of y -axis trapping fields for calculated results from Matlab, (solid and dashed lines), and simulated results from Amperes, (graphs with symbols).

When an RF current of 0.1 A at 0.6 MHz is added in the rings, the potential seen by the cold atoms becomes dressed. The shape of the dressed potential is shown in the yz -plane in Fig. 4.8. Amperes has in this case been used to compute the B-field components from the DC and RF excitations in two separate simulations. The resulting dressed potential has then been calculated in Matlab according to equation (2.1). A similar meshplot of the effective potential in the xz -plane can be found in Fig. 5 in [138].

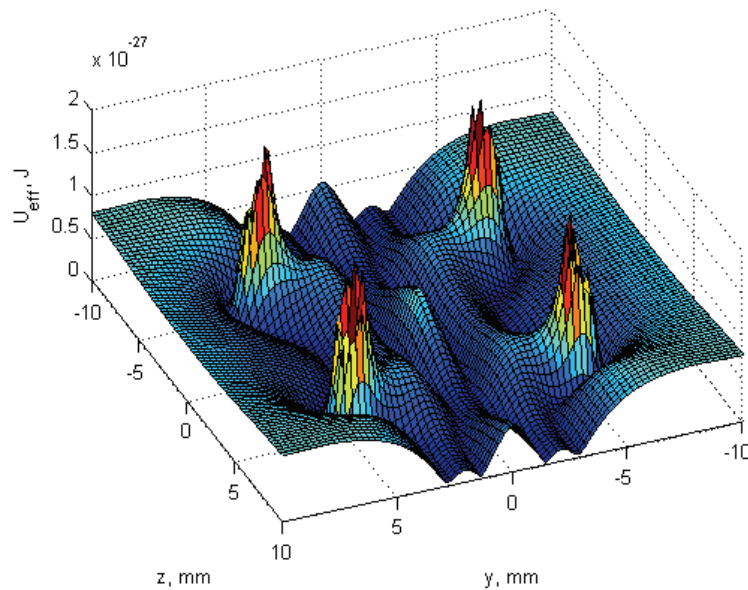


Fig. 4.8. The RF induced effective potential in the yz -plane from Amperes.

Fig. 4.9 and Fig. 4.10 are both contour plots of the effective potential in the xz -plane. In Fig. 4.9 U_{eff} has been calculated from the field components from two Amperes simulations. In Fig. 4.10 the effective potential has been calculated in Matlab using the equations for infinitesimally thin rings. The contour levels are the same in the two figures. The two plots are very similar but there are some minor differences. The potential inside the rings is seen only in Fig. 4.9. A number of small shifts in the contour lines can also be seen. The smallest value of the potential from Matlab is for example $3.55\text{e-}30$ J, compared to $2.24\text{e-}29$ J for the figure based on the Amperes simulations. It seems that the maxima and minima in the potential become a bit sharper when infinitesimally thin bias rings are assumed.

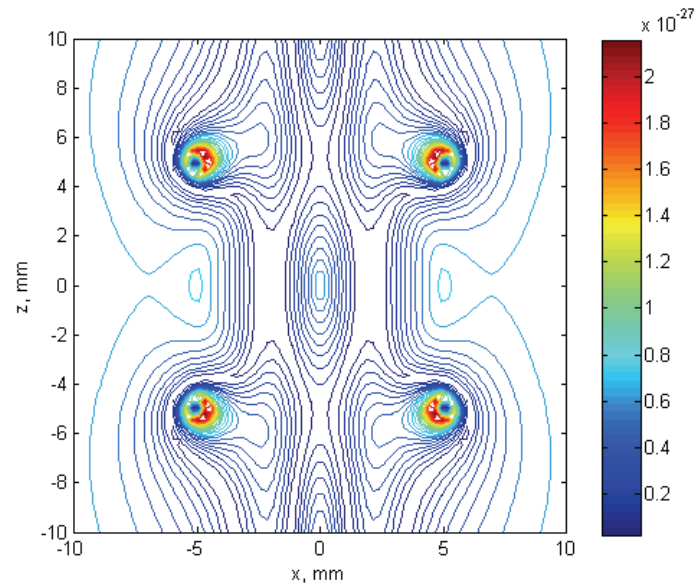


Fig. 4.9. U_{eff} in the xz -plane from field components computed by Amperes.

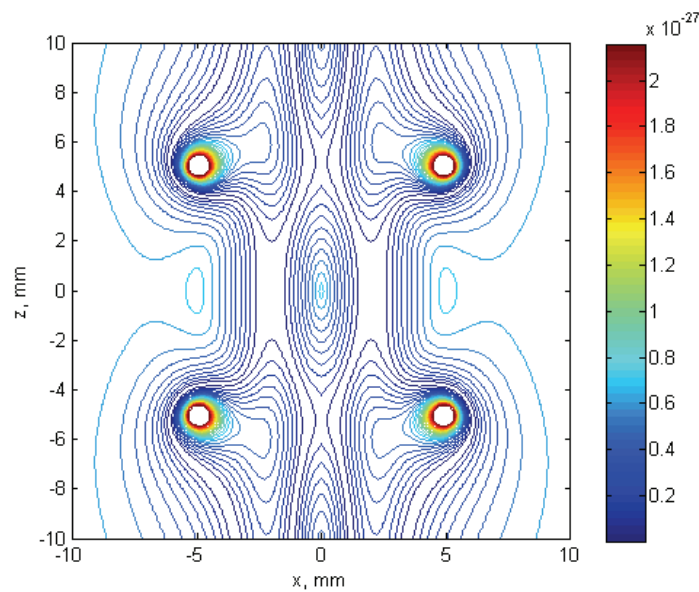


Fig. 4.10. U_{eff} in the xz -plane calculated in Matlab. Infinitesimally thin bias rings have been used.

The shape of the effective potential is shown in Fig. 4.11(a) for ring currents of $|I_{DC, ring}| = 0.5$ A and $|I_{RF, ring}| = 0.1$ A. ($f_{RF} = 0.6$ MHz.) An increase in the bar currents has the effect of compressing the potential surfaces between the Ioffe-bars. This is illustrated in Fig. 4.11(b), where $|I_{DC, bar}| = 1$ A.

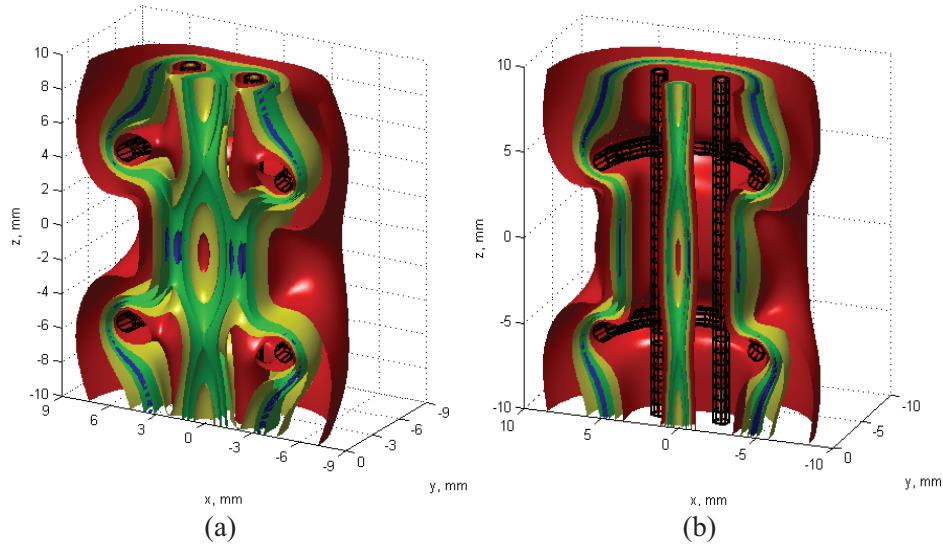


Fig. 4.11. U_{eff} calculated in Matlab. (a) $|I_{DC, bar}| = 0.5$ A, (b) $|I_{DC, bar}| = 1$ A. The potential surfaces are $U_{eff} = 3e-29$ J (blue), $U_{eff} = 1e-28$ J (green), $U_{eff} = 3e-28$ J (yellow) and $U_{eff} = 6e-28$ J (red).

It has become clear that there is no single circular minimum of uniform depth around the local maximum at the centre of the trap. The circular minimum typically contains four slightly deeper points, one on each side between the Ioffe-bars. This is illustrated in Fig. 4.12 for bar currents of $|I_{DC, bar}| = 0.5$ A, and ring currents of $|I_{DC, ring}| = 0.5$ A and $|I_{RF, ring}| = 0.1$ A. The ripple in the effective potential around the circular minimum is approximately $1e-29$ J in the figure. If the RF current amplitude in the rings is increased, the height of the ripple increases proportionally to the increase in the RF ring currents.

A potential barrier is also found to low potential manifolds just outside the Ioffe-bars. These low potential manifolds are much closer on two sides. This is seen clearly in Fig. 4.12. This barrier appears to be practically constant with the magnitude of the RF current in the rings. The barrier is approximately $2.6e-29$ J for bar currents of $|I_{DC, bar}| = 0.5$ A, and ring currents of $|I_{DC, ring}| = 0.5$ A and $|I_{RF, ring}| = 0.1$ A or 0.45 A. If the bar current

is increased to $|I_{\text{DC, bar}}| = 1.0$ A the height of the barrier increases to about $1 \text{e-}27$ J for the same ring currents.

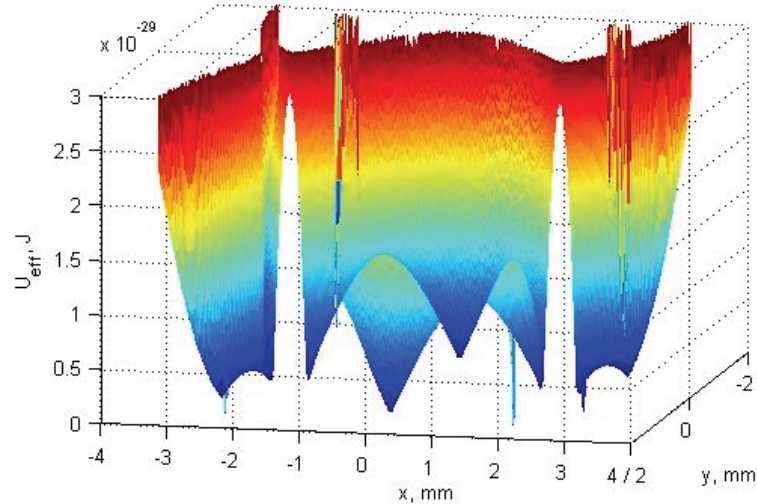


Fig. 4.12. U_{eff} below $3 \text{e-}29$ J near the centre of the quadrupolar trap.

When the DC ring current is increased to 0.85 A, with $|I_{\text{DC, bar}}| = 0.5$ A and $|I_{\text{RF, ring}}| = 0.1$ A ($f_{\text{RF}} = 0.6$ MHz), the shape of the effective potential is changed significantly as shown in Fig. 4.13(a). There are now only two minimum potential areas to the side of the local potential maximum at the centre of the trap. Two additional minimum potential areas also appear above and below the local maximum at the centre. This is illustrated in Fig. 4.14, which shows the potential surface $U_{\text{eff}} = 2 \text{e-}29$ J. This makes it difficult to directly compare the effective potential with the situation before the DC ring current was increased.

If the bar current is increased to $|I_{\text{DC, bar}}| = 1$ A, with $|I_{\text{DC, ring}}| = 0.85$ A and $|I_{\text{RF, ring}}| = 0.1$ A, the shape of the effective potential again becomes similar to how it was for DC ring currents of 0.5 A. The height of the barrier to the low potential regions outside of the Ioffe-bars has however been reduced a little. The height of the potential ripple ($0.5 \text{e-}29$ J) in the circular minimum around the central maximum stays about the same as for DC bar currents of 1 A and DC ring currents of 0.5 A. The height of the ripple thus appears to be determined by the combination of the DC bar currents and the RF ring currents, which are the same in both cases. It is accordingly insensitive to the DC ring currents.

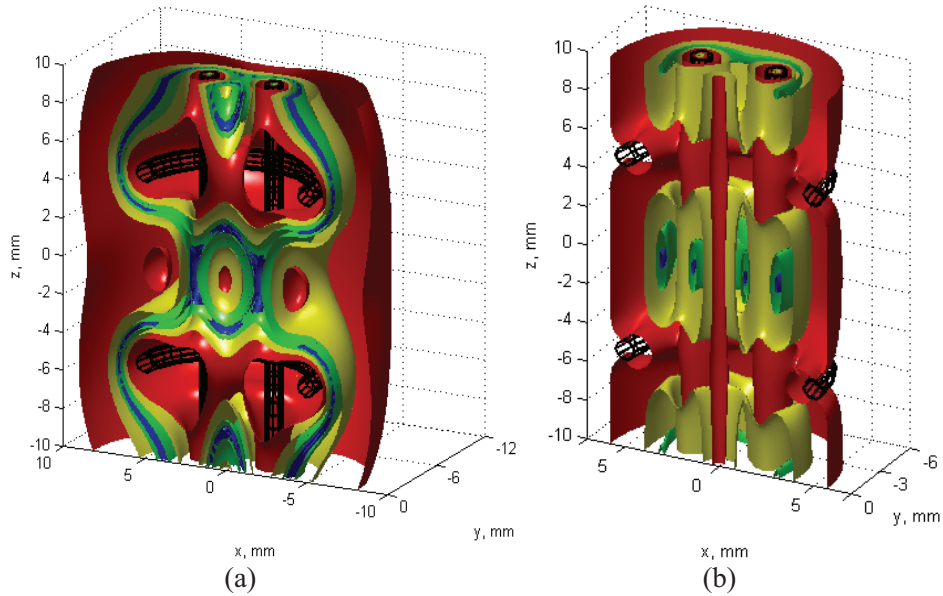


Fig. 4.13. U_{eff} calculated in Matlab. (a) $|I_{\text{DC, bar}}| = 0.5$ A, $|I_{\text{DC, ring}}| = 0.85$ A and $|I_{\text{RF, ring}}| = 0.1$ A. (b) $|I_{\text{DC, bar}}| = 0.5$ A and $|I_{\text{RF, ring}}| = 0.45$ A ($|I_{\text{DC, ring}}| = 0$). The potential surfaces are $U_{\text{eff}} = 3\text{e-}29$ J (blue), $U_{\text{eff}} = 1\text{e-}28$ J (green), $U_{\text{eff}} = 3\text{e-}28$ J (yellow) and $U_{\text{eff}} = 6\text{e-}28$ J (red).

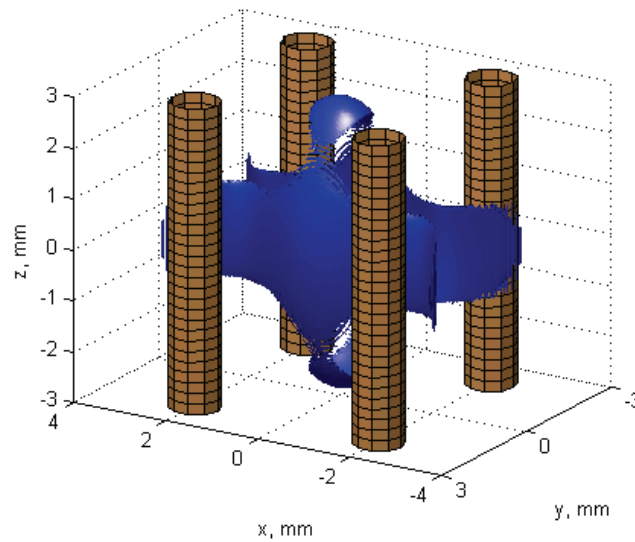


Fig. 4.14. The surface $U_{\text{eff}} = 2\text{e-}29$ J for $|I_{\text{DC, ring}}| = 0.85$ A, $|I_{\text{RF, ring}}| = 0.1$ A and $|I_{\text{DC, bar}}| = 0.5$ A.

If the bias rings are excited by only RF currents the shape of the effective potential becomes quite different. This is illustrated in Fig. 4.13(b), where $|I_{\text{RF, ring}}| = 0.45$ A and $f_{\text{RF}} = 0.6$ MHz. There are also in this case four slightly deeper points within the circular minimum around the local maximum at the centre of the trap. The minimum potential points are very similar to in the case where $|I_{\text{DC, ring}}| = 0.5$ A and $|I_{\text{RF, ring}}| = 0.45$ A. One difference is that the distance to the low potential regions outside of the Ioffe-bars has increased a little.

The main problems with only RF ring currents are that the four minima around the centre are unstable because of zero RF coupling and that the local maximum at the centre of the trap is not confined in the direction of the bars. This can be seen in Fig. 4.13(b). The potential maximum at the centre in fact increases a bit at the positions of the rings. Hence this maximum can not be used to trap ground state atoms for example. This potential topology is therefore of little interest in practise.

To round off the examination of this geometry the effective potential is compared for the remaining so far mentioned current excitations along the z -axis in Fig. 4.15, and along the x -axis and y -axis in Fig. 4.16(a) and (b) respectively. The graphs for the effective potential in the z -direction show that the potential at the centre of the trap ($7.95 \cdot 10^{-28}$ J) is independent of the current excitations in the bars and rings. This value is the constant

$$m_F \cdot \sqrt{(-\hbar \cdot 2\pi f_{\text{RF}})^2} = m_F \cdot \hbar \cdot 2\pi f_{\text{RF}} = 2 \cdot 1.055 \cdot 10^{-34} \cdot 2\pi \cdot 6 \cdot 10^5 [J].$$

As can be seen in Fig. 4.11 and Fig. 4.13(a) there are usually relative minima in the effective potential along the z -axis at the positions of the rings. These relative minima are not quite as deep as on a manifold around the z -axis (See e.g. Fig. 4.9 and Fig. 4.10). However, curve (3) in Fig. 4.15 shows that when the DC ring current is increased to 0.85 A, relative potential maxima appear instead at the positions of the rings.

Curve (2) shows that an increase in the RF ring current has the effect of reducing the depth of the relative minima at the positions of the rings. Just as for the B-field it makes no difference to the curves in Fig. 4.15 whether the DC bar currents are 0.5 A or 1 A. This is because the fields from the Ioffe-bars do not have a component in the direction of the bars.

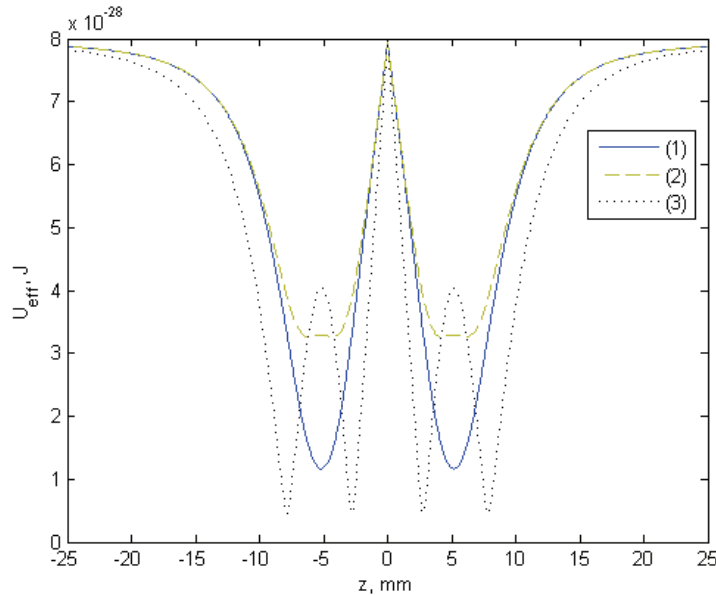


Fig. 4.15. Curves for U_{eff} in the z -direction. The bar and ring currents are:

- (1) $I_{\text{bar}} = 0.5 \text{ A}$ or 1.0 A , $I_{\text{DC}, \text{ring}} = 0.5 \text{ A}$, $I_{\text{RF}, \text{ring}} = 0.1 \text{ A}$,
- (2) $I_{\text{bar}} = 0.5 \text{ A}$ or 1.0 A , $I_{\text{DC}, \text{ring}} = 0.5 \text{ A}$, $I_{\text{RF}, \text{ring}} = 0.45 \text{ A}$,
- (3) $I_{\text{bar}} = 0.5 \text{ A}$ or 1.0 A , $I_{\text{DC}, \text{ring}} = 0.85 \text{ A}$, $I_{\text{RF}, \text{ring}} = 0.1 \text{ A}$.

In Fig. 4.16 it can be seen that the bar currents have a big impact on the graphs for the effective potential along the x - and y -axes. The magnitude of the RF ring current does not alter the potential since the RF coupling is zero along the x - and y -axes. An increase in the DC ring current from 0.5 A to 0.85 A typically increases the effective potential for distances inside the radius of the rings and decreases the potential for distances outside the radius of the rings. The exception to this is along the x -axis for bar currents of 1 A . An increase of the DC ring currents to 0.85 A here reduces the value of the effective potential both inside and outside of the radius of the rings, except for a narrow region just inside the radius of the rings.

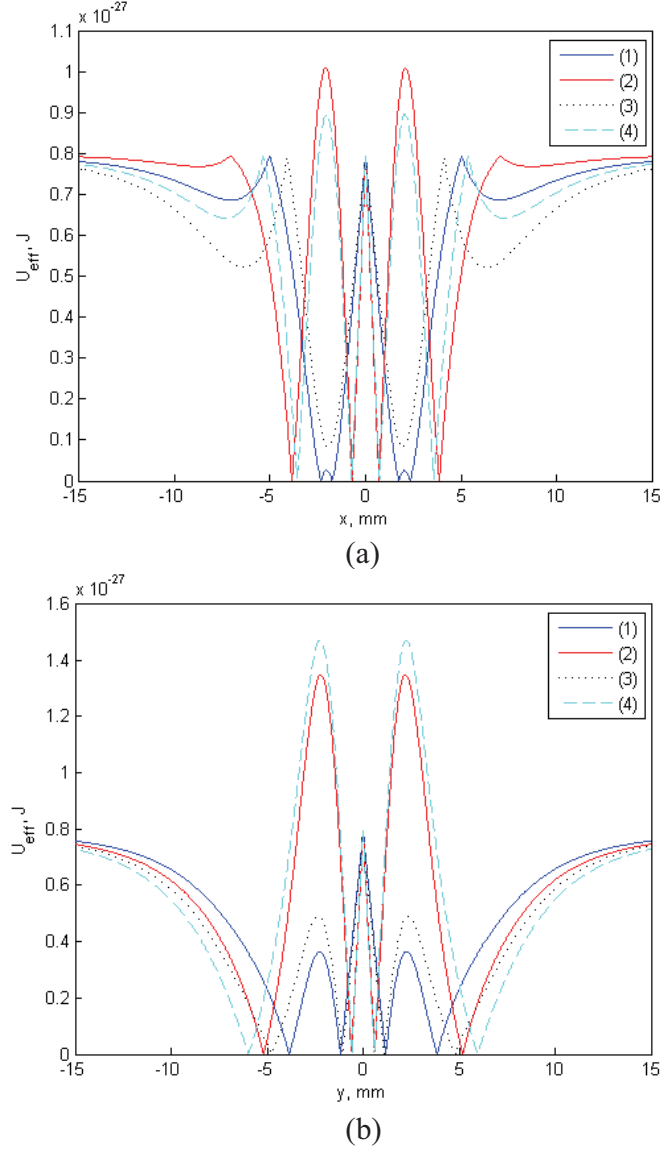


Fig. 4.16. Curves for U_{eff} in the x -direction (a) and y -direction (b). The bar and ring currents are:

- (1) $I_{\text{bar}} = 0.5$ A, $I_{\text{DC}, \text{ring}} = 0.5$ A, $I_{\text{RF}, \text{ring}} = 0.1$ A or 0.45 A,
- (2) $I_{\text{bar}} = 1.0$ A, $I_{\text{DC}, \text{ring}} = 0.5$ A, $I_{\text{RF}, \text{ring}} = 0.1$ A or 0.45 A,
- (3) $I_{\text{bar}} = 0.5$ A, $I_{\text{DC}, \text{ring}} = 0.85$ A, $I_{\text{RF}, \text{ring}} = 0.1$ A,
- (4) $I_{\text{bar}} = 1.0$ A, $I_{\text{DC}, \text{ring}} = 0.85$ A, $I_{\text{RF}, \text{ring}} = 0.1$ A.

4.3 The effect of changing the bias ring spacing in a quadrupolar trap

A millimetre sized quadrupolar trap with a rectangular ring cross-section has also been simulated in Amperes. The geometry is shown in Fig. 4.17. The rings have a height of $h = 1$ mm and a width of $w = 1.5$ mm as shown. The trap was simulated with gaps between the rings of 5 mm, 2 mm and 0.2 mm. The currents used in the simulation were $|I_{DC, \text{bar}}| = |I_{DC, \text{ring}}| = 1$ A. Another simulation with $|I_{DC, \text{bar}}| = 0.1$ A and $|I_{DC, \text{ring}}| = 0.2$ A was done for the geometry with a gap size of 2 mm.

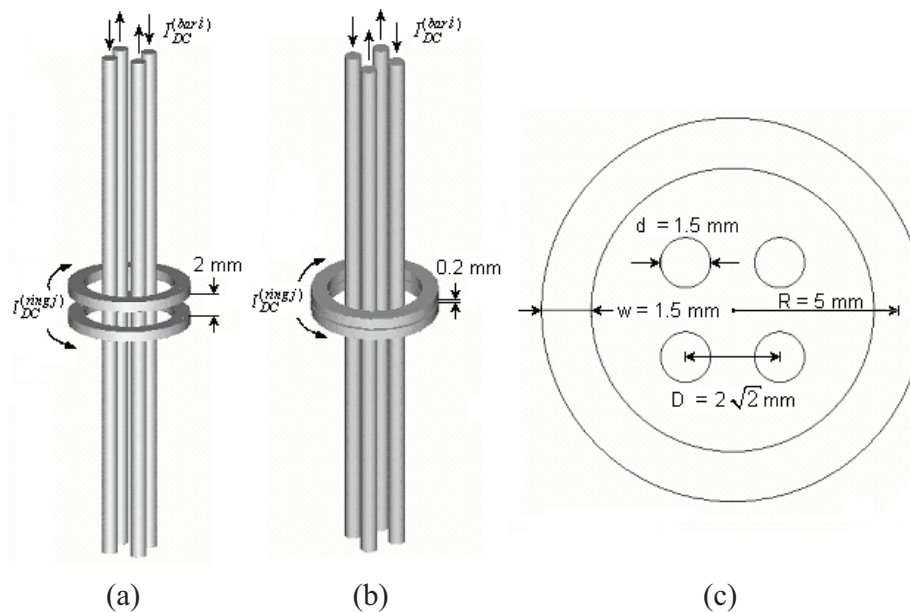


Fig. 4.17. The quadrupolar trap geometry. (a) 3D view with a gap of 2 mm, (b) 3D view with a gap of 0.2 mm, and (c) view from above.

To illustrate what happens when the gap between the rings is reduced contour plots of the magnitude of the B-field from Amperes are provided on the next pages for a gap size of 5 mm in Fig. 4.18, for a gap size of 2 mm in Fig. 4.19 and for a gap size of 0.2 mm in Fig. 4.20.

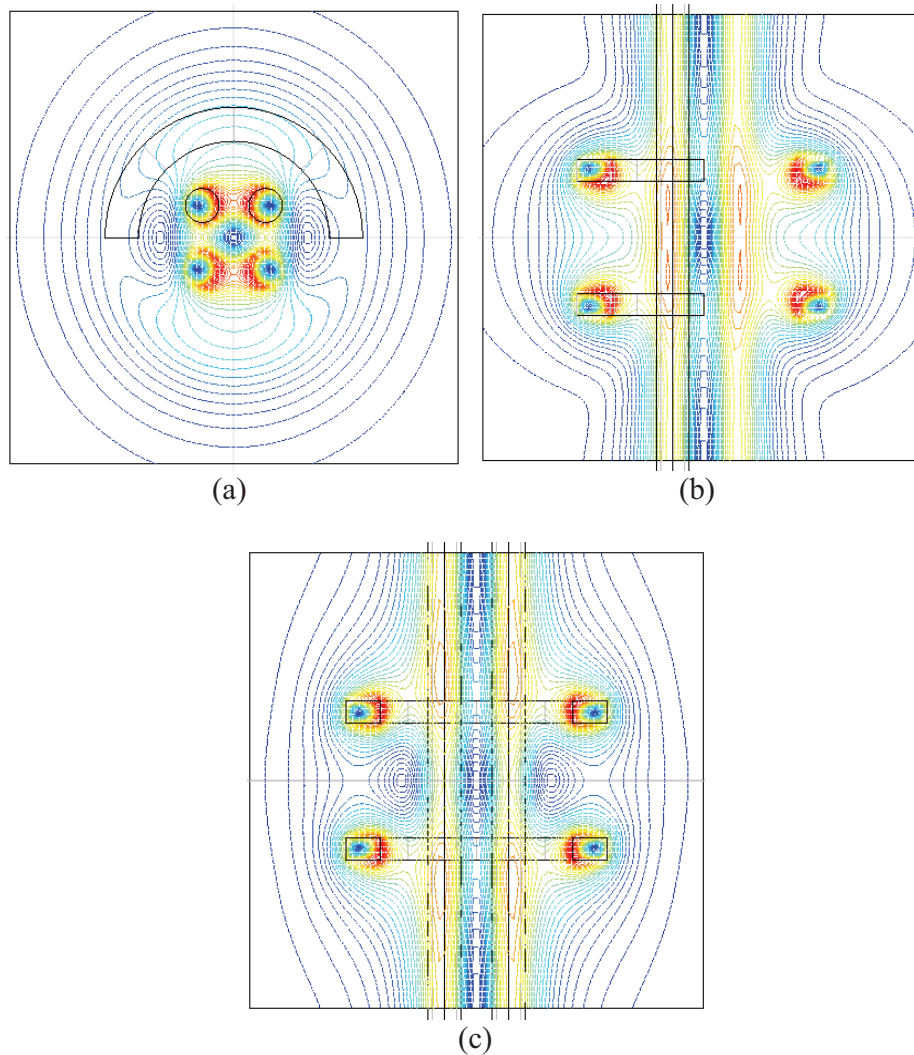


Fig. 4.18. Contour plots of B_m for a gap size of 5 mm. (a) The xy -plane for $z = 0$ mm, (b) the yz -plane for $y = 0$ mm, and (c) the xz -plane for $x = 0$ mm.

In all of the contour plots two additional field minima are seen on either side in the xz -plane. These minima are a result of the field lines being pulled in on the sides as the ring currents are increased or as the gap size is reduced. The 1.0 A DC ring currents cause these minima to be formed already for a gap size of 5 mm. As the gap size is reduced it quickly becomes difficult to avoid the two additional minima by reducing the ring

currents. The two minima are however isolated and should not prevent the use of the trap.

In Fig. 4.19(d) and Fig. 4.20(d) contour plots in the xz -plane calculated in Matlab are shown for comparison. The data ranges for which contours are drawn have been adapted to give the contour plots a similar appearance and the contour levels are not exactly the same as in the plots from Amperes.

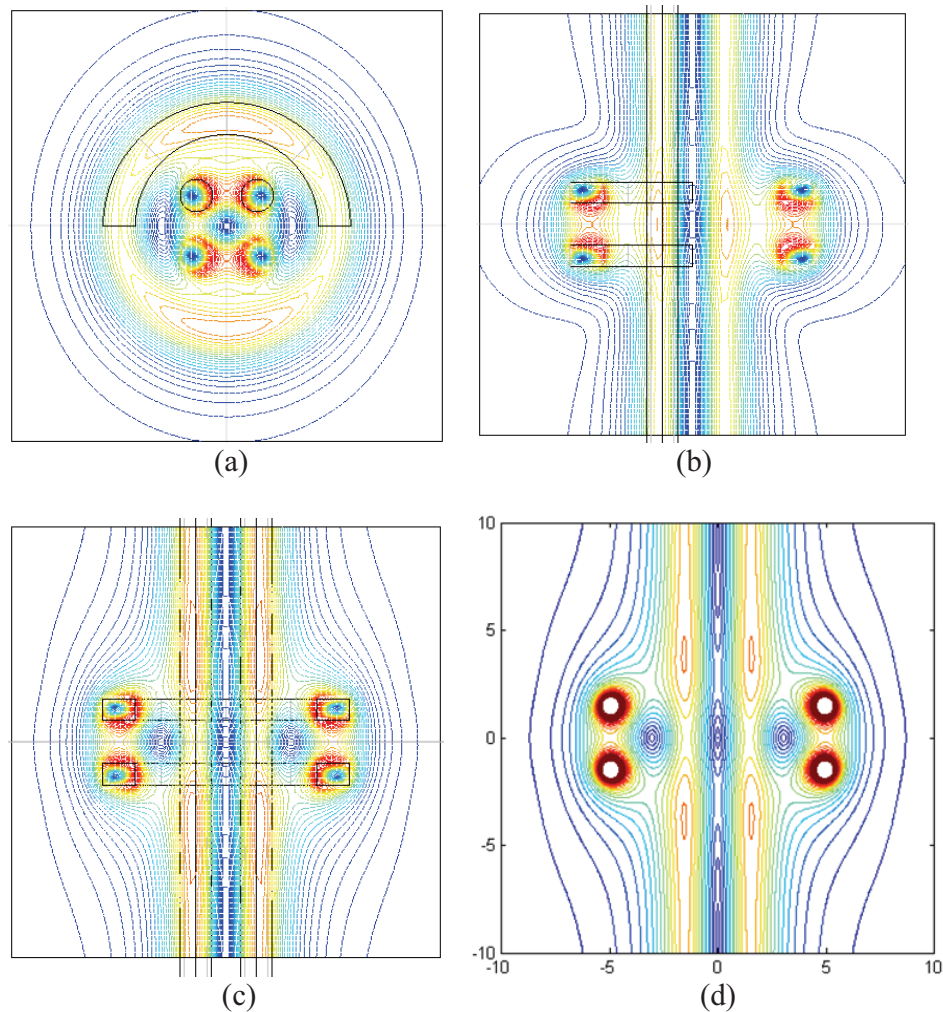


Fig. 4.19. Contour plots of B_m for a gap size of 2 mm. (a) the xy -plane for $z = 0$ mm, (b) the yz -plane for $y = 0$ mm, and (c, d) the xz -plane for $x = 0$ mm. The figure in (d) is calculated using Matlab.

Inside the white circles close to the infinitesimally thin rings the calculated B-field increases sharply. For the 2 mm gap the Matlab figure deviates both within and close to the rings. It is also slightly different in the gap between the rings. For the 0.2 mm gap the Matlab figure is obviously totally wrong at the centre of the gap between the rings. There are also some differences in the field further away from the rings.

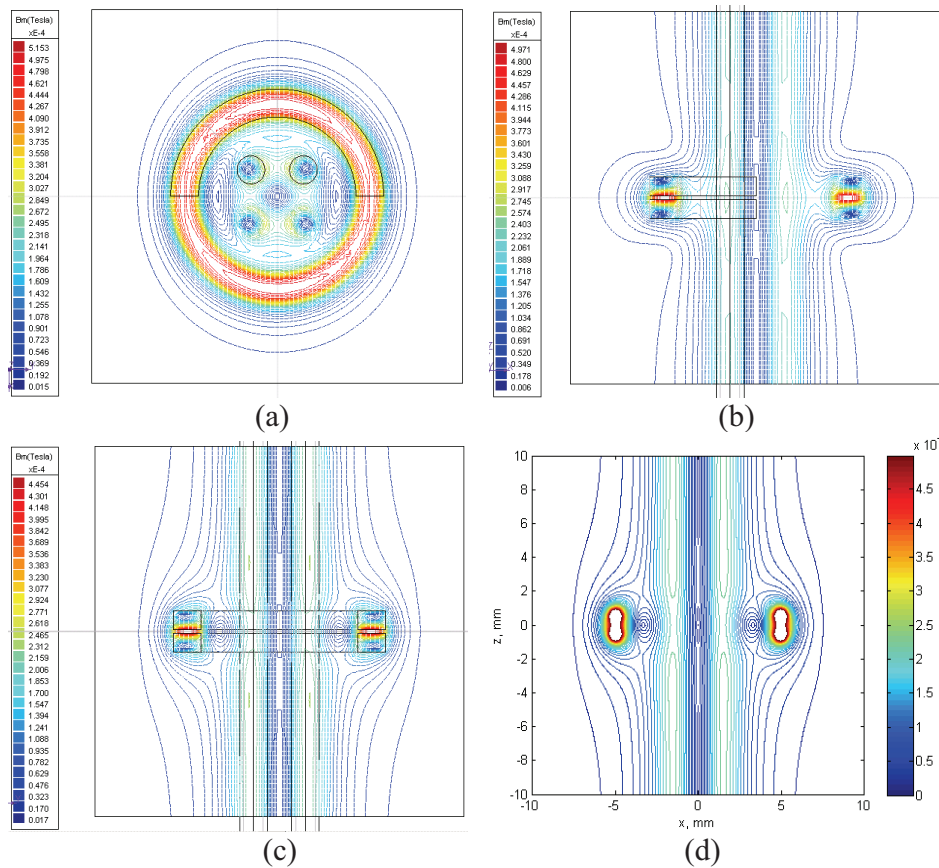


Fig. 4.20. Contour plots of B_m [T] for a gap size of 0.2 mm. (a) The xy -plane for $z = 0$ mm, (b) the yz -plane for $y = 0$ mm, and (c, d) the xz -plane for $x = 0$ mm. The figure in (d) is calculated using Matlab.

The magnitudes of the B-field in the z -direction are shown in Fig. 4.21. The three first curves come from simulations with $|I_{DC, \text{bar}}| = |I_{DC, \text{ring}}| = 1.0$ A and different gap sizes. The last curve is for a gap size of 2 mm with $|I_{DC, \text{bar}}| = 0.1$ A and $|I_{DC, \text{ring}}| = 0.2$ A. Corresponding plots of the magnitude of the B-field in the x -direction and y -direction through the centre of the trap ($z = 0$)

are shown in Fig. 4.22 and Fig. 4.23. In the figures “low I” refers to the simulation with $|I_{\text{DC, bar}}| = 0.1$ A and $|I_{\text{DC, ring}}| = 0.2$ A. As shown in Fig. 4.22 and Fig. 4.23 the magnitude of the B-field increases to about 0.46 mT or 0.52 mT between the rings for a gap size of 0.2 mm.

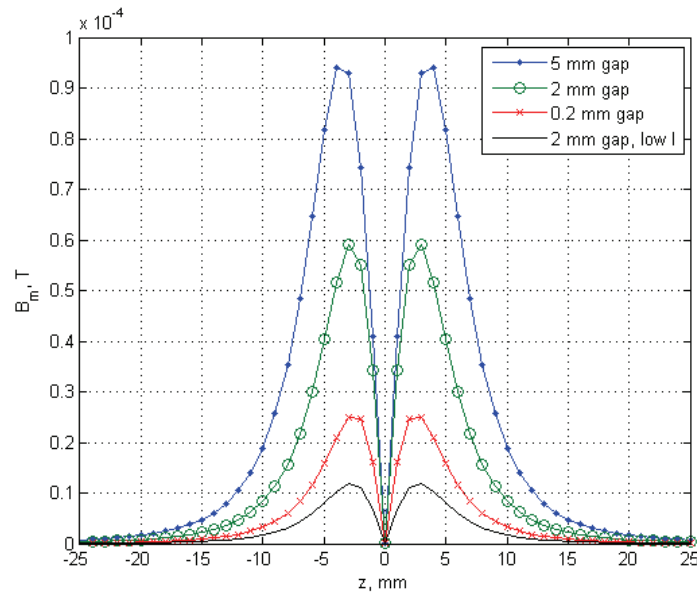
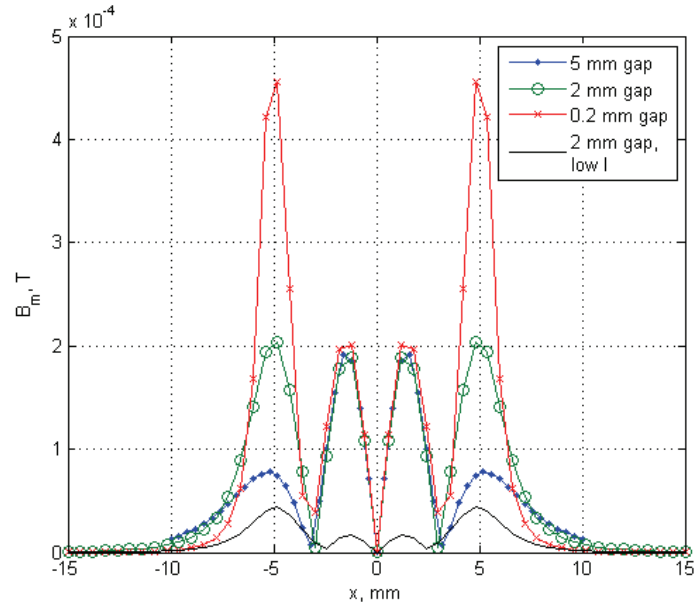
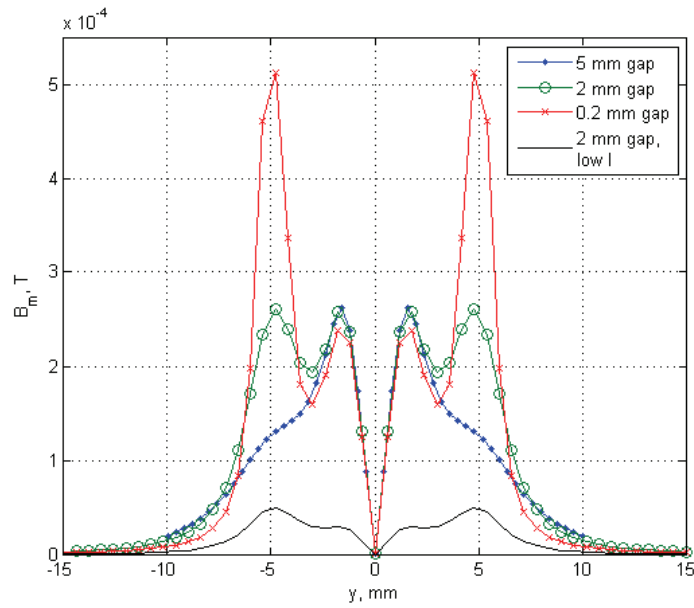


Fig. 4.21. B_m along the z -axis from Amperes for different gap sizes.

Fig. 4.22. B_m along the x -axis from Amperes for different gap sizes.Fig. 4.23. B_m along the y -axis from Amperes for different gap sizes.

The curves in Fig. 4.22 and Fig. 4.23 show that the strength of the magnetic field increases gradually between the rings as the gap is reduced from 5 mm (blue curves), to 2 mm (green curves) and to 0.2 mm (red curves). The magnitude of the magnetic field changes very little on the inside and on the outside of the bias rings for different gap sizes so long as the currents in the trap remain the same. This is because the B-field gradient of the bias rings is reduced when they are brought closer together. The contribution of the bias rings to the overall B-field gradient is therefore masked by the much larger contribution of the bars.

The same curves have also been calculated in Matlab assuming infinitesimally thin rings for otherwise the same geometry. The resulting curves became as good as identical to those in Fig. 4.21 – Fig. 4.23 except for the curve segments between the rings along the x - and y -axes for gap sizes of 0.2 mm and 2 mm. The difference was here very large (over 30 %) for the 0.2 mm gap size and quite small (5 – 6 %) for the 2 mm gap size.

Three additional simulations were initially done in Amperes with a micrometre-sized geometry that explored the use of very broad disc-shaped rings with only a narrow gap between them. This was done in an attempt to make an even smaller magnetic trap in the direction of the Ioffe-bars. The result was that the broad rings caused a sharp fall in the strength of the trapping magnetic field in the direction of the bars. When the average radius of the broad rings was subsequently increased to reduce the effect of opening up the physical rings to inject the currents, the strength of the trapping magnetic field fell much more. Increasing the ring currents finally had the effect of increasing the magnetic field again.

Because simulation results for the magnetic field scale with the size of the geometry and the magnitude of the currents they can be presumed to be relevant also for millimetre sized quadrupolar traps. It thus seems clear that the rings should go quite closely around the Ioffe-bars to maximize the trapping strength for a given ring current. If the rings are made relatively broad the ring currents must be increased to maintain the effectiveness of the rings. This would be practical only to a limited extent, especially if the gap is narrow between the rings. Otherwise the magnetic field would become too strong within the gap.

4.4 Conclusion

In this Chapter the results of simulations of a quadrupolar trap have been presented. Simulation results from Amperes have been compared favourably with computations in Matlab. The quadrupolar trap has been studied with combined DC and RF excitation of the bias rings to explore the effective potential topologies for trapping strong-field-seeking atoms or a combination of strong- and weak-field-seeking atoms. The possibility of placing the bias rings relatively close together has additionally been examined.

A number of figures and graphs from simulations of the quadrupolar trap in Amperes have been compared to calculated results in Matlab assuming infinitesimally thin bias rings with good agreement between the results. The use of ideal current rings in Matlab resulted in some differences especially inside and close to the bias rings.

Computations have shown that several different effective potential patterns can be created in the quadrupolar trap by varying the DC currents in the Ioffe-bars and bias rings and the RF current in the bias rings. The circular potential minimum around the local maximum at the centre of the trap typically contains four slightly deeper points. The barrier between these points is however very low at $\sim 0.36 \mu\text{K}$ for $|I_{\text{DC, bar}}| = 1 \text{ A}$, ($\sim 0.72 \mu\text{K}$ for $|I_{\text{DC, bar}}| = 0.5 \text{ A}$), and $|I_{\text{RF, ring}}| = 0.1 \text{ A}$. Although this ripple in the potential minimum is undesirable it does not preclude the trap from being used to trap weak-field-seeking atoms in the circular potential minimum.

DC bar currents of 1 A provide a barrier of $72.4 \mu\text{K}$ to the minimum potential manifolds just outside of the Ioffe-bars for $|I_{\text{DC, ring}}| = 0.5 \text{ A}$ and $|I_{\text{RF, ring}}| = 0.1 \text{ A}$. This is more than sufficient for trapping of weak-field-seeking atoms in the circular potential minimum around the centre of the trap. The smallest acceptable potential barrier is about $15 \mu\text{K}$. An increase of the DC ring currents to 0.85 A was found to be disadvantageous in this case and an increase of the RF ring currents increases the ripple in the circular potential minimum. DC bar currents of 0.5 A are much too small to allow trapping of weak-field-seeking atoms since the potential barrier becomes only $\sim 1.9 \mu\text{K}$ in this case. The potential maximum at the centre of the trap is at $28.8 \mu\text{K}$ ($m_{\text{F}} = 1$). This is more than sufficient for trapping of strong-field-seeking atoms. The quadrupolar trap can thus be used to trap both strong-field-seeking atoms and weak-field-seeking atoms if the DC bar currents are sufficiently large.

It has been found that bias rings can be placed relatively close together to compress clouds of cold atoms into successively smaller traps. As the gap distances become very small the B-field becomes very strong between the bias rings and there is a risk of dielectric breakdown.

If the rings are made very broad and flat this appears to reduce the trapping field along the centre of the trap so that the ring currents must be greatly increased for the rings to have the same effect. The width to height ratio of the ring cross-sections should be kept modest to allow the ring currents to go relatively tightly around the Ioffe-bars. This will keep the necessary current in the rings to a minimum.

The Ioffe-Pritchard trap with currents in the same direction in both bias loops eliminates the zero potential minimum at the centre of the trap. The quadrupolar traps discussed in this Chapter do not remove the zero potential minimum. The underlying problem seems to be the perfect symmetry between the bias loops. In our view a reversal of the current in one of the bias loops is just one of several ways of disrupting this symmetry. It comes at the cost of a smaller field gradient between the bias loops. The zero potential minimum may alternatively be removed by creating asymmetry between the practical bias loops. One loop could for example have a piece-wise-linear circumference, a rectangular cross-section or a slightly different radius. Optical techniques for removing the field zero are also possible. The temperature of the cold atoms determines the lowest acceptable level of the potential minimum.

Chapter 5

A Cylinder Guide for Cold Atoms

5.1 Introduction

The cylinder guide consists of a solid metal cylinder with a small hole inside it near the periphery. An external current carrying wire is placed close to the cylinder in line with the hole. DC currents are then sent through the cylinder and the wire to create a minimum in the magnetic field inside the hole.

The Chapter begins by describing the analytical equations for the magnetic field inside the cylinder with the hole. An equation is presented for placing a zero in the B-field inside the hole. A second zero in the B-field appears inside the cylinder between the centre of the cylinder and the hole and its position can be found as one of the roots of a third order polynomial. The equations for a wire with a finite radius have already been presented in Chapter 1.

In Section 5.3 results from numeric simulations in Amperes for five different cylinder sizes are presented. The simulated cylinders have radii of 2 mm, 3 mm, 5 mm, 7.5 mm and 10 mm. The B-field is also calculated using the analytical equations in Matlab for the same cylinder geometries and the results are compared.

In Section 5.4 bias rings are placed around the cylinder geometry. With the exception of a single Amperes simulation with rings with a finite circular cross-section, analytical equations for infinitesimally thin bias rings are used. It is also here expected that the computed fields are very similar if not identical outside of the volume of the corresponding practical rings with a finite cross-section. The bias rings are essential for pumping the cold atoms through the hole in the cylinder and also serve to remove the absolute zero in the B-field inside the hole.

5.2 Cylinder equations and expressions for zeros in the B-field

The geometry of the cylinder atom guide is shown in Fig. 5.1 for a cylinder radius of 2 mm. The complete geometry is shown Fig. 5.1(a), and the modelled geometry is shown in Fig. 5.1(b, c), where a symmetry-plane has been defined at $y = 0$.

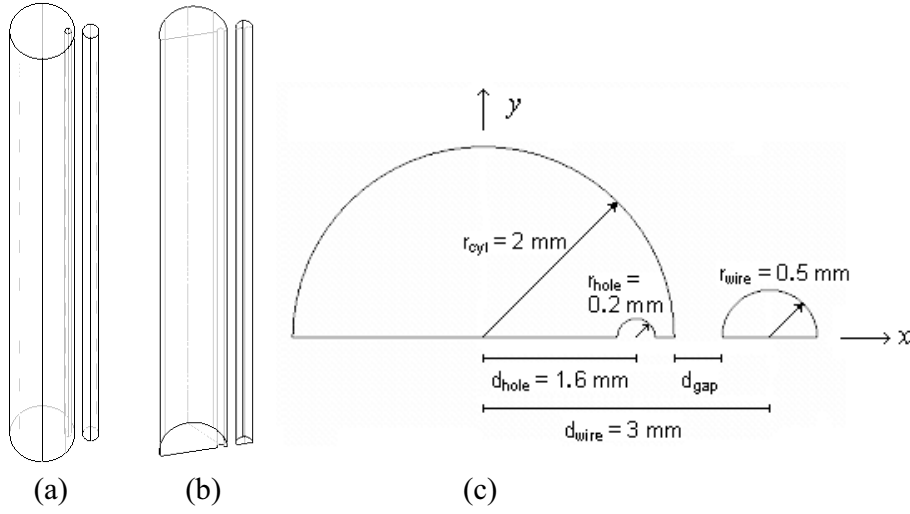


Fig. 5.1. Cylinder geometry. (a) 3D view, and (b, c) modelled geometry.

The analytical equations for the magnetic field inside the cylinder are as follows. Inside the hole in the cylinder:

$$B_x = 0 \quad (5.1)$$

$$B_y = \frac{\mu_0 I_{cyl} d_{hole}}{2\pi (r_{cyl}^2 - r_{hole}^2)} \quad (5.2)$$

Inside the rest of the cylinder:

$$B_x = \frac{-\mu_0 I_2 \cdot y}{2\pi \cdot r_{cyl}^2} - \frac{\mu_0 I_1 \cdot y}{2\pi \left((x - d_{hole})^2 + y^2 \right)} \quad (5.3)$$

$$B_y = \frac{\mu_0 I_2 \cdot x}{2\pi \cdot r_{cyl}^2} + \frac{\mu_0 I_1 (x - d_{hole})}{2\pi \left((x - d_{hole})^2 + y^2 \right)} \quad (5.4)$$

Outside of the cylinder:

$$B_x = \frac{-\mu_0 I_2 \cdot y}{2\pi(x^2 + y^2)} - \frac{\mu_0 I_1 \cdot y}{2\pi((x - d_{hole})^2 + y^2)} \quad (5.5)$$

$$B_y = \frac{\mu_0 I_2 \cdot x}{2\pi(x^2 + y^2)} + \frac{\mu_0 I_1 (x - d_{hole})}{2\pi((x - d_{hole})^2 + y^2)} \quad (5.6)$$

In the equations $I_1 = -I_{cyl} \cdot r_{hole}^2 / (r_{cyl}^2 - r_{hole}^2)$ and $I_2 = I_{cyl} \cdot r_{cyl}^2 / (r_{cyl}^2 - r_{hole}^2)$. A set of equations for the magnetic field of a cylinder with a hole are found in the book “Problems & Solutions on Electromagnetism”, on p178 – 179 [159], for a geometry where the circumference of the hole touches the centre of the cylinder and where the cylinder has a radius that is three times that of the hole. These equations were used by comparing terms to validate the equations in (5.1) – (5.6) for the case of the geometry in the book. The equations above are for a hole with an arbitrary radius and position along a line through the cylinder. Simulations made in Amperes have later proved to be in perfect agreement with the equations in (5.1) – (5.6).

Amperes simulations have shown that for cylinder and wire currents that lead to a magnetic field minimum inside the hole, a second field minimum appears inside the cylinder not far from the hole. It is possible to have a single B-field minimum at the inner wall of the hole, but then the atom guide can not function.

To be able to use the atom guide one B-field minimum must first be placed inside the hole by careful adjustment of the currents in the cylinder and the wire. An equation will now be derived that can be solved for the wire current, the cylinder current or the position along the x -axis of the B-field minimum inside the hole. The equation also shows that the B-field minimum inside the hole is in fact an absolute zero in the field.

The equation for the field inside the hole in the cylinder along the x -axis is

$$|B_{DC}| = b_y^2 = \left[\frac{\mu_0 \cdot I_{cyl} \cdot d_{hole}}{2\pi \cdot (r_{cyl}^2 - r_{hole}^2)} + \frac{\mu_0 \cdot I_{wire}}{2\pi \cdot (x - d_{wire})} \right]^2, \quad (5.7)$$

where $d_{wire} = r_{cyl} + r_{wire} + d_{gap}$ and $(d_{hole} - r_{hole}) \leq x \leq (d_{hole} + r_{hole})$.

Here d_{gap} is the gap between the cylinder wall and the surface of the external wire. For $|B_{\text{DC}}|$ to be zero inside the hole the following statement must be true

$$\frac{I_{\text{cyl}} \cdot d_{\text{hole}}}{(r_{\text{cyl}}^2 - r_{\text{hole}}^2)} + \frac{I_{\text{wire}}}{(x - d_{\text{wire}})} = 0. \quad (5.8)$$

This gives the following equation for the wire current given the position x of the field zero and I_{cyl} . (The x -position must be inside the hole).

$$I_{\text{wire}} = \frac{-I_{\text{cyl}} \cdot d_{\text{hole}}}{(r_{\text{cyl}}^2 - r_{\text{hole}}^2)} \cdot (x - d_{\text{wire}}). \quad (5.9)$$

This equation can also be solved for the x -position of the field zero with I_{wire} and I_{cyl} given, or for I_{cyl} with x and I_{wire} given. The equations are then

$$x = \frac{-I_{\text{wire}}(r_{\text{cyl}}^2 - r_{\text{hole}}^2)}{I_{\text{cyl}} \cdot d_{\text{hole}}} + d_{\text{wire}}, \quad (5.10)$$

$$I_{\text{cyl}} = \frac{-I_{\text{wire}}(r_{\text{cyl}}^2 - r_{\text{hole}}^2)}{d_{\text{hole}}(x - d_{\text{wire}})}. \quad (5.11)$$

As a numeric example, with I_{cyl} and I_{wire} as given below for the geometry in Fig. 5.1:

$$x = \frac{-3.2((2e-3)^2 - (2e-4)^2)}{5.6 \cdot 1.6e-3} + 3e-3 = \underline{1.586 \text{ mm}}. \quad 1.4e-3 < x < 1.8e-3 \quad (5.12)$$

In this case the field zero is not exactly at the geometric centre of the hole at $x = 1.6$ mm. To get the field zero exactly at the centre of the hole the wire current should be $I_{\text{wire}} = 3.1676$ A instead of 3.2 A.

An interesting question is now where the second field minimum inside the cylinder is to be found. Because the wire and cylinder currents have been chosen the solution must now be for the position of the second minimum along the x -axis. It is clear from the equations that this second minimum is also an absolute zero in the B-field.

The equation for the B-field inside the rest of the cylinder along the x -axis is

$$|B_{DC}| = b_y^2 = \left[\frac{\mu_0 \cdot I_{cyl} \cdot x}{2\pi(r_{cyl}^2 - r_{hole}^2)} - \frac{\mu_0 \cdot I_{cyl} \cdot r_{hole}^2}{2\pi \cdot (x - d_{hole})(r_{cyl}^2 - r_{hole}^2)} + \frac{\mu_0 \cdot I_{wire}}{2\pi \cdot (x - d_{wire})} \right]^2. \quad (5.13)$$

For $|B_{DC}|$ to be zero the terms in the expression for b_y must cancel out

$$\frac{\mu_0 \cdot I_{cyl} \cdot x}{2\pi(r_{cyl}^2 - r_{hole}^2)} - \frac{\mu_0 \cdot I_{cyl} \cdot r_{hole}^2}{2\pi \cdot (x - d_{hole})(r_{cyl}^2 - r_{hole}^2)} + \frac{\mu_0 \cdot I_{wire}}{2\pi \cdot (x - d_{wire})} = 0. \quad (5.14)$$

Placed on a common denominator the expression becomes

$$\frac{\mu_0 \cdot I_{cyl} \cdot x(x - d_{hole})(x - d_{wire}) - \mu_0 \cdot I_{cyl} \cdot r_{hole}^2(x - d_{wire}) + \dots}{2\pi \cdot (r_{cyl}^2 - r_{hole}^2)(x - d_{hole})(x - d_{wire})} + \frac{\mu_0 \cdot I_{wire}(x - d_{hole})(r_{cyl}^2 - r_{hole}^2)}{2\pi \cdot (r_{cyl}^2 - r_{hole}^2)(x - d_{hole})(x - d_{wire})}. \quad (5.15)$$

Multiplying out terms yields

$$\frac{\mu_0 \cdot I_{cyl} \cdot x^3 - \mu_0 \cdot I_{cyl} (d_{wire} + d_{hole})x^2 + \mu_0 \cdot I_{cyl} \cdot d_{hole} \cdot d_{wire} \cdot x \dots - \mu_0 \cdot I_{cyl} \cdot r_{hole}^2 \cdot x + \mu_0 \cdot I_{cyl} \cdot r_{hole}^2 \cdot d_{wire} + \mu_0 \cdot I_{wire} (r_{cyl}^2 - r_{hole}^2)x + \dots}{2\pi \cdot (r_{cyl}^2 - r_{hole}^2)(x^2 - (d_{hole} + d_{wire})x + d_{hole} \cdot d_{wire})}. \quad (5.16)$$

Collection of terms leads to the following fraction of two polynomials

$$\frac{\mu_0 \cdot I_{cyl} \cdot x^3 - \mu_0 \cdot I_{cyl} (d_{wire} + d_{hole})x^2 + \dots}{2\pi \cdot (r_{cyl}^2 - r_{hole}^2)x^2 - 2\pi \cdot (r_{cyl}^2 - r_{hole}^2)(d_{hole} + d_{wire})x + \dots} + \frac{\mu_0 \left(I_{cyl} (d_{hole} \cdot d_{wire} - r_{hole}^2) + I_{wire} (r_{cyl}^2 - r_{hole}^2) \right) x + \dots}{2\pi \cdot (r_{cyl}^2 - r_{hole}^2)x^2 - 2\pi \cdot (r_{cyl}^2 - r_{hole}^2)(d_{hole} + d_{wire})x + \dots}. \quad (5.17)$$

The roots of the polynomials can be found numerically, for example by using the ‘roots’ function in Matlab. The third order numerator polynomial has a complex conjugate pair of roots and one real root. The real root is the sought x -position of the field zero inside the cylinder. The real part of the complex conjugate roots has an x -value that lies somewhere inside the hole, where the equation is not valid. The imaginary parts are relatively small. The second order denominator polynomial has roots for d_{hole} and d_{wire} , which both lie outside the validity range of the equation.

It can be of interest to find an analytical solution for the roots of the numerator polynomial. This is however easier said than done, especially since the analytical expression is not known for any of the roots. There is also a risk that the expressions become so cumbersome to use that they become impractical compared to a numeric solution.

5.3 Numerical and calculated results for unbiased cylinder guides

As mentioned in the introduction five cylinder atom guides with radii of $r = 2$ mm, $r = 3$ mm, $r = 5$ mm, $r = 7.5$ mm and $r = 10$ mm have been simulated in Amperes. The material in the cylinder and wire was chosen to be solid copper. In all cases the wire radius was 0.5 mm and the gap between the wire and the cylinder wall 0.5 mm. The hole in the cylinder had a radius of 0.2 mm and was placed with its centre 0.4 mm from the outer wall of the cylinder for all five cylinders.

Before looking at results for the complete geometry it is instructive to look at the magnetic field for the cylinder alone. Fig. 5.2 shows the B-field for a cylinder of radius $r = 2$ mm in the xy -plane and along the x -axis for a cylinder current of $I_{\text{cyl}} = 5$ A. In Fig. 5.2(a) the x - and y -axes range from -4 mm to +4 mm, $z = 0$ and a symmetry plane has been defined at $y = 0$. In Fig. 5.2(b) the distance reading along the x -axis is relative to $x = -5$ mm. The figure shows that the magnetic field inside the hole is constant and that the field drops to zero at the centre of the cylinder. The slight field gradient seen inside the hole in Fig. 5.2(b) is a result of the positions of the two data points next to the hole not being exactly on the rim of the hole.

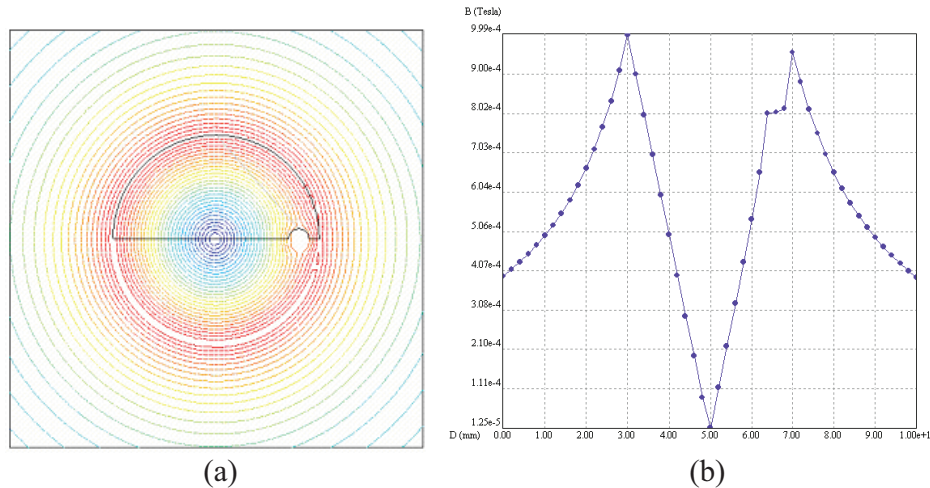


Fig. 5.2. The B -field for a cylinder with a hole (without the wire). (a) A contour plot in the xy -plane and (b) a graph along the x -axis.

Five cylinder atom guide geometries have been examined in a series of eight Amperes simulations. The simulations have afterwards been compared with computations in Matlab, where the equations for a cylinder with a hole from the previous section were used. The eight simulations are described in Table 5.1. In Amperes a symmetry plane was defined at $y = 0$ and only half of the geometry was modelled. Consequently the currents used were also only half of those specified in Table 5.1. The last two columns in Table 5.1 quantify the height of the barrier and the calculated distance between the zeros in the B -field inside the cylinder and near the centre of the hole. The two zeros in the B -field and the barrier between them will be illustrated by figures shortly.

For the three largest cylinders there is a slight discrepancy between the results from Amperes and Matlab when it comes to the height of the barrier. The approximate barrier height from the Amperes simulation is shown denoted by an (A), and the calculated barrier height in Matlab is denoted by an (M). For the two smallest cylinders there is essentially no difference, as seen for example in Fig. 5.6, and the barrier height from Amperes has been used. The distances between the B -field zeros have all been calculated in Matlab, but show good agreement with the Amperes simulations.

Table 5.1. Eight simulations in Amperes supported by calculations in Matlab.

Cylinder radius	I_{cyl}	I_{wire}	Barrier height between zeros	Distance between B-field zeros
$r = 2$ mm	10 A	5.60 A	10.48e-5 T	0.5375 mm
	7.72 A	4.34 A	7.879e-5 T	0.5239 mm
	5.6 A	3.20 A	5.069e-5 T	0.4651 mm
	1.6 A	0.90 A	1.626e-5 T	0.5219 mm
$r = 3$ mm	3.6 A	1.42 A	3.169e-5 T	1.3807 mm
$r = 5$ mm	5.0 A	1.256 A	4.008e-5 T (A)	3.3065 mm
			4.122e-5 T (M)	
$r = 7.5$ mm	5.4 A	0.93 A	4.116e-5 T (A)	5.7903 mm
			4.421e-5 T (M)	
$r = 10$ mm	6.0 A	0.754 A	4.210e-5 T (A)	8.4028 mm
			4.718e-5 T (M)	

In connection with trapping of cold atoms it is often convenient to measure the barrier height in micro-Kelvin. To do that one should first calculate the effective potential as $U_{\text{eff}} = m_F \mu_B g_F |B_{\text{DC}}|$ [J], where $m_F = 2$, $\mu_b = 9.2741\text{e-}24$ J/T and $g_F = 0.66$. The barrier height is then found as $T = U_{\text{eff}}/k_B$ [K], where $k_B = 1.3807\text{e-}23$ J/K is Boltzmann's constant. For the cylinder with $r = 2$ mm the potential barrier ranges from 92.9 – 14.4 μK depending on the cylinder and wire currents. For the cylinder with $r = 3$ mm the potential barrier is 28.1 μK and for the three largest cylinders the potential barrier is in the range 35 – 42 μK .

To visualize the shape of the magnetic field for the cylinder atom guides two figures from computations in Matlab have been included. In Fig. 5.3 a mesh-plot of the B-field is shown for the guide with $r = 3$ mm. The currents are as defined in Table 5.1. The B-field is strongest along the rim of the cylinder and around the wire. A minimum in the field is seen close to the centre of the wire. This minimum is in fact pulled closer to the cylinder by the DC current in the cylinder. The figure also shows that the zero in the magnetic field inside the hole is more pointed than the zero in the field inside the cylinder.

In Fig. 5.4 the four isosurfaces $B_m = 2\text{e-}5$ T (blue), $B_m = 8\text{e-}5$ T (green), $B_m = 1.2\text{e-}4$ T (yellow) and $B_m = 2\text{e-}4$ T (red) are shown for the guide with $r = 5$ mm. The figure shows the guide from a different perspective.

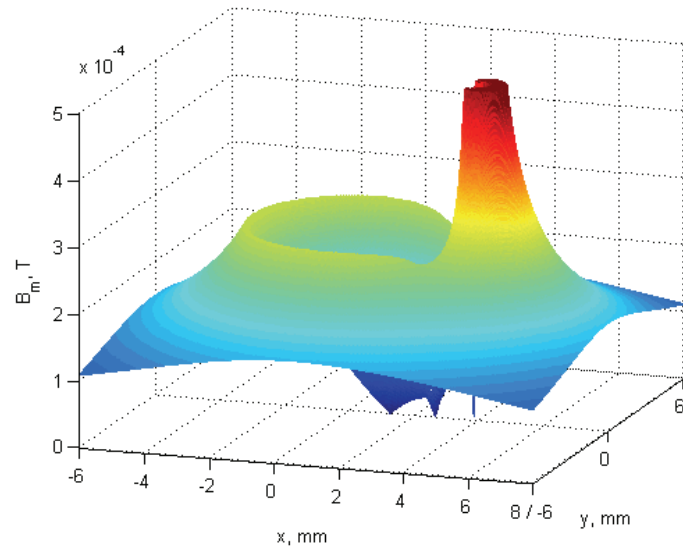


Fig. 5.3. B_m in the xy -plane for the cylinder guide with $r = 3$ mm. $z = 0$.

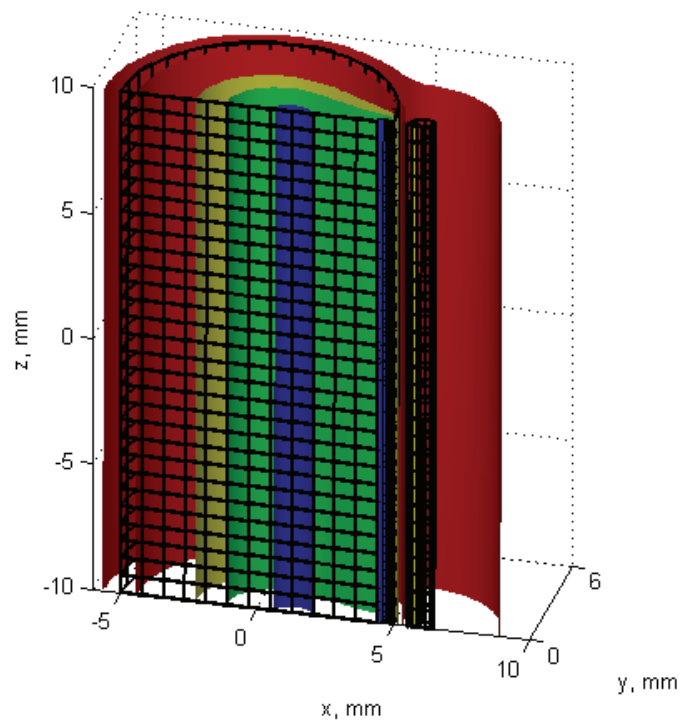


Fig. 5.4. Isosurface plot of B_m for the cylinder guide with $r = 5$ mm.

The B-field along the x -axis is shown for all five cylinders in Table 5.1 in Fig. 5.5. The x -axis is oriented along the symmetry plane through the centre of the cylinder and the wire. For the smallest cylinder with $r = 2$ mm a cylinder current of 5.6 A, and a wire current of 3.2 A has been used, corresponding to line three in Table 5.1. The graphs in the figure have been calculated in Matlab and the dotted markers on the graphs correspond to the data points simulated in Amperes.

The data points from Amperes in general match the graphs calculated in Matlab well. A quite small but increasing difference can however be seen in the magnitude of the B-field toward the rim of the cylinders for the biggest cylinders. The centres of the holes in the different cylinders lie at $x = 1.6, 2.6, 4.6, 7.1$ and 9.6 mm respectively.

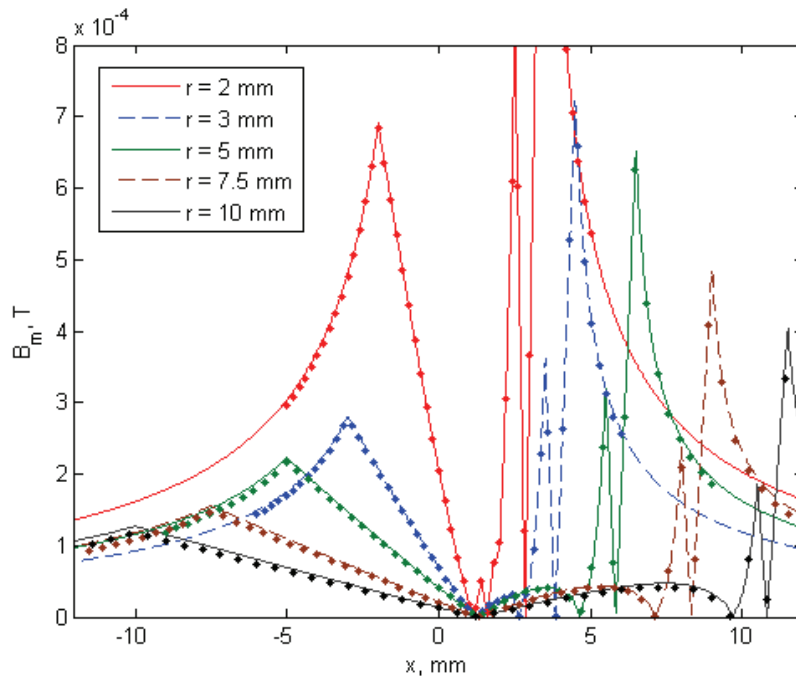


Fig. 5.5. B_m along x -axis for 5 cylinders. The data is from Amperes and Matlab.

In the case of the smallest cylinder, with radius $r = 2$ mm, four different current levels were found in the cylinder and external wire that gave a minimum in the magnetic field inside the hole. These four simulations are listed first in Table 5.1. An enlarged view of the region of interest containing the zeros in the B-field is shown in Fig. 5.6. The hole in this cylinder has its centre at $x = 1.6$ mm and has a radius of 0.2 mm.

A thing that is particular for this cylinder geometry is that the barrier between the two field zeros has its maximum at the inner rim of the hole in the cylinder. It has later become clear that the cylinder and wire currents that produce a zero in the magnetic field in the same point inside the hole scale linearly by the same factor. The resulting barrier height also scales by the same factor. Setting the barrier height to a specific level is therefore not very difficult if the accompanying currents are acceptable.

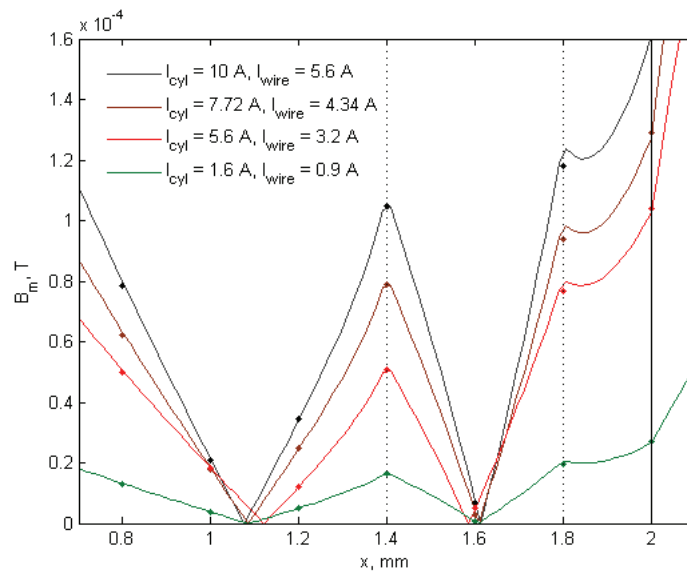


Fig. 5.6. The shape of the barrier for the cylinder atom guide with $r = 2$ mm.

For the largest cylinder a set of similar graphs are shown in Fig. 5.7. The graphs have been calculated in Matlab and have not been simulated using Amperes. The barrier here has its maximum far away from the hole in the cylinder. Note that the cylinder currents are slightly higher for this cylinder compared to the cylinder with $r = 2$ mm in Fig. 5.6, and that the maximum barrier height is reduced. This is not surprising since the current density in the cylinder scales roughly with the cylinder's cross-sectional area. The reason that the barrier height is not reduced even more may be the much longer distance between the two field zeros.

It is in any case apparent that the cylinder current must be increased significantly to maintain the same barrier height when the radius of the cylinder is increased. The reduced current in the external wire comes as a benefit however, since the current carrying ability of the cylinder is normally far greater than that of the wire.

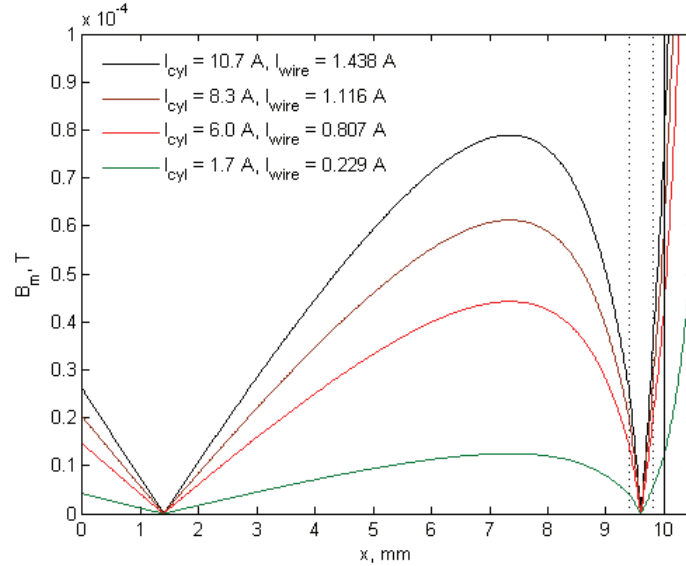


Fig. 5.7. The shape of the barrier for the cylinder atom guide with $r = 10$ mm.

The original idea was to place a single minimum in the B-field inside the hole in the cylinder. The simulations in Amperes and the calculations in Matlab suggest however that this is not possible. It appears that a single field minimum inside the cylinder can only be moved outwards to the inner wall of the hole by adjustment of the cylinder and wire currents, but not inside the hole. A further reduction in the wire current leads to two field zeros, where the outer field zero can be moved to the centre of the hole. This is illustrated in Fig. 5.8 for the cylinder with $r = 2$ mm and in Fig. 5.9 for the cylinder with $r = 10$ mm. In both cases the red graphs place a field zero close to the centre of the hole. The black graphs give a single field minimum inside the cylinder.

It may at this point seem to be a good idea to simply move the hole to where the single minimum is. This has been tried, but does not lead to any improvement. The single minimum can again only be moved to where the inner wall of the hole is. Instead the barrier between the two field zeros, where the outer field zero is at the centre of the hole, becomes smaller. For the cylinder with $r = 10$ mm the two field zeros in this case come very close together at $x \approx 4.9$ mm and $x \approx 5.5$ mm and the barrier between them becomes very low indeed.

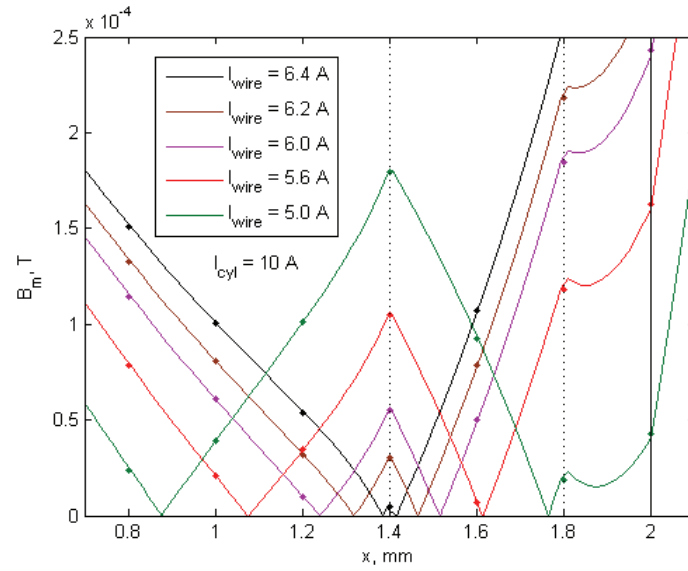


Fig. 5.8. Different wire currents for the cylinder atom guide with $r = 2$ mm.

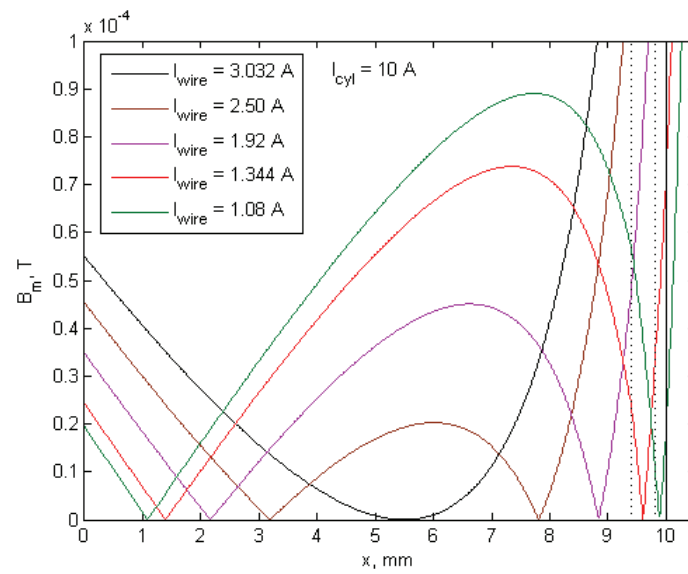


Fig. 5.9. Different wire currents for the cylinder atom guide with $r = 10$ mm.

5.4 Trapping and pumping of cold atoms in cylinder guides

To enable pumping of atoms in the weak-field-seeking state along the cylinder guide bias rings can be placed at regular intervals around the cylinder and wire. The rings also provide a small B-field component in the direction along the guide, which in turn prevents losses due to Majorana transitions between trapped and untrapped spin states as the atoms cross the B-field zero inside the hole. The situation is essentially analogous to the case of the side guide described in [136].

Other ways of moving cold atoms through the guide than with the use of bias rings may also be considered. If the length of the atom guide is short it may for example be adequate to give the guide a slight downward tilt so that it functions as a slide for cold atoms. This has previously been reported done for a four wire magnetic guide in a laboratory setup [160]. The problem of Majorana losses due to non-adiabatic spin flips as the atoms cross the B-field zero inside the hole must however be handled in some other way. If the solution is to use an external bias field to remove the absolute zero in the B-field inside the hole this alternative way of moving the cold atoms becomes much less attractive. It seems that lasers are not practical for pumping cold atoms along the guide. The B-field zero inside the hole and possible bends in the guide make it impossible to use laser light in a straight line through the guide or even reflected off the sides of the hole. Alternatives to the use of bias rings for moving cold atoms through the guide will not be considered in the following.

The cylinder with radius $r = 5$ mm was simulated in Amperes with two bias rings placed at a height of $z = \pm 5$ mm. The rings had a cross-sectional radius of 0.75 mm and a radius of 8 mm from the centre of the xy -plane. The cylinder and the external wire were both moved 0.75 mm in the negative x -direction. This distance is half the gap between the cylinder and the wire plus half the diameter of the wire. The modelled geometry is shown in Fig. 5.10(a). The current in the cylinder was 5 A and the current in the external wire 1.256 A. The ring currents were 0.5 A in opposite directions in the two bias rings. The geometry in Fig. 5.10(b), which pertains to the computations of the B-field in Matlab, will be explained shortly.

Amperes is a relatively simple program and the B-field from the cylinder and external wire and the B-field from the bias rings must be

simulated separately and afterwards added together in a computational program such as Matlab. The reason for this is that the cylinder and external wire require symmetry about the plane $y = 0$, whereas the bias rings require angular periodicity about the z -axis.

In Amperes volume currents can only be assigned to six-sided volumes and a current entry surface must also be defined. The program does not allow the complete cylinder with the hole to be simulated, since the volume then contains “trimmed surfaces”, which is not allowed. The bias rings must in any case be defined to be angularly periodic about the z -axis. Otherwise there will not be a current entry surface. It is therefore most convenient to model the bias rings in two sections centred on the origin and to displace the cylinder and the external wire in the negative x -direction.

The simulation technique is made further cumbersome by the need to simulate the B_x , B_y and B_z components of the B-field separately for both simulations, so that the total magnetic field can be found by summation. For each field component a slice through the geometry is defined, and the plot ranges of the different slices must be defined to be identical in each case. Amperes is accordingly not very convenient to use in this case, but the final result for the B-field is reliable.

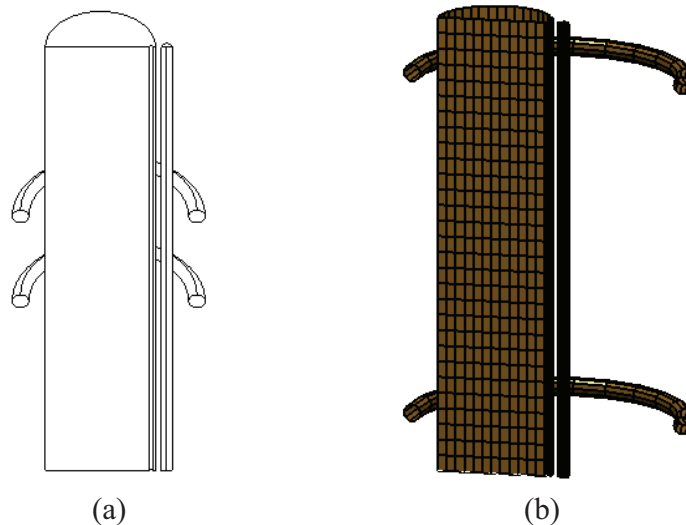


Fig. 5.10. Guide geometry with bias rings in (a) Amperes, and (b) Matlab.

Simulations were made in Amperes of the xy -plane for $z = 0$ and the xz -plane for $y = 0$. In the xz -plane the B_x and B_z field components for the simulation of the cylinder with the external wire were reported to be

constant scalars by Amperes, and files for them could not be saved. A closer examination of the equations for the B-field in the cylinder with the hole and the external wire has shown that $B_x = B_z = 0$ in this case.

The B-field in the xy -plane for the geometry in Fig. 5.10(a) is shown in Fig. 5.11. The figure clearly shows that the field minimum inside the hole in the cylinder has been moved downwards. If the currents in the bias rings had been reversed the field minimum would have been moved upwards instead. To avoid this distortion of the field the bias rings must be centred on the hole in the cylinder. Because the one month evaluation version of Amperes which had been used had long since been returned to Canada when this was discovered, additional simulations in Amperes were not practical to make.

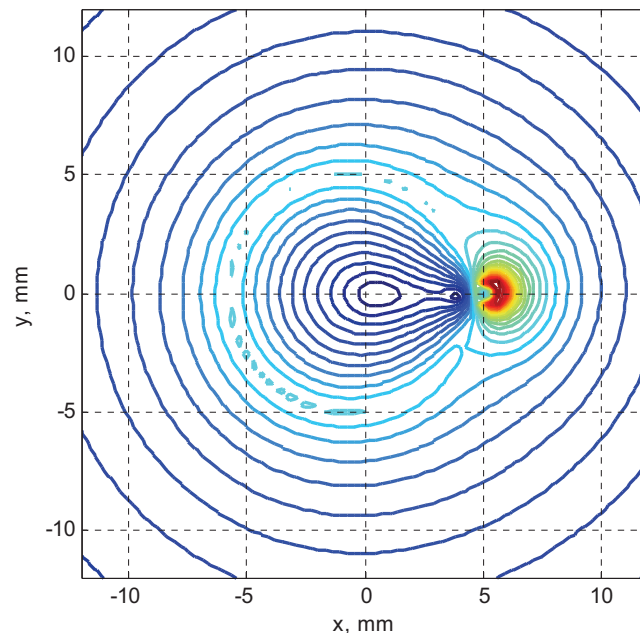


Fig. 5.11. The B-field in the xy -plane ($z = 0$) for the geometry in Fig. 5.10(a).

After the B-field equations for the cylinder with the hole had been derived it became straightforward to calculate the magnetic field for the complete geometry in Matlab. The geometry for the Matlab computations is shown sliced in half in Fig. 5.10(b). The slicing in two has been done for easy comparison with the geometry in Amperes, but is also convenient for showing the field inside the cylinder. The bias rings in the figure have a cross-sectional radius of 0.75 mm for comparison with the Amperes

geometry, but the computations have been made using the equations for infinitesimally thin rings. The radius of the bias rings placed at $z = \pm 15$ mm is $r_{\text{ring}} = d_{\text{hole}} + r_{\text{cyl}} + 2.25$ mm = 11.85 mm. The ring currents are 0.8 A (DC), this time in the same direction in both rings. The radius of the cylinder is $r = 5$ mm.

The computed magnetic field is shown in the xy -plane in Fig. 5.12 and in the xz -plane in Fig. 5.13. Owing to the use of bias currents in the same direction in both rings there is now no sign of a twist in the B-field inside the cylinder in the xy -plane. If ring currents in opposite directions had been used instead one would have seen a sideways displacement of the field zero inside the cylinder and no sideways shift for the field zero inside the hole. Circular contours can also be seen around the centre of the hole, which is where the dotted lines intersect. In the xz -plane a closed contour is seen between the bias rings that encloses the centre of the hole at $x = 4.6$ mm, here marked with a dotted line.

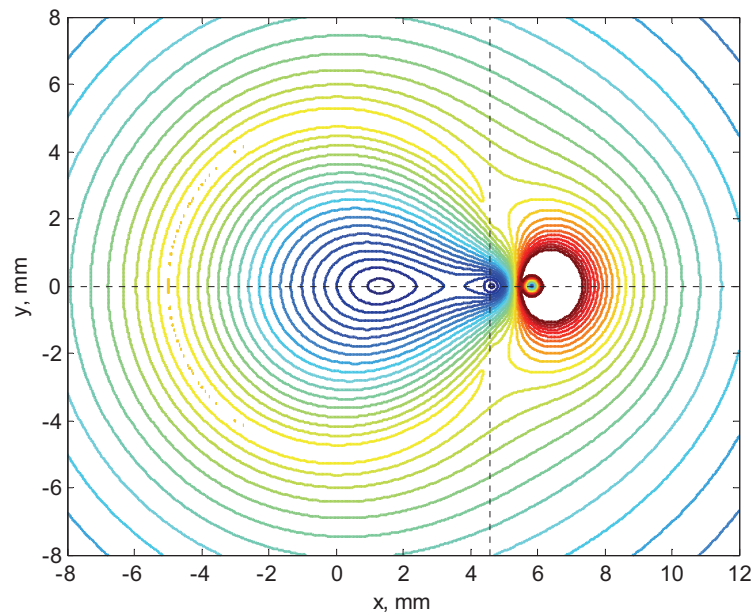


Fig. 5.12. The B-field in the xy -plane ($z = 0$) for the geometry in Fig. 5.10(b).

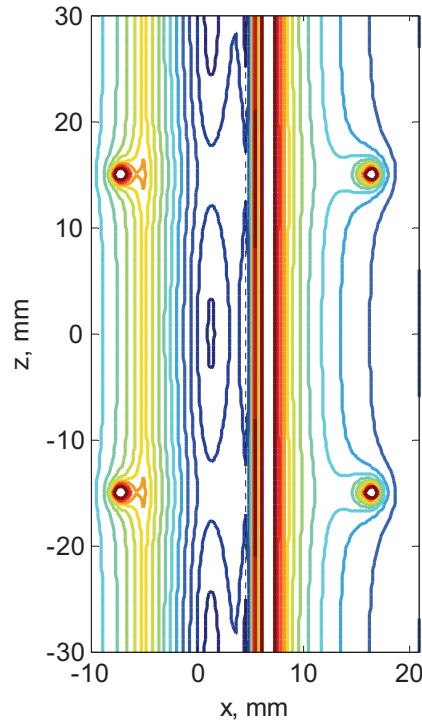


Fig. 5.13. The B-field in the xz -plane ($y = 0$) for the geometry in Fig. 5.10(b).

The magnetic field can also be illustrated in 3D by an isosurface plot such as shown in Fig. 5.14. The isosurfaces in the figure are $B_m = 3e-5$ T (blue), $B_m = 7e-5$ T (green), $B_m = 1.5e-4$ T (yellow) and $B_m = 2e-4$ T (red). The equations for infinitesimally thin rings have once again been used. It is possible that this could have shifted the red isosurface slightly where it is close to the bias rings, but the difference is not expected to be noticeable. In Fig. 5.14 there is a narrow blue isosurface inside the hole in the cylinder, although not quite at the centre of the hole, which is difficult to see. Those who are reading an electronic version of this text may be able to just see this isosurface by increasing the magnification.

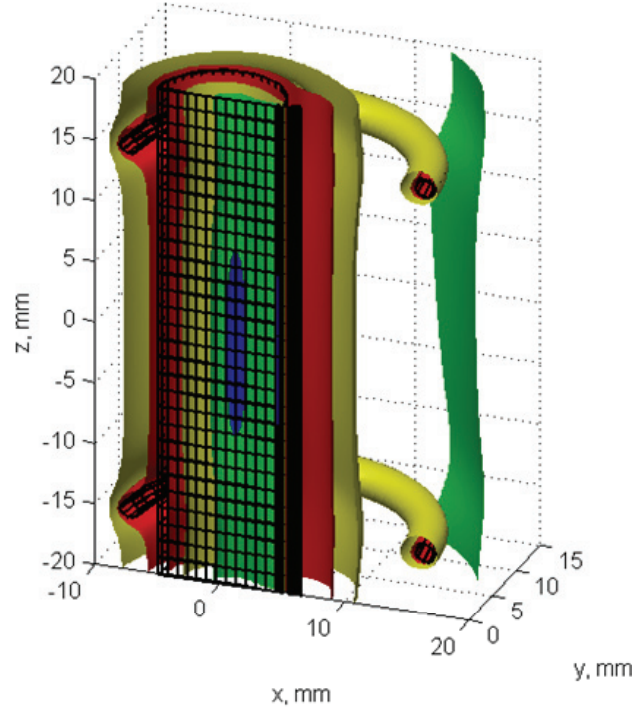


Fig. 5.14. Isosurfaces showing B_m for the cylinder with $r = 5$ mm.

Similar figures to Fig. 5.12 – Fig. 5.14 can be made for the other cylinders in Section 5.3. A snag is that the amplitude of the DC ring currents must be adjusted in each case before one sees a closed contour around the centre of the hole, such as in Fig. 5.13. Alternatively the lowest contour levels can be adjusted. As a consequence the contour plots for the different cylinders can not be compared directly. The differences between the different cylinder guides have not been found to be sufficiently interesting to justify further coverage in this text.

The existence of a field minimum inside the hole in the cylinder is of course independent of the precise amplitude of the ring currents. A plot of the effective potential temperature in the z -direction along the centre of the hole in the different cylinders is shown in Fig. 5.15. The effective potential is in this case given by the magnitude of the B-field B_m scaled by the factor $m_F \cdot \mu_b \cdot g_F$, where $m_F = 2$, $\mu_b = 9.2741\text{e-}24$ J/T, and $g_F = 0.66$. The temperature of the potential is $T = U_{\text{eff}} / k_B$ [K], where $k_B = 1.3807\text{e-}23$ J/K.

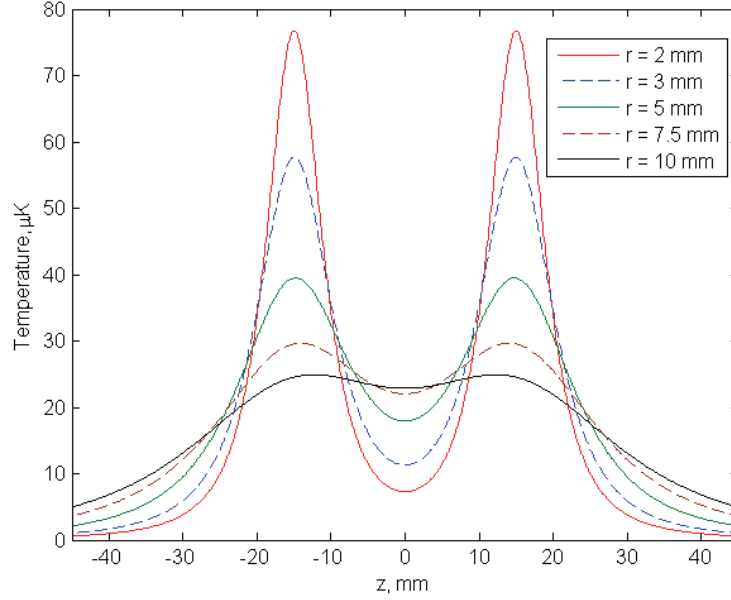


Fig. 5.15. $T = U_{\text{eff}} / k_B$ along the centre of the hole for the five cylinder guides.

Fig. 5.15 requires some further explanation. The ring currents are 0.8 A for all five graphs in the figure. The rings are placed at $z = \pm 15$ mm. The radii of the bias rings have been set so that a minimum distance of 2.25 mm is kept between the cylinder and the centre of the rings. If the bias rings have a cross-sectional radius of 0.75 mm the minimum gap between the cylinder and the rings is 1.5 mm. The ring radius is given by $r_{\text{ring}} = d_{\text{hole}} + r_{\text{cyl}} + 2.25 \times 10^{-3}$. The radius of the external wire is 0.5 mm as before. Because the wire currents in Table 5.1 for the five cylinders do not place a field zero exactly at the centre of the hole in each cylinder new wire currents have been calculated which do just that. The cylinder and wire currents, the distances from the centre of the cylinder to the centre of the hole, and the bias ring radii for the five cylinders are listed in Table 5.2.

Table 5.2. Parameters used in the calculation of the graphs in Fig. 5.15.

Cylinder radius	I_{cyl}	I_{wire}	d_{hole}	Ring radius
$r_{\text{cyl}} = 2$ mm	5.6 A	3.1677 A	1.6 mm	5.85 mm
$r_{\text{cyl}} = 3$ mm	3.6 A	1.4625 A	2.6 mm	7.85 mm
$r_{\text{cyl}} = 5$ mm	5.0 A	1.2901 A	4.6 mm	11.85 mm
$r_{\text{cyl}} = 7.5$ mm	5.4 A	0.9549 A	7.1 mm	16.85 mm
$r_{\text{cyl}} = 10$ mm	6.0 A	0.8067 A	9.6 mm	21.85 mm

The x -position of the centre of the bias rings in Fig. 5.15 has been offset one micrometre from the centre of the hole to enable the graphs to be computed. The equations for the rings were found not to be numerically stable along a line exactly through the centre of the rings in this case.

The height of the trapping barrier along the centre of the hole scales linearly with the amplitude of the DC ring currents when the ring currents are of equal magnitude. When the minimum is moved by using DC currents of different magnitude in the two rings, the larger cylinders show higher sensitivity to the difference in bias currents for a constant distance between the bias rings. The distance between the bias rings should therefore be increased by the same factor as the radius of the bias rings.

It is also seen in Fig. 5.15 that the bias rings become less effective as they become wider with increasing cylinder size. The DC ring currents should in fact also be increased by the same factor as the radius of the bias rings. If both the distance between the bias rings and the DC ring currents are scaled with the increase in the radius of the rings, the height of the trapping barrier along the z -axis stays unchanged. This is shown in Fig. 5.16. It is not so clearly seen in Fig. 5.15 due to the bias currents being in the same direction in both rings.

The scaling factors for the radius of the rings, the DC ring currents and the distances between the bias rings in Fig. 5.16 are $7.85/5.85 = 1.342$ for the cylinder with $r = 3$ mm, $11.85/5.85 = 2.026$ for the cylinder with $r = 5$ mm, $16.85/5.85 = 2.880$ for the cylinder with $r = 7.5$ mm and $21.85/5.85 = 3.735$ for the cylinder with $r = 10$ mm. The graph for the cylinder with $r = 2$ mm has a scaling factor of one.

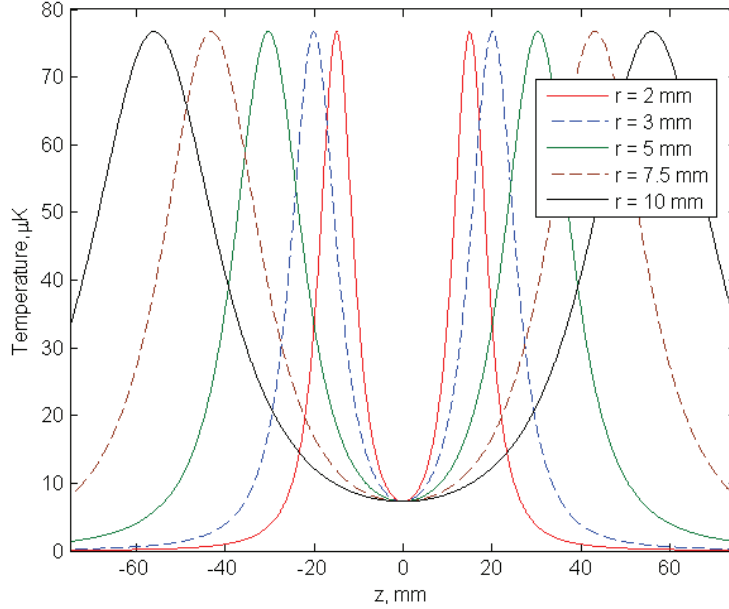


Fig. 5.16. $T = U_{\text{eff}} / k_B$ along the centre of the hole when the DC ring currents and the ring spacing have both been scaled by the same factor as the ring radius.

5.5 Conclusion

In this Chapter a new cylinder atom guide for cold matter has been presented. Pertinent analytical results have been derived including B-field equations for a cylinder with a hole and equations that can be solved for the positions of the B-field minima inside of the cylinder and the hole. Simulation results have been presented for five cylinder guides of different radii, and the shape of the trapping potential has been studied as a function of cylinder geometry. The effects of placing bias rings around the cylinder guide have also been examined and it is shown how the bias ring configuration should be scaled with cylinder size.

In Section 5.2 equations have been presented for the magnetic field of a cylinder with a hole. An equation has been derived that can be solved for either the cylinder current, the wire current or the position of the B-field zero inside the hole if the other two variables are known. The coefficients of a third order polynomial, whose only real root gives the position of a second B-field zero inside the cylinder, have also been obtained. The coefficients allow the position of the B-field zero inside the cylinder to be found numerically.

The magnetic field has been simulated for five different cylinder guides in Amperes. The same cylinder guides have afterwards been studied with the use of the equations in Section 5.2 in Matlab. There is good agreement in general between the results from Amperes and Matlab. For the biggest cylinders a small difference has however been seen in the magnitude of the B-field toward the rim of the cylinders.

It has become apparent that it is only possible to place a field zero at the centre of the hole in the cylinder when a second field zero exists further inside the cylinder. The height of the barrier between the two field zeros scales linearly with the currents in the cylinder and wire, and the distance between the field zeros depends on the size of the cylinder and the position of the hole within it. The barrier is maximized by placing the hole close to the rim of the cylinder. The radius of the hole has here been kept at 0.2 mm. Minor changes to the size of the hole are not expected to have a disproportionate effect on the main results.

The smallest cylinder guide with $r = 2$ mm had the highest barrier between the two B-field zeros for a given cylinder current. The required wire current in this case is more than 50 % of the cylinder current, although the gap between the cylinder and the wire also plays a part. If the radius of the cylinder is increased the required cylinder current for a given barrier height also increases, but the necessary wire current is reduced. The width of the barrier between the B-field zeros increases if the radius of the cylinder is increased and the hole is kept close to the cylinder rim.

The potential barrier between the B-field zeros inside the cylinder and hole is more than sufficient in all except one of the simulations for the cylinder to be used as a guide for cold matter. The potential barrier for the cylinder guide with $r = 2$ mm, $I_{\text{cyl}} = 1.6$ A and $I_{\text{wire}} = 0.9$ A is only ~ 14.4 μK , which is a little too low.

A cylinder atom guide with bias rings has been simulated in Amperes. Because results must be saved for three field components in separate simulations for the cylinder with the external wire and for the bias rings, Amperes is in this case most impractical to use. Computations in Matlab have shown that the bias rings must be centred on the hole in the cylinder to prevent the B-field minimum from being moved outside of the hole.

When the radius of the cylinder is increased the radius of the bias rings must also increase to get around the cylinder with at least a minimum gap to spare. To maintain the same trapping barrier along the centre of the hole the DC ring currents as well as the distance between the rings must be

increased by the same factor as the radius of the bias rings. The necessary bias ring currents thus increase with increasing cylinder size.

The radius of the cylinder should be chosen so that the resulting barrier width between the two B-field zeros inside the cylinder and the hole becomes acceptable. The current in the external wire must also be acceptable for the desired barrier height. One option may be to increase the wire radius a bit if this is practical. Otherwise the cylinder radius has to be increased. The cylinder radius should not be made larger than necessary since this will increase the required ring currents.

The trapping barrier along the centre of the hole is high enough to trap cold atoms inside the hole in the cylinder in all cases discussed, except for ring currents of 0.8 A and a fixed bias ring spacing of 30 mm for the cylinders with radii's of 7.5 mm and 10 mm. The cylinder guide hence seems promising as a hermetic guide for cold matter. Bias rings are however necessary, both to pump atoms along the guide and to remove the zero in the B-field inside the hole.

Chapter 6

Conclusion

In this thesis new hardware for trapping and handling of cold matter has been developed and simulated. This includes the one-wire guide, the four-wire cell trap, the dual-well trap and the wire-grids developed in Chapter 2, and the cylinder guide in Chapter 5. The research has additionally led to the discovery of the quasi-synaptic effect between two crossed wires, which opened up the possibility of cold matter transfer between the wires. The traps in Chapter 2 have been scaled down to millimetre and nanometre size in Chapter 3. A quadrupolar trap which is similar to the Ioffe-Pritchard trap except for ring currents in opposite directions has been simulated in Chapter 4.

A cylindrical minimum potential manifold exists around wires excited by DC and RF currents. Design formulas have been derived for the distance d to the minimum potential manifold around a single conductor, between two crossed conductors and between two parallel conductors. These formulas and the B-field equations for a straight conductor and an infinitesimally thin ring defined in Chapter 1 have been essential to the development of the one-wire guide and the study of prospective atom transfer between two crossed wires. It has furthermore been shown that the magnitude of the RF current does not change the effective potential along a line between two crossed or parallel wires for equal DC and RF current magnitudes in the two wires when the DC currents are of given signs and the RF currents are phase-synchronized. The equations for the distance d can accordingly be derived using only the first term under the root sign in equation (2.1) if the currents meet the given conditions.

The one-wire guide has been found to rely on bias rings placed around the wire to eliminate a potential minimum of zero and to move the circular potential minimum up or down along the wire. Strong RF bias currents have been found to be best suited to preserve the circular minimum potential and to give the highest potential gradient for a given bias current magnitude.

The minimum potential surfaces around two crossed wires have been found to touch for certain critical values of the DC currents in the two wires. The RF currents in the wires should be of the same magnitude and frequency to avoid distortion. By changing the RF current magnitudes in the bias rings around the wires the prospective transfer of cold matter between the wires has been demonstrated. The minimum potential surfaces around two parallel wires also touch for critical DC currents in opposite directions in the two wires. It is most likely not worthwhile to attempt electrically controlled transfer of cold atoms between two parallel wires since this requires the use of too many bias rings.

A novel four-wire cell trap made from two pairs of parallel wires which cross in different planes has been designed and developed. It has been optimized in Matlab, and the calculated distances between two free-standing crossed or parallel wires have been used as initial values in the optimization routine. The four-wire cell can be used to trap both strong- and weak-field-seeking atoms and may possibly be used to study collision and entanglement between the two sorts of atoms. The trapping barriers have been found to be ample in all directions. With only DC excitation the four-wire cell becomes a trap for only weak-field-seeking atoms. It then has a minimum of zero at its centre and steps must be taken to avoid Majorana spin-flip transitions.

A 3 x 3 wire structure has been designed and optimized in Matlab. It forms a double-peak/well potential that is prospective for the study of entanglement of BEC matter placed in the two wells. The trapping barrier in the direction normal to the wire-planes has been found to be worryingly small ($< 10 \mu\text{K}$) for strong-field-seeking atoms when the peaks are merged. Additional biasing may thus be necessary for this wire structure to be useful in practise.

Cell-grids which are stackable in three dimensions have been designed and optimized in Matlab. The optimization technique used has shown weaknesses for the larger structures because of limited complexity. Further improvement of the optimization is likely to require a different and better optimization scheme.

Scaling has been demonstrated to micrometre and nanometre size for a number of structures. Such scaling requires both thermally induced spin-flip transitions and the effect of the Casimir-Polder force to be taken into account. The effect of the Casimir-Polder force is minimized with the use of carbon nanotubes as conductors and the minimum feasible trapping

distance is expected to be no less than 100 nm from the surface of the nanotubes.

A four micro-wire cell and a 3 x 3 micro-wire structure adapted for future realization on a micro-machined substrate have been designed and optimized. Prospective atom transfer between two crossed nanotubes, a four-nanotube cell and several nanotube cell-grids have also been demonstrated. The depth of the trapping potential has been found to be proportional to the RF frequency. For a given geometry size the RF frequency corresponds to a certain DC current level in the conductors. If the RF frequency is increased then the DC current level must also increase to maintain the same DC current to angular frequency ratio. The trapping depth is accordingly also proportional to the DC current level in the conductors. The trapping depth is thus ultimately limited by the maximum conductor current.

A quadrupolar trap has been studied with combined DC and RF excitation of the bias rings. A circular potential minimum with four slightly deeper points has been seen to form around a local potential maximum at the centre of the trap. This ripple in the potential minimum is undesirable but does not preclude the trap from being used to trap weak-field-seeking atoms in the circular potential minimum. Trapping of weak-field-seeking atoms in the circular potential minimum requires that the DC currents in the Ioffe-bars are large enough to provide a sufficiently high potential barrier to minimum potential manifolds located just outside of the Ioffe-bars. The potential maximum at the centre of the quadrupolar trap is more than sufficient for trapping of strong-field-seeking atoms. It has also been found that the bias rings of a quadrupolar trap can be placed relatively close together to compress clouds of cold atoms into successively smaller traps. As the gap distances become very small the B-field becomes very strong between the bias rings and there is a risk of dielectric breakdown.

A new metallic cylinder atom guide has been developed and equations have been presented for the B-field inside the cylinder. Five cylinder guides of different sizes have been studied and simulations carried out in Amperes have generally been found to agree well with results computed in Matlab. It has been found that there can only be a B-field zero at the centre of the hole in the cylinder when a second field zero exists further inside the cylinder. The potential barrier between the B-field zeros is maximized by placing the hole close to the rim of the cylinder. The smallest cylinder with radius $r = 2$ mm was found to have the tallest barrier between the B-field zeros for a

given cylinder current. The width of the barrier increases with increasing cylinder radius and the necessary current in the external wire is at the same time reduced.

Bias rings used to pump cold atoms along the guide and to remove the zero in the B-field inside the hole must be centred on the hole in the cylinder. The DC ring currents and the spacing between the bias rings must be increased by the same factor as the radius of the rings when the radius of the cylinder is increased to maintain the same trapping barrier along the centre of the hole.

The single wire guide in this thesis may find application for short distance atom transport inside a vacuum chamber. Atoms may also be routed to a collision area along different crossing wires under electronic control. The four-wire cell and the quadrupolar trap with DC and RF currents are able to trap both strong- and weak-field-seeking atoms and are prospective for the study of collision and entanglement between the two types of atoms. The 3 x 3 conductor structure could be used as a matter-wave beam splitter, but further work is necessary to determine whether the effective potential topology is good enough for this purpose. The various cell-grids described in this thesis may find use as part of a quantum register in a quantum computer based on interacting drops of BEC matter. The cylinder atom guide, which can be made hermetically sealed, is well suited for atom transport outside of a vacuum chamber in a laboratory.

6.1 Suggestions for future work

The single conductor and crossed conductor geometries are by and large ready for experimental realization if simulations indicate that the specific geometry and plans for pumping cold atoms along the conductors show promise.

In the case of the four-conductor cell there are one or two additional matters to consider. One is to explore specific methods of loading the cell through simulations. To enable a practical realization the four-wire cell should also be adapted to a design suitable for planar fabrication. This requires either equations for the magnetic field for conductors with a rectangular cross-section or the use of a suitable simulation program. One possibility is to use AMPERES. But because the program requires that the field components from the DC and RF excitations must be simulated separately, two simulations are necessary. This makes it difficult to

optimize the final design except by trial and error, which becomes difficult when two variables are to be optimized simultaneously. A more suitable simulation program that can be used for both the field computations and the optimization may still be found.

The multi-cell structures may also require adaptation to a planar design in a similar way to the four-conductor cell. It may be possible to also find a better optimization technique that is more efficient and dependable especially for the larger structures.

When it comes to the nanometre-sized structures the use of a substrate and conductors with a rectangular cross-section is not so relevant. The work that remains here is to calculate the spin-flip lifetime and Casimir-Polder potential for the specific nanotube structures. This will lead to a more accurate estimate of the minimum feasible trapping distance d .

The computations and simulations done for the quadrupolar trap and the cylinder atom guides in chapters four and five of this thesis are reasonably complete. Because of an infinite number of possible current excitations and geometric variations it has been practical only to seek to obtain quite general results.

A next step in the research would be to simulate the dynamics of cold atoms and Bose-Einstein condensates by solution of the linear and non-linear Schrödinger equations for some of the guides and traps in this thesis. The linear Schrödinger equation describes the behaviour of a single cold atom in the effective potential. The non-linear Schrödinger equation is given by the Gross-Pitaevskii equation for interacting trapped cold particles. An innovative implementation of a numerical technique for solving these equations has recently been considered in [161].

Appendix A: The AMPERES software tool

The program AMPERES (Version 6.2) by Integrated Engineering Software has been used in this thesis to simulate different quadrupolar traps and the cylinder atom guide. This is a program that is not available through the university. A one month evaluation version of the program was ordered and paid for by my supervisor Professor Guennadi Kouzaev. The program fortunately continued to work until it was belatedly returned after almost six weeks. This made it possible to obtain some useful simulation results both for the cylinder atom guide and several quadrupolar trap geometries. The complete version of the program is quite expensive and would in general not be worthwhile to procure in order to simulate the geometries studied in this thesis.

AMPERES uses the boundary element method to solve for the equivalent source [162]. The equivalent source is then used to calculate potentials and fields. The program is able to compute fields and inductance and capacitance. The boundary element method requires that boundaries in the model must be discretized into individual sections known as boundary elements. Elements are required on surfaces with an assigned surface charge or boundary condition and on surfaces that separate regions with different permeability, permittivity or conductivity depending on the solver settings. A direct or iterative matrix solver is used. The program is able to simulate RF currents, but not DC and RF currents together in the same simulation.

The creation of boundary elements is for the most part handled automatically when a model is drawn and materials and currents are specified. Three dimensional shapes are usually made by expanding a two dimensional surface [163]. As explained in Chapter 5 the requirements that volume currents can only be assigned to six-sided volumes, and that a current entry surface must be defined, have turned out to be serious limitations to the applicability of the program. Some form of symmetry must often be defined in the model to accommodate these requirements. This in turn restricts the complexity of the geometries that can be modelled. The simulation results are however both accurate and quickly obtained

when the geometry can be modelled without breaking these rules. The field results are calculated only in a predefined window or plane through the geometry as shown in Fig. A.1. This means that three-dimensional field results are practically impossible to obtain, including 3D-data for use in other programs.

AMPERES has been used in this thesis to compute the total magnetic field B_m (or $|\mathbf{B}|$) or the B_x -, B_y -, and B_z -components of the magnetic field. In the latter case data files have been saved for the field components. The data in these files has afterwards been imported into Matlab through the use of specially written scripts to allow the effective potential to be calculated. Data from six files, the B_x -, B_y -, and B_z -components from both the DC simulation and the RF simulation, are usually required to calculate the effective potential. The exceptions are if certain field components happen to be zero or if there is no DC or RF excitation. Importing data into Matlab also gives access to Matlab's better and more flexible plotting options, where contour levels and line thickness and line colour can be changed and contours can be labelled to give a few examples.

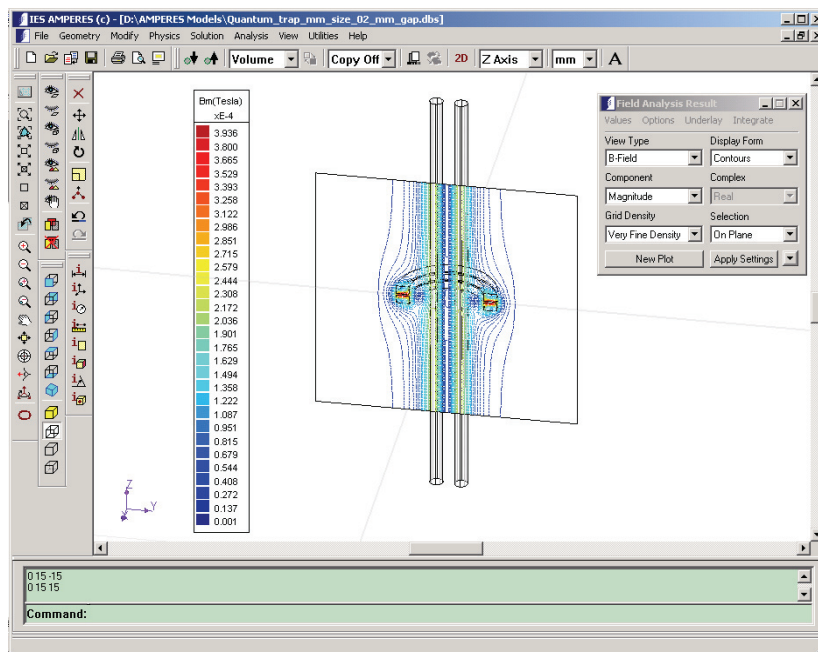


Fig. A.1. The AMPERES program window

The AMPERES program window features a drop-down menu bar at the top and different tool bars and scroll bars placed around the workspace in the middle [162]. Underneath the workspace there is a message area and a command line, which is used to input data when a model is being drawn or to specify a plot window. A status bar is found beneath the command line.

To sum up AMPERES is a program where the geometry is modelled in 3D. Some form of symmetry or anti-symmetry is usually defined for the geometry. Field results are then computed in a 2D window or plane through the geometry. The program's ability to model complex geometries is limited. It is not so clear to what extent the limitations stem from the boundary element method itself or from the specific implementation of it in the program.

To put things in perspective a Matlab based program called Comsol Multiphysics, which utilizes the finite element method, was at first attempted used to simulate a version of the Ioffe-Pritchard trap. It turned out that a relatively large volume with a fine mesh, (i.e. a large number of elements), was necessary to show the B-field around the conductors and to obtain a correct and reliable solution. As a consequence it became necessary to reduce the number of mesh points to avoid running out of computer memory. This in turn caused the solutions to become coarse and inaccurate. The simulations were in addition extremely time-consuming. This goes to show that not any computer program or simulation method is suitable for modelling the geometries described in this thesis. Other programs have not been tried for reasons of time and money.

References

- [1] V. I. Balykin, V. G. Minogin, and V. S. Letokhov, “Electromagnetic trapping of cold atoms”, *Rep. Prog. Phys.*, vol. 63, pp. 1429-1510, 2000.
- [2] P. R. Berman, and P. Hannaford, *Atom Interferometry*, Lavoisier, 1997.
- [3] W. Stern, and O. Gerlach, “Der experimentelle nachweis des magnetischen moments des silberatoms”, *Z. Phys.*, vol. 8, pp. 110-111, 1921.
- [4] H. Friedburg, and W. Paul, “Optical presentation with neutral atoms”, *Naturwiss.*, vol. 38, p. 159, 1951.
- [5] A. Lemonick, F. M. Pipkin, and D. R. Hamilton, “Focusing atomic beam apparatus”, *Rev. Sci. Instrum.*, vol. 26, pp. 1112-1119, 1955.
- [6] K-J. Kügler, W. Paul, and U. Trinks, “A magnetic storage ring for neutrons”, *Phys. Lett. B*, vol. 72B, pp. 422-424, January 1978.
- [7] K-J. Kügler, K. Moritz, W. Paul, and U. Trinks, “Nestor – A magnetic storage ring for slow neutrons”, *Nucl. Instrum. Methods A.*, vol. 228, pp. 240-258, 1985.
- [8] R. Golub, and J. M. Pendlebury, “Ultra-cold neutrons”, *Rep. Prog. Phys.*, vol. 42, pp. 439-501, 1979.
- [9] Y. V. Gott, M. S. Ioffe, and V. G. Tel’kovskii, “Some new results on confinement in magnetic traps”, *Nucl. Fusion (Suppl.)*, vol. 3, p. 1045, January 1962.
- [10] L. A. Artsimovich, “Controlled thermonuclear reactions”, (Engl. Transl. Oliver and Boyd, Edinburgh), 1964.
- [11] N. A. Krall, and A. W. Trivelpiece, *Principles of Plasma Physics*, (New York: McGraw-Hill), 1973.
- [12] V. V. Vladimirkii, “Magnetic mirrors, channels and bottles for cold neutrons”, *Zh. Eksp. Teor. Fiz.*, vol. 39, pp. 1062-1070, 1960.
- [13] C. V. Heer, “Feasibility of containment of quantum magnetic dipoles”, *Rev. Sci. Instrum.*, vol. 34, p. 531, May 1963.
- [14] V. S. Letokhov, and V. G. Minogin, “Possibility of accumulation and storage of gold atoms in magnetic traps”, *Opt. Commun.*, vol. 35, pp. 199-202, 1980.
- [15] D. E. Pritchard, “Cooling neutral atoms in a magnetic trap for precision spectroscopy”, *Phys. Rev. Lett.*, vol. 51, p. 1336, 1983.

- [16] H. J. Metcalf, "Magnetic trapping of decelerated neutral atoms", *Prog. Quantum Electron.*, vol. 8, pp. 169-175, 1984.
- [17] T. Bergeman, G. Erez, and H. J. Metcalf, "Magnetostatic trapping fields for neutral atoms", *Phys. Rev. A*, vol. 35, pp. 1535-1546, 1987.
- [18] V. S. Letokhov, "Narrowing of the Doppler width in a standing light wave", *Pis. Zh. Eksp. Teor. Fiz.*, vol. 7, p. 348, (Engl. Transl. *1968 JETP Lett.*, vol. 7, p. 272), 1968.
- [19] A. P. Kazantsev, *Zh. Eksp. Teor. Fiz.*, vol. 63, p. 1628, 1972, [*Sov. Phys. JETP*, vol. 36, p. 861, 1973].
- [20] V. S. Letokhov, and B. D. Pavlik, "Spectral line narrowing in a gas by atoms trapped in a standing light wave", *Appl. Phys. A*, vol. 9, pp. 229-237, March 1976.
- [21] A. Ashkin, "Acceleration and trapping of particles by radiation pressure", *Phys. Rev. Lett.*, vol. 24, pp. 156-159, 1970.
- [22] A. Ashkin, "Applications of laser radiation pressure", *Science*, vol. 210, pp. 1081-1088, December 1980.
- [23] A. Ashkin, *Laser in Life Sciences*, Berichte der Bunsen-Gesellschaft für Physikalische Chemie, Band 93 N3, pp. 255-260, 1988.
- [24] W. E. Lamb Jr., "Theory of an optical maser", *Phys. Rev. A*, vol. 134, pp. 1429-1450, 1964.
- [25] P. H. Lee, and M. L. Skolnick, "Saturated neon absorption inside a 6238-A laser", *Appl. Phys. Lett.*, vol. 10, p. 303, June 1967.
- [26] V. S. Letokhov, "Self-stabilization of laser optic-oscillator frequency by nonlinear absorption in gas", *Pis. Zh. Eksp. Teor. Fiz.*, vol. 6, pp. 597-600, August 1967.
- [27] V. N. Lisitsyn, and V. P. Chebotaev, "Hysteresis and 'hard' excitation in a gas laser", *Zh. Eksp. Teor. Fiz. Pis'ma*, vol. 7, p. 3, (Engl. Transl. *1968 JETP Lett.*, vol. 7, pp. 1-3), 1968.
- [28] R. L. Barger, and J. L. Hall, "Pressure shift and broadening of methane line at 3.39 μ studied by laser-saturated molecular absorption", *Phys. Rev. Lett.*, vol. 22, pp. 4-8, January 1969.
- [29] C. J. Bordè, "Spectroscopie d'absorption saturée de diverses molécules au moyen des lasers à gaz carbonique et à protoxyde d'azote", *C. R. Acad. Sc. Paris*, vol. 271B, pp. 371-374, 1970.
- [30] L. S. Vasilenko, V. P. Chebotaev, and A. V. Shishaev, "Line shape of two-photon absorption in a standing-wave field in a gas", *Pis. Zh. Eksp. Teor. Fiz.*, vol. 12, p. 113, (Engl. Transl. *1970 JETP Lett.*, vol. 12, pp. 113-116), 1970.
- [31] V. S. Letokhov, "Nonlinear high resolution laser spectroscopy", *Science*, vol. 190, pp. 344-351, 1975.

- [32] R. Grimm, M. Weidemüller, and Y. B. Ovchinnikov, “Optical dipole traps for neutral atoms”, *Adv. At. Mol. Opt. Phys.*, vol. 42, 95, 2000.
- [33] T. W. Hänsch, and A. L. Shawlow, “Cooling of gases by laser radiation”, *Opt. Commun.*, vol. 13, pp. 68-69, 1975.
- [34] V. S. Letokhov, V. G. Minogin, and B. D. Pavlik, “Cooling and trapping of atoms and molecules by a resonant laser field”, *Opt. Commun.*, vol. 19, pp. 72-75, 1976.
- [35] V. S. Letokhov, V. G. Minogin, and B. D. Pavlik, “Cooling and capture of atoms and molecules by a resonant light field”, *Zh. Eksp. Teor. Fiz.*, vol. 72, p. 1328, (Engl. Transl. *Sov. Phys. – Journal Exp. Theor. Phys.*, vol. 45, p. 698), 1977.
- [36] V. I. Balykin, V. S. Letokhov, and V. I. Mushin, “Observation of the cooling of free sodium atoms in a resonance laser field with a scanning frequency”, *Pis. Zh. Eksp. Teor. Fiz.*, vol. 29, p. 614, (Engl. Transl. *1979 JETP Lett.*, vol. 29, pp. 560-564), 1979.
- [37] V. I. Balykin, V. S. Letokhov, and V. I. Mishin, “Cooling of sodium atoms by resonant laser radiation”, *Zh. Eksp. Teor. Fiz.*, vol. 78, pp. 1376-1385, April 1980.
- [38] V. I. Balykin, V. S. Letokhov, and A. I. Sidorov, “Formation of an intense steady flux of cold atoms by the laser slowing of an atomic beam”, *Zh. Eksp. Teor. Fiz.*, vol. 86, p. 2019, (Engl. Transl. *Sov. Phys. – JETP*, vol. 59, pp. 1174-1179), 1984.
- [39] S. V. Andreev, V. I. Balykin, V. S. Letokhov, and V. G. Minogin, “Radiative slowing and reduction of the energy spread of a beam of sodium atoms to 1.5 K in an oppositely directed laser beam”, *Pis. Zh. Eksp. Teor. Fiz.*, vol. 34, p. 463, (Engl. Transl. *1981 JETP Lett.*, vol. 34, pp. 442-445), 1981.
- [40] S. V. Andreev, V. I. Balykin, V. S. Letokhov, and V. G. Minogin, “Radiative slowing down and monochromatization of a beam of sodium atoms in a counterpropagating laser beam”, *Pis. Zh. Eksp. Teor. Fiz.*, vol. 82, p. 1429, (Engl. Transl. *Sov. Phys. – JETP*, vol. 55, pp. 828-834), 1982.
- [41] W. D. Phillips, and H. Metcalf, “Laser deceleration of an atomic beam”, *Phys. Rev. Lett.*, vol. 48, pp. 596-599, 1982.
- [42] J. V. Prodan, W. D. Phillips, and H. Metcalf, “Laser production of a very slow monoenergetic atomic beam”, *Phys. Rev. Lett.*, vol. 49, pp. 1149-1153, 1982.

- [43] S. Chu, L. Hollberg, J. E. Bjorkholm, A. Cable, and A. Ashkin, “Three-dimensional viscous confinement and cooling of atoms by resonance radiation pressure”, *Phys. Rev. Lett.*, vol. 55, pp. 48-51, 1985.
- [44] P. D. Lett, R. N. Watts, C. I. Westbrook, W. D. Phillips, P. L. Gould, and H. J. Metcalf, “Observation of atoms laser cooled below the Doppler limit”, *Phys. Rev. Lett.*, vol. 61, pp. 169-172, 1988.
- [45] V. S. Letokhov, and V. G. Minogin, “Laser radiation pressure on free atoms”, *Phys. Rep.*, vol. 73, pp. 1-65, 1981.
- [46] V. I. Balykin, V. S. Letokhov, and V. G. Minogin, “Cooling atoms by means of laser radiation pressure”, *Usp. Fiz. Nauk.*, vol. 147, p. 117, (Engl. Transl. *Sov. Phys. – Usp.*, vol. 28, pp. 803-826), 1985.
- [47] C. S. Adams, and E. Riis, “Laser cooling and trapping of neutral atoms”, *Prog. Quantum Electron.*, vol. 21, pp. 1-79, 1997.
- [48] W. D. Phillips, “Laser cooling and trapping of neutral atoms”, *Rev. Mod. Phys.*, vol. 70, pp. 721-741, 1998.
- [49] J. Dalibard, and C. Cohen-Tannoudji, “Laser cooling below the Doppler limit by polarization gradients: Simple theoretical models”, *J. Opt. Soc. Am. B*, vol. 6, pp. 2023-2045, November 1989.
- [50] P. J. Ungar, D. S. Weiss, E. Riis, and S. Chu, “Optical molasses and multilevel atoms: Theory”, *J. Opt. Soc. Am. B*, vol. 6, pp. 2058-2071, November 1989.
- [51] S. Chang, B. M. Garraway, and V. G. Minogin, “Deep cooling of three-level atoms in two standing waves”, *Opt. Commun.*, vol. 77, pp. 19-25, 1990.
- [52] S. Chang, B. M. Garraway, and V. G. Minogin, “Dynamics of five-level atoms in two standing electromagnetic waves”, *J. Phys. Soc. Jpn.*, vol. 59, pp. 3155-3166, 1990.
- [53] S. Chang, T. Y. Kwon, H. S. Lee, and V. G. Minogin, “Light-induced ground-state coherence, constructive interference, and two-photon laser cooling mechanism in multilevel atoms”, *Phys. Rev. A*, vol. 60, pp. 2308-2311, September 1999.
- [54] S. Chang, T. Y. Kwon, H. S. Lee, and V. G. Minogin, “Two-photon laser-cooling mechanism in multilevel interaction schemes”, *Phys. Rev. A*, vol. 60, pp. 3148-3159, October 1999.
- [55] C. Cohen-Tannoudji, “Nobel lecture: Manipulating atoms with photons”, *Rev. Mod. Phys.*, vol. 70, pp. 707-719, July 1998.
- [56] J. W. Jun, S. Chang, T. Y. Kwon, H. S. Lee, and V. G. Minogin, “Kinetic theory of the magneto-optical trap for multilevel atoms”, *Phys. Rev. A*, vol. 60, pp. 3960-3972, 1999.

- [57] J. W. Jun, S. Chang, H. S. Lee, V. G. Minogin, and W. Jhe, “Double-structure potential due to multiphoton processes in a magneto-optical trap”, *Phys. Rev. A*, vol. 60, pp. 4738-4742, 1999.
- [58] A. Aspect, E. Arimondo, R. Kaiser, N. Vansteenkiste, and C. Cohen-Tannoudji, “Laser cooling below the one-photon recoil energy by velocity-selective coherent population trapping”, *Phys. Rev. Lett.*, vol. 61, pp. 826-829, 1988.
- [59] M. Kasevich, and S. Chu, “Laser cooling below a photon recoil with three-level atoms”, *Phys. Rev. Lett.*, vol. 69, pp. 1741-1744, 1992.
- [60] J. Lawall, S. Kulin, F. Bardou, B. Saubamea, N. Bigelow, M. Leduc, and C. Cohen-Tannoudji, “Three-dimensional laser cooling of helium beyond the single-photon recoil limit”, *Phys. Rev. Lett.*, vol. 75, pp. 4194-4197, 1995.
- [61] H. J. Lee, C. S. Adams, M. Kasevich, and S. Chu, “Raman cooling of atoms in an optical dipole trap”, *Phys. Rev. Lett.*, vol. 76, pp. 2658-2661, 1996.
- [62] A. L. Migdal, J. V. Prodan, W. D. Phillips, T. H. Bergeman, and H. J. Metcalf, “First observation of magnetically trapped neutral atoms”, *Phys. Rev. Lett.*, vol. 54, pp. 2596-2599, 1985.
- [63] M. H. Anderson, J. R. Ensher, M. R. Matthews, C. E. Wieman, and E. A. Cornell, “Observation of Bose-Einstein condensation in a dilute atomic vapor”, *Science*, vol. 269, pp. 198-201, July 1995.
- [64] W. Petrich, M. H. Anderson, J. R. Ensher, and E. A. Cornell, “Stable, tightly confining magnetic trap for evaporative cooling of neutral atoms”, *Phys. Rev. Lett.*, vol. 74, pp. 3352-3355, 1995.
- [65] K. B. Davis, M.-O. Mewes, M. R. Andrews, N. J. van Druten, D. S. Durfee, D. M. Kurn, and W. Ketterle, “Bose-Einstein condensation in a gas of sodium atoms”, *Phys. Rev. Lett.*, vol. 75, p. 3969, 1995.
- [66] C. C. Bradley, C. A. Sackett, J. J. Tollett, and R. G. Hulet, “Evidence of Bose-Einstein condensation in an atomic gas with attractive interactions”, *Phys. Rev. Lett.*, vol. 75, p. 1687, August 1995.
- [67] R. J. Cook, “Quantum-mechanical fluctuations of the resonance-radiation force”, *Phys. Rev. Lett.*, vol. 44, pp. 976-979, April 1980.
- [68] R. J. Cook, “Theory of resonance-radiation pressure”, *Phys. Rev. A*, vol. 22, pp. 1078-1098, September 1980.
- [69] J. P. Gordon, and A. Ashkin, “Motion of atoms in a radiation trap”, *Phys. Rev. A*, vol. 21, pp. 1606-1617, May 1980.
- [70] J. Dalibard, S. Reynaud, and C. Cohen-Tannoudji, “Proposals of stable optical traps for neutral atoms”, *Opt. Commun.*, vol. 47, pp. 395-399, October 1983.

- [71] J. Dalibard, S. Reynaud, and C. Cohen-Tannoudji, "Potentialities of a new σ_+ - σ_- laser configuration for radiative cooling and trapping", *J. Phys. B: At. Mol. Phys.*, vol. 17, pp. 4577-4594, 1984.
- [72] R. V. E. Lovelace, C. Mehanian, T. J. Tommila, and D. M. Lee, "Magnetic confinement of a neutral gas", *Nature*, vol. 318, p. 30, November 1985.
- [73] E. A. Cornell, C. Monroe, and C. E. Wieman, "Multiply loaded, ac magnetic trap for neutral atoms", *Phys. Rev. Lett.*, vol. 67, pp. 2439-2442, October 1991.
- [74] M. Morinaga, and F. Shimizu, *Laser Phys.*, vol. 4, p. 412, 1994.
- [75] V. G. Minogin, and J. Javanainen, "A tetrahedral light pressure trap for atoms", *Opt. Commun.*, vol. 43, pp. 119-122, September 1982.
- [76] A. Ashkin, and J. P. Gordon, "Stability of radiation-pressure particle traps: An optical Earnshaw theorem", *Opt. Lett.*, vol. 8, p. 511-513, October 1983.
- [77] J. Dalibard, Personal communication to V. I. Balykin, 1987.
- [78] E. L. Raab, M. Prentiss, A. Cable, S. Chu, and D. E. Pritchard, "Trapping of neutral sodium atoms with radiation pressure", *Phys. Rev. Lett.*, vol. 59, pp. 2631-2634, December 1987.
- [79] R. J. Cook, and R. K. Hill, "An electromagnetic mirror for neutral atoms", *Opt. Commun.*, vol. 43, pp. 258-260, October 1982.
- [80] M. A. Ol'Shanii, Yu. B. Ovchinnikov, and V. S. Letokhov, "Laser guiding of atoms in a hollow optical fiber", *Opt. Commun.*, vol. 98, pp. 77-79, April 1993.
- [81] C. M. Savage, S. Marksteiner, and P. Zoller, "Atomic waveguides and cavities from hollow optical fibers", *Fundamentals of Quantum Optics III, Lecture Notes in Physics*, vol. 420, p. 60, ISBN 978-3-540-57218-3, Springer, 1993.
- [82] S. Marksteiner, C. M. Savage, P. Zoller, and S. L. Rolston, "Coherent atomic waveguides from hollow optical fibers: Quantized atomic motion", *Phys. Rev. A*, vol. 50, pp. 2680-2690, September 1994.
- [83] M. J. Renn, D. Montgomery, O. Vdovin, D. Z. Anderson, C. E. Wieman, and E. A. Cornell, "Laser-guided atoms in hollow-core optical fibers", *Phys. Rev. Lett.*, vol. 75, pp. 3253-3256, 1995.
- [84] M. J. Renn, E. A. Donley, E. A. Cornell, C. E. Wieman, and D. Z. Anderson, "Evanescent-wave guiding of atoms in hollow optical fibers", *Phys. Rev. A*, vol. 53, pp. R648-R651, February 1996.

- [85] H. Ito, T. Nakata, K. Sakaki, M. Ohtsu, K. I. Lee, and W. Jhe, "Laser spectroscopy of atoms guided by evanescent waves in micron-sized hollow optical fibers", *Phys. Rev. Lett.*, vol. 76, pp. 4500-4503, June 1996.
- [86] F. K. Fatemi, M. Bashkansky, and S. Moore, "Side-illuminated hollow-core optical fiber for atom guiding", *Optics Express*, vol. 13, pp. 4890-4895, June 2005.
- [87] H. Wallis, J. Dalibard, and C. Cohen-Tannoudji, "Trapping atoms in a gravitational cavity", *Appl. Phys. B*, vol. 54, pp. 407-419, 1992.
- [88] C. G. Aminoff, A. M. Steand, P. Bouyer, P. Desbiolles, J. Dalibard, and C. Cohen-Tannoudji, "Cesium atoms bouncing in a stable gravitational cavity", *Phys. Rev. Lett.*, vol. 71, pp. 3083-3086, 1993.
- [89] Yu. B. Ovchinnikov, J. Söding, and R. Grimm, "Cooling atoms in dark gravitational laser traps", *Pis. Zh. Eksp. Teor. Fiz.*, vol. 61, pp. 23-27, (Engl. Transl. 1995 *JETP Lett.*, vol. 61, pp. 21-26), 1995.
- [90] J. Söding, R. Grimm, and Yu. B. Ovchinnikov, "Gravitational laser trap for atoms with evanescent-wave cooling", *Opt. Commun.*, vol. 119, pp. 652-662, September 1995.
- [91] J. P. Dowling, and J. Gea-Banacloche, "Schrödinger modal structure of cubical, pyramidal, and conical, evanescent light-wave gravitational atom traps", *Phys. Rev. A*, vol. 52, pp. 3997-4003, November 1995.
- [92] J. D. Weinstein, and K. G. Libbrecht, "Microscopic magnetic traps for neutral atoms", *Phys. Rev. A*, vol. 52, pp. 4004-4009, Nov. 1995.
- [93] J. H. Thywissen, M. Olshanii, G. Zabow, M. Drndic, K. S. Johnson, R. M. Westervelt, and M. Prentiss, "Microfabricated magnetic waveguides for neutral atoms", *Eur. Phys. J.*, vol. D7, p. 361, 1999.
- [94] N. H. Dekker, C. S. Lee, V. Lorent, J. H. Thywissen, S. P. Smith, M. Drndic, R. M. Westervelt, and M. Prentiss, "Guiding neutral atoms on a chip", *Phys. Rev. Lett.*, vol. 84, p. 1124, 2000.
- [95] J. A. Sauer, M. D. Barrett, and M. S. Chapman, "Storage ring for neutral atoms", *Phys. Rev. Lett.*, vol. 87, No. 270401, Dec. 2001.
- [96] J. Reichel, W. Hänsel, and T. W. Hänsch, "Atomic micromanipulation with magnetic surface traps", *Phys. Rev. Lett.*, vol. 83, p. 3398, 1999.
- [97] W. Hänsel, P. Hommelhoff, T. W. Hänsch, and J. Reichel, "Bose-Einstein condensation on a microelectronic chip", *Nature*, vol. 413, pp. 498-501, 2001.

- [98] H. Ott, J. Fortagh, G. Schlotterbeck, A. Grossmann, and C. Zimmermann, “Bose-Einstein condensation in a surface microtrap”, *Phys. Rev. Lett.*, vol. 87, No. 230401, 2001.
- [99] P. Krüger, X. Luo, M. W. Klein, K. Brugger, A. Haase, S. Wildermuth, S. Groth, I. Bar-Joseph, R. Folman, and J. Schmiedmayer, “Trapping and manipulating neutral atoms with electrostatic fields”, *Phys. Rev. Lett.*, vol. 91, No. 233201, 2003.
- [100] D. Cassettari, B. Hessmo, R. Folman, T. Maier, and J. Schmiedmayer, “Beam splitter for guided atoms”, *Phys. Rev. Lett.*, vol. 85, pp. 5483-5487, 2000.
- [101] D. Müller, E. A. Cornell, M. Prevedelli, P. D. D. Schwindt, A. Zozulya, and D. Z. Anderson, “Waveguide atom beam splitter for laser-cooled neutral atoms”, *Opt. Lett.*, vol. 25, pp. 1382-1384, September 2000.
- [102] P. Hommelhoff, W. Hänsel, T. Steinmetz, T. W. Hänsch, and J. Reichel, “Transporting, splitting and merging of atomic ensembles in a chip trap”, *New J. Phys.*, vol. 7, p. 3, 2005.
- [103] Y. Shin, C. Sanner, G.-B. Jo, T. A. Pasquini, M. Saba, W. Ketterle, and D. E. Pritchard, “Interference of Bose-Einstein condensates split with an atom chip”, *Phys. Rev. A*, vol. 72, No. 021604, 2005.
- [104] O. Zobay, and B. M. Garraway, “Two-dimensional atom trapping in field-induced adiabatic potentials”, *Phys. Rev. Lett.*, vol. 86, pp. 1195-1198, February 2001.
- [105] H. F. Hess, “Evaporative cooling of magnetically trapped and compressed spin-polarized hydrogen”, *Phys. Rev. B.*, vol. 34, p. 3476, 1986.
- [106] Y. Colombe, E. Knyazchyan, O. Morizot, B. Mercier, V. Lorent, and H. Perrin, “Ultracold atoms confined in rf-induced two-dimensional trapping potentials”, *Europhys. Lett.*, vol. 67, pp. 593-599, 2004.
- [107] T. Schumm, S. Hofferberth, L.M. Andersson, S. Wildermuth, S. Groth, I. Bar-Joseph, J. Schmiedmayer, and P. Krüger, “Matter-wave interferometry in a double well on an atom chip”, *Nature*, vol. 1, October 2005.
- [108] M. Albiez, R. Gati, J. Fölling, S. Hunsmann, M. Cristiani, and M. K. Oberthaler, “Direct observation of tunnelling and nonlinear self-trapping in a single bosonic Josephson junction”, *Phys. Rev. Lett.*, vol. 95, No. 010402, 2005.

- [109] I. Lesanovsky, T. Schumm, S. Hofferberth, L. M. Andersson, P. Krüger, and J. Schmiedmayer, “Adiabatic radio-frequency potentials for the coherent manipulation of matter waves”, *Phys. Rev. A*, vol. 73, No. 033619, 2006.
- [110] O. Morizot, Y. Colombe, V. Lorent, H. Perrin, and B. M. Garraway, “Ring trap for ultracold atoms”, *Phys. Rev. A*, vol. 74, No. 023617, 2006.
- [111] Ph. W. Courteille, B. Deh, J. Fortágh, A. Günther, S. Kraft, C. Marzok, S. Slama, and C. Zimmermann, “Highly versatile atomic micro traps generated by multifrequency magnetic field modulation”, *J. Phys. B: At. Mol. Opt. Phys.*, vol. 39, pp. 1055-1064, 2006.
- [112] J. Billy, V. Josse, Z. Zuo, A. Bernard, B. Hambrecht, P. Lugan, D. Clément, L. Sanchez-Palencia, P. Bouyer, and A. Aspect, “Direct observation of Anderson localization of matter-waves in a controlled disorder”, *Nature (London)*, vol. 453, p. 891, 2008.
- [113] G. Roati, C. D’Errico, L. Fallani, M. Fattori, C. Fort, M. Zaccanti, G. Modugno, M. Modugno, and M. Inguscio, “Anderson localization of a non-interacting Bose-Einstein condensate”, *Nature*, vol. 453, pp. 895-898, 2008.
- [114] R. Gerritsma, and R. J. C. Spreeuw, “Topological constraints on magnetostatic traps”, *Phys. Rev. A*, vol. 74, No. 043405, 2006.
- [115] I. Lesanovsky, and W. von Klitzing, “Time-averaged adiabatic potentials: Versatile traps and waveguides for ultracold quantum gases”, *arXiv: cond-mat/0612213v1*, 8. Dec. 2006.
- [116] M. Gildemeister, E. Nugent, B. E. Sherlock, M. Kubasik, B. T. Sheard, and C. J. Foot, “Trapping ultracold atoms in a time-averaged adiabatic potential”, *Phys. Rev. A*, vol. 81, No. 031402(R), 2010.
- [117] D. A. Allwood, T. Schrefl, G. Hrkac, I. G. Hughes, and C. S. Adams, “Mobile atom traps using magnetic nanowires”, *Appl. Phys. Lett.*, vol. 89, No. 014102, 2006.
- [118] R. Fermani, S. Scheel, and P. L. Knight, “Trapping cold atoms near carbon nanotubes: Thermal spin flips and Casimir-Polder potential”, *Phys. Rev. A*, vol. 75, No. 062905, 2007.
- [119] C. Henkel, and M. Wilkens, “Heating of trapped atoms near thermal surfaces”, *Europhys. Lett.*, vol. 47, pp. 414-420, 1999.
- [120] A. T. Fromhold Jr., *Quantum Mechanics for Applied Physics and Engineering*, ISBN 0-486-66741-3, Dover Publications Inc., 1991.
- [121] P. L. Gould, G. A. Ruff, and D. E. Pritchard, “Diffraction of atoms by light: The near-resonant Kapitza-Dirac Effect”, *Phys. Rev. Lett.*, vol. 56, pp. 827-830, 1986.

- [122] F. Dalfovo, S. Giorgini, L. P. Pitaevskii, and S. Stringari, “Theory of Bose-Einstein condensation in trapped gases”, *Rev. Mod. Phys.*, vol. 71, pp. 463-512, April 1999.
- [123] B. Lu, and W. A. van Wijngaarden, “Bose-Einstein condensation in a QUIC trap”, *Can. Jour. Phys.*, <http://cjp.nrc.ca/>, 8. March 2004.
- [124] S. Kragset, E. Babaev, and A. Sudbø, “Thermal fluctuations of vortex matter in trapped Bose-Einstein condensates”, *Phys. Rev. Lett.*, vol. 97, No. 170403, 2006.
- [125] C. A. Sackett, “Cold meeting at a junction”, *Nature*, vol. 449, p. 546, October 2007.
- [126] S. Levy, E. Lahoud, I. Shomroni, and J. Steinhauer, “The a.c. and d.c. Josephson effects in a Bose-Einstein condensate”, *Nature*, vol. 449, pp. 579-583, October 2007.
- [127] M. A. Nielsen, and I. L. Chuang, *Quantum Computation and Quantum Information*, (Ninth printing 2007), ISBN 0-521-63503-9, Cambridge University Press, 2000.
- [128] P. W. Shor, “Algorithms for quantum computation: Discrete logarithms and factoring”, in *Proc. 35th Annual Symposium on Foundations of Computer Science, Los Alamitos, CA*, IEEE Computer Society Press, New York, pp. 124-134, 1994.
- [129] L. K. Grover, “A fast quantum mechanical algorithm for database search”, in *Proc. 28th Annual Symposium on the Theory of Computing, Philadelphia, PA*, ACM Press, New York, pp. 212-218, 1996.
- [130] P. Domokos, J. M. Raimond, M. Brune, and S. Haroche, “Simple cavity-QED two-bit universal quantum logic gate: The principle and expected performances”, *Phys. Rev. Lett.*, vol. 52, p. 3554, 1995.
- [131] R. Blatt, and D. Wineland, “Entangled states of trapped atomic ions”, *Nature*, vol. 453, pp. 1008-1015, 2008.
- [132] J. E. Mooij, T. P. Orlando, L. Levitov, L. Tian, C. H. van der Wal, and S. Lloyd, “Josephson persistent-current qubit”, *Science*, vol. 285, pp. 1036-1039, August 1999.
- [133] G.K. Brennen, C. M. Caves, P. S. Jessen, and I. H. Deutsch, “Quantum logic gates in optical lattices”, *Phys. Rev. Lett.*, vol. 82, pp. 1060-1063, February 1999.
- [134] B. E. Kane, “A silicon-based nuclear spin quantum computer”, *Nature*, vol. 393, pp. 133-137, May 1998.

- [135] R. Vrijen, E. Yablonovitch, K. Wang, H. W. Jiang, A. Balandin, V. Roychowdhury, T. Mor, and D. DiVincenzo, "Electron-spin-resonance transistors for quantum computing in silicon-germanium heterostructures", *Phys. Rev. A*, vol. 62, No. 012306, 2000.
- [136] J. Denschlag, D. Cassettari, A. Chenet, S. Schneider, and J. Schmiedmayer, "A neutral atom and a wire: Towards mesoscopic atom optics", *Appl. Phys. B*, vol. 69, pp. 291-301, 1999.
- [137] G. A. Kouzaev, and K. J. Sand, "RF controllable Ioffe-Pritchard trap", *arXiv: cond-mat/0602210v3*, 9. Feb. 2006.
- [138] G. A. Kouzaev, and K. J. Sand, "RF controllable Ioffe-Pritchard trap for cold dressed atoms", *Mod. Phys. Lett. B*, vol. 21, p. 59-68, January 2007.
- [139] K. R. Demarest, *Engineering Electromagnetics*, Prentice Hall, 1998.
- [140] J. Reichel, "Microchip traps and Bose-Einstein condensation", *Appl. Phys. B*, vol. 75, pp.469-487, 2002.
- [141] J. Dellacontrada, "UB engineers target nanoelectronics", <http://www.buffalo.edu/ubreporter/archives/vol37/vol37n21/articles/Nanoelectronics.html>, 16. February, 2006.
- [142] K. Eichele, "Euler Angles", <http://anorganik.uni-tuebingen.de/klaus/nmr/conventions/euler/euler.html>, 17. October 2007.
- [143] O. Zobay, and B. M. Garraway, "Atom trapping and two-dimensional Bose-Einstein condensates in field-induced adiabatic potentials", *Phys. Rev. A*, vol. 69, No. 023605, 2004.
- [144] I. Lesanovsky, S. Hofferberth, J. Schmiedmayer, and P. Schmelcher, "Manipulation of ultracold atoms in dressed adiabatic radio-frequency potentials", *Phys. Rev. A*, vol. 74, No. 033619, 2006.
- [145] N. R. Thomas, C. J. Foot, and A. C. Wilson, "Double-well magnetic trap for Bose-Einstein condensates", *Phys. Rev. A*, vol. 65, No. 063406, 2002.
- [146] G. A. Kouzaev, and K. J. Sand., "Inter-wire transfer of cold dressed atoms", *Modern Phys. Lett. B*, vol. 21, pp. 1653-1665, 2007.
- [147] G. A. Kouzaev, and K. J. Sand., "Quasi-synaptic effect to control the cold matter transfer", *NeuroQuantology*, vol. 6, p. 22, March 2008.
- [148] K. J. Sand, and G. A. Kouzaev, "Controlling the cold matter by the RF and DC fields", *Selected Papers from the WSEAS Conf. in Istanbul, Turkey*, p. 90, May 27-30, 2008.
- [149] C. Henkel, S. Pötting, and M. Wilkens, "Loss and heating of particles in small and noisy traps", *Appl. Phys. B*, vol. 69, pp. 379-387, 1999.

- [150] P. K. Rekdal, S. Scheel, P. L. Knight, and E. A. Hinds, “Thermal spin flips in atom chips”, *Phys. Rev. A*, vol. 70, No. 013811, 2004.
- [151] G. A. Kouzaev, and K. J. Sand, “3D multicell designs for registering of Bose-Einstein condensate clouds”, *Modern Phys. Lett. B*, vol. 22, pp. 2469-2479, 2008.
- [152] H. B. G. Casimir, and D. Polder, “The influence of retardation on the London-van der Waals forces”, *Phys. Rev.*, vol. 73, p. 360, 1947.
- [153] S. Y. Buhmann, L. Knöll, D.-G. Welsch, and H. T. Dung, “Casimir-Polder forces: A nonperturbative approach”, *Phys. Rev. A*, vol. 70, No. 052117, 2004.
- [154] S. Y. Buhmann, H. T. Dung, and D.-G. Welsch, “The van der Waals energy of atomic systems near absorbing and dispersing bodies”, *J. Opt. B: Quantum Semiclass.*, Opt. 6, pp. S127-S135, 2004.
- [155] A. Goodsell, T. Ristroph, J. A. Golovchenko, and L. V. Hau, “Field ionization of cold atoms near the wall of a single carbon nanotube”, *Phys. Rev. Lett.*, vol. 104, No. 133002, 2010.
- [156] D. Kielpinski, C. Monroe, and D. J. Wineland, “Architecture for a large-scale ion-trap quantum computer”, *Nature*, vol. 417, p. 709, 2002.
- [157] M. White, H. Gao, M. Pasienski, and B. DeMarco, “Bose-Einstein condensates in rf-dressed adiabatic potentials”, *Phys. Rev. A*, vol. 74, No. 023616, 2006.
- [158] K. J. Sand, and G. A. Kouzaev, “Numerical simulations of the Ioffe-Pritchard trap for cold dressed atoms”, *Wave Processes and Radiotechnical Systems*, vol. 10, p. 53, 2007.
- [159] L. Yung-kuo, *Problems and Solutions on Electromagnetism*, Univ. of Science and Technology of China, pp. 178-179, World Scientific.
- [160] “Wave-guide: Magnetic atom guides and atom transport”, <http://cold-atoms.physics.lsa.umich.edu/projects/waveguide/genguides.html>.
- [161] G. A. Kouzaev, “Co-design of quantum and electronic integrations by available circuit simulators”, *Proc. Of the 13th WSEAS Int. Conf. on CIRCUITS*, ISBN 960-474-096-3, p. 152, 2009.
- [162] AMPERES *Program Guide*, Integrated Engineering Software Inc.
- [163] AMPERES *Quick Start Guide*, Integrated Engineering Software Inc., Winnipeg, 2005.